KINETIC AND TRANSPORT MODELING IN PROTON EXCHANGE MEMBRANE FUEL CELLS

A Dissertation
Presented to
The Academic Faculty

by

Brian Patrick Setzler

In Partial Fulfillment
of the Requirements for the Degree
Doctor of Philosophy in the
School of Chemical & Biomolecular Engineering

Georgia Institute of Technology
August 2015

KINETIC AND TRANSPORT MODELING IN PROTON EXCHANGE MEMBRANE FUEL CELLS

Approved by:

Dr. Thomas F. Fuller, Advisor
School of Chemical & Biomolecular Engineering
Georgia Institute of Technology

Dr. Paul A. Kohl
School of Chemical & Biomolecular Engineering
Georgia Institute of Technology

Dr. Clifford L. Henderson
School of Chemical & Biomolecular Engineering
Georgia Institute of Technology

Dr. William J. Koros
School of Chemical & Biomolecular Engineering
Georgia Institute of Technology

Dr. Faisal Alamgir
School of Materials Science & Engineering
Georgia Institute of Technology

Date Approved: May 6, 2015

ACKNOWLEDGEMENTS

A debt of gratitude is owed to a great number of people for the support I have received over the years leading up to this dissertation. First, I would like to thank Dr. Tom Fuller for his guidance and support throughout my time at Georgia Tech. His patience and perspective has been a blessing. I would also like to thank my thesis committee, Dr. Faisal Alamgir, Dr. Cliff Henderson, Dr. Paul Kohl, and Dr. Bill Koros for their advice and time. Dr. Masao Sudoh at Shizuoka University in Hamamatsu, Japan, is recognized for his support and hospitality over the summer of 2012, as well as the entire Sudoh group, who could not have been more welcoming.

Acknowledgements are made to Toyota Motor Engineering & Manufacturing North America Inc. for supporting this work. Additional thanks are given to the National Science Foundation and the Japan Society for the Promotion of Science for support through the 2012 East Asia and Pacific Summer Institute / JSPS Summer Program.

I would like to thank my lab mates, past and present, who have offered technical help and camaraderie over the years. I am fortunate to have a fantastic group of friends, and I would like to thank Vyran George, Tapesh Joshi, Rajiv Jaini, Saujan Sivaram, Steph Didas, Katie Vermeersch, Aubrey Tiernan, Ashley Allen, and Graham Wenz for keeping my spirits high, especially at the conclusion of this process.

Most of all, I owe thanks to my family for their loving support, especially as this process has come to a conclusion. They have been a constant source of encouragement and inspiration, and I couldn’t ask for more. Thank you, Mom, Dad, Eric, Jessica, Cathy, Jeff, Autumn, and Erin.

TABLE OF CONTENTS

LIST OF TABLES

LIST OF FIGURES

LIST OF ABBREVIATIONS

AC	Alternating current
CCL	Cathode catalyst layer
CL	Catalyst layer
CPE	Constant phase element
CV	Cyclic voltammetry
DC	Direct current
ECA	Electrochemically active area
EIS	Electrochemical impedance spectroscopy
FCTS	Fuel cell test stand
FRA	Frequency response analyzer
GDL	Gas diffusion layer
HFR	High frequency resistance
MEA	Membrane electrode assembly
MPL	Microporous layer
PCI	Phase change induced
PEMFC	Proton exchange membrane fuel cell
PFSA	Perfluorosulfonic acid
RH	Relative humidity
RMS	Root mean square

LIST OF SYMBOLS

a	Chemical activity, unitless
a	Empirical parameter in series-parallel model (Section 3.2.3.1), unitless
a	Characteristic length in Thiele modulus (Section 6.3), m
A_i	Cross sectional area for process i, m^2
a_{Pt}	Interfacial area of platinum, m^2/m^3
b	Empirical parameter in series-parallel model (Section 3.2.3.1), unitless
c	Concentration, mol/m^3
c_1	Constant in empirical pressure drop correlation, Pa·cm^2/sccm
c_2	Constant in empirical pressure drop correlation, Pa·cm^4/sccm^2
c_{dl}	Total double layer capacitance including carbon, F/m$^2_{\mathrm{Pt}}$
c_P	Specific heat capacity, J/g·K
d_f	Agglomerate ionomer film thickness, m
$D_{i,j}$	Diffusion coefficient of species i in phase j (concentration driving force), m^2/s
D_{ij}	Binary (gas phase) diffusion coefficient between species i and j, m^2/s
D_{im}	Frictional diffusion coefficient between species i and pore wall, m^2/s
D_{K_i}	Knudsen diffusion coefficient of species i, m^2/s
D_{O_2}	Diffusion coefficient of oxygen in gas mixture (dilute limit), m^2/s
E	Cell potential, V

ECA	Electrochemically active area, m^2/g_{Pt}
EW	Equivalent weight of ionomer, kg/mol $-SO_3H$
f	Frequency, Hz
F	Faraday's constant, 96485 C/equiv
h	Heat transfer coefficient, $W/m^2 \cdot K$
$H_{O_2,i}$	Henry's law constant for oxygen in ionomer, $Pa \cdot m^3/mol$
ΔH_v	Enthalpy of water vaporization from ionomer, J/mol
i	Current density, A/m^2
i_{ox}	Oxide formation current density, A/m^2
J	Leverett J-function, unitless
J_c	Fitting parameter in van Genuchten correlation, unitless
j_{ORR}	Homogeneous equivalent rate of ORR, $mol/m^3 \cdot s$
j_v	Water vaporization rate from ionomer, $mol/m^3 \cdot s$
k	Surface rate constant, s^{-1}
k	Thermal conductivity, $W/m \cdot K$
K	Single-phase permeability, m^2
k'	Homogenous rate constant for ORR in agglomerate, $mol/m^3 \cdot s$
$k_{p,i}$	Mass transport coefficient for oxygen in ionomer, partial pressure driving force, $mol/m^2 \cdot s \cdot Pa$
K_r	Relative liquid-phase permeability, unitless
$k_{x,g}$	Mass transport coefficient for oxygen in GDL, mole fraction driving force, $mol/m^2 \cdot s$

ℓ^{i}	Thickness of layer i, m
L_{Pt}	Catalyst loading, mg_{Pt}/cm^2
L_{wire}	Cable inductance, H
m	ORR reaction order, unitless
m	Fitting parameter in van Genuchten correlation, unitless
MW	Molecular weight, kg/mol
n	Fitting parameter in van Genuchten correlation, unitless
N_{ch}	Molar flow rate in channel per MEA area, $mol/m^2 \cdot s$
N_i	Molar flux of species i, $mol/m^2 \cdot s$
P	Total pressure, Pa
p_c	Capillary pressure, Pa
p_i	Partial pressure of species i, Pa
Q_{dl}	Double layer CPE admittance, s^{ϕ}/Ω
q_{dl}	Double layer volumetric charge, C/m^3
R	Molar gas constant, 8.3145 $J/mol \cdot K$
R_{agg}	Agglomerate radius, m
R_{CL}	Catalyst layer ionomer resistance, $\Omega \cdot m^2$
r_f	Fiber radius, m
R_{mem}	Membrane resistance, $\Omega \cdot m^2$
r_{ORR}	Surface rate of ORR, $mol/m^2 \cdot s$
s	Liquid water saturation, unitless

s_0	Maximum saturation (modified van Genuchten correlation), unitless
s_p	Percolation saturation, unitless
t	Time, s
T	Temperature, K
U	Reversible potential @ 80 °C, V
U_H	Thermoneutral potential @ 80 °C, V
χ	Oxide coverage per unit of heterogeneity, mol/J
x_j	Mole fraction of gas *j*, unitless
X_e	Fraction of all surface atoms that are edge atoms, unitless
y	Down-the-channel coordinate, unitless
z	Through-plane coordinate, m
Z'	Real component of impedance, $\Omega\cdot m^2$
Z''	Imaginary component of impedance, $\Omega\cdot m^2$
α	Diffusion coefficient of water in ionomer referenced to a chemical potential driving force, $mol^2/J\cdot m\cdot s$
α	Butler-Volmer transfer coefficient, unitless
α_D	Ratio of oxygen diffusivity in humidified helium to that in humidified nitrogen, unitless
β	Scaling factor for enhanced vapor diffusion, Pa^{-1}
γ	Surface tension, N/m
Γ	Surface concentration, mol/m^2
$\Delta\mu$	Chemical potential shift of oxide due to heterogeneity, J/mol

ε_i^J	Volume fraction of phase *i* in layer *J*, unitless
η	Effectiveness factor for ORR in agglomerate, unitless
θ	Surface coverage, unitless
θ	Contact angle, °
κ	Ionic conductivity of ionomer, S/m
λ	Water content of membrane, mol H_2O/mol $-SO_3H$
μ	Chemical potential, J/mol
μ	Viscosity, Pa·s
ξ	Electro-osmotic drag coefficient of water in ionomer, unitless
Π	Linearized two-phase Darcy's law driving force, Pa
ρ	Density, kg/m^3
σ	Electronic conductivity of carbon phase, S/m
σ_{ij}	Lennard-Jones intermolecular distance for gas pair ij, nm
τ_i^J	Tortuosity of phase *i* in layer *J*, unitless
ϕ	Thiele modulus, unitless
ϕ	Constant phase element exponent, unitless
Φ	Potential, V
χ	Chemisorption sites blocked per PtO_2 unit, unitless
ψ	Distribution of oxides formed, mol/J
ω	Angular frequency, s^{-1}
ω	Frumkin interaction energy, J/mol
Ω_{ij}	Collision integral for gas pair ij according to kinetic theory, unitless

Subscripts

0	Oxygen reduction reaction or planar-site platinum atoms
1	Carbon phase or OH_{ads}
2	Ionomer phase or planar-site PtO_2 (species or formation reaction)
3	Edge-site PtO_2 (species or formation reaction)
a	Anodic
agg	Catalyst agglomerate
c	Cathodic
eff	Effective transport property, (ε/τ) × intrinsic property
g	Gas phase
i	Ionomer phase
ins	Insulator on current collector plate
N	Nitrogen
o	Water (Chapter 2 only)
O	Oxygen
ORR	Oxygen reduction reaction
ref	Reference condition (p_{ref} = 1 bar)
v	Vaporization from ionomer or vacant chemisorption sites
w	Water
*	Chemisorption sites

Superscripts

C	Cathode catalyst layer
ch	Gas flow channel

F	Flow field
G	Gas diffusion layer
M	Membrane layer
–	Steady-state portion of variable
~	Transient portion of variable, complex
^	Normalized variable

SUMMARY

Proton exchange membrane fuel cells (PEMFCs) provide a compact, refuellable power source with high efficiency, multiple fuel sources, and no pollutant emissions. It is easy to understand why major automakers have spent decades researching PEMFCs in the hope of bringing them to market. Cost and durability remain the major barriers to commercialization, with improved performance a key to overcoming these challenges.

The improvement of PEMFC performance and durability requires a quantitative understanding of the processes that cause performance losses. Physics-based models with experimental validation are the best route to achieve this understanding. A review of previous modeling efforts is presented and the common approaches compared. In this work, two models are developed incorporating new processes that have been poorly described or neglected in previous literature sources (catalyst oxide layer, hardware effects, enhanced vapor diffusion, and interfacial saturation). These models are tested against experiments and shown to perform well.

Electrochemical impedance spectroscopy (EIS) provides a simple, inexpensive, and in-operando technique for separating contributions to cell impedance by process, but the interpretation of this experiment using approximate analogies has limited its utility. A new physics-based model is developed to simulate EIS experiments, and the kinetic effect of the platinum oxide layer is added. The oxide layer is found to cause a large, low-frequency inductive loop over a variety of conditions that matches experimental measurements. Accounting for the inductive loop unifies steady-state measurements of resistance with EIS measurements, solving a long-standing barrier to accurate interpretation of EIS, and improving the prediction of performance under transient loads.

Power density in PEMFCs is limited by the requirement of high efficiency, both to reduce fuel costs and to reduce system complexity due to heat rejection. Therefore, every millivolt of loss in the cell must be accounted for and minimized, so that the gains can be invested in cost reduction and increased power density. Flooding losses due to two-phase water transport are one of the most significant and poorly understood losses and are a major area for improvement. Existing models do not provide a satisfactory explanation of the full range of severity of flooding losses that is observed. A new model is developed to study two-phase mass transport and heat transport in more detail. The addition of an interfacial saturation effect is found to provide the best explanation of flooding. Furthermore, heat transfer is shown to be the controlling factor in the performance of PEMFCs with certain gas diffusion layer parameters. Neglecting 2-D heat transfer and thermal contact resistance is found to produce a large disagreement between model and experiments, but with these effects, the model accurately predicts heat-transfer limited performance. Therefore, thermal conductivity is an important material property to optimize in PEMFC design in order to reduce or eliminate flooding losses.

The advancements of this dissertation in the modeling of the oxide layer and two-phase transport phenomena represent the first steps towards the ultimate goals of routine EIS analysis by physics-based model and a mathematical understanding of performance degradation due to carbon corrosion. Recommendations are provided for new experiments and modeling approaches to further develop the models of this dissertation and progress towards the goals of the PEMFC community.

CHAPTER 1

INTRODUCTION

Proton exchange membrane fuel cells (PEMFC) are a promising technology for energy conversion that could dramatically reshape the automotive industry. PEMFCs generate electricity from hydrogen through an electrochemical process at near ambient temperatures with high efficiency compared to traditional internal combustion engines (1). PEMFCs emit no pollutants, mostly due to the use of hydrogen as a fuel, but also due to the low temperature, which eliminates NO_x formation unlike air-breathing combustion engines. The high efficiency compensates for the extra step of producing hydrogen from natural gas or electricity.

The first commercial success for low-temperature fuel cells was in the space program as a lightweight, efficient means of generating electricity on spacecraft (2). PEMFCs were invented at General Electric in the 1950s and were used in the Gemini space program. Later, the Apollo program switched to an alkaline fuel cell. The original PEMFCs developed by General Electric used hydrocarbon membranes with poor durability, and a major advancement came with the development of perfluorosulfonic acid (PFSA) membranes, Nafion®, by E. I. du Pont de Nemours and Company in the 1960s. State-of-the-art membranes today use similar ionomers, although with a number of improvements such as reinforcement. Further advancements came in the 1980s, sparked by improvements in catalyst layer structure at Los Alamos National Laboratory (3) that greatly reduced the platinum loading while increasing performance. The 1990s and 2000s saw a dramatic acceleration of research, with most automakers investing in PEMFCs and strong government support through the U.S. Department of Energy (DOE) FreedomCAR program and similar efforts in other countries. DOE support for fuel cell research was severely cut in 2010 in an effort to refocus funding on technologies with more near-term potential. However, research funding has increased somewhat in subsequent years (4). In addition to light-duty vehicles, PEMFCs have been developed and deployed at small scale for buses and forklifts.

PEMFCs already meet the minimum performance requirements for automotive uses (5), and some automakers are beginning limited production of fuel cell vehicles. For example, the Toyota Mirai is currently being sold in Japan and is expected to be available in California in late 2015. A recent DOE-sponsored cost estimate projected manufacturing costs of approximately \$55 / kW (\$4400 for an 80 kW system) at 500,000 units per year volume, while the DOE has set a 2020 cost target of \$40 / kW (5). Present-day production costs are much higher due to low volume and non-recurring engineering expenses, which are excluded from the DOE cost estimates. Regardless, these cost estimates indicate that PEMFCs have commercial potential. Meanwhile, a limited deployment of hydrogen fueling stations is underway in California, Japan, and elsewhere to support the initial production of fuel cell vehicles. Together, these developments highlight the promise of PEMFCs.

In addition to their use in the automotive industry, the combination of electrolyzers and fuel cells could be used for grid-scale energy storage as an alternative to batteries, pumped hydro, compressed air, or natural gas peaking plants. Fuel cells have excellent efficiency compared to thermal generation, but poor efficiency compared to batteries or pumped hydro storage (6). For this reason, most of the efforts in PEMFCs have focused on automotive applications, although higher temperature varieties of fuel cells have been developed for combined heat and power applications. Meanwhile, conventional batteries and flow batteries are under development for grid-scale energy storage. However, hydrogen energy storage does have one advantage compared to batteries and even flow batteries – storage capacity. Hydrogen can be stored more cheaply than any flow battery electrolyte, especially if stored geologically instead of in tanks (7). Capital costs are the main impediment to grid-scale energy storage, and for economic reasons, initial deployment will likely focus on short-term storage that can achieve hundreds of cycles per year. Longer-term imbalances in electricity supply and demand would need to be handled by fossil fuel generation. If, eventually, this residual fossil fuel usage were to be eliminated, very low cost and very long duration storage beyond the capabilities of batteries would be needed (7).

1.1 Principles of Operation

A fuel cell directly converts the chemical potential energy of the reactants into electricity. As in any galvanic electrochemical cell, the fuel cell achieves the conversion by splitting a chemical reaction into two half reactions involving ions and electrons. By physically separating the two half reactions, the flow of electrons can be harnessed to do useful work. In a hydrogen-fueled PEMFC (1), the two half reactions are the hydrogen oxidation reaction (HOR),

$$\mathrm{H_2} \rightleftharpoons \mathrm{2H^+ + 2e^-} \quad E^0 \equiv 0\ \mathrm{V_{SHE}}, \tag{1.1}$$

and the oxygen reduction reaction (ORR),

$$O_2 + 4H^+ + 4e^- \rightleftharpoons 2H_2O \quad E^0 = 1.23\ V_{SHE}. \qquad [1.2]$$

The two half reactions are physically separated by the proton exchange membrane, which allows facile transport of protons, but blocks electron and gas transport. For neutral chemical species, the chemical potential can only be manipulated through the effects of temperature, pressure, and composition, but charged species add the variable of potential. When pairs of half reactions are combined the difference in chemical potential of the reactants is converted to a difference in electrical potential. The theoretical cell potential is 1.23 V for a PEMFC. Thermodynamically, the theoretical cell potential is related to the Gibbs free energy,

$$E_{Cell} = \frac{-\Delta G}{nF}, \qquad [1.3]$$

where n is the number of electrons exchanged and F is Faraday’s constant.

The PEMFC is made up of five layers plus supporting hardware, as illustrated in Figure 1-1. The central layer is the membrane, which divides the two electrodes and provides a proton conduction path between them. On either side of the membrane are the anode and cathode catalyst layers. These are the active layers of the cell and the site of the electrode half reactions. The HOR takes place at the anode, and the ORR takes place at the cathode. The catalyst layers typically consist of a mixture of carbon-supported platinum, an ionomer of similar composition to the membrane, and gas pore space. The two catalyst layers and membrane are sandwiched between two gas diffusion layers (GDLs), which facilitate hydrogen and oxygen transport to the catalyst layers, product water removal, and conduct electrons to and from the catalyst layers. The GDLs are typically made of carbon fiber paper or carbon cloth with high porosity and are coated with a small amount of PTFE to improve liquid water removal. Often, a microporous layer (MPL), consisting of carbon black and PTFE, is added to the catalyst layer side of the GDL as a strategy to reduce liquid water buildup in the cell. Together, the five layers are referred to as a membrane electrode assembly (MEA).

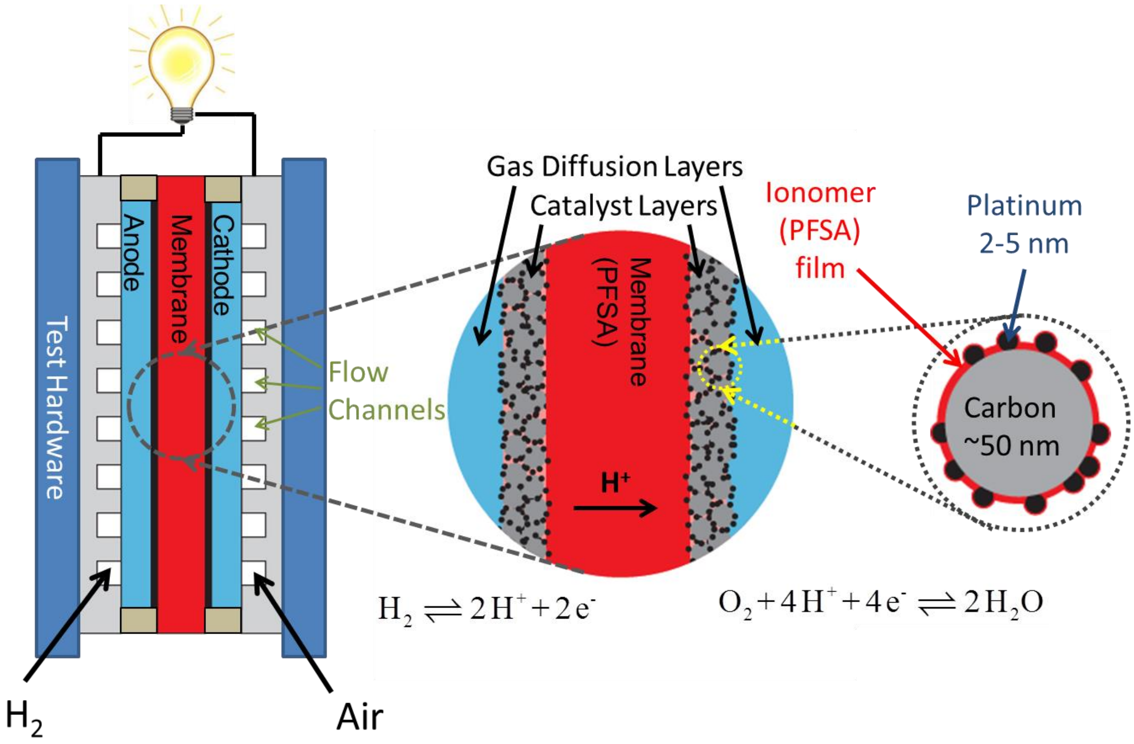

Figure 1-1: Schematic illustration of the layers of a PEMFC.

For research applications, MEAs are tested in single-cell hardware, but in commercial applications, the cells are combined into stacks to increase voltage and improve space efficiency. In a stack, MEAs are separated by bipolar plates, which connect the MEAs in series, anode to cathode. The bipolar plates have flow channels on each side, to provide hydrogen to the anode and air or oxygen to the cathode. Sealed coolant channels are also contained within the bipolar plate for heat rejection. Each cell is sealed with a gasket, and the stack is compressed between end plates. The bipolar plates also provide connections to inlet and outlet manifolds for hydrogen and oxygen supply and exhaust.

The basic performance of a PEMFC is characterized with a polarization curve, which shows the cell potential as a function of cell current density under steady-state operating conditions. A typical polarization curve is shown in Figure 1-2a. The potential losses in the cell can be sorted into three basic categories as illustrated in Figure 1-2b: activation losses, ohmic losses, and mass transport losses. Another term for potential losses is overpotential, which represents the additional potential needed to drive a process at a non-zero rate. Activation losses are due to the kinetic overpotential required to drive the HOR and ORR reactions at the desired rate. The HOR reaction is very fast on platinum in the absence of poisons such as carbon monoxide, and the activation overpotential is very small. The ORR is a much more difficult reaction to catalyze, and although platinum and platinum alloys are the best catalysts available, the ORR overpotential is the largest loss under normal operating conditions. The ORR overpotential is described by the Tafel equation,

$$\eta = b \ln\left(\frac{i}{i_0}\right), \tag{1.4}$$

where η is overpotential, b is the Tafel slope, and i_0 is the exchange current density, which represents the forward reaction rate at zero overpotential. The Tafel equation neglects the reverse reaction and is valid at high overpotential. Due to the logarithmic dependence on current density, activation overpotential dominates at low current densities and is responsible for the curvature in this region.

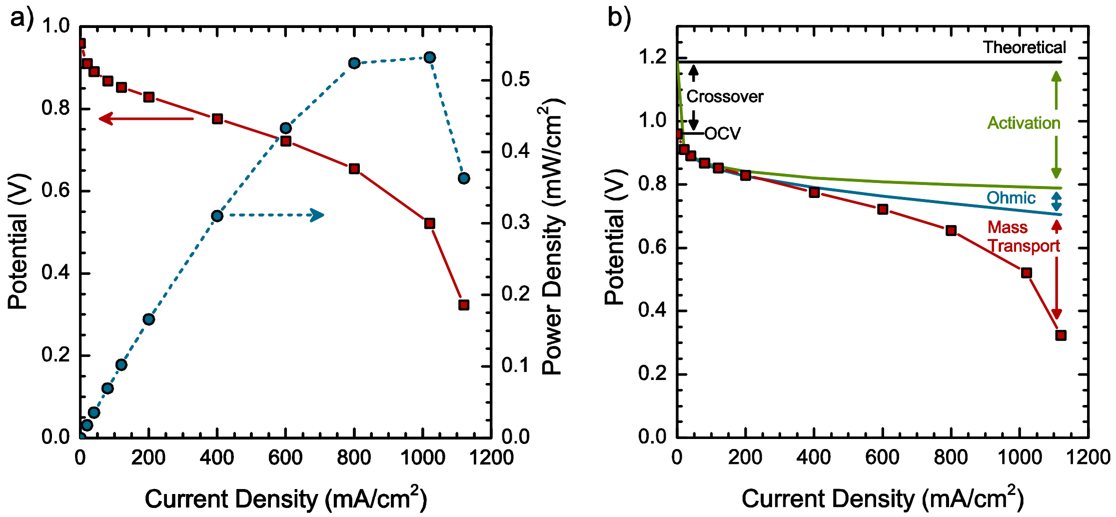

Figure 1-2: a) Typical polarization curve showing cell potential and power density as a function of current density. b) Polarization curve with estimate of losses from each category.

The next source of overpotential in the cell is the ohmic loss. Ohmic losses are characterized by Ohm's law,

$$\eta = iR, \qquad [1.5]$$

and are caused by electronic and ionic conduction resistances. The ohmic losses are dominated by the proton conduction resistance in the membrane and catalyst layer, but also include electronic resistance in the catalyst layers, GDLs, bipolar plates, and current collectors, as well as contact resistances between layers. Ohmic losses are linear with current density and contribute to the roughly linear portion of the polarization curve at intermediate current densities.

Finally, the remaining losses in the cell are primarily due to mass transport processes. These losses are difficult to characterize with a simple equation and require detailed physics-based modeling to predict accurately. These losses are mostly due to oxygen transport to the catalyst surface. Additional overpotential is required to make up for the reduced oxygen concentration at the catalyst surface. Oxygen transport losses are caused by diffusion through the gas pores of the GDL and catalyst layer as well as diffusion through the ionomer covering the catalyst surface. The losses are greatly enhanced when pores are blocked by liquid water. Hydrogen and proton concentration gradients can contribute additional overpotential when there are impurities in the anode feed or membrane, respectively. Mass transport losses are largest at high current densities and increase non-linearly. A limiting current is observed when the catalyst surface concentration approaches zero and additional overpotential cannot further increase the reaction rate.

Efficiency is determined by both the potential losses and the current losses. Current losses are primarily due to hydrogen crossover through the membrane, which also lowers the open circuit voltage (OCV). Additionally, a small amount of hydrogen may be purged periodically to reduce the buildup of inert gases in the anode fuel loop. Together, these losses are generally very small, and as an approximation, efficiency can be estimated as the ratio of the cell potential to the theoretical cell potential. While the maximum power density occurs at a potential below 0.6 V, a design potential of 0.65-0.7 V usually provides a better tradeoff between efficiency and power density (8). System efficiency is also impacted by compressor power and other parasitic losses.

1.2 Primary Challenges

The primary challenge inhibiting the commercialization of PEMFCs is cost (2, 5, 9). Part of the issue with cost is the small manufacturing scale of PEMFCs today, and cost is expected to decrease dramatically as production scales up. However, the ultimate mass-produced cost of PEMFCs is still higher than ideal (5) due to a variety of factors.

Platinum is an expensive catalyst, and its use must be minimized to reduce cost. No amount of mass production will reduce the bulk price per ounce of platinum, although the processing steps are also expensive and could be improved. Fluorinated membranes are a low-volume chemical and are currently expensive. However, cost estimates predict that the membrane price will be sufficiently reduced by scale and the current high price does not reflect a fundamental limitation of the material (9).

The most straightforward route to reducing cost in PEMFCs is improving power density. Increased performance allows a smaller stack to produce the same power output, reducing the cost of every single component in the stack by simply reducing the amount needed. Improved performance can also be used to increase operating efficiency, which simplifies heat rejection and improves the competitiveness of hydrogen as a fuel compared to the alternatives. Heat rejection has increasingly become an area of concern for automakers and the DOE (8), as PEMFC operating temperature is lower than that of an internal combustion engine, and the ability to reuse existing radiator designs would reduce system cost and bulk. Improvements in performance are supported by mathematical modeling efforts (10). In order to extract every millivolt of available performance out of a PEMFC cell, it is necessary to understand the source of losses.

Durability is a second major challenge in PEMFCs and is intrinsically linked to cost and performance (11). A limited lifetime reduces the commercial value of a PEMFC system, while performance loss may require a system to be overbuilt in order to meet the application requirements at the end of its specified lifetime. Often, improvements in durability can be directly translated into improvements in cost and performance. For example, early research on PEMFCs typically used 180 µm thick Nafion 117 membranes, which provided good mechanical strength and durability but caused high ohmic losses and anode dryout. Improvements in the chemical stability of PFSA led to Nafion 212, which is 50 µm thick, but still provides acceptable durability. The use of a reinforcement layer, developed by W.L. Gore and Associates, allowed even thinner membranes to be used without sacrificing mechanical durability. Today, 18 µm Gore membranes are commonly employed by researchers studying high-power operation, and even thinner membranes, down to 5 µm, have been developed that meet DOE targets for membrane durability (12). The tenfold or more reduction of membrane thickness improves power density while simultaneously reducing material usage, and was enabled by improvements in durability. Even the external humidification requirements are reduced with thinner membranes, reducing the balance of system cost.

Catalyst layer durability is an area of active research. The biggest challenges are platinum dissolution and carbon corrosion (11). Platinum dissolution leads to deposition of platinum in the membrane and Ostwald ripening, reducing catalyst active area and demanding higher initial catalyst loadings to compensate. Carbon corrosion leads to thinning of the catalyst layer with loss of porosity, increase in mass-transport resistance, and agglomeration of platinum. Strategies to improve catalyst layer durability include heat-treating carbon supports (13) or even removing the support entirely through nanostructured thin-film catalysts (14). The increase in mass-transport losses caused by catalyst layer degradation is poorly understood, and mathematical modeling coupled to experiments is needed to determine the mechanisms responsible for this performance loss.

Finally, hydrogen storage and the hydrogen distribution infrastructure are barriers to the commercialization of PEMFCs. Hydrogen is the lightest gas and as a result has low volumetric energy density. Despite extensive research into alternatives such as metal hydride storage, compressed hydrogen storage at 350 or 700 bar remains the standard (15). Compression to these high pressures results in significant distribution and dispensation costs (16), which reduce the competitiveness of hydrogen as a fuel. However, the challenges of hydrogen storage have not prevented the development of fuel cell vehicles, and Toyota claims a range of 300 miles for the production Mirai (17).

1.3 Present Contribution

To support the efforts towards improvement of PEMFC durability and performance, mathematical modeling of kinetic and transport processes is needed. In this work, physics-based models of a single-cell PEMFC have been developed with improvements in the modeling of the catalyst oxide layer and two-phase water transport in particular. These models are validated against both steady-state and transient experiments. Accurate, physics-based models are especially needed in the interpretation of electrochemical impedance spectroscopy (EIS) experiments, where present data analysis techniques limit the utility of the technique (10, 18). The models developed in this work are shown to match experimental EIS results under a variety of conditions using parameters determined by independent experiments rather than data fitting. This work represents a significant step towards the use of physics-based models in place of simple measurement models for EIS analysis. Additionally, the two-phase flooding model can be extended to explain the performance losses observed with catalyst layer degradation, a major goal of modeling efforts.

1.4 References

1. M. M. Mench, *Fuel cell engines*, p. xi, John Wiley & Sons, Hoboken, N.J. (2008).

2. M. L. Perry and T. F. Fuller, *J. Electrochem. Soc.*, **149**, S59 (2002).

3. I. D. Raistrick, in *Diaphragms, Separators, and Ion-Exchange Membranes*, J. W. Van Zee, R. E. White, K. Kinoshita and H. S. Burney Editors, p. 156, The Electrochemical Society Proceedings Series, Boston (1986).

4. Fuel Cell Technologies Office FY2015 Budget At-A-Glance, in, U.S. Department of Energy (2014).

5. Fuel Cell Technical Team Roadmap, in, U.S. DRIVE Partnership (2013).

6. M. Skyllas-Kazacos, M. H. Chakrabarti, S. A. Hajimolana, F. S. Mjalli and M. Saleem, *J. Electrochem. Soc.*, **158**, R55 (2011).

7. M. Melaina and J. Eichman, Hydrogen Energy Storage: Grid and Transportation Services (Technical Report), in *Related Information: NREL (National Renewable Energy Laboratory)*, p. Medium: ED; Size: 66 pp. (2015).

8. B. D. James, J. M. Moton and W. G. Colella, Mass Production Cost Estimation of Direct H2 PEM Fuel Cell Systems for Transportation Applications: 2013 Update, in, Strategic Analysis Inc., Arlington, VA (2014).

9. M. Mathias, H. Gasteiger, R. Makharia, S. Kocha, T. Fuller and J. Pisco, *Abstracts of Papers of the American Chemical Society*, **228**, U653 (2004).

10. A. Z. Weber, R. L. Borup, R. M. Darling, P. K. Das, T. J. Dursch, W. B. Gu, D. Harvey, A. Kusoglu, S. Litster, M. M. Mench, R. Mukundan, J. P. Owejan, J. G. Pharoah, M. Secanell and I. V. Zenyuk, *J. Electrochem. Soc.*, **161**, F1254 (2014).

11. R. Borup, J. Meyers, B. Pivovar, Y. S. Kim, R. Mukundan, N. Garland, D. Myers, M. Wilson, F. Garzon, D. Wood, P. Zelenay, K. More, K. Stroh, T. Zawodzinski, J. Boncella, J. E. McGrath, M. Inaba, K. Miyatake, M. Hori, K. Ota, Z. Ogumi, S. Miyata, A. Nishikata, Z. Siroma, Y. Uchimoto, K. Yasuda, K. I. Kimijima and N. Iwashita, *Chem. Rev.*, **107**, 3904 (2007).

12. B. Kienitz, J. Kolde, S. Priester, C. Baczkowski and M. Crum, *ECS Transactions*, **41**, 1521 (2011).

13. K. G. Gallagher, G. Yushin and T. F. Fuller, *J. Electrochem. Soc.*, **157**, B820 (2010).

14. M. K. Debe, A. K. Schmoeckel, G. D. Vernstrorn and R. Atanasoski, *J. Power Sources*, **161**, 1002 (2006).

15. D. J. Durbin and C. Malardier-Jugroot, *Int. J. Hydrogen Energy*, **38**, 14595 (2013).

16. G. Parks, R. Boyd, J. Cornish and R. Remick, Hydrogen Station Compression, Storage, and Dispensing Technical Status and Costs: Systems Integration, in *Related Information: Independent review published for the U.S. Department of Energy Hydrogen and Fuel Cells Program*, p. Medium: ED; Size: 74 pp. (2014).

17. Toyota Mirai - The Turning Point, in, Toyota Motor Sales, USA (2015).

18. S. M. R. Niya and M. Hoorfar, *Electrochim. Acta*, **120**, 193 (2014).

CHAPTER 2

LITERATURE REVIEW

Over the past few decades, substantial improvements have been made in the performance and durability of PEMFCs. While the performance of PEMFCs can be understood qualitatively in terms of the kinetic, ohmic, and mass transport overpotentials described in Chapter 1, a quantitative understanding of performance requires mathematical modeling. As the field progresses and the biggest limitations of the devices are addressed, the remaining challenges demand an increasingly precise understanding of the fuel cell physics. Modeling promotes clear thinking by forcing ideas to be written explicitly and mathematically. Through modeling, the properties of new materials, measured through ex-situ tests, can be linked to their actual performance as part of a PEMFC. Once a model has been developed and validated, new material properties and operating conditions can be simulated with virtually no cost. Furthermore, through modeling, the performance limits of a PEMFC can be analyzed to determine how close existing devices are to achieving the full potential of their materials, and which materials are limiting the performance most.

In this chapter, a review of the PEMFC modeling literature is provided. First, steady-state models are introduced, discussing each component of the PEMFC in turn. Some of the basic model equations are provided, and different approaches compared. The main focus of the review is on 1-D modeling of transport in the through-plane direction, but 2-D and 3-D effects are briefly discussed as well. Finally, physics-based impedance models are reviewed, and the promise of physics-based modeling to address the current deficiencies in analysis of experiments is described.

2.1 Steady-state Models

The first PEMFC models were developed in the late 1980s and early 90s. Several groups were actively developing fuel cell models in parallel and records of their progress can be found in papers and conference presentations (1-3) detailing various sub-models. The first full PEMFC model to be published was that of Springer et al. at Los Alamos National Laboratory (4), published in 1991. In the next couple years, models were published by Bernardi and Verbrugge from General Motors (3, 5) and Fuller and Newman at the University of California and Lawrence Berkeley Laboratory (6, 7). These three early models differed in both their dimensionality and the specific transport models employed, but all three were very influential and spawned numerous derivative models in the decades that followed. Rather than introduce entire models one-by-one, this review will focus on individual components of the fuel cell and compare the approaches taken by the pioneering modelers and subsequent improvements.

The state of PEMFC modeling was recently reviewed by Weber et al. (8), and previous reviews by Sousa and Gonzalez (9), Bıyıkoğlu (10), and Weber and Newman (11) may provide the reader with further historical perspective. A more specialized review of two-phase transport and flooding was performed by by Li et al. (12), while pore-scale modeling of two-phase transport phenomena was reviewed by Mukherjee et al. (13). Experiments and modeling concerning effective transport properties in the porous layers of the PEMFC were reviewed by Zamel and Li (14). Finally, physics-based impedance modeling was recently reviewed by Niya and Hoorfar (15) and previously by Gomadam and Weidner (16).

2.1.1 Membrane

For decades, the standard membrane used in PEMFCs has been perfluorosulfonic acid, most commonly DuPont's Nafion®. The chemical structure and an approximate morphological model of Nafion are shown in Figure 2-1. The polymer consists of a PTFE backbone with perfluoroether sulfonic acid side chains. Each side chain contains one fixed $-SO^{3-}$ anionic group, which requires a mobile cation to balance the charge. These ions tend to cluster to form highly hydrophilic domains (17, 18), as shown in Figure 2-1, which absorb water even at low relative humidity. The PTFE backbone is very hydrophobic, and segregates from the hydrophilic pore and channel network, providing mechanical strength even at high hydration levels. The high cation concentration, 0.9 meq/g[1] for 1100 equivalent weight (EW) Nafion, combined with high mobility due to high water sorption gives PFSA membranes very good ionic conductivity, a key requirement for PEMFC membranes. In addition to possessing good conductivity, PEMFC membranes have to be conducive to water management in the cell. During operation, the proton current drags water from anode to cathode, a process called electro-osmosis. To prevent the anode from drying out and minimize external humidification requirements, the membrane should have a high water diffusion coefficient so that product water diffuses to the anode without too large a concentration gradient.

---

[1] An equivalent (eq) is the quantity of an ion with a charge equal to a mole of electrons or protons.

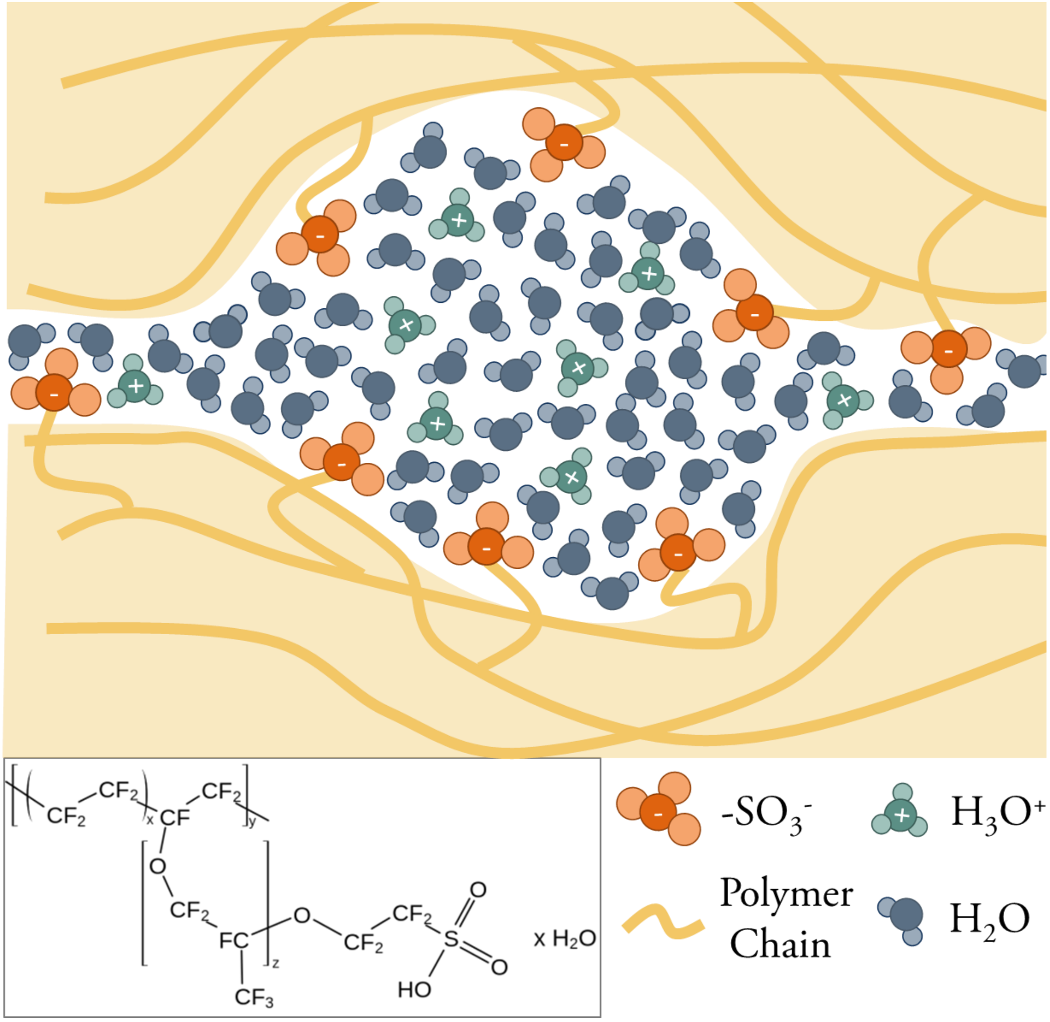

Figure 2-1: Nafion chemical structure and idealized nanoscale morphology (18). The hydrophobic polymer matrix is represented by the yellow shaded region.

A membrane model must include proton and water transport. There are three main approaches to modeling transport in PEMFC membranes, corresponding to the three pioneering models. Springer et al. (4) used dilute solution theory with an ad-hoc consideration of electro-osmotic drag, Fuller and Newman (6, 7, 19) used concentrated solution theory, and Bernardi and Verbrugge (3, 5) used a hydraulic model. The equations used for current and water flux are compared in Table 2-1. In dilute solution theory, the flux of protons (current) depends only on the potential gradient, and the flux of water depends only on the water concentration gradient. In concentrated solution theory, the driving forces are equated to the drag between each pair of species,

$$\nabla \mu_i = \sum_{j \neq i} K_{ij} \left(v_j - v_i \right), \tag{2.1}$$

where v_i is the velocity of species i and $K_{ij} = K_{ji}$ is a frictional coefficient between pairs of species. The membrane system contains three species, protons (+), water (o), and polymer (m). Through the water-proton interaction, concentrated solution theory accounts for electro-osmosis and its complementary process, the streaming potential, whereby a water concentration gradient induces either a potential gradient or a flow of current. The equations used by Springer et al. include a term for electro-osmosis in the water flux equation, but do not consider the corresponding streaming potential effect, which for constant electro-osmotic drag coefficient, ξ, is (19)

$$\Delta\Phi_{sp} = \frac{\xi RT}{F} \ln\left(\frac{a_o^A}{a_o^C} \right), \tag{2.2}$$

where a_o^A and a_o^C are the activity of water in the anode and cathode, respectively. The typical value for the electro-osmotic drag coefficient is 1 (20, 21), meaning that each proton transported through the membrane drags one water molecule with it. However, at high hydration levels, values as high as 3 have been measured (4, 19, 22, 23). Generally, the omission of the streaming potential is not too serious unless there is a large water concentration gradient across the membrane (11).

Table 2-1: Comparison of literature membrane flux models.

Model	Current		Water Flux	
Dilute Solution (4)	$i = -\kappa \nabla \Phi$	[2.3]	$N_o = -\frac{\kappa \xi}{F} \nabla \Phi - \alpha \nabla \mu_o$	[2.4]
Concentrated Solution (7)	$i = -\kappa \nabla \Phi - \frac{\kappa \xi}{F} \nabla \mu_o$	[2.5]	$N_o = -\frac{\kappa \xi}{F} \nabla \Phi - \left(\alpha + \frac{\kappa \xi^2}{F^2} \right) \nabla \mu_o$	[2.6]
Hydraulic (5)	$i = -\left(\kappa + c_+{}^2 F^2 \frac{k_\phi}{\mu} \right) \nabla \Phi$ $-c_o c_+ F \frac{k_P}{\mu} \nabla \mu_o$	[2.7]	$N_o = c_o c_+ F \frac{k_\phi}{\mu} \nabla \Phi - c_o{}^2 \frac{k_P}{\mu} \nabla \mu_o$	[2.8]

The third typical approach to modeling the membrane is the hydraulic model used by Bernardi and Verbrugge (3, 5). The parameters in the hydraulic model are electrokinetic permability, k_ϕ, hydraulic permeability, k_P, viscosity, μ, and conductivity κ. In this model, the concentration of water is fixed, and hydraulic pressure is the main driving force for water transport. If one includes the total pressure in the definition of chemical potential, the hydraulic model is similar to the concentrated solution theory model. In fact, Weber and Newman derived a model accounting for both diffusive and hydraulic transport using a unified chemical potential driving force (24-26). The hydraulic model includes electro-osmosis through the electrokinetic permeability term and includes a streaming potential due to the convective flow of protons with water. However, the proton flux is modeled using dilute solution theory, ignoring the interaction between protons and the membrane. Although the hydraulic model has three transport properties, k_ϕ / μ, k_P / μ, and κ, ignoring the drag between the membrane and protons is equivalent to specifying $K_{+m} = 0$ in concentrated solution theory. By comparing terms in Table 2-1, the model of Bernardi and Verbrugge (5) can only be cast in terms of concentrated solution theory if $k_P = k_\phi$, reflecting the symmetry between electro-osmosis and streaming potential. With this equality enforced, the three concentrated solution theory transport properties are interrelated by

$$\alpha = \frac{\kappa\xi}{F^2}\left(\frac{c_o}{c_+} - \xi\right). \qquad [2.9]$$

It must be noted that conductivity, κ, as defined in concentrated solution theory has a different value than in the hydraulic model. In concentrated solution theory, conductivity is defined as the dependence of current on the potential gradient in the absence of a water chemical potential gradient. In the hydraulic model, conductivity is defined as the dependence of current on the potential gradient in the absence of water flux, which would require a pressure or chemical potential gradient to maintain.

A final membrane phenomenon worth noting is Schroeder's paradox, the tendency of liquid-equilibrated membranes to exhibit higher water uptake than vapor-equilibrated membranes, even though the chemical potential of liquid water and saturated vapor are equal. Several explanations of Schroeder's paradox have been given in the literature, often focusing on the difference in surface energy between a membrane exposed to gas and exposed to liquid (27-29). The surface energy explanation is not entirely satisfying, as the bulk water uptake is the variable affected, and no dependence on surface area to volume ratio has yet been demonstrated. Some researchers have attempted to explain Schroeder's paradox in terms of pretreatment procedures (30, 31), which undoubtedly play a role. However, the experimental observations are too numerous to explain through careless pretreatment procedures alone. Zawodzinski et al. (32) explicitly mentioned that the phenomenon was reversible; membranes removed from liquid water and placed into saturated water vapor lost the extra water. This observation cannot be explained by pretreatment. Vallieres et al. have suggested the possibility of a van der Waals loop in the thermodynamics of water uptake (29), meaning that both states of the membrane have identical chemical potential, with water contents between the two states being meta-stable.

Schroeder's paradox has led a number of researchers to consider the state of water in contact with the membrane when determining water content. It has been suggested that the hydraulic model is best for liquid-equilibrated models, while the concentrated solution or dilute solution model is best for vapor-equilibrated models. However, Weber and Newman demonstrated that the concentrated solution theory approach can be modified to include hydraulic pressure driven flow through the membrane by including the pressure gradient in the chemical potential driving force (24-26). As mentioned previously, the only differences between concentrated solution theory and the hydraulic model come from ignoring the membrane proton interactions. Therefore, concentrated solution theory is preferred in this work. As a full thermodynamic explanation of Schroeder's paradox has not yet been developed, the phenomenon is ignored in the present work.

2.1.2 Gas Diffusion Layer

The gas diffusion layer (GDL) serves to distribute gases from the flow channels to the catalyst layer surface, while providing electrical and thermal conductivity. A typical GDL is made of carbon cloth or carbon paper with high porosity, and may also include a microporous layer (MPL) on the catalyst-facing side made of carbon black and PTFE. The macroporous GDL is usually treated with a small amount of PTFE to reduce liquid water flooding. The MPL was introduced to further reduce flooding losses. Single-phase 1-D modeling of the GDL is fairly simple, but the complexity can increase substantially when accounting for two-phase effects as well as 2-D and 3-D effects of the flow field pattern.

The Stefan-Maxwell multicomponent diffusion equation has served as the basis for gas transport in the vast majority of works, including the earliest models (3-7). Similarly to concentrated solution theory, Stefan Maxwell diffusion considers the interaction between pairs of molecules,

$$\nabla x_i = RT \sum_{j \neq i} \frac{x_i N_j - x_j N_i}{P D_{ij}^{eff}} . \qquad [2.10]$$

The next complication added is to consider the effects of Knudsen diffusion. The MPL and catalyst layer both have small pores on the order of 50-500 nm for which Knudsen diffusion is expected to be significant (8, 33). Knudsen diffusion was included in the model of Bevers et al. (34) by adding an additional term to Stefan-Maxwell diffusion,

$$\nabla x_i = RT \sum_{j \neq i} \frac{x_i N_j - x_j N_i}{P D_{ij}^{eff}} - RT \frac{N_i}{P D_{K_i}^{eff}} , \qquad [2.11]$$

which can be thought of as a series resistance, or as the binary interaction between species i and the pore wall. Many other models have included Knudsen diffusion since (35, 36).

The largest complication in modeling the GDL comes from the presence of liquid water and the behavior of two-phase flow. Liquid water flow in two-phase media can occur in three flow regimes: viscous fingering, capillary fingering, and stable displacement (37, 38). In the viscous fingering regime, invasion is controlled by the viscous pressure drop due to flow through pores. The liquid front will advance through all pores, but advances fastest through the large pores due to their higher hydraulic permeability. In the capillary fingering regime, the flow velocity is low enough that viscous effects can be ignored. The liquid front is held back by the surface tension in each pore throat and advances solely through the largest available pores, which have the smallest capillary pressures. Finally, stable displacement represents a condition where a relatively compact liquid front advances uniformly through the material. Two dimensionless numbers, capillary number (Ca) and viscosity ratio (M),

$$Ca = \frac{u\mu_{nw}}{\sigma}, \tag{2.12}$$

$$M = \frac{\mu_{nw}}{\mu_{wet}}, \tag{2.13}$$

determine the flow regime. The wetting phase ($_{wet}$) is air and the non-wetting phase ($_{nw}$) is water. The non-wetting phase velocity is u, the surface tension is σ, and the viscosity is μ. The viscosity ratio of water and air ranges from 18-55, and the capillary number is 10^{-8}, based on a water superficial velocity of 10^{-6} m/s. These values put the fuel cell GDL firmly in the capillary fingering regime (37, 38).

Low temperature operation and the dependence of membrane conductivity on hydration make condensation nearly unavoidable in PEMFCs. To operate efficiently, condensed water must be removed from the MEA without significantly impeding oxygen transport. Therefore, the transport of liquid water and the effects of liquid water on gas transport are naturally of great interest to modelers.

Wang et al. (39) developed one of the first two-phase PEMFC models to consider the effects of flooding on oxygen mass transport. Their model was 2-D, including the MEA through-plane and along-the-channel dimensions. Their two-phase transport description was based on the multiphase mixture model developed by Wang and Cheng (40-42). The multiphase mixture model treats the two-phase mixture as a single phase with equivalent transport properties determined by the constituent phases. The individual phases are treated as components of a mixture and have a diffusive flux relative to each other. This scheme had certain computational advantages, but a more standard two-phase approach is most common in the literature. As often observed in early two phase models, the maximum predicted water saturation was low (ca. 0.06), and the effect on cell performance was relatively minor.

The macrohomogeneous approach to two-phase modeling relies on empirical relationships between saturation and effective transport properties. Saturation, s, is the fraction of the pore space filled by liquid water. Nam and Kaviany (43) used pore-scale modeling to determine the influence of porosity and water saturation on both in-plane and through-plane effective diffusivity. Then, the derived relationships were used in a 1-D macrohomogeneous model of two-phase transport based on Darcy's Law. Their approach is representative of many subsequent models, and is detailed here. Water flux through the porous media is described by Darcy's Law,

$$N_l = -\frac{KK_{rl}}{V_m \mu_l} \nabla p_c , \tag{2.14}$$

where K is the absolute permeability, K_{rl} is the saturation-dependent relative permeability of the liquid water phase, p_c is the capillary pressure, V_m is the molar volume of water. A Leverett J-function is used for capillary pressure vs. saturation,

$$p_c = \frac{\sigma \cos\theta_c}{\sqrt{K/\varepsilon}} J\left(S\right), \tag{2.15}$$

where θ_c is the contact angle, ε is the porosity, and $J\left(S\right)$ is an empirical polynomial function of reduced saturation, which is adjusted for the percolation threshold, $S \equiv \frac{s - s_{im}}{1 - s_{im}}$. Relative permeability is usually modeled as a power-law function of saturation,

$$K_{rl} = S^3. \tag{2.16}$$

Finally, gas phase effective diffusivity is modeled as a function of porosity and saturation,

$$D_{ij}^{eff} = D_{ij}\varepsilon \left(\frac{\varepsilon - 0.11}{1 - 0.11}\right)^{0.785} \left(1 - s\right)^2, \tag{2.17}$$

although their simulations yielded several values for the saturation exponent, ranging from 2 for in-plane diffusivity to 3-4 for through-plane diffusivity, depending on the distribution of water.

One of the early challenges facing two-phase models was that most models predicted very low values of saturation, which had only small impacts on performance. GDL permeability is roughly 10^{-11} m^2, (44) and at 1 A/cm^2, if all of the generated water leaves as a liquid through the cathode GDL, the superficial velocity is only ca. 1 µm/s. Capillary pressure is generally assumed or measured to fall in the range of 1-10 kPa (45-48). Using the numbers above with a 200 µm GDL thickness, the liquid permeability required is 2×10^{-17} - 2×10^{-16} m^2 (see Equation [2.14]), 4-6 orders of magnitude smaller than the absolute permeability. In two-phase models, permeability is a strong function of saturation, but even using $K_{rl} = s^3$, saturation need not rise above 0.1 to remove product water (39, 49).

Several approaches have been taken to reconcile the experimental observations of significant flooding losses with model predictions of low saturation. He et al. (50) and Natarajan and Van Nguyen (51) used very low values of permeability (ca. 10^{-14} m^2) combined with low values of capillary pressure (ca. 20 Pa) to obtain large values of saturation and a good fit to experimental data. Weber and Newman (52) assumed a combination of hydrophilic and hydrophobic pores, based on the notion that untreated carbon fibers were hydrophilic but some fibers were covered in PTFE. Hydrophilic pores had a negative capillary pressure, and since the GDL boundary condition used was zero capillary pressure, the hydrophilic pore network was essentially always full. Thus, the minimum value of saturation (except when dry) was the fraction of hydrophilic pores, and filling of hydrophobic pores to provide a positive capillary pressure only added to this base.

Meng and Wang (53) considered partial coverage of the GDL-channel interface with water droplets. Most previous models assumed a saturation of zero at the channel boundary, either directly, or through the assumption of zero capillary pressure, which usually corresponded to zero saturation. By assuming a higher boundary value for saturation due to the need for droplets to grow to a certain size before detaching from the GDL surface, Meng achieved higher saturation values throughout the GDL. This combination of assumptions also led to the result that saturation gradients in the cell were quite small, as the vast majority of liquid transport resistance now occurred at the channel interface.

Finally, it must be noted that low values of GDL saturation are consistent with experimental in-situ imaging studies (54-57). Therefore, existing models might not be wrong for predicting low bulk saturation in the GDL, but instead may be missing the true mechanism by which flooding leads to performance losses. In particular, the role of interfacial saturation has been emphasized as an area needing further study (8).

2.1.3 Catalyst Layer

The catalyst layer is the most complicated of the fuel cell layers. In general, the ionomer and gas-phase transport can be modeled in the same manner as the membrane and GDL, respectively. However, the rate of reaction must be considered in mass balances, and a kinetic rate equation is needed. Furthermore, certain additional processes and complications arise in the catalyst layer due microstructural considerations.

In the initial model of Springer et al. (4), the catalyst layer was treated as a planar interface with no transport losses. However, in the next iteration of their model, a fully flooded 1-D catalyst layer was considered (58). The fully flooded cathode approach assumes that all oxygen transport must occur through the ionomer phase of the catalyst layer, according to Fick’s Law. Similarly, Bernardi and Verbrugge (3, 5) considered oxygen or hydrogen transport through the catalyst layers via diffusion and advection in the liquid water phase, consistent with their hydraulic modeling framework. In contrast, Fuller and Newman (6, 7) included the gas phase in their catalyst layer, modeling transport with the standard Stefan-Maxwell approach as used in the GDL. The fully flooded catalyst layer approach severely over-predicts cathode mass transport losses when the bulk value of ionomer oxygen permeability is used. However, including gas-phase transport without accounting for Knudsen diffusion and ionomer film transport greatly under-predicts the cathode mass transport losses. Furthermore effective transport properties are lower than often assumed in fuel cell materials (14, 59-62). The Bruggeman power-law relationship,

$$D_{ij}^{eff} = \varepsilon^{1.5} D_{ij}, \tag{2.18}$$

is frequently used for lack of experimental data. However, measurements on carbon paper GDLs have found that an exponent of 3.8 provides the best fit (63). In catalyst layers, experimental measurements by Shen et al. (64) found an effective diffusivity that was 28 times lower than predicted by the Bruggeman approximation. This discrepancy was attributed to Knudsen diffusion and increased tortuosity, although the individual contributions were not isolated.

Even after properly accounting for Knudsen diffusion and tortuosity for gas phase transport in the catalyst layer, the effect of oxygen transport in ionomer films should be accounted for. In order for a platinum particle to be electrochemically active, it must have an ionic connection to the membrane. Thus, oxygen usually has to diffuse through a thin coating of ionomer to reach the platinum surface, as pictured in Figure 2-2. One of the first models to account for oxygen diffusion in the ionomer phase was by Ridge et al. (65). Their model of a gas diffusion electrode actually predates (ca. 1989) all of the previously mentioned models, but focuses solely on the cathode and GDL, ignoring the anode and the membrane. In the Ridge et al. model, catalyst particles and ionomer form cylindrical agglomerates through which oxygen diffuses while simultaneously reacting. The agglomerates may be coated with a thin film of ionomer or water, through which oxygen must diffuse before reaching the active zone of the agglomerate, although Ridge et al. set this film thickness to zero in their model. An illustration of the agglomerate model as well as the common thin-film model (66) is provided in Figure 2-2. In the thin-film model, a uniform mass-transfer resistance to the catalyst surface is assumed, while in the agglomerate model, the core of the agglomerate is less accessible than the surface.

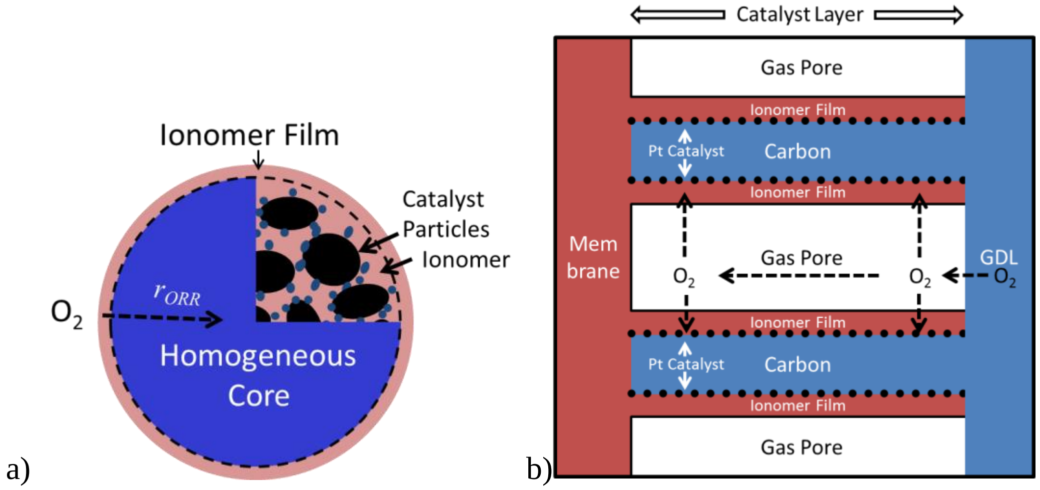

Figure 2-2: Illustration of common ionomer diffusion models. a) Agglomerate model. b) Thin-film model.

The oxygen reduction reaction (ORR) kinetics are usually represented by the Tafel equation (4, 6, 8, 67),

$$i = i_0 \frac{p_{O_2}}{p_{ref}} \exp\left(\frac{\eta}{b}\right), \qquad [2.19]$$

where i_0 is the exchange current density, η is the overpotential, and b is the Tafel slope, which is often reported as mV/decade (i.e. $2.303b$). Various modifications can be made to match observed experimental results. Neyerlin et al. measured a constant potential reaction order with respect to oxygen of 0.79 (68) from experiments spanning a partial pressure range of 60-426 kPa and a temperature range from 35-90 °C. It should be noted that overpotential is actually defined based on the thermodynamic reversible potential at the reaction conditions, which includes a 0.25 order dependence on oxygen partial pressure. However, it is generally more convenient to use $\Phi - U$ in place of overpotential and define reaction orders at constant potential instead of constant overpotential.

Many researchers have found an approximately doubled Tafel slope for ORR at low potentials (69-76). While a doubled Tafel slope can occur due to mass-transport artifacts such as agglomerate diffusion, and some researchers have expressed skepticism of the existence of a dual Tafel slope (68), the experimental evidence for the dual Tafel slope is in fact overwhelming. Furthermore, the change in Tafel slope can be explained by the onset of oxide formation, as modeled by Wang et al. (75) and Holewinski and Linic (76).

Finally, liquid water condensation may occur in the catalyst layer. Although the effects of water saturation on gas-phase transport are usually modeled in the same manner as the GDL, further complications may arise when considering oxygen transport to the catalyst surface. The simplest approach to handling liquid blocking of catalyst sites is to add a $\left(1-s\right)$ term to the kinetic rate equation, assuming a linear decrease in accessible surface area with saturation (39, 50, 51, 77). An alternative approach is to add a variable thickness thin film of water to the agglomerate model (8). While this model is mathematically more rigorous compared to the empirical $\left(1-s\right)$ term, it is not clear whether the underlying physical model of water dispersed as a thin film is any more accurate than an empirical $\left(1-s\right)$ term.

2.1.4 Along-the-Channel Dimension

The gas composition in the fuel cell flow channel varies from inlet to outlet as reactants are consumed and water is produced. One design goal for PEMFC systems is to maximize utilization of fuel and air to minimize parasitic losses and humidification demands. As utilization increases, the variation in channel composition increases considerably. Furthermore, depending on flow field design, pressure drop through the flow channels can be considerable. In addition to performance impact of changing reactant partial pressure, the buildup of water can have quite dramatic effects on performance, especially upon crossing the vapor saturation point. These considerations have motivated several approaches to modeling the channel dimension.

The simplest approach to including the effects of reactant utilization in a model is to include a 0-D channel mass balance. Some of the earliest models treated the channel as a continuous stirred-tank reactor (CSTR), where the outlet gas composition was assumed to be the average channel composition (3-5). The concentration of oxygen continuously decreases from inlet to outlet, so assuming the outlet composition applies to the entire MEA is somewhat pessimistic. This approach was later refined to using the average of the inlet and outlet gas compositions (58).

Typical 1-D PEMFC models are not very computationally demanding, and a natural extension is to add the flow channel as another model dimension. These models are generally referred to as 1+1-D or pseudo 2-D models, as transport in the MEA sandwich is only considered in the through-plane dimension, and this 1-D model is simply repeated at every point down the channel. Fuller and Newman were the first to demonstrate this approach in PEMFC modeling (6, 7), and used it to investigate water management and the non-uniform current distribution as reactant utilization was varied. Due to the 2-3 order of magnitude difference in channel length and MEA thickness, there is no benefit to a full 2-D treatment with in-plane transport in the MEA for a standard flow channel design. Usually, 1+1D models treat the flow channel as a straight channel and do not consider the possibility of gas shortcutting through the GDL as in serpentine flow channel designs. For computational efficiency, it is very beneficial if none of the variables in the 1-D MEA model depend on downstream conditions. This allows for block decomposition of the problem into a series of 1-D problems from inlet to outlet that can be solved independently (8).

2.1.5 Across-the-Channel Dimension

The standard flow channel architecture has channel and land widths that are larger than the MEA thickness. As a result, the actual mass-transport path through the GDL may be multiple times the GDL thickness, and the assumption of 1-D transport is inaccurate. Furthermore, in serpentine flow channel configurations, the pressure in adjacent channels varies significantly, and flow through the GDL should be considered. These considerations have led to a family of 2-D models including the MEA thickness and the across the channel dimensions.

West and Fuller developed one of the first of these models to explore the effect of changing land width on current distribution and water balance. For a GDL thickness of 300 μm and land widths up to 1.2 mm, the effect of the land on the current density distribution was small, but the effects on water management were significant, with the membrane water content increasing under the land compared to the 1-D result. The model did not consider water condensation, and the increased buildup of water under the land was cited as further motivation towards the development of two-phase models. The model also did not consider convection through the GDL due to channel pressure differences, which may be negligible for parallel flow channel configurations, but are very important for serpentine configurations (78). Finally, it should be noted that the conclusion that current distribution is nearly uniform applies to the conditions studied, but other conditions may amplify the land-channel effects. Since the 1990s, researchers have shifted to somewhat thinner GDLs, and combined effect of liquid water saturation, convection, and greater-than-Bruggeman tortuosity may result in a less uniform current distribution.

Pressure gradients and two-phase flow were considered by He et al. (50) in their model of a PEMFC with interdigitated flow fields. Their model demonstrated that performance is very sensitive to differential pressure between the channels for pressure differences near 1 kPa. The significance of convection at small values of differential pressure indicates that convection may be significant in serpentine flow channel designs and even in parallel flow channel designs if two-phase flow induces pressure fluctuations in the channel (79).

Although 1+1-D and 2-D PEMFC models are generally not limited by computational resources, issues of model convergence do become more challenging as the system size increases, especially due to the discontinuities present in most two-phase model equations. Additionally, transient behavior is particularly interesting for automotive applications. Thus, approximations to reduce model dimensionality are always welcome. One such approximation is the treatment of 2-D across-the-channel effects by the use of an effective GDL thickness (80). Weber used conformal mapping to simplify 2-D transport to an equivalent 1-D domain. The technique is effective for any flux with a first-order dependence on a driving force, even if the flux equation is non-linear, as is the case for two-phase flow. Using the technique, Weber calculated the effective thickness for GDL transport processes where the channel is conducting (e.g. mass transport) or the rib is conducting (e.g. electron transport or heat transport). However, the approach is not applicable to advective-diffusive transport that occurs when a differential pressure exists between two channels because the mass flux depends on two independent driving forces, mole fraction and total pressure.

In the previous sections, typical modeling approaches for all of the most important PEMFC transport processes were discussed. While the approaches were typically developed for steady-state models, generally only the conservation equations need to be modified in transient models. The transport equations maintain the same form. In the next section, a specific application of transient modeling is discussed: the simulation of AC impedance through physics-based models. These capabilities are useful both as a tool for experimentalists and to provide additional opportunities for model development and validation.

2.2 Impedance Models

Electrochemical impedance spectroscopy (EIS) is a popular experimental technique that extracts additional information out of the current-potential relationship compared to steady-state techniques by probing the cell at different frequencies. When processes occur over different characteristic timescales, EIS can separate out their contributions to the differential cell impedance and can provide additional information about the type of process via the phase of the response. EIS requires modeling to interpret the results, but for ease of use, most researchers have used equivalent electrical circuit models rather than physics-based models. Equivalent circuit models are easy to apply, but the resulting circuit parameters cannot be interpreted without establishing the mathematical link between an equivalent circuit and the underlying process it represents (16).

An alternative approach is to model the physical processes occurring in an electrochemical cell during EIS experiments. This approach was pioneered by De Levie (81), who calculated an analytical solution for the impedance of a porous electrode with a potential gradient, assuming linear kinetics and no concentration gradient. Keddam et al. (82) considered the alternative case of a concentration gradient without a potential gradient. Cachet and Wiart (83) considered both concentration and potential gradients for reactions following Tafel kinetics. Lasia (84) extended the De Levie model to consider Butler-Volmer kinetics, then further extended the model to consider concentration gradients in addition to potential gradients (85). The generic porous electrode model with concentration and potential gradients has served as a foundation for device-specific impedance models.

The subset of PEMFC models simulating impedance has been reviewed by Gomadam and Weidner (16) and more recently by Niya and Hoorfar (86). A sampling of these PEMFC impedance models are described below. Additionally, the parallel development of physics-based impedance models in the lithium battery literature provides important context and insight, beginning with the work of Doyle et al. (87) and Meyers et al. (88).

The impedance response of a fuel cell membrane was calculated by Fuller (6) based on the membrane transport model of his full PEMFC model (6, 7). Using zero water flux boundary conditions, the membrane impedance was calculated to be

$$Z = \frac{\ell}{\kappa}\left(1 + \frac{\kappa\xi^2}{\alpha F^2}\frac{\tanh\sqrt{j\omega\ell^2/D}}{\sqrt{j\omega\ell^2/D}}\right), \qquad [2.20]$$

where α and D are thermodynamically related through

$$D = \alpha\frac{d\mu_o}{dc_o}. \qquad [2.21]$$

In theory, all three transport properties of the membrane could be measured from a single EIS spectrum, but satisfying the boundary conditions of zero water flux with reversible hydrogen electrodes is probably impractical.

One of the first impedance models of a PEMFC was developed by Springer et al. (62). They used a 1-D macro-homogeneous model of the cathode catalyst layer (CCL) and GDL to fit a series of impedance spectra at different potentials and to demonstrate the effect of various model parameters on the modeled impedance. In the catalyst layer, gas phase and ionomer phase oxygen diffusion were lumped together into a single, 1D diffusivity. The GDL was modeled using Stefan-Maxwell multicomponent diffusion, with the assumption of saturated water vapor. The impedance was calculated by introducing a small perturbation in each variable around the steady-state solution. Assuming linearity, a new system of ODEs for the perturbation variables was produced. The impedance was calculated by solving this system of ODEs.

Springer et al. fit a set of six experimental EIS spectra over a wide range of potentials using six adjustable parameters: high frequency resistance, catalyst layer proton resistance, catalyst layer oxygen permeability, exchange-current density (geometric basis), double-layer capacitance, and GDL tortuosity. The model fit the experimental spectra well, showing two capacitive loops: catalyst-layer impedance at high frequency and GDL oxygen transport at low frequency. Single spectrum fits produced substantial variance in the model parameters, and the authors stressed that simultaneous fits over a range of potentials produce more reliable parameter estimates.

Bautista et al. (89) produced a 2D model of the MEA in order to include down-the-channel effects. The GDL was simplified by using a mass-transfer coefficient, while the catalyst layer included mass-transport effects, but no ionic potential drop, following the example of Keddam et al. (82). The gas channel was modeled as a plug flow reactor. The influence of working conditions and geometric parameters on EIS spectra was investigated.

Guo and White (90) extended the standard catalyst and backing layer impedance model with a flooded agglomerate model in the catalyst layer. Previous models considered a completely flooded cathode and required unrealistically high values for oxygen permeability in the ionomer. By separating out the catalyst layer transport resistance into gas phase transport and localized ionomer phase transport, realistic values of oxygen permeability in the ionomer could be used. Additionally, by adding an extra dimension for catalyst utilization, Guo and White were able to show a quadrupled Tafel slope in cases where both agglomerate oxygen transport and ionic conduction were limiting.

Kulikovsky (91) described a simple 1D model for the catalyst layer impedance, considering oxygen diffusion, ionic conduction, and Butler-Volmer kinetics. Approximate analytical solutions were developed for limiting cases, and the numerical solution for the general case was analyzed in detail.

While the aforementioned authors have focused mainly on oxygen and proton transport, others have focused on the low-frequency behavior in EIS. It is frequently observed in the literature that the slope of the polarization curve does not match the low-frequency intercept (ca. 0.1 - 1 Hz) of EIS experiments (92). Some mismatch can occur if polarization curves are done at constant gas stoichiometry, while EIS is done at constant flow rate (93). The remaining inconsistency is explained by a low-frequency inductive loop, the beginning of which can be observed in EIS experiments extended below 0.1 Hz (92). Several explanations for this low-frequency inductive loop have been given, including water buildup in the membrane (15, 94-97), buildup of ORR intermediates (98-100), and platinum oxide formation from water (99, 101).

The effect of water buildup in the membrane was measured experimentally by Schneider et al. (94, 102, 103), using a superimposed high-frequency perturbation to monitor conductivity changes during EIS. By directly measuring the changes in conductivity at the low frequencies where an inductive loop is observed, the authors conclusively proved that membrane conductivity changes were the major cause of the inductive loop for thick membranes at low relative humidity. Wiezell et al. (95) developed an MEA model further explaining this effect. All five layers of the MEA were considered, in addition to a simple flow channel mass balance. The resulting spectra included capacitive loops due to ORR kinetics and mass transport, HOR kinetics, channel oxygen depletion, and electro-osmosis-induced anode dryout. An inductive loop was observed due to the effects of water generation on conductivity and anode kinetics. The features of the simulated spectra closely matched experimental results from the same group (96). The authors also fit their model to experimental EIS results for a range of membrane thicknesses, relative humidities, and current densities. The fitting parameters were consistent over the various conditions, and agreed with results from H_2/H_2 operation.

While water buildup manipulates the cell Ohmic losses, ORR intermediates and the oxide layer can produce inductive loops through kinetic effects. Antoine et al. (98), Bultel et al. (100), and Roy et al. (99) modeled ORR mechanisms involving one or more intermediates and were able to simulate inductive loops. Roy et al. (99) also modeled the inductive loop through the ORR poisoning effect of platinum oxide growth. The oxide growth model was based on that of Darling and Meyers (104), but with simpler kinetics. Mathias et al. (101) combined a two-step ORR mechanism with the Darling and Meyers model for oxide growth to further study the ORR poisoning hypothesis. The ORR mechanism involved a surface intermediate that was distinct from the slow oxide species. Characteristic frequencies for the relaxation of both the ORR intermediate and the oxide poison were derived from the model. In contrast to earlier reports, the ORR intermediate relaxation was too fast to match the low-frequency inductive loop. However, using the rate constants reported by Darling and Meyers, the oxide growth process produced an inductive loop consistent with experiments.

A better understanding of inductive loop processes is still needed. The inductive loop must be accounted for to obtain consistent parameters when fitting a model to EIS and steady-state results, especially in the case of kinetic inductive loops. As Mathias et al. (101) pointed out, in their model, the EIS and steady-state apparent transfer coefficients differ due to the relaxation of the oxide layer. If the steady-state transfer coefficient is applied to EIS analysis, kinetic resistance may be mistaken for mass-transport resistance. Additionally, model validation is under-addressed in the literature, with only a handful of studies making quantitative comparisons between impedance models and experimental results. Most quantitative comparisons are merely model fits, and not separate validation experiments. Fitting without validation increases the likelihood that EIS losses are assigned to the wrong process due to a missing effect in a model. These deficiencies are addressed in Chapter 5, where independent experiments are used for parameter fitting and model validation.

2.3 References

1. M. W. Verbrugge and R. F. Hill, *J. Electrochem. Soc.*, **137**, 886 (1990).
2. M. W. Verbrugge and R. F. Hill, *J. Electrochem. Soc.*, **137**, 1131 (1990).
3. D. M. Bernardi and M. W. Verbrugge, *AlChE J.*, **37**, 1151 (1991).
4. T. E. Springer, T. A. Zawodzinski and S. Gottesfeld, *J. Electrochem. Soc.*, **138**, 2334 (1991).
5. D. M. Bernardi and M. W. Verbrugge, *J. Electrochem. Soc.*, **139**, 2477 (1992).
6. T. F. Fuller, Solid-Polymer-Electrolyte Fuel Cells, in *Department of Chemical Engineering*, University of California, Berkeley, CA (1992).
7. T. F. Fuller and J. Newman, *J. Electrochem. Soc.*, **140**, 1218 (1993).
8. A. Z. Weber, R. L. Borup, R. M. Darling, P. K. Das, T. J. Dursch, W. B. Gu, D. Harvey, A. Kusoglu, S. Litster, M. M. Mench, R. Mukundan, J. P. Owejan, J. G. Pharoah, M. Secanell and I. V. Zenyuk, *J. Electrochem. Soc.*, **161**, F1254 (2014).
9. R. Sousa Jr and E. R. Gonzalez, *J. Power Sources*, **147**, 32 (2005).
10. A. Bıyıkoğlu, *Int. J. Hydrogen Energy*, **30**, 1181 (2005).
11. A. Z. Weber and J. Newman, *Chem. Rev.*, **104**, 4679 (2004).
12. H. Li, Y. Tang, Z. Wang, Z. Shi, S. Wu, D. Song, J. Zhang, K. Fatih, J. Zhang, H. Wang, Z. Liu, R. Abouatallah and A. Mazza, *J. Power Sources*, **178**, 103 (2008).
13. P. P. Mukherjee, Q. Kang and C.-Y. Wang, *Energy & Environmental Science*, **4**, 346 (2011).
14. N. Zamel and X. Li, *Prog. Energy Combust. Sci.*, **39**, 111 (2013).

15. S. M. R. Niya and M. Hoorfar, *Electrochim. Acta*, **120**, 193 (2014).

16. P. M. Gomadam and J. W. Weidner, *International Journal of Energy Research*, **29**, 1133 (2005).

17. T. Colinart, S. Didierjean, O. Lottin, G. Maranzana and C. Moyne, *J. Electrochem. Soc.*, **155**, B244 (2008).

18. K. D. Kreuer, S. J. Paddison, E. Spohr and M. Schuster, *Chem. Rev.*, **104**, 4637 (2004).

19. T. F. Fuller and J. Newman, *J. Electrochem. Soc.*, **139**, 1332 (1992).

20. T. A. Zawodzinski, J. Davey, J. Valerio and S. Gottesfeld, *Electrochim. Acta*, **40**, 297 (1995).

21. K. G. Gallagher, B. S. Pivovar and T. F. Fuller, *J. Electrochem. Soc.*, **156**, B330 (2009).

22. T. A. Zawodzinski, C. Derouin, S. Radzinski, R. J. Sherman, V. T. Smith, T. E. Springer and S. Gottesfeld, *J. Electrochem. Soc.*, **140**, 1041 (1993).

23. B. P. Setzler, A. Dabonot and T. F. Fuller, in *AIChE Annual Meeting*, Minneapolis, MN (2011).

24. A. Z. Weber and J. Newman, *J. Electrochem. Soc.*, **150**, A1008 (2003).

25. A. Z. Weber and J. Newman, *J. Electrochem. Soc.*, **151**, A311 (2004).

26. A. Z. Weber and J. Newman, *J. Electrochem. Soc.*, **151**, A326 (2004).

27. P. H. Choi and R. Datta, *J. Electrochem. Soc.*, **150**, E601 (2003).

28. V. Freger, *The Journal of Physical Chemistry B*, **113**, 24 (2008).

29. C. Vallieres, D. Winkelmann, D. Roizard, E. Favre, P. Scharfer and M. Kind, *Journal of Membrane Science*, **278**, 357 (2006).

30. L. M. Onishi, J. M. Prausnitz and J. Newman, *The Journal of Physical Chemistry B*, **111**, 10166 (2007).

31. S. Jeck, P. Scharfer and M. Kind, *Journal of Membrane Science*, **373**, 74 (2011).

32. T. A. Zawodzinski, T. E. Springer, J. Davey, R. Jestel, C. Lopez, J. Valerio and S. Gottesfeld, *J. Electrochem. Soc.*, **140**, 1981 (1993).

33. N. Nonoyama, S. Okazaki, A. Z. Weber, Y. Ikogi and T. Yoshida, *J. Electrochem. Soc.*, **158**, B416 (2011).

34. D. Bevers, M. Wo¨Hr, K. Yasuda and K. Oguro, *J. Appl. Electrochem.*, **27**, 1254 (1997).

35. A. A. Kulikovsky, J. Divisek and A. A. Kornyshev, *J. Electrochem. Soc.*, **146**, 3981 (1999).

36. M. Wöhr, K. Bolwin, W. Schnurnberger, M. Fischer, W. Neubrand and G. Eigenberger, *Int. J. Hydrogen Energy*, **23**, 213 (1998).

37. R. Lenormand, E. Touboul and C. Zarcone, *J. Fluid Mech.*, **189**, 165 (1988).

38. P. K. Sinha, P. P. Mukherjee and C.-Y. Wang, *J. Mater. Chem.*, **17**, 3089 (2007).

39. Z. H. Wang, C. Y. Wang and K. S. Chen, *J. Power Sources*, **94**, 40 (2001).

40. C. Y. Wang and P. Cheng, *Int. J. Heat Mass Transfer*, **39**, 3607 (1996).

41. P. Cheng and C. Y. Wang, *Int. J. Heat Mass Transfer*, **39**, 3619 (1996).

42. C. Y. Wang and P. Cheng, in *Advances in Heat Transfer*, T. F. I. J. Y. I. C. James P. Hartnett and A. G. George Editors, p. 93, Elsevier (1997).

43. J. H. Nam and M. Kaviany, *Int. J. Heat Mass Transfer*, **46**, 4595 (2003).

44. J. T. Gostick, M. W. Fowler, M. D. Pritzker, M. A. Ioannidis and L. M. Behra, *J. Power Sources*, **162**, 228 (2006).

45. J. Gostick, Multiphase Mass Transfer and Capillary Properties of Gas Diffusion Layers for Polymer Electrolyte Membrane Fuel Cells, in *Chemical Engineering*, University of Waterloo, Waterloo, Ontario, Canada (2008).

46. J. T. Gostick, M. W. Fowler, M. A. Ioannidis, M. D. Pritzker, Y. M. Volfkovich and A. Sakars, *J. Power Sources*, **156**, 375 (2006).

47. J. T. Gostick, M. A. Ioannidis, M. W. Fowler and M. D. Pritzker, *Electrochem. Commun.*, **10**, 1520 (2008).

48. J. T. Gostick, M. A. Ioannidis, M. W. Fowler and M. D. Pritzker, *J. Power Sources*, **194**, 433 (2009).

49. G. S. Hwang, M. Kaviany, J. H. Nam, M. H. Kim and S. Y. Son, *J. Electrochem. Soc.*, **156**, B1192 (2009).

50. W. He, J. S. Yi and T. Van Nguyen, *AlChE J.*, **46**, 2053 (2000).

51. D. Natarajan and T. Van Nguyen, *J. Electrochem. Soc.*, **148**, A1324 (2001).

52. A. Z. Weber, R. M. Darling and J. Newman, *J. Electrochem. Soc.*, **151**, A1715 (2004).

53. H. Meng and C.-Y. Wang, *J. Electrochem. Soc.*, **152**, A1733 (2005).

54. K. T. Cho and M. M. Mench, *PCCP*, **14**, 4296 (2012).

55. J. D. Fairweather, D. Spernjak, A. Z. Weber, D. Harvey, S. Wessel, D. S. Hussey, D. L. Jacobson, K. Artyushkova, R. Mukundan and R. L. Borup, *J. Electrochem. Soc.*, **160**, F980 (2013).

56. A. Z. Weber and M. A. Hickner, *Electrochim. Acta*, **53**, 7668 (2008).

57. J. M. LaManna, S. Chakraborty, J. J. Gagliardo and M. M. Mench, *Int. J. Hydrogen Energy*, **39**, 3387 (2014).

58. T. E. Springer, M. S. Wilson and S. Gottesfeld, *J. Electrochem. Soc.*, **140**, 3513 (1993).

59. R. Barbosa, J. Andaverde, B. Escobar and U. Cano, *J. Power Sources*, **196**, 1248 (2011).

60. C. Chan, N. Zamel, X. Li and J. Shen, *Electrochim. Acta*, **65**, 13 (2012).

61. J. M. LaManna and S. G. Kandlikar, *Int. J. Hydrogen Energy*, **36**, 5021 (2011).

62. T. E. Springer, T. A. Zawodzinski, M. S. Wilson and S. Gottesfeld, *J. Electrochem. Soc.*, **143**, 587 (1996).

63. M. J. Martínez, S. Shimpalee and J. W. Van Zee, *J. Electrochem. Soc.*, **156**, B80 (2009).

64. J. Shen, J. Zhou, N. G. C. Astrath, T. Navessin, Z.-S. Liu, C. Lei, J. H. Rohling, D. Bessarabov, S. Knights and S. Ye, *J. Power Sources*, **196**, 674 (2011).

65. S. J. Ridge, R. E. White, Y. Tsou, R. N. Beaver and G. A. Eisman, *J. Electrochem. Soc.*, **136**, 1902 (1989).

66. Y. W. Rho, S. Srinivasan and Y. T. Kho, *J. Electrochem. Soc.*, **141**, 2089 (1994).

67. J. S. Newman and K. E. Thomas-Alyea, *Electrochemical systems*, p. xx, J. Wiley, Hoboken, N.J. (2004).

68. K. C. Neyerlin, W. B. Gu, J. Jorne and H. A. Gasteiger, *J. Electrochem. Soc.*, **153**, A1955 (2006).

69. A. Parthasarathy, C. R. Martin and S. Srinivasan, *J. Electrochem. Soc.*, **138**, 916 (1991).

70. A. Parthasarathy, S. Srinivasan, A. J. Appleby and C. R. Martin, *J. Electrochem. Soc.*, **139**, 2856 (1992).

71. A. Parthasarathy, B. Dave, S. Srinivasan, A. J. Appleby and C. R. Martin, *J. Electrochem. Soc.*, **139**, 1634 (1992).

72. T. Lehtinen, G. Sundholm, S. Holmberg, F. Sundholm, P. Björnbom and M. Bursell, *Electrochim. Acta*, **43**, 1881 (1998).

73. V. I. Basura, P. D. Beattie and S. Holdcroft, *J. Electroanal. Chem.*, **458**, 1 (1998).

74. P. D. Beattie, V. I. Basura and S. Holdcroft, *J. Electroanal. Chem.*, **468**, 180 (1999).

75. J. X. Wang, F. A. Uribe, T. E. Springer, J. L. Zhang and R. R. Adzic, *Faraday Discuss.*, **140**, 347 (2008).

76. A. Holewinski and S. Linic, *J. Electrochem. Soc.*, **159**, H864 (2012).

77. D. Natarajan and T. Van Nguyen, *J. Power Sources*, **115**, 66 (2003).

78. J. P. Feser, A. K. Prasad and S. G. Advani, *J. Power Sources*, **161**, 404 (2006).

79. Z. Lu, S. G. Kandlikar, C. Rath, M. Grimm, W. Domigan, A. D. White, M. Hardbarger, J. P. Owejan and T. A. Trabold, *Int. J. Hydrogen Energy*, **34**, 3445 (2009).

80. A. Z. Weber, *Electrochim. Acta*, **54**, 311 (2008).

81. R. de Levie, in *Advances in Electrochemistry and Electrochemical Engineering Vol. 6*, P. Delahay Editor, p. 329, Interscience, New York (1967).

82. M. Keddam, C. Rakotomavo and H. Takenouti, *J. Appl. Electrochem.*, **14**, 437 (1984).

83. C. Cachet and R. Wiart, *J. Electroanal. Chem.*, **195**, 21 (1985).

84. A. Lasia, *J. Electroanal. Chem.*, **397**, 27 (1995).

85. A. Lasia, *J. Electroanal. Chem.*, **428**, 155 (1997).

86. S. M. R. Niya and M. Hoorfar, *J. Power Sources*, **240**, 281 (2013).

87. M. Doyle, J. P. Meyers and J. Newman, *J. Electrochem. Soc.*, **147**, 99 (2000).

88. J. P. Meyers, M. Doyle, R. M. Darling and J. Newman, *J. Electrochem. Soc.*, **147**, 2930 (2000).

89. M. Bautista, Y. Bultel and P. Ozil, *Chem. Eng. Res. Des.*, **82**, 907 (2004).

90. Q. Z. Guo and R. E. White, *J. Electrochem. Soc.*, **151**, E133 (2004).

91. A. A. Kulikovsky, *J. Electroanal. Chem.*, **669**, 28 (2012).

92. R. Makharia, M. F. Mathias and D. R. Baker, *J. Electrochem. Soc.*, **152**, A970 (2005).

93. G. Maranzana, J. Mainka, O. Lottin, J. Dillet, A. Lamibrac, A. Thomas and S. Didierjean, *Electrochim. Acta*, **83**, 13 (2012).

94. I. A. Schneider, M. H. Bayer, A. Wokaun and G. G. Scherer, *J. Electrochem. Soc.*, **155**, B783 (2008).

95. K. Wiezell, N. Holmström and G. Lindbergh, *J. Electrochem. Soc.*, **159**, F379 (2012).

96. N. Holmstrom, K. Wiezell and G. Lindbergh, *J. Electrochem. Soc.*, **159**, F369 (2012).

97. B. P. Setzler and T. F. Fuller, *ECS Transactions*, **58**, 95 (2013).

98. O. Antoine, Y. Bultel and R. Durand, *J. Electroanal. Chem.*, **499**, 85 (2001).

99. S. K. Roy, M. E. Orazem and B. Tribollet, *J. Electrochem. Soc.*, **154**, B1378 (2007).

100. Y. Bultel, L. Genies, O. Antoine, P. Ozil and R. Durand, *J. Electroanal. Chem.*, **527**, 143 (2002).

101. M. Mathias, D. Baker, J. Zhang, Y. Liu and W. Gu, *ECS Transactions*, **13**, 129 (2008).

102. I. A. Schneider, M. H. Bayer, P. Boillat, A. Wokaun and G. G. Scherer, *ECS Transactions*, **11**, 461 (2007).

103. I. A. Schneider, M. H. Bayer, A. Wokaun and G. G. Scherer, *ECS Transactions*, **25**, 937 (2009).

104. R. M. Darling and J. P. Meyers, *J. Electrochem. Soc.*, **150**, A1523 (2003).

CHAPTER 3

MODEL DEVELOPMENT

Two 1-D models were developed to study the electrochemical impedance spectroscopy (EIS) response and flooding losses of PEMFCs. The first model is a transient model, where impedance is modeled in the time domain. The model is designed to study the basic mass and heat transport phenomena as well as the effects of the oxide layer. Only vapor phase water transport is considered, and the model is restricted to sub-saturated conditions. The second model is a steady-state model designed to study flooding losses. The focus of the second model is two-phase transport phenomena including phase change induced flow. Both models were implemented using the modeling platform, gPROMS ModelBuilder v3.5.3 (Process Systems Enterprise Ltd). A perturbation model was also derived from the steady-state model and could be used for impedance modeling.

3.1 Single Phase Transient Model

The 1-D transient model consists of eight parts representing the five layers of the membrane electrode assembly (MEA), the two flow fields, and a frequency response analyzer (FRA). First, a brief description of the model physics and assumptions is given. A detailed description of the modeled equations follows.

3.1.1 Model Overview

The MEA model, illustrated in Figure 3-1, is a 1-D continuum model, with Stefan-Maxwell diffusion in the gas phase and concentrated solution theory in the ionomer phase. Ionomer transport parameters are a function of ionomer water content. The anode catalyst layer is modeled as a fully reversible, planar electrode. The cathode catalyst layer (CCL) includes an additional dimension of oxygen transport through the flooded agglomerate with thin film model, which utilizes the pseudo-steady-state approximation. The oxygen reduction reaction (ORR) follows Tafel kinetics with an additional oxide layer effect, as described later in this section. As the model is 1-D, the ORR rate changes with overpotential, oxygen concentration, and oxide coverage through the thickness of the catalyst layer. Oxide growth and double-layer capacitance also contribute to the current.

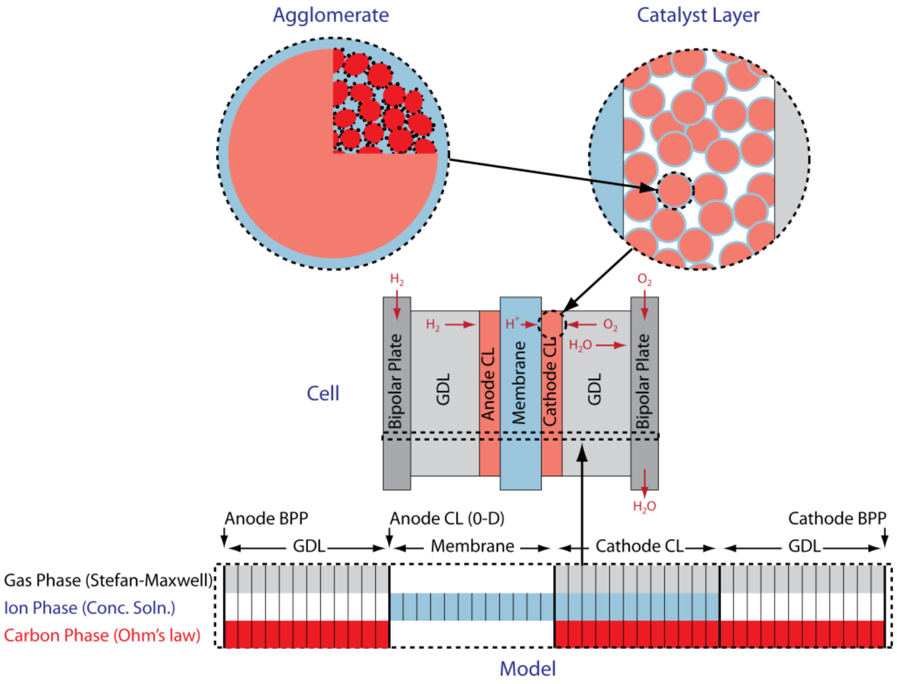

Figure 3-1: Schematic of 1-D MEA model showing the phases considered in each layer.

Convection in the GDL is not modeled explicitly, but its effect is approximated by reducing the tortuosity parameter to match the mass-transfer resistance. Knudsen diffusion is neglected. While Knudsen diffusion may account for a significant fraction of the gas-phase mass-transport resistance in the catalyst layer (1), the overall effect would be small because the total gas-phase mass-transport resistance is small in the catalyst layer. Water condensation is not included in the model, and care is taken to restrict the use of the model to sub-saturated conditions.

Joule heating, membrane hydration, ORR overpotential, and half-reaction enthalpies are all accounted for as heat-generation sources, and heat transfer occurs through conduction. The heat capacity of each layer is included, although the transient effect is negligible except for the flow fields. The most significant effect of temperature is on relative humidity, resulting in ionomer dryout. All other effects of temperature are assumed negligible, including effects on transport and kinetic parameters.

The flow fields are modeled with separate 1-D domains for channel flow and heat transport. Channel flow is modeled with a 1-D mass balance, assuming a uniform gas flux into the GDL determined by the -1D MEA model, which lacks a down-the-channel dimension. Flow channel pressure drop is accounted for by an empirical correlation, and a linear pressure profile is assumed. Partial pressure boundary conditions for the MEA model are determined from the average over the 1-D channel at any given point in time. This scheme approximates the important 2-D effects without the additional model complexity. The 1-D heat transport domain is needed to account for the thermal resistance of the thick graphite flow fields in typical research hardware. An additional heat-transfer resistance is applied at the outer boundary to account for the electrical insulator between the current collectors and the temperature-controlled end plates. Unlike in the thin MEA, the heat-transfer time constant in the thick graphite flow field is slow enough to be relevant in EIS.

The platinum oxide layer is critical to the model results. Following the work of Redmond et al. (2), the oxide model includes a fast, chemisorbed oxide and two slow, “place-exchanged” oxides (planar-site and edge-site oxide). The reaction scheme uses empirical rate laws and is not broken down into elementary steps, as the exact oxide structures and reaction mechanisms have not been agreed upon in the literature. However, the general scheme of an initial reversible species that is replaced by a kinetically irreversible oxide has been well documented in the literature (3). Generally, the transition to the irreversible oxide has been called “place-exchange,” based on the suggestion that surface platinum atoms and adsorbed oxygen atoms swap positions to form a compact oxide layer. In the work of Redmond et al., the slow “place-exchanged” oxide is treated separately on the planar and edge sites due to the observation of a second reduction peak that is only present on nanoparticle platinum and decreases with particle coarsening (2).

In the model, the slow oxides block chemisorption sites, such that the initial reversible chemisorbed oxide is gradually replaced with kinetically irreversible place-exchanged oxide. In order to account for the oxide layer effect on ORR kinetics, the ORR rate equation is first order in vacant chemisorption sites. In other words, the active sites for chemisorption are also the active sites for ORR. Other researchers have used a double-trap model for ORR kinetics and oxide growth (4, 5), in which oxygen is reduced through two parallel routes involving adsorbed intermediates. The oxide layer consists of these adsorbed intermediates, and their buildup at high potentials causes the dual Tafel slope. However, in experiments, oxide growth continues over very long timescales (6), which are not compatible with the short timescales for ORR intermediates required to support a reasonable reaction rate (7). For this reason, oxide growth was treated as a separate process and modeled independently of ORR using the Redmond et al. model.

Impedance is calculated following the approach of Boaventura et al. (8). EIS is simulated in the time domain, and the results are transformed to the frequency domain following the operating principles of an analog frequency response analyzer (FRA) (9). The FRA uses a finite Fourier transform,

$$E(\omega) = \frac{1}{\sqrt{2\pi}} \int_0^{2\pi\omega} E(t) e^{j\omega t} dt \,, \qquad [3.1]$$

to determine the magnitude and phase of the response at a given frequency according to the following process. Real and imaginary excitation signals which are 90° out of phase with each other are defined. The cell voltage is multiplied by these excitation signals and integrated using an ODE built into the model. The same procedure is done for the cell current, and the ratio of the complex voltage and current determines the impedance. The time-domain approach allows easy implementation of EIS with any transient model.

3.1.2 Detailed Model Description

The CCL is the most complex sub-model, and consists of mass, charge, and heat balances, transport equations, and kinetic equations. The GDLs and membrane are modeled with a subset of the CCL model, excluding the absent phases. Additionally, the flow channels and end plates are considered with simplified mass and energy balances. The CCL model is described in detail below, followed by the flow channel and end plate model.

3.1.2.1 Cathode Catalyst Layer Model

The conserved variables are gas partial pressures, concentration of water in the ionomer, double layer charge, and temperature. The seven balance equations for oxygen, water vapor, nitrogen, ionomer water, electronic charge, ionic charge, and heat are:

$$\frac{\varepsilon_g}{RT}\frac{\partial p_{O_2}}{\partial t} = -\frac{\partial N_{O_2}}{\partial z} - j_{ORR}, \tag{3.2}$$

$$\frac{\varepsilon_g}{RT}\frac{\partial p_{H_2O}}{\partial t} = -\frac{\partial N_{H_2O,g}}{\partial z} + 2j_{ORR} + j_v, \tag{3.3}$$

$$\frac{\varepsilon_g}{RT}\frac{\partial p_{N_2}}{\partial t} = -\frac{\partial N_{N_2}}{\partial z}, \tag{3.4}$$

$$\varepsilon_i \frac{\rho_i}{EW_i}\frac{\partial \lambda}{\partial t} = -\frac{\partial N_{w,i}}{\partial z} - j_v \tag{3.5}$$

$$\frac{\partial q_{dl}}{\partial t} = -\frac{\partial i_1}{\partial z} + a_{Pt} i_{ox} + nFj_{ORR}, \tag{3.6}$$

$$\frac{\partial q_{dl}}{\partial t} = \frac{\partial i_2}{\partial z} + a_{Pt} i_{ox} + nFj_{ORR}, \tag{3.7}$$

$$c_P\rho\frac{\partial T}{\partial t} = -\frac{\partial q_H}{\partial z} + nFj_{ORR}\left(\Phi_1 - \Phi_2 - U_{H,0}\right) - i_1\frac{\partial \Phi_1}{\partial z} - i_2\frac{\partial \Phi_2}{\partial z} - j_v\Delta H_v. \tag{3.8}$$

Several key symbols will be defined as they are introduced, but all symbols are included in the List of Symbols section. The concentration of water in the membrane is expressed as moles of water per equivalent of acid, λ. The generation term, j_{ORR}, is the rate of the oxygen reduction reaction (ORR) on a volumetric basis, while j_v, is the rate of water evaporation from the ionomer.

Different transport equations are used for each phase. In the gas phase, the Stefan-Maxwell equations,

$$\frac{1}{RT}\frac{\partial p_i}{\partial z}=\frac{1}{P}\sum_{j\neq i}\frac{p_iN_j-p_jN_i}{D_{ij,eff}}, \qquad [3.9]$$

describe multicomponent diffusion. D_{ij} is the binary diffusion coefficient for a pair of gases and is estimated from kinetic theory (10) as

$$D_{ij}=1.8583\times10^{-9}\frac{T^{3/2}\sqrt{\frac{1}{MW_i}+\frac{1}{MW_j}}}{P\sigma_{ij}{}^2\Omega_{ij}}. \qquad [3.10]$$

Pressure, P, is measured in bar, and average molecular diameter, σ_{ij}, is measured in nm to give D_{ij} in units of m^2/s. Parameters were obtained from Ref. (11). The Stefan-Maxwell equations, [3.9], and the requirement that total pressure is the sum of all partial pressures together yield three independent equations.

The ionomer phase is described using concentrated solution theory, as detailed in Fuller and Newman (12). The three transport properties are conductivity, κ, water diffusivity, α, and electro-osmotic drag coefficient, ξ. The transport equations are

$$N_w=-\frac{\kappa_{eff}\xi}{F}\frac{\partial\Phi_2}{\partial z}-\left(\alpha_{eff}+\frac{\kappa_{eff}\xi^2}{F^2}\right)\frac{\partial\mu_w}{\partial z}, \qquad [3.11]$$

$$i_2=-\kappa_{eff}\frac{\partial\Phi_2}{\partial z}-\frac{\kappa_{eff}\xi}{F}\frac{\partial\mu_w}{\partial z}. \qquad [3.12]$$

The subscript, *eff*, denotes effective transport properties, which take into account the porosity and tortuosity of the relevant phase. The chemical potential referenced diffusion coefficient, α, was determined from the Fick's law diffusion coefficient of water, $D_{w,i}$, according to an approximation,

$$\alpha=D_{w,i}\frac{\partial c_w}{\partial\lambda}\frac{\partial\lambda}{\partial a_w}\frac{\partial a_w}{\partial\mu_w}\approx D_{w,i}\frac{\rho_i\rho_w}{EW\rho_w+\lambda\rho_iMW_w}\left(17.81-79.7a_w+108a_w{}^2\right)\frac{a_w}{RT}. \qquad [3.13]$$

The gas species are described by the ideal gas equation of state, and water in the ionomer is described by the empirical correlation of Springer et al.(13),

$$\lambda = 0.043 + 17.81 a_w - 39.85 a_w^{\ 2} + 36.0 a_w^{\ 3} . \qquad [3.14]$$

The double layer charge is determined by the interfacial potential difference,

$$\frac{\partial q_{DL}}{\partial t} = a_{Pt} c_{dl} \left(\frac{\partial \Phi_1}{\partial t} - \frac{\partial \Phi_2}{\partial t} \right) . \qquad [3.15]$$

The ORR rate equation,

$$r_{ORR} = k_0 \left(\frac{p_{O_2}}{P_{ref}} \right)^m \Gamma_v \exp\left(-\frac{\alpha_{0c} F}{RT} \left(\Phi_1 - \Phi_2 - U_0 \right) \right) \qquad [3.16]$$

is based on the Tafel equation, with a first order dependence on vacant catalytic sites, Γ_v, and a power-law dependence on oxygen partial pressure. In order to model the effect of the oxide layer, it is necessary to model the growth of the oxide layer. A previously developed oxide-growth model (2) is used with some minor adjustments. Although this is not the first time vacant sites have been used to explain the oxide layer ORR hindrance (14), most previous attempts have used simple equilibrium oxide coverage models, which do not match experimental oxide coverage results very well. The oxide growth model of Redmond et al. matches growth rates and coverages over a wide range of timescales.

The oxide layer is formed according to the reaction scheme

$$1) \quad * + \mathrm{H_2O} \rightleftharpoons \mathrm{OH_{ads}} + \mathrm{H^+} + \mathrm{e^-} \qquad [3.17]$$

$$2) \quad \mathrm{Pt} + \mathrm{OH_{ads}} + \mathrm{H_2O} \rightleftharpoons \mathrm{PtO_2} + 3\mathrm{H^+} + 3\mathrm{e^-} \qquad [3.18]$$

$$3) \quad \mathrm{Pt^{edge}} + 2\mathrm{H_2O} \rightleftharpoons \mathrm{PtO_2}^{\mathrm{edge}} + 4\mathrm{H^+} + 4\mathrm{e^-} , \qquad [3.19]$$

which consists of three components: chemisorbed OH, place-exchanged PtO_2 on planar sites, and place-exchanged PtO_2 on edge sites. A brief introduction to the notation will be helpful. Surface concentration (mol/m^2) is represented by Γ, where Γ_0 is a constant equal to the surface concentration of planar-site platinum atoms (excludes edges), and Γ_1, Γ_2, and Γ_3 are the surface concentrations of adsorbed OH, planar-site PtO_2, and edge-site PtO_2, respectively. Chemisorption sites are disrupted by PtO_2, and the surface concentration of chemisorption sites is Γ_*. Surface coverage is represented by θ, and defined by the following relationships:

$$\theta_1 = \frac{\Gamma_1}{\Gamma_*}, \qquad [3.20]$$

$$\theta_2 = \frac{\Gamma_2}{\Gamma_0}, \qquad [3.21]$$

$$\theta_3 = \frac{1-X_e}{X_e}\frac{\Gamma_3}{\Gamma_0}, \qquad [3.22]$$

where X_e is the fraction of platinum surface atoms on edges. Both PtO_2 species exhibit heterogeneity in formation energy represented by $\Delta\mu$. The coverage at each formation energy is x_2 or x_3, related to total coverage by,

$$\theta_2 = \int_{-\infty}^{\infty} x_2 d\Delta\mu, \qquad [3.23]$$

$$\theta_3 = \int_{-\infty}^{\infty} x_3 d\Delta\mu. \qquad [3.24]$$

The degree of heterogeneity is determined by the initial distribution of oxides formed in the anodic process, ψ. A normal distribution with variance σ_2 and σ_3 is used for planar and edge oxides:

$$\psi_2 = \frac{1}{\sigma_2\sqrt{2\pi}}\exp\left(-\frac{\Delta\mu^2}{2\sigma_2{}^2}\right), \qquad [3.25]$$

$$\psi_3 = \frac{1}{\sigma_3\sqrt{2\pi}} \exp\left(-\frac{\Delta\mu^2}{2{\sigma_3}^2}\right). \qquad [3.26]$$

Both forms of PtO_2 disrupt chemisorption sites according to (cf. eq. 10 in ref. (2))

$$\Gamma_* = \Gamma_0 \exp\left(-\chi \frac{\Gamma_2 + \Gamma_3}{\Gamma_0}\right), \qquad [3.27]$$

where χ is the number of sites disrupted by a single unit of PtO_2. In ref. (2), only planar-site PtO_2 is assumed to disrupt chemisorption sites. Equation [3.27] applies given the assumption that PtO_2 units are placed randomly on the surface and may overlap.

Chemisorption is a fast, quasi-equilibrated reaction and follows the equilibrium expression (cf. eq. 15 in ref. (2)),

$$\theta_1 = (1-\theta_1)\exp\left(-\frac{\omega_1}{RT}\theta_1^2 + \frac{F}{RT}(\Phi_1 - \Phi_2 - U_1)\right). \qquad [3.28]$$

The rate equation (cf. eq. 16 in ref. (2)) for planar PtO_2 is

$$\begin{aligned}\frac{\partial x_2}{\partial t} = k_2 \Bigg\{ & \frac{\Gamma_1}{\Gamma_0}\psi_2 \exp\left[-\frac{\omega_2}{RT}\frac{x_2}{\psi_2} + \frac{\omega_1}{RT}\theta_1^2 + \frac{\alpha_{2a}F}{RT}(\Phi_1 - \Phi_2 - U_2)\right] \\ & - x_2 \exp\left[\frac{\Delta\mu}{RT} - \frac{\alpha_{2c}F}{RT}(\Phi_1 - \Phi_2 - U_2)\right]\Bigg\}\end{aligned}, \qquad [3.29]$$

A small change in the anodic Frumkin term has been made from ref. (2), with θ_2, the total coverage, being replaced by $\frac{x_2}{\psi_2}$, the coverage at a particular $\Delta\mu$ relative to the distribution function. During the course of normal CV simulations, this change is inconsequential; however, after long holds the former version results in a very inert oxide layer, while the latter version retains some reactivity. Similarly, for the edge site oxide, the rate equation is (cf. eq. 18 in ref. (2))

$$\begin{aligned}\frac{\partial x_3}{\partial t} = k_3 \Bigg\{ & \psi_3 \exp\left[-\frac{\omega_3}{RT}\frac{x_3}{\psi_3} + \frac{\alpha_{3a}F}{RT}\left(\Phi_1 - \Phi_2 - U_3\right) \right] \\ & - x_3 \exp\left[\frac{\Delta\mu}{RT} - \frac{\alpha_{3c}F}{RT}\left(\Phi_1 - \Phi_2 - U_3\right) \right] \Bigg\}\end{aligned}. \qquad [3.30]$$

The current due to oxide formation is

$$i_{ox} = F\,\frac{\partial\left(\Gamma_1 + 4\Gamma_2 + 4\Gamma_3\right)}{\partial t}. \qquad [3.31]$$

Finally, the surface concentration of vacant chemisorption sites, required in the ORR rate equation [3.16], is

$$\Gamma_v = \left(1 - \theta_1\right)\Gamma_*. \qquad [3.32]$$

To model oxygen transport through the ionomer in the catalyst layer, a flooded agglomerate model with an extra ionomer film is used (cf. Figure 2-2a). Assuming an mth-order reaction, an approximate analytical solution is possible. First, an equivalent homogenous rate constant, k' is defined as

$$k' = \frac{a_{Pt} r_{ORR}}{{p_{O_2}}^m}. \qquad [3.33]$$

Next, the Thiele modulus, ϕ, is defined for the active core of the agglomerate as

$$\phi = \left(R_{agg} - d_f\right)\sqrt{\frac{\left(m+1\right){p_{O_2,f}}^{m-1} H_{O_2,i} k'}{2 D_{O_2,i,eff}}}, \qquad [3.34]$$

where $p_{O_2,f}$ is the partial pressure of oxygen at the film-agglomerate core interface, and $D_{O_2,i,eff}$ is the effective diffusivity of the agglomerate core. The effectiveness factor, which is the ratio of the average rate to the rate in the absence of mass-transfer limitations, is a function of the Thiele modulus,

$$\eta = \frac{3}{\phi^2}\left(\phi \coth \phi - 1\right). \qquad [3.35]$$

The film transport resistance causes a drop in $p_{O_2,f}$, according to

$$p_{O_2} - p_{O_2,f} = \frac{H_{O_2,i} j_{ORR} R_{agg}}{3D_{O_2,i}\left(1-\varepsilon_g\right)\left(\frac{1}{d_f} - \frac{1}{R_{agg}}\right)}. \qquad [3.36]$$

Note that the film is pure ionomer, so no effective property correction is needed for the diffusivity. With the effectiveness factor, rate constant, and film partial pressure defined, the macroscopic homogeneous reaction rate is calculated as

$$j_{ORR} = \eta k' {p_{O_2,f}}^m \left(1-\varepsilon_g\right)\left(1-\frac{d_f}{R_{agg}}\right)^3. \qquad [3.37]$$

The transport properties of the ionomer are dependent on the level of hydration. Conductivity and electro-osmotic drag coefficient were determined experimentally as detailed in Chapter 5. The diffusion coefficient of water is taken from Fuller and Newman (12),

$$D_{w,i} = 3.5\times10^{-6}\lambda \exp\left(\frac{-2436}{T}\right) \quad \left[\mathrm{m^2/s}\right]. \qquad [3.38]$$

The agglomerate dimensions, GDL tortuosity, oxide parameters, and ORR rate equation were all determined by experiment as described in Chapter 5. The remaining model parameters are listed in Table 3-2 and are sourced from literature, manufacturer-provided data, or simple calculations.

3.1.2.2 Flow Channel and End Plate Model

In addition, several test hardware effects are considered. A schematic of these hardware effects is shown in Figure 3-2. The changing composition of the gas in the flow channel is considered using a 1-D mass balance,

$$\frac{\ell_{eff}^{ch}}{RT}\frac{\partial p_i}{\partial t} = -\frac{\partial N_{ch,i}}{\partial y} + N_i^G \big|_{z=L} , \qquad [3.39]$$

where y is the dimensionless distance down the flow channel, ℓ_{eff}^{ch} is the ratio of flow channel volume to MEA area, $N_{ch,i}$ is the molar flow rate of gas i in the channel, normalized by MEA area, and N_i^G is the flux of gas i into the flow channel from the GDL. As the MEA model is 1-D, a uniform gas flux into the GDL must be assumed down the length of the channel. A linear pressure drop profile is assumed down the length of the flow channel, and the inlet total pressure is determined by an experimentally measured correlation,

$$P_{in} = P_{out} + c_1 \sum_i N_{ch,i} + c_2 \left(\sum_i N_{ch,i} \right)^2 , \qquad [3.40]$$

using the parameters listed in Table 3-1. The measured pressure drop is shown in Figure 3-3. The pressure drop is determined by a mix of viscous and inertial effects. While the dynamic viscosity of nitrogen and helium are similar, the molecular weight of nitrogen is 7x larger. The pressure drop for nitrogen is 35-50% larger than for helium, indicating that both effects are significant.

The partial pressures and molar flow rates are related by

$$\frac{N_{ch,i}}{\sum_i N_{ch,i}} = \frac{p_i}{P_{in} + y\left(P_{out} - P_{in}\right)}. \qquad [3.41]$$

The GDL boundary partial pressures are set to the average partial pressures in the channel. This boundary condition couples the time-varying channel composition to the MEA model, capturing the dynamic effects of finite gas stoichiometry.

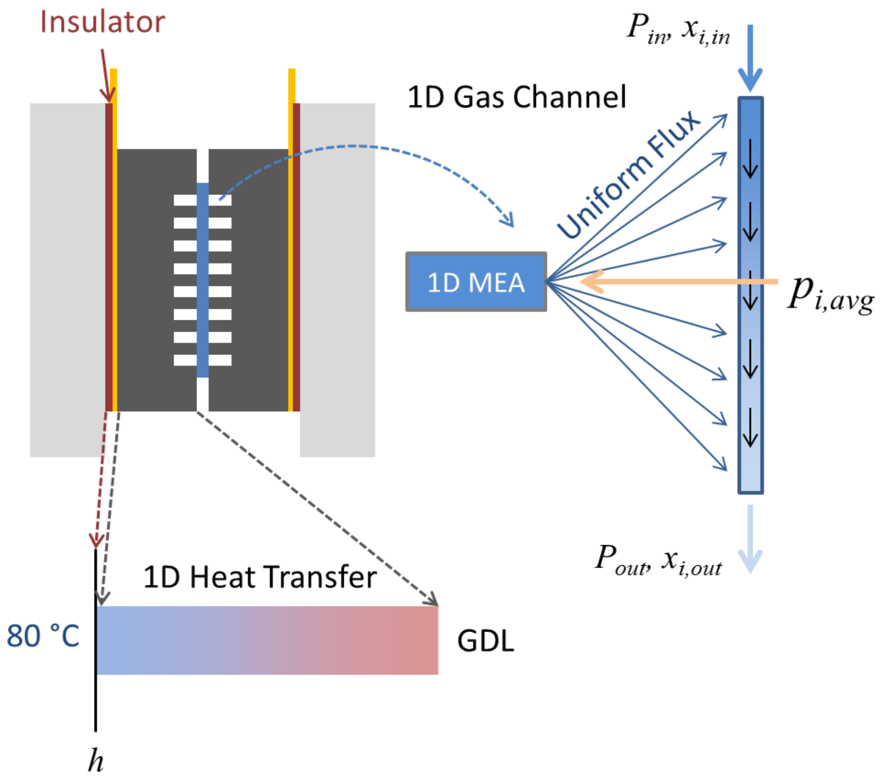

Figure 3-2: Schematic illustration of test hardware models. The flow channel model is shown on the right, with the MEA flux applied evenly over the length of the flow channel and the average partial pressure applied as the MEA boundary condition. The 1-D heat transfer domain for the flow field block is illustrated at the bottom.

Table 3-1: Pressure drop correlation parameters.

Parameter	Units	Hydrogen	Helium	Nitrogen / Air
c_1	Pa·cm^2/sccm	97.2	194	263
c_2	Pa·cm^4/sccm^2	1.04	0.205	0.476

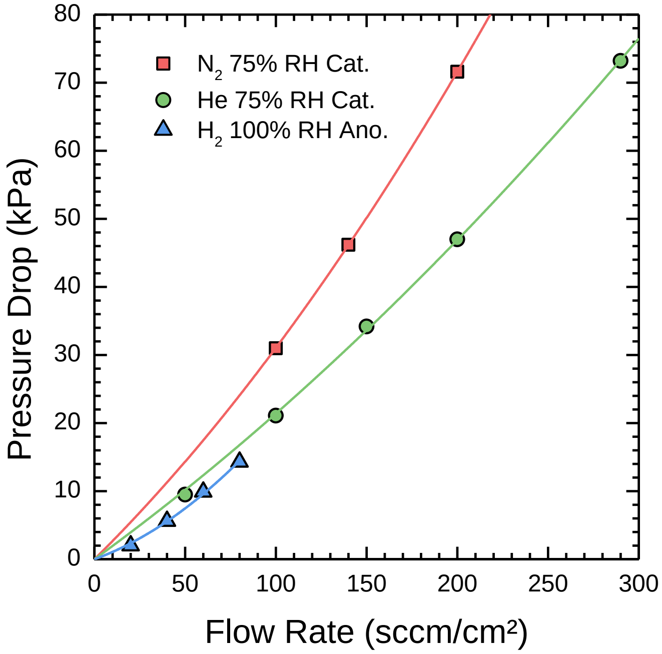

Figure 3-3: Measured pressure drop in the PEMFC hardware at 80 °C under different gases. The lines are the correlation in Equation [3.40].

Two heat-transfer resistances in the test hardware are considered. The graphite flow field is modeled with a 1-D heat balance,

$$\frac{A_{c_P}}{A_{MEA}} c_P^F \rho^F \frac{\partial T}{\partial t} = -\frac{A_k}{A_{MEA}} k^F \frac{\partial^2 T}{\partial z^2}, \tag{3.42}$$

where A_{c_P} and A_k are the effective cross-sectional areas for heat storage and heat conduction, accounting for the larger cross-sectional area of the flow field than the MEA (58.1 cm^2 vs. 25 cm^2). The thin, electrically insulating sheet between the current collector and the end plate also adds a small thermal resistance, which is modeled as a boundary condition rather than a 1-D domain. The boundary condition is

$$-\frac{A_k}{A_{MEA}} k^F \left.\frac{\partial T}{\partial x}\right|_{z=\ell^F} = \frac{A_h}{A_{MEA}} h_{ins} \left(T\big|_{z=\ell^F} - T_0 \right), \qquad [3.43]$$

where $h_{ins,eff}$ is the effective heat transfer coefficient of the insulating layer, and T_0 is the regulated temperature of the end plates.

The effective cross-sectional areas were determined with a steady-state 3D model of heat transfer in the flow field and electrical insulator. The ratio of heat fluxes and heat storage in the 3-D model to the 1-D model were used to calculate the effective cross sectional areas listed in Table 3-2. Most model parameters were sourced from the literature or manufacturer data sheets. These parameters, as well as any parameters assumed or measured directly are also listed in Table 3-2. Several of the most critical parameters were determined by experiment as detailed in Chapter 5 and listed in Table 5-1 and Table 5-2.

Table 3-2: Model parameters sourced from the literature or manufacturer data sheets, calculated from known quantities, or assumed.

Symbol	Name	Value	Source
A_{c_p}	Effective heat storage area of flow field	31 cm^2	Calc.
A_h	Effective heat transfer area of insulator	41.5 cm^2	Calc.
A_k	Effective heat conduction area of flow field	31 cm^2	Calc.
A_{MEA}	MEA active area	25 cm^2	Mfr.
c_P^M	Specific heat capacity of membrane	1.3 J/g·K	Assumed
$c_P^C \rho^C$	Volumetric heat capacity of CCL	0.66 MJ/m^3·K	Assumed
$c_P^F \rho^F$	Volumetric heat capacity of flow field	1.26 MJ/m^3·K	Mfr.
$c_P^G \rho^G$	Volumetric heat capacity of GDL	0.46 MJ/m^3·K	Assumed
$D_{O_2,i}$	Diffusion coefficient of oxygen in ionomer	1.22x10^{-10} m^2/s	(15)
EW	Equivalent weight of ionomer	1.1 kg/mol	Mfr.
h_{ins}	Heat transfer coefficient of insulator	5400 W/m^2·K	Calc.[a]
$H_{O_2,i}$	Henry's law constant of oxygen in ionomer	20.4 kPa-m^3/mol	(15)
ΔH_v	Heat of vaporization of water from ionomer	41.7 kJ/mol	(16)[b]
k^F	Thermal conductivity of flow field	95 W/m·K	Mfr.
k^M	Thermal conductivity of membrane	0.25 W/m·K	(17)
k_{eff}^C	Effective thermal conductivity of CCL	0.27 W/m·K	(18)
k_{eff}^G	Effective thermal conductivity of GDL	1.45 W/m·K	(19)
ℓ^C	CCL thickness	17 µm	Measured
ℓ_{eff}^{ch}	Effective flow channel thickness	0.5 mm	Measured
ℓ^F	Flow field thickness	12.7 mm	Measured
ℓ^G	GDL thickness	140 µm	Measured[c]
ℓ^M	Membrane thickness	50 µm	Mfr.
L_{Pt}	Catalyst loading	0.3 mg/cm^2	Mfr.
m_0	ORR reaction order (O_2)	0.79	(20)
U_0	ORR reversible potential	1.183 V	(16)
$U_{H,0}$	ORR thermoneutral potential	1.256 V	(16)
$U_{H,HOR}$	HOR thermoneutral potential	0 V	Assumed
X_e	Fraction of edge atoms on surface	0.36	(2)
α_{0c}	ORR transfer coefficient on oxide-free Pt	0.5	(14)
α_{2a}	Oxide reaction 2 anodic transfer coefficient	1.5	(2)
α_{2c}	Oxide reaction 2 cathodic transfer coefficient	1.5	(2)
α_{3a}	Oxide reaction 3 anodic transfer coefficient	2.5	(2)
α_{3c}	Oxide reaction 3 cathodic transfer coefficient	1.5	(2)

Table 3-2 (cont.)

Symbol	Name	Value	Source
Γ_0	Surface concentration of planar-site Pt atoms	$\left(1-X_e\right)\frac{2.1}{F}\frac{\mathrm{C}}{\mathrm{m}^2}$	(2)
ε_g^C	CCL porosity	0.65	Measured
ε_g^G	GDL porosity	0.69	Mfr.^{c}
ε_i^C	CCL ionomer volume fraction	0.16	Assumed
ρ_i	Ionomer density	1980 kg/m^3	Mfr.
σ_{eff}^C	CCL effective electronic conductivity	1000 S/m	Assumed
σ_{eff}^G	GDL effective electronic conductivity	1250 S/m	Mfr.
τ_{agg}	Agglomerate ionomer tortuosity	1	Assumed
τ_g^C	CCL gas phase tortuosity	$\left(\varepsilon_g^C\right)^{-0.5}$	Assumed
χ	Chemisorption sites blocked per PtO_2 unit	8	(2)

a Based on manufacturer (mfg.) provided thermal conductivity of ca. 1 W/m·K.
b Assumed equal to the heat of vaporization of liquid water at 80 °C.
c Compressed values. Uncompressed thickness and porosity are 190 µm and 0.77.

3.2 Two-phase Steady-State Model

The second model is a steady-state model developed to understand the effects of liquid water on performance. In this section, the liquid water transport equations are discussed first. Next, the effect of liquid water saturation on gas-phase transport is discussed, and a novel approach is derived for modeling the differences between transport of water vapor and transport of other gases in partially saturated media. Finally, the complete set of model equations is introduced. Throughout the section, certain critical details of the numerical implementation are discussed, including reformulated equations that improve model convergence and initialization procedures that generate acceptable initial guesses for the model variables.

3.2.1 Liquid Water Transport

Liquid water transport is modeled using a macrohomogeneous approach commonly employed in the PEMFC literature (21-26). The liquid water flux is specified by Darcy's law,

$$N_{W,l} = -\frac{K_{rl}K}{V_m \mu}\frac{\partial p_c}{\partial z}, \qquad [3.44]$$

where K_{rl} is the relative liquid-phase permeability, K is the absolute single-phase permeability, and p_c is the capillary pressure. Saturation is assumed to be a monotonic function of capillary pressure, but the exact choice of fitting function is left to Chapter 6, where capillary pressure relationships in the literature are discussed. In general, the model can handle any monotonic relationship between capillary pressure and saturation. The steady-state model is not capable of modeling capillary pressure hysteresis, as in that case capillary pressure is a function of the time derivative of saturation. Additionally, the existence of two values of saturation with the same capillary pressure, as can arise from polynomial fitting functions (27), causes instability in the model. The choice of fitting function can have a large influence on the model results, especially if the saturation at zero capillary pressure is non-zero. Liquid-phase permeability is assumed to have a power-law dependence on saturation,

$$K_{rl} = s^4, \qquad [3.45]$$

where the exponent is taken from Ref. (28). The dependence of permeability on saturation accounts for the increasing number of connected water-transport pathways as saturation increases.

At the interface between two-phase and one-phase regions of the porous media, the rapid decrease in liquid-phase permeability as saturation approaches zero can be especially difficult to solve numerically. The numerical stability of the model is greatly improved by defining an equivalent linear driving force, Π, for liquid flux, such that

$$N_{W,l} = -\frac{K}{V_m \mu}\frac{\partial \Pi}{\partial z}. \qquad [3.46]$$

By comparing Equation [3.44] and Equation [3.46], the definition of Π is

$$\Pi = \int K_{rl}\, dp_c = \int s^4 dp_c\ . \qquad [3.47]$$

Using a linear driving force is also more accurate with large grid spacing, where using the average value of s over an interval will not correctly describe the permeability over that interval. Although the use of an equivalent linear driving force is recommended, some forms of the capillary pressure saturation relationship do not allow the integral in Equation [3.47] to be evaluated. In this case, the standard form of Darcy’s law, Equation [3.44], can be used, taking care to use the average of the relative permeability at the two adjacent scalar grid points.

Another aspect of the two-phase model that can cause numerical difficulties is the equilibrium between liquid and vapor phases. Assuming a sharp transition between saturated and sub-saturated conditions,

$$\begin{array}{ll} p_W + \frac{RT}{V_m} s > p_v : & p_W = p_v \\ p_W + \frac{RT}{V_m} s \le p_v : & s = 0 \end{array} , \qquad [3.48]$$

causes problems due to the sharpness of the transition. If instead the increase in the chemical potential of liquid water due to capillary pressure is considered, a smooth transition occurs based on the true equilibrium relation,

$$V_m p_c = RT \ln\left(\frac{p_W}{p_v}\right). \tag{3.49}$$

3.2.2 Flooding Effects

In the catalyst layer, liquid water blocks oxygen transport to the catalyst surface. In the model, it is assumed that liquid water completely blocks a fraction of the catalyst agglomerates equal to the saturation. Thus, the volumetric ORR rate is (cf. Equation [3.37])

$$j_{ORR} = \eta k' p_{O_2,f}{}^{m}\left(1-\varepsilon_g\right)\left(1-s\right)\left(1-\frac{d_f}{R_{agg}}\right)^3 . \tag{3.50}$$

The presence of liquid water impedes gas transport in the porous layers. Most literature models assume a power-law relationship between effective diffusivity and $\left(1-s\right)$, with some models using the same exponent as for porosity in a Bruggeman-type correlation (24, 29) and others using an independent exponent (30, 31). As an example, Hwang and Weber (32) recommend

$$D_{ij,2ph}^{eff} = D_{ij}\varepsilon^{3.6}\left(1-s\right)^3, \tag{3.51}$$

for gas transport in a partially saturated GDL. Previous PEMFC models apply a similar correction to all gas-phase diffusion coefficients. However, water vapor is not fully impeded by liquid water droplets because it can condense and evaporate to travel through the droplet as illustrated in Figure 3-4. On the contrary, water vapor often displays enhanced diffusivity in a two-phase system (33). The driving force required for bulk flow of water within a droplet is negligible, but a mass-transport resistance still occurs due to the finite thermal conductivity of water. Condensation and evaporation cause a heat flux through the liquid droplet that is proportional to the water flux. The heat flux produces a temperature gradient and a vapor pressure gradient. Although the mechanism is different from diffusion, the relationship between the vapor pressure gradient and the water flux can be described using an equivalent diffusion coefficient. Ignoring heat conduction through the GDL fibers in contact with the water droplet, the equivalent diffusion coefficient of water vapor through liquid water is

$$D_{w,l} = RTk_{liq}\left(\Delta H_v \frac{dp_v}{dT}\right)^{-1}. \qquad [3.52]$$

The dependence of the equivalent vapor-liquid diffusion coefficient on temperature is shown in Figure 3-5 and is compared to the binary diffusion coefficient of water vapor and nitrogen. Liquid water properties are taken from Refs. (34, 35). Transport through liquid water actually becomes slower than vapor transport above 70 °C at 1 bar and above 100 °C at 3 bar.

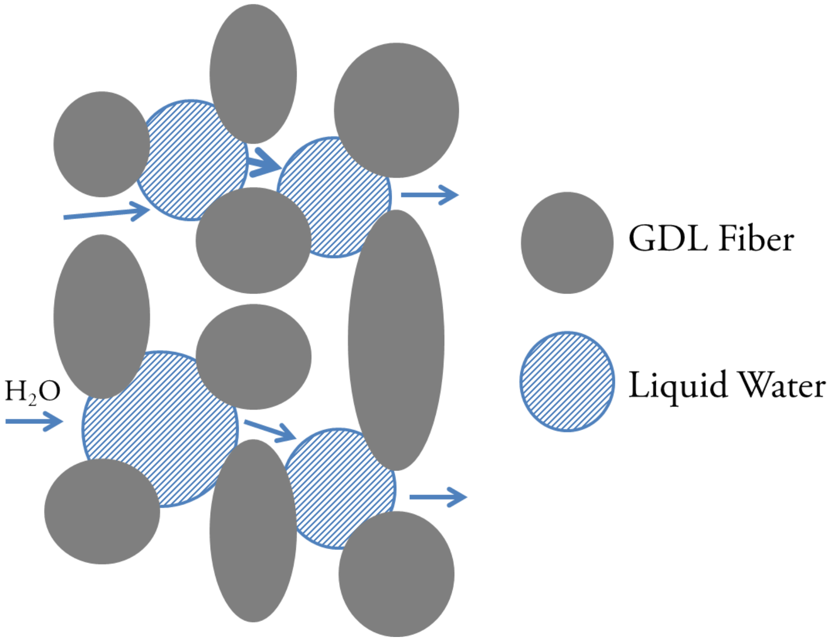

Figure 3-4: Illustration of enhanced vapor diffusion effect in a cross section of a GDL. Liquid water droplets provide shortcuts for water vapor diffusion.

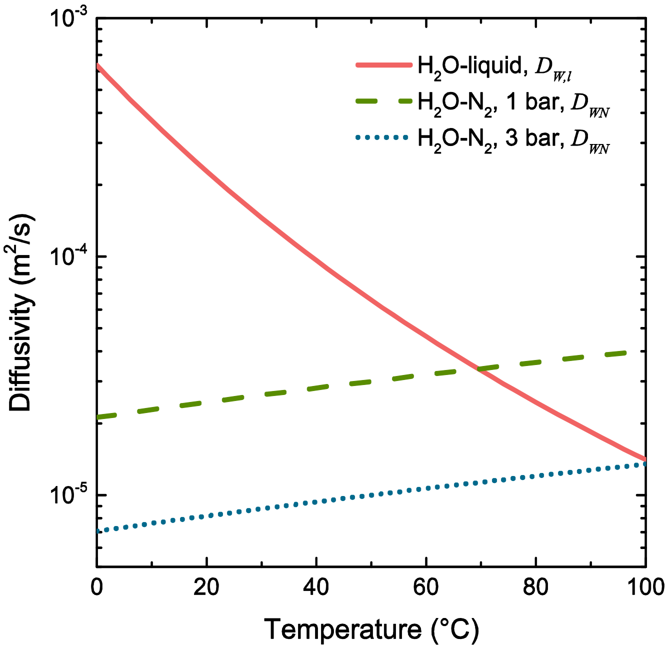

Figure 3-5: Diffusivity of water vapor through liquid water as a function of temperature. Binary diffusivity of water vapor and nitrogen at two pressures is provided for comparison.

3.2.3 Enhanced Vapor Diffusion

No previous models have considered the effect of enhanced vapor diffusion due to liquid saturation. Additionally, no experimental measurements of the effect in PEMFC materials exist. However, from the comparison between the equivalent diffusivity of water vapor through liquid and the water-nitrogen binary diffusivity in Figure 3-5, it is clear that over most of the operating range of a PEMFC, liquid water would enhance vapor transport. For modeling purposes, a simple series-parallel model is used to describe the effect of saturation on transport. The series-parallel model has a free parameter, which is fit to the empirical saturation effect for oxygen transport described by Equation

[3.51]. This approach allows the known impact of liquid water on oxygen diffusion to be used to derive the impact of liquid water on water vapor diffusion.

3.2.3.1 Series-Parallel Model

Assume that the pore volume in the GDL can be divided into three regions as illustrated in Figure 3-6. Regions 1 and 2 contain no liquid water, and Region 3 is fully saturated. Regions 2 and 3 provide parallel transport paths, and together are in series with Region 1. Region 3 may represent a water droplet blocking a gas flow path, while Region 2 represents the parallel path bypassing the water droplet. Region 1 represents the space between droplets where water vapor and other gases must diffuse together. The total volume is divided between the regions using the parameters a and b, such that the volume fraction of Region 1 is $(1-a)$, the volume fraction of Region 2 is $a(1-b)$, and the volume fraction of Region 3 is ab. Thus, the liquid saturation can be expressed as

$$s = ab. \qquad [3.53]$$

The exact dependence of a and b on saturation provides a degree of freedom that will be used later to fit the model to existing correlations for gas transport in partially saturated GDLs.

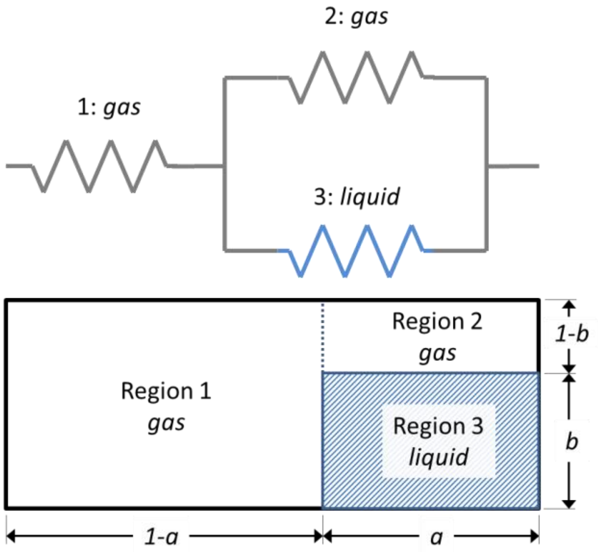

Figure 3-6: Schematic of the series-parallel model for transport around and through liquid water in the porous layers of a PEMFC.

Transport in the gaseous regions is described by the modified binary friction model (36), assuming that single-phase effective transport properties apply, according to

$$\frac{1}{P}\nabla p_i = \nabla x_i + \frac{x_i}{P}\nabla P = RT\sum_j \frac{x_i N_j - x_j N_i}{PD_{ij}^{eff}} - RT\frac{N_i}{PD_{im}^{eff}}, \qquad [3.54]$$

where D_{im}^{eff} accounts for the interactions between species i and the porous medium m. Realistically, water saturation and porosity occur on the same length scale, and assuming that the effects of porosity can be handled separately from liquid water through effective transport properties may not be correct. Porosity could be accounted for in this series-parallel model by treating single-phase, two-phase, and three-phase regions all in series, but the equations would be unwieldy. In the modified binary friction model, D_{im} consists of Knudsen and viscous terms,

$$D_{im} = D_{K_i} + \frac{B_0}{\mathrm{X}_i}, \qquad [3.55]$$

where B_0 is the permeability of a single pore and X_i is a viscous friction term defined as

$$\mathrm{X}_i = \frac{\mu\sqrt{M_i}}{\sum_j p_j\sqrt{M_j}} . \qquad [3.56]$$

Knudsen diffusivity is calculated by

$$D_{K_i} = \frac{d}{3}\sqrt{\frac{8RT}{\pi M_i}} , \qquad [3.57]$$

where d is the pore diameter. For the case where all gas components have the same molecular weight and Knudsen diffusivity can be neglected, Equation [3.54] can be summed over all species to give

$$-\frac{B_0^{eff}}{\mu}\nabla P = \frac{RT}{P}\sum_i N_i . \qquad [3.58]$$

By comparison to Darcy's law, it is seen that $B_0^{eff} = K$, and Equation [3.55] becomes

$$D_{im}^{eff} = D_{K_i}^{eff} + \frac{K}{\mathrm{X}_i} . \qquad [3.59]$$

This result holds even when mixtures with different molecular weights are considered, because B_0 is not composition dependent. However, Equation [3.58] is not valid for mixtures with different molecular weights; Darcy's law is valid for mass-averaged velocity, not molar-averaged velocity.

The fluxes in the three regions are related to the overall flux by

$$N_i = N_{i,1} = (1-b)N_{i,2} + bN_{i,3} , \qquad [3.60]$$

and for the mole fraction gradients,

$$\nabla p_i = (1-a)\nabla p_{i,1} + a\nabla p_{i,2} , \qquad [3.61]$$

$$\nabla p_{i,2} = \nabla p_{i,3} . \qquad [3.62]$$

For water vapor in Region 3 (liquid), flux is written as

$$N_{W,3}=-\frac{D_{W,l}^{eff}}{RT}\nabla p_{W,3}, \qquad [3.63]$$

while for other gases,

$$N_{i,3}=0 \quad i\neq Water. \qquad [3.64]$$

Two final assumptions are made. First, the division into regions occurs on a small enough scale that the mole fractions in each region can be considered equal (i.e. $\Delta p_i \ll p_i$). Second, D_{im}^{eff} is equal in both gas regions and unaffected by liquid saturation, meaning that liquid water produces only fully blocked and fully open pores, with no partially blocked pores.

Equations [3.54] and [3.61] can be combined for water vapor to yield

$$\frac{\nabla p_W}{RTP}=(1-a)\sum_{j\neq W}\frac{x_W N_j-x_j N_W}{PD_{Wj}^{eff}}-(1-a)\frac{N_W}{PD_{Wm}^{eff}}+\frac{a}{1-b}\sum_{j\neq W}\frac{x_W N_j-x_j(1-b)N_{W,2}}{PD_{Wj}^{eff}}-a\frac{N_{W,2}}{PD_{Wm}^{eff}}. \qquad [3.65]$$

The equation is rearranged to group terms with $N_{W,2}$, resulting in

$$\frac{\nabla p_W}{RTP}=\left(1+\frac{ab}{1-b}\right)\sum_{j\neq W}\frac{x_W N_j}{PD_{Wj}^{eff}}-(1-a)\left(\sum_{j\neq W}\frac{x_j}{PD_{Wj}^{eff}}+\frac{1}{PD_{Wm}^{eff}}\right)N_W-a\left(\sum_{j\neq W}\frac{x_j}{PD_{Wj}^{eff}}+\frac{1}{PD_{Wm}^{eff}}\right)N_{W,2}. \qquad [3.66]$$

The intermediate variable $N_{W,2}$ can be expressed as (cf. Equations [3.60] and [3.63])

$$N_{W,2}=\frac{N_W}{1-b}+\frac{b}{1-b}\frac{D_{W,l}^{eff}}{RT}\nabla p_{W,3}, \qquad [3.67]$$

and in turn $\nabla p_{W,3}$ can be written as

$$\nabla p_{W,3}=\frac{\nabla p_W}{a}-\frac{1-a}{a}\nabla p_{W,1}. \qquad [3.68]$$

Using Equation [3.54], the last intermediate variable is eliminated through

$$\frac{1}{P}\nabla p_{W,1} = RT\sum_{j\neq W}\frac{x_W N_j - x_j N_W}{PD_{Wj}^{eff}} - RT\,\frac{N_W}{PD_{Wm}^{eff}}\,. \qquad [3.69]$$

Making all of the above substitutions, Equation [3.66] becomes

$$\frac{\nabla p_W}{RTP} = \left(1+\frac{ab}{1-b}+\frac{(1-a)b}{1-b}\beta P\right)\left(\sum_{j\neq W}\frac{x_W N_j - x_j N_W}{PD_{Wj}^{eff}} - \frac{N_W}{PD_{Wm}^{eff}}\right) - \frac{b}{1-b}\beta\frac{\nabla p_w}{RT}\,, \qquad [3.70]$$

where

$$\beta = D_{W,l}^{eff}\left(\sum_{j\neq W}\frac{x_j}{PD_{Wj}^{eff}} + \frac{1}{PD_{Wm}^{eff}}\right). \qquad [3.71]$$

Solved explicitly for ∇p_W, Equation [3.70] becomes

$$\frac{\nabla p_W}{RTP} = \frac{1-b+ab+(1-a)b\beta P}{1-b+b\beta P}\left(\sum_{j\neq W}\frac{x_W N_j - x_j N_W}{PD_{Wj}^{eff}} - \frac{N_W}{PD_{Wm}^{eff}}\right). \qquad [3.72]$$

A similar process is followed for each non-water species i. First,

$$\frac{\nabla p_i}{RTP} = \begin{aligned} &(1-a)\frac{x_i N_W - x_W N_i}{PD_{iW}^{eff}} + (1-a)\sum_{j\neq i,W}\frac{x_i N_j - x_j N_i}{PD_{ij}^{eff}} - (1-a)\frac{N_i}{PD_{im}^{eff}} \\ &+ a\frac{(1-b)\,x_i N_{W,2} - x_W N_i}{(1-b)\,PD_{iW}^{eff}} + a\sum_{j\neq i,W}\frac{x_i N_j - x_j N_i}{(1-b)\,PD_{ij}^{eff}} - \frac{a}{1-b}\frac{N_i}{PD_{im}^{eff}} \end{aligned}\,. \qquad [3.73]$$

Then, terms are combined to yield

$$\frac{\nabla p_i}{RTP} = a\frac{x_i N_{W,2}}{PD_{iW}^{eff}} + (1-a)\frac{x_i N_W}{PD_{iW}^{eff}} + \left(1+\frac{ab}{1-b}\right)\left\{-\frac{x_W N_i}{PD_{iW}^{eff}} - \frac{N_i}{PD_{im}^{eff}} + \sum_{j\neq i,W}\frac{x_i N_j - x_j N_i}{PD_{ij}^{eff}}\right\}. \qquad [3.74]$$

Substitutions are made to result in

$$\frac{\nabla p_i}{RTP} = \left(1+\frac{ab}{1-b}\right)\left(\sum_{j\neq i}\frac{x_i N_j - x_j N_i}{PD_{ij}^{eff}} - \frac{N_i}{PD_{im}^{eff}}\right) - \frac{\beta_i b}{1-b}(1-a)\left(P\sum_{j\neq W}\frac{x_W N_j - x_j N_W}{PD_{Wj}^{eff}} - \frac{N_W}{D_{Wm}^{eff}}\right) + \frac{\beta_i b}{1-b}\frac{\nabla p_W}{RT}\,, \qquad [3.75]$$

where

$$\beta_i = \frac{x_i D_{W,l}^{eff}}{PD_{iW}^{eff}} \qquad [3.76]$$

Finally, substituting Equation [3.72] into Equation [3.75] gives

$$\frac{\nabla p_i}{RTP}=\left(1+\frac{ab}{1-b}\right)\left(\sum_{j\neq i}\frac{x_iN_j-x_jN_i}{PD_{ij}^{eff}}-\frac{N_i}{PD_{im}^{eff}}\right)+\left\{\frac{ab\beta_iP}{(1-b)(1-b+b\beta P)}\right\}\left(\sum_{j\neq W}\frac{x_WN_j-x_jN_W}{PD_{Wj}^{eff}}-\frac{N_W}{PD_{Wm}^{eff}}\right). \quad [3.77]$$

The total pressure drop is determined by adding all of the Stefan-Maxwell equations,

$$\frac{\nabla P}{RTP}=\left(1+\frac{ab}{1-b}\right)\sum_i\left(-\frac{N_i}{PD_{im}^{eff}}\right)-\frac{ab}{(1-b)(1-b+b\beta P)}\frac{D_{W,l}^{eff}}{D_{Wm}^{eff}}\left(\sum_{j\neq W}\frac{x_WN_j-x_jN_W}{PD_{Wj}^{eff}}-\frac{N_W}{PD_{Wm}^{eff}}\right). \quad [3.78]$$

The relationship between a and b is arbitrary and can be specified to match the empirical $(1-s)^3$ correction recommended for gas diffusivity in the GDL. If vapor diffusion through the liquid is set to zero ($D_{W,l}=0$), Equation [3.77] results in

$$1+\frac{ab}{1-b}=(1-s)^{-3}. \quad [3.79]$$

Combined with Equation [3.53],

$$b=\frac{2-2s^2+s^3}{3-3s+s^2}, \quad [3.80]$$

$$a=\frac{3s-3s^2+s^3}{2-2s^2+s^3}. \quad [3.81]$$

These expressions can be substituted into Equations [3.72], [3.77], and [3.78] to give

$$\frac{\nabla p_W}{RTP}=\frac{1+\left(2-3s+s^2\right)\beta P}{(1-s)^3+\left(2-2s^2+s^3\right)\beta P}\left(\sum_{j\neq W}\frac{x_WN_j-x_jN_W}{PD_{Wj}^{eff}}-\frac{N_W}{PD_{Wm}^{eff}}\right), \quad [3.82]$$

$$\frac{\nabla p_i}{RTP}=(1-s)^{-3}\left(\sum_{j\neq i}\frac{x_iN_j-x_jN_i}{PD_{ij}^{eff}}-\frac{N_i}{PD_{im}^{eff}}\right)+\left\{\frac{\left[(1-s)^{-3}-1\right]\beta_iP}{(1-s)^3+\left(2-2s^2+s^3\right)\beta P}\right\}\left(\sum_{j\neq W}\frac{x_WN_j-x_jN_W}{PD_{Wj}^{eff}}-\frac{N_W}{PD_{Wm}^{eff}}\right), \quad [3.83]$$

$$\frac{\nabla P}{RTP}=(1-s)^{-3}\sum_i\left(-\frac{N_i}{PD_{im}^{eff}}\right)-\frac{(1-s)^{-3}-1}{(1-s)^3+\left(2-2s^2+s^3\right)\beta P}\frac{D_{W,l}^{eff}}{D_{Wm}^{eff}}\left(\sum_{j\neq W}\frac{x_WN_j-x_jN_W}{PD_{Wj}^{eff}}-\frac{N_W}{PD_{Wm}^{eff}}\right). \quad [3.84]$$

These three equations, [3.82]-[3.84] are the final result of the series-parallel model and are used to describe gas transport in the cathode catalyst layer and MPLs. In the macroporous GDL, wall friction is neglected ($D_{Wm}^{eff} = \infty$), pressure is constant, and only Equations [3.83] and [3.84] are used.

3.2.4 Full Model Description

The remainder of the model is similar to the transient model described in detail previously. Several of the equations are identical to those used in Section 3.1.2, but in the interest of a comprehensive and centralized model specification, they are repeated here in the appropriate section. The steady-state model is described first, and the linearized impedance model is described next. The model equations can be grouped into conservation equations, equilibrium equations, transport equations, and kinetic equations. Additionally, composition and temperature dependent transport properties are specified.

3.2.4.1 Conservation Equations

Each conserved quantity requires a conservation equation. As a simplifying assumption, the enthalpy of water is equal in the liquid and ionomer phases, and the rate of exchange between the two phases does not need to be calculated. Only the combined rate of phase change from water or ionomer to the gas phase, j_v, is calculated. Thus, conservation equations are written for total water across all phases, liquid and ionomer water, oxygen, heat, and ionic current,

$$\frac{dN_{W,g}}{dz} + \frac{dN_{W,l}}{dz} + \frac{dN_{W,i}}{dz} = 2\,j_{ORR}\,, \qquad [3.85]$$

$$\frac{dN_{W,l}}{dz} + \frac{dN_{W,i}}{dz} = -j_v\,, \qquad [3.86]$$

$$\frac{dN_O}{dz} = -j_{ORR}\,, \tag{3.87}$$

$$\frac{dq_h}{dz} = -4Fj_{ORR}\left(\Phi_1 - \Phi_2 - U_{H,ORR}\right) + \frac{i_2^{\,2}}{\kappa^{eff}} + \frac{i_1^{\,2}}{\sigma^{eff}} - \Delta H_v j_v\,, \tag{3.88}$$

$$\frac{di_2}{dz} = -4Fj_{ORR}\,. \tag{3.89}$$

The total current in the cell is constant for a 1-D model, so the balance equation for electronic current is replaced with

$$i_1 + i_2 = I\,. \tag{3.90}$$

Nitrogen flux into the membrane is zero (crossover is ignored), and nitrogen is inert, leaving

$$N_N = 0\,. \tag{3.91}$$

In the GDL and the MPL, there is no reaction, and the total water flux is constant, replacing Equation [3.85] with

$$\text{(GDL, MPL only)} \qquad N_{W,g} + N_{W,l} = N_{W,t}\,. \tag{3.92}$$

Electronic conductivity is assumed infinite in the GDL and MPL, and the heat balance can be combined with the water balance and integrated to eliminate j_v. Thus, Equations [3.86] and [3.88] are replaced by

$$\text{(GDL, MPL only)} \quad q_h = q_h^v\big|_{CL-MPL} + \Delta H_v N_{W,l}\,, \tag{3.93}$$

where $q_h^v\big|_{CL-MPL}$ is the heat flux at the catalyst layer-MPL interface assuming all water flux is in the vapor phase.

3.2.4.2 Equilibrium Equations

Next, there are a number of thermodynamic equilibrium expressions that can be specified. Equilibrium between water in the vapor, ionomer, and liquid phases is described by,

$$a_W = \frac{x_W}{x_{sat}}, \tag{3.94}$$

$$x_{sat}P = 10^5 \exp\left(11.6832 - \frac{3816.44}{T - 46.13}\right) \quad [\mathrm{Pa}] \tag{3.95}$$

$$\lambda = 0.043 + 17.81 a_W - 39.85 {a_W}^2 + 36.0 {a_W}^3, \tag{3.96}$$

$$p_c V_l = RT \ln a_W, \tag{3.97}$$

where a_W is the activity of water. In this modeling scheme, liquid water is always in equilibrium with vapor, even at low RH, but the resulting capillary pressure is very large and negative, and saturation is effectively zero. The relationship between capillary pressure and saturation is specified in Equation [6.4] and discussed in the surrounding text. The advantage of the modeling scheme is that no switch needs to be made when the cell reaches 100% RH. Additionally, the sum of mole fractions is one,

$$x_W + x_O + x_N = 1. \tag{3.98}$$

3.2.4.3 Transport Equations

Mass, momentum, and heat transport equations are needed. First, ionomer mass transport is modeled with concentrated solution theory,

$$N_{W,i} = -\frac{\kappa_{eff}\xi}{F}\frac{\partial \Phi_2}{\partial z} - \left(\alpha_{eff} + \frac{\kappa_{eff}\xi^2}{F^2}\right)\frac{RT}{a_W}\frac{\partial a_W}{\partial z}, \tag{3.99}$$

$$i_2 = -\kappa_{eff} \frac{\partial \Phi_2}{\partial z} - \frac{\kappa_{eff} \xi}{F} \frac{RT}{a_W} \frac{\partial a_W}{\partial z}. \qquad [3.100]$$

Next, the gas-phase mass and momentum transport equations derived in the previous section are applied,

$$\frac{1}{RTP} \frac{d\left(x_W P\right)}{dz} = \frac{1+\left(2-3s+s^2\right)\beta P}{\left(1-s\right)^3+\left(2-2s^2+s^3\right)\beta P} \left(\frac{x_W N_O - x_O N_W}{PD_{WO}^{eff}} + \frac{x_W N_N - x_N N_W}{PD_{WN}^{eff}} - \frac{N_W}{PD_{Wm}^{eff}} \right), \qquad [3.101]$$

$$\frac{1}{RTP} \frac{d\left(x_O P\right)}{dz} = \begin{array}{l} \left(1-s\right)^{-3} \left(\dfrac{x_O N_W - x_W N_O}{PD_{WO}^{eff}} + \dfrac{x_O N_N - x_N N_O}{PD_{ON}^{eff}} - \dfrac{N_O}{PD_{Om}^{eff}} \right) \\ + \left\{ \dfrac{\left[\left(1-s\right)^{-3} - 1\right] \beta_O P}{\left(1-s\right)^3 + \left(2-2s^2+s^3\right)\beta P} \right\} \left(\dfrac{x_W N_O - x_O N_W}{PD_{WO}^{eff}} + \dfrac{x_W N_N - x_N N_W}{PD_{WN}^{eff}} - \dfrac{N_W}{PD_{Wm}^{eff}} \right) \end{array}, \qquad [3.102]$$

$$\frac{1}{RTP} \frac{dP}{dz} = \begin{array}{l} -\left(1-s\right)^{-3} \left(\dfrac{N_W}{PD_{Wm}^{eff}} + \dfrac{N_O}{PD_{Om}^{eff}} + \dfrac{N_N}{PD_{Nm}^{eff}} \right) \\ - \dfrac{\left(1-s\right)^{-3} - 1}{\left(1-s\right)^3 + \left(2-2s^2+s^3\right)\beta P} \dfrac{D_{W,l}^{eff}}{D_{Wm}^{eff}} \left(\dfrac{x_W N_O - x_O N_W}{PD_{WO}^{eff}} + \dfrac{x_W N_N - x_N N_W}{PD_{WN}^{eff}} - \dfrac{N_W}{PD_{Wm}^{eff}} \right) \end{array}. \qquad [3.103]$$

Liquid water transport is modeled with Darcy's law,

$$N_{W,l} = -\frac{K}{V_m \mu} \frac{\partial \Pi}{\partial z}. \qquad [3.104]$$

Heat is transported through conduction,

$$q_h = -k^{eff} \frac{dT}{dz}. \qquad [3.105]$$

Finally, in the catalyst layer, electronic current is described by Ohm's law,

$$i_1 = \sigma^{eff} \frac{d\Phi_1}{dz}, \qquad [3.106]$$

although the electronic resistance could justifiably be neglected. Electronic resistance is neglected in the MPL and GDL to simplify the energy balance.

3.2.4.4 Kinetic Equations

An agglomerate model is used to model kinetics and mass transport through the ionomer film coating the catalyst particles. Except for one modification, the same equations were used in the previous transient single-phase model (cf. Equations [3.33]-[3.37]), but they are repeated here in order to present a comprehensive list of the model equations in the steady-state two-phase model. The equivalent homogenous reaction rate, k', is

$$k' = \frac{a_{Pt} k_0 \Gamma_v}{P_{ref}{}^{m}} \exp\left(-\frac{\alpha_{0c} F}{RT} \left(\Phi_1 - \Phi_2 - U_0 \right) \right). \qquad [3.107]$$

The Thiele modulus, ϕ, is defined for the active core of the agglomerate as

$$\phi = \left(R_{agg} - d_f \right) \sqrt{\frac{(m+1)\, p_{O,f}{}^{m-1} H_{O,i} k'}{2 D_{O,i}^{eff}}}, \qquad [3.108]$$

where $p_{O,f}$ is the partial pressure of oxygen at the film-agglomerate core interface, and $D_{O,i}^{eff}$ is the effective diffusivity of oxygen in the agglomerate core. Using this definition of the Thiele modulus, the exact solution for a 1st order reaction,

$$\eta = \frac{3}{\phi^2} \left(\phi \coth\phi - 1 \right), \qquad [3.109]$$

provides a very good approximation for arbitrary reaction orders. The oxygen concentration difference across the ionomer film is

$$x_O P - p_{O,f} = \frac{H_{O,i} j_{ORR} R_{agg}}{3 D_{O,i} \left(1 - \varepsilon_g \right) (1 - s) \left(\frac{1}{d_f} - \frac{1}{R_{agg}} \right)}, \qquad [3.110]$$

where the added $(1-s)$ term accounts for the fraction of agglomerates blocked by liquid water. Similarly, j_{ORR} is reduced by liquid water saturation according to

$$j_{ORR} = \eta k' p_{O_2,f}{}^{m} \left(1-\varepsilon_g\right)\left(1-s\right)\left(1-\frac{d_f}{R_{agg}}\right)^3 . \qquad [3.111]$$

The ORR rate equation is first-order in vacant chemisorption sites, Γ_v, which necessitates the inclusion of a platinum oxide model, as described previously. The equilibrium expressions for the three oxide species, chemisorbed OH, planar-site PtO_2, and edge-site PtO_2 are

$$\omega_1\theta_1^{*2} + RT\ln\left(\frac{\theta_1^*}{1-\theta_1^*}\right) = F\left(\Phi_1-\Phi_2-U_1\right), \qquad [3.112]$$

$$\omega_2\frac{x_2}{\psi_2} + RT\ln\left(\frac{1}{\theta_1^*\theta_*}\frac{x_2}{\psi_2}\right) = \omega_1\theta_1^{*2} + 3F\left(\Phi_1-\Phi_2-U_2\right) - \Delta\mu \;, \qquad [3.113]$$

$$\omega_3\frac{x_3}{\psi_3} + RT\ln\left(\frac{x_3}{\psi_3}\right) = 4F\left(\Phi_1-\Phi_2-U_3\right) - \Delta\mu , \qquad [3.114]$$

where θ_* is the fraction of chemisorption sites not disrupted by PtO_2 and θ_1^* is the coverage of chemisorbed OH as a fraction of the non-disrupted chemisorption sites. Equations [3.113] and [3.114] are derived from Equations [3.29] and [3.30] by setting the reaction rate to zero. The fraction of remaining chemisorption sites is

$$\theta_* = \exp\left[-\chi\theta_2 + \chi\frac{X_e}{1-X_e}\theta_3\right], \qquad [3.115]$$

and the surface concentration of vacant chemisorption sites is

$$\Gamma_v = \Gamma_0\theta_*\left(1-\theta_1^*\right). \qquad [3.116]$$

The planar-site and edge-site coverages of PtO_2 are integrated over the heterogeneity parameter,

$$\theta_2 = \int_{-\infty}^{\infty} x_2 d\Delta\mu , \tag{3.117}$$

$$\theta_3 = \int_{-\infty}^{\infty} x_3 d\Delta\mu , \tag{3.118}$$

respectively. The distribution of oxides formed at high overpotential is described by ψ, where

$$\psi_2 = \frac{1}{\sigma_2\sqrt{2\pi}} \exp\left(-\frac{\Delta\mu^2}{2{\sigma_2}^2} \right), \tag{3.119}$$

$$\psi_3 = \frac{1}{\sigma_3\sqrt{2\pi}} \exp\left(-\frac{\Delta\mu^2}{2{\sigma_3}^2} \right). \tag{3.120}$$

3.2.4.5 Transport Properties

The remaining model equations specify the various temperature and composition dependent transport properties.

$$\beta = D_{W,l}^{eff} \left(\sum_{j \neq W} \frac{x_j}{PD_{Wj}^{eff}} + \frac{1}{PD_{Wm}^{eff}} \right) \tag{3.121}$$

$$\beta_O = \frac{x_O D_{W,l}^{eff}}{PD_{WO}^{eff}} \tag{3.122}$$

$$D_{W,l} = \frac{RTk_{liq}}{3.81644 \times 10^8 \Delta H_v} \left(T - 46.13 \right)^2 \exp\left(-11.6832 + \frac{3816.44}{T - 46.13} \right) \tag{3.123}$$

$$D_{im}^{eff} = D_{K_i}^{eff} + \frac{KP}{\mu\sqrt{M_i}} \sum_j x_j \sqrt{M_j} \tag{3.124}$$

where the temperature dependence of gaseous and Knudsen diffusion coefficients is neglected due to the small magnitude of the effect. In the ionomer, transport properties are a function of ionomer hydration and temperature,

$$D_{W,i} = 3.5\times 10^{-6}\lambda \exp\left(\frac{-2436}{T}\right) \quad \left[\mathrm{m^2/s}\right], \tag{3.125}$$

$$\xi = 1.1 + \frac{0.9}{1+\exp\left[-2\left(\lambda - 5.5\right)\right]}, \tag{3.126}$$

$$\kappa = 1.45\exp\left[1268\left(\frac{1}{353}-\frac{1}{T}\right)+2.29a_W\right] \quad \left[\mathrm{S/m}\right], \tag{3.127}$$

and the Fick's law diffusion coefficient, $D_{W,l}$ is related to the chemical potential diffusion coefficient, α, by

$$\alpha = \frac{\frac{D_{W,i}}{RT}\frac{\rho_i}{EW}\left(17.81a_W - 79.7a_w{}^2 + 108a_W{}^3\right)}{\left[1+\frac{MW\rho_i}{EW\rho_w}\left(0.043+17.81a_W - 39.85a_W{}^2 + 36a_W{}^3\right)\right]^2}. \tag{3.128}$$

Liquid water transport can be described by an equivalent linear driving force, Π,

$$\Pi = \frac{p_c^*}{48}\left\{\begin{array}{l} 24\left(\frac{p_c - p_{c,0.5}}{p_c^*}\right) + 24\ln\left(\cosh\left(\frac{p_c - p_{c,0.5}}{p_c^*}\right)\right) - 22\tanh\left(\frac{p_c - p_{c,0.5}}{p_c^*}\right) \\ +\cosh^{-2}\left(\frac{p_c - p_{c,0.5}}{p_c^*}\right)\left[6+\tanh\left(\frac{p_c - p_{c,0.5}}{p_c^*}\right)\right] \end{array}\right\}, \tag{3.129}$$

which includes the saturation dependence of relative permeability.

The remaining properties are specified as a function of nominal cell temperature, but are not adjusted for spatial or temporal temperature variations within the MEA. These properties are considered model parameters. First, the Knudsen diffusion coefficient is

$$D_{K_i}^{eff} = \frac{\varepsilon}{\tau}\frac{d}{3}\sqrt{\frac{8RT_0}{\pi M_i}}. \tag{3.130}$$

The Henry's law constant and diffusion coefficient of oxygen in the ionomer are

$$H_{O,i} = 1.348\times 10^5 \exp\left(\frac{-666}{T_0}\right) \quad \left[\mathrm{Pa\cdot m^3/mol}\right], \tag{3.131}$$

$$D_{O,i} = 3.1\times10^{-7}\exp\left(\frac{-2768}{T_0}\right)\ \left[\mathrm{m^2/s}\right]. \qquad [3.132]$$

3.2.4.6 Boundary Conditions

At the internal MEA interfaces, the appropriate concentrations and fluxes are equated across layer boundaries. Due to the various equilibrium expressions, only certain variables need to be equated. At gas-phase boundaries (GDL-MPL and MPL-CL), the variables equated across the interface are capillary pressure, $n-2$ mole fractions, pressure, temperature, electronic potential, total water flux, flux of each gas except water vapor, heat flux, and electronic current. Due to equilibrium between water phases, only one concentration variable and the total flux need to be equated. This and the requirement that mole fractions sum to one reduce the number of species for which mole fractions can be equated to $n-2$. The heat flux is specified assuming all water flux is in the vapor form. Any deviation from this assumption is accounted for by the energy balance in the first control volume of the channel-side domain. If an interfacial heat transfer resistance were to be added, then liquid water flux would need to be equated to determine the exact interfacial heat flux.

At the ionomer boundary (catalyst layer-membrane), the variables equated across the interface are water activity, ionic potential, temperature, total water flux, ionic current, and heat flux. Here, evaporation from the membrane surface into the catalyst layer pores is accounted for when equating the heat flux,

$$q_h\Big|_{z=L}^{M} - q_h\Big|_{z=0}^{C} = \Delta H_v N_{W,g}\Big|_{z=0}^{C}\ . \qquad [3.133]$$

At the two catalyst layer boundaries, certain zero-flux boundary conditions are applied for the phases that do not cross the interface. At the catalyst layer-membrane interface, gas fluxes other than water vapor and electronic current are set to zero. At the catalyst layer-MPL interface, ionic current is set to zero.

The anode catalyst layer is reduced to an interface between the anode MPL and membrane for simplicity. Across this interface, temperature and total water flux are equated. Electronic current in the MPL is equated to ionic current in the membrane. The flux of hydrogen is determined by current density according to Faraday’s law. The heat flux is equated after accounting for water transport and half reaction enthalpy (assumed to be zero due to a lack of consistent literature values),

$$q_h\Big|_{z=0}^{M} - q_h\Big|_{z=L}^{AMPL} = \Delta H_v N_{W,g}\Big|_{z=L}^{AMPL} + I\left(\Phi_1\Big|_{z=L}^{AMPL} - \Phi_2\Big|_{z=0}^{M} - U_{H,RHE}\right). \qquad [3.134]$$

Water activity is equated using activity in the membrane and capillary pressure in the MPL, or

$$V_l p_c\Big|_{z=L}^{AMPL} = RT\Big|_{z=0}^{M} \ln\left(a_W\Big|_{z=0}^{M}\right). \qquad [3.135]$$

The hydrogen oxidation reaction is assumed to be at equilibrium, described by the Nernst equation,

$$\Phi_1\Big|_{z=L}^{AMPL} - \Phi_2\Big|_{z=0}^{M} = -\frac{RT\Big|_{z=L}^{AMPL}}{2F}\ln\left(\frac{\left(x_H P\right)\Big|_{z=L}^{AMPL}}{P_{ref}}\right). \qquad [3.136]$$

The channel-GDL interfaces are the external boundaries of the MEA model. For the gas composition, at the anode, only water capillary pressure or mole fraction needs to be specified when pure hydrogen is the fuel. At the cathode, oxygen mole fraction and either water capillary pressure or mole fraction are specified. Temperature and pressure must be specified at each boundary. Potential is arbitrarily set to zero at the anode GDL-channel interface. Finally, either current density or the potential at the cathode GDL-channel interface can be specified, but current density is preferred to simplify model initialization.

3.2.4.7 Numerical Procedures

The model equations are discretized along the spatial dimension using the control-volume method (37, 38). In this method, the spatial domain is divided into N volumes. Scalar quantities are defined at the center of each volume, while vector quantities are defined at the boundaries between volumes. This approach is well suited to typical mass transport problems where concentration is related to the divergence of flux, and flux is related to the gradient of concentration. Central finite difference approximations can be used to define the gradient of a scalar quantity at an edge point and the divergence of a vector quantity at a center point. The approach conserves mass and energy regardless of the grid spacing, as the flux leaving a volume through a boundary is also the flux entering the opposite volume through the boundary.

The control-volume method is not built into gPROMS, but is implemented using two grids with finite-difference approximations. The spatial coordinate, z, is normalized by dividing by the layer thickness. The scalar grid is defined with N interior points placed at

$$z_i = \frac{i - 1/2}{N}, \quad i = 1 \ldots N . \qquad [3.137]$$

Derivatives are discretized by a forward finite difference approximation. The vector grid is defined with $N-1$ interior points placed at uniform intervals,

$$z_i = \frac{i}{N}, \quad i = 1 \ldots N-1 . \qquad [3.138]$$

Derivatives are discretized by a backward finite difference approximation. To illustrate how the discretization technique works to produce the correct control-volume formulation in gPROMS, consider the first interior point, $i = 1$, on each of the above grids. On the scalar grid, the first interior point is bounded by the $i = 0$ and $i = 1$ points on the vector grid (i.e. the first control volume exists between the external boundary and the first internal boundary). Thus, a backward finite difference approximation is appropriate for the vector grid. On the vector grid, the first interior point is bounded by the $i = 1$ and $i = 2$ points on the scalar grid (i.e. the first internal boundary exists between the first and second control volumes). Thus, a forward finite difference approximation is appropriate for the scalar grid.

Often, transport equations, which are defined at edge points, require concentration- or temperature-dependent transport properties. The value of these transport properties must be defined at an edge point, while concentration and temperature are defined at center points. In these cases, the scalar quantity is averaged between the two adjacent center points.

An initialization procedure is used to assist the numerical solver with model initialization. First, a simplified model is solved, and the results are used the initial guesses in a more complex model. This process is iterated until all simplifications have been removed. gPROMS uses a block decomposition solver for initialization that recognizes independent blocks of variables and equations that can be solved from the known boundary conditions and any previously solved blocks. The initial simplified problem is designed such that no block contains unknown variables from more than two control volumes. The list of simplifications made is:

1. No heat or water transport across the anode catalyst layer. Temperature is still equated, breaking conservation of energy (i.e. heat flux is zero in the membrane, but non-zero in the MPL).
2. Ignore Joule heating in the membrane.
3. Assume uniform heat generation in the catalyst layer based on the known current density and a guessed cell potential.
4. Assume a uniform current distribution in the catalyst layer. In the ORR rate equation, ignore oxide coverage. Use the ionic potential at the membrane interface and the electronic potential and oxygen partial pressure at the MPL interface.
5. Ignore the heat of vaporization throughout the MEA.
6. When scalar quantities are evaluated at vector grid points, use the value from the channel-side scalar grid point instead of the average of the two adjacent scalar grid points.

Assumptions 1-3 and 5 allow the heat flux and temperature profile to be calculated from the membrane through the cathode layers point-by-point, one equation at a time. Equating temperature and breaking conservation of energy still requires the heat flux and temperature to be solved simultaneously through the anode GDL and MPL, but this problem is simple enough to solve even with a large number of points. The simplified energy balance could be analytically integrated to determine the heat flux, but this step proved unnecessary. Assumption 4 allows the ionic and electronic potential gradients in the catalyst layer to be solved volume-by-volume. Normally, the exact current and concentration profiles are needed to determine the potential gradients, as the ionic and electronic potential boundary conditions are supplied from opposite ends. Finally, Assumption 6 is helpful for flux equations with concentration- or temperature-dependent transport properties. When the average value from the two adjacent volumes is used instead, most of the variables from the edge and the downstream volume must be solved for simultaneously. If the upstream value is used, which is already known, usually a single downstream variable can be solved for at a time. The assumptions are removed in order, from 1 to 6. In the final problem, the majority of the equations are solved simultaneously, but with the suitable initial guesses provided by the earlier approximations, the solver converges.

3.2.4.8 Linearized AC Perturbation Equations

The transient solution for small sinusoidal perturbations of frequency, ω, can be solved with a linear set of equations derived from a transient model. Each variable, x, can be written as

$$x(t) = \bar{x} + \mathrm{Re}\left(\tilde{x}\exp(j\omega t)\right), \tag{3.139}$$

where $\bar{x}$ is the steady-state value, and $\tilde{x}$ is a complex number representing the magnitude and phase of the variation of x with time. The time derivative can be evaluated analytically and is

$$\frac{\partial x(t)}{\partial t} = \mathrm{Re}\left(j\omega\tilde{x}\exp(j\omega t)\right). \tag{3.140}$$

Any differential equation involving the variables $x_1, x_2, ...x_n$ can be converted into a linear equation involving $\tilde{x}_1, \tilde{x}_2, ...\tilde{x}_n$ if the steady-state solution is known, by taking a Taylor series expansion, neglecting the higher-order terms, canceling the steady-state part, and dividing the remaining first-order terms by $\exp(j\omega t)$. Thus, the equation

$$f\left(x_1,\ldots x_n\right)=\frac{\partial}{\partial t}g\left(x_1,\ldots x_n\right) \qquad [3.141]$$

is converted to

$$\left.\frac{\partial f}{\partial x_1}\right|_{\bar{x}_1\ldots\bar{x}_n}\tilde{x}_1+\ldots+\left.\frac{\partial f}{\partial x_n}\right|_{\bar{x}_1\ldots\bar{x}_n}\tilde{x}_n=j\omega\left(\left.\frac{\partial g}{\partial x_1}\right|_{\bar{x}_1\ldots\bar{x}_n}\tilde{x}_1+\ldots+\left.\frac{\partial g}{\partial x_n}\right|_{\bar{x}_1\ldots\bar{x}_n}\tilde{x}_n\right). \qquad [3.142]$$

This approach is applied systematically to all of the previously described model equations. While the implementation of this model is left as a recommendation in Chapter 8, the equations are presented in this section as an aid to future modelers.

For the conservation equation, accumulation terms are included similar to those used in the transient model of Section 3.1. The equations for conservation of total water mass, liquid and ionomer water mass, oxygen, nitrogen, energy, ionomer current, and total current are

$$j\omega\left[\frac{\varepsilon_g\left(1-\bar{s}\right)\bar{x}_W\bar{P}}{R\bar{T}}\left(\frac{\tilde{x}_W}{\bar{x}_W}+\frac{\tilde{P}}{\bar{P}}-\frac{\tilde{s}}{1-\bar{s}}-\frac{\tilde{T}}{\bar{T}}\right)+\frac{\varepsilon_g}{V_l}\tilde{s}+\frac{\varepsilon_i\rho_i}{EW}\tilde{\lambda}\right]=-\frac{d\tilde{N}_{W,g}}{dz}-\frac{d\tilde{N}_{W,l}}{dz}-\frac{d\tilde{N}_{W,i}}{dz}+2\tilde{j}_{ORR}, \qquad [3.143]$$

$$j\omega\left[\frac{\varepsilon_g}{V_l}\tilde{s}+\frac{\varepsilon_i\rho_i}{EW}\tilde{\lambda}\right]=-\frac{d\tilde{N}_{W,l}}{dz}-\frac{d\tilde{N}_{W,i}}{dz}-\tilde{j}_v, \qquad [3.144]$$

$$j\omega\frac{\varepsilon_g\left(1-\bar{s}\right)\bar{x}_O\bar{P}}{R\bar{T}}\left(\frac{\tilde{x}_O}{\bar{x}_O}+\frac{\tilde{P}}{\bar{P}}-\frac{\tilde{s}}{1-\bar{s}}-\frac{\tilde{T}}{\bar{T}}\right)=-\frac{d\tilde{N}_O}{dz}-\tilde{j}_{ORR}, \qquad [3.145]$$

$$j\omega\frac{\varepsilon_g\left(1-\bar{s}\right)\bar{x}_N\bar{P}}{R\bar{T}}\left(\frac{\tilde{x}_N}{\bar{x}_N}+\frac{\tilde{P}}{\bar{P}}-\frac{\tilde{s}}{1-\bar{s}}-\frac{\tilde{T}}{\bar{T}}\right)=-\frac{d\tilde{N}_N}{dz}, \qquad [3.146]$$

$$j\omega\overline{c_P\rho}\tilde{T}=-\frac{d\tilde{q}_h}{dz}-4F\tilde{j}_{ORR}\left(\bar{\Phi}_1-\bar{\Phi}_2-U_{H,ORR}\right)-4F\bar{j}_{ORR}\left(\tilde{\Phi}_1-\tilde{\Phi}_2\right)+\frac{2\bar{i}_2\tilde{i}_2}{\bar{\kappa}^{eff}}-\frac{\bar{i}_2^{\,2}\tilde{\kappa}^{eff}}{\left(\bar{\kappa}^{eff}\right)^2}+\frac{2\bar{i}_1\tilde{i}_1}{\sigma^{eff}}-\Delta H_v\tilde{j}_v, \qquad [3.147]$$

$$j\omega c_{DL}\left(\tilde{\Phi}_1-\tilde{\Phi}_2\right)=\frac{d\tilde{i}_2}{dz}-a_{Pt}\tilde{i}_{ox}+4F\tilde{j}_{ORR}, \qquad [3.148]$$

$$\tilde{i}_1+\tilde{i}_2=\tilde{I}. \qquad [3.149]$$

The equilibrium conditions of Equations [3.94] - [3.98] in linearized form are

$$\tilde{a}_W = \frac{\tilde{x}_W}{\bar{x}_{sat}} - \frac{\bar{x}_W \tilde{x}_{sat}}{\bar{x}_{sat}^{\ 2}}, \qquad [3.150]$$

$$\tilde{x}_{sat}\bar{P} + \bar{x}_{sat}\tilde{P} = \frac{3.81644\times10^8}{\left(\bar{T}-46.13\right)^2}\exp\left(11.6832 - \frac{3816.44}{\bar{T}-46.13}\right)\tilde{T} \quad \left[\mathrm{Pa}\right], \qquad [3.151]$$

$$\tilde{\lambda} = \left(17.81 - 79.70\bar{a}_W + 108.0\bar{a}_W^{\ 2}\right)\tilde{a}_W, \qquad [3.152]$$

$$\tilde{p}_c V_l = R\tilde{T}\ln\bar{a}_W + \frac{R\bar{T}}{\bar{a}_W}\tilde{a}_W, \qquad [3.153]$$

$$\tilde{s} = \frac{\tilde{p}_c}{2p_c^*}\left(1 - \tanh^2\left(\frac{\bar{p}_c - p_{c,0.5}}{p_c^*}\right)\right), \qquad [3.154]$$

$$\tilde{x}_W + \tilde{x}_O + \tilde{x}_N = 0. \qquad [3.155]$$

The linearized forms of the ionomer transport equations are

$$\tilde{N}_{W,i} = \left\{ \begin{array}{l} -\dfrac{\bar{\kappa}_{eff}\bar{\xi}}{F}\dfrac{\partial\tilde{\Phi}_2}{\partial z} - \dfrac{\bar{\kappa}_{eff}\tilde{\xi} + \tilde{\kappa}_{eff}\bar{\xi}}{F}\dfrac{\partial\bar{\Phi}_2}{\partial z} - \left(\tilde{\alpha}_{eff} + \dfrac{\tilde{\kappa}_{eff}\bar{\xi}^2 + 2\bar{\kappa}_{eff}\bar{\xi}\tilde{\xi}}{F^2}\right)\dfrac{R\bar{T}}{\bar{a}_W}\dfrac{\partial\bar{a}_W}{\partial z} \\ -\left(\bar{\alpha}_{eff} + \dfrac{\bar{\kappa}_{eff}\bar{\xi}^2}{F^2}\right)\left[\dfrac{R\bar{T}}{\bar{a}_W}\dfrac{\partial\tilde{a}_W}{\partial z} + \left(\dfrac{R\tilde{T}}{\bar{a}_W} - \dfrac{R\bar{T}\tilde{a}_W}{\bar{a}_W^{\ 2}}\right)\dfrac{\partial\bar{a}_W}{\partial z}\right] \end{array} \right\}, \qquad [3.156]$$

$$\tilde{i}_2 = -\bar{\kappa}_{eff}\frac{\partial\tilde{\Phi}_2}{\partial z} - \tilde{\kappa}_{eff}\frac{\partial\bar{\Phi}_2}{\partial z} - \frac{\bar{\kappa}_{eff}\bar{\xi}}{F}\frac{R\bar{T}}{\bar{a}_W}\left[\frac{\partial\tilde{a}_W}{\partial z} + \frac{\partial\bar{a}_W}{\partial z}\left(\frac{\tilde{\kappa}_{eff}}{\bar{\kappa}_{eff}} + \frac{\tilde{\xi}}{\bar{\xi}} + \frac{\tilde{T}}{\bar{T}} - \frac{\tilde{a}_W}{\bar{a}_W}\right)\right]. \qquad [3.157]$$

The gas-phase transport equations are cumbersome, and are divided into parts using intermediate variables,

$$\frac{1}{RTP}\frac{dx_W P}{dz} = \frac{A}{B}C, \qquad [3.158]$$

$$\frac{1}{RTP}\frac{dx_O P}{dz} = \left(1-s\right)^{-3}E + \frac{D}{B}C, \qquad [3.159]$$

$$\frac{1}{RTP}\frac{dP}{dz} = G + \frac{H}{B}C\,, \qquad [3.160]$$

where

$$A = 1 + \left(2 - 3s + s^2\right)\beta P\,, \qquad [3.161]$$

$$B = \left(1-s\right)^3 + \left(2 - 2s^2 + s^3\right)\beta P\,, \qquad [3.162]$$

$$C = \frac{x_W N_O - x_O N_W}{PD_{WO}^{eff}} + \frac{x_W N_N - x_N N_W}{PD_{WN}^{eff}} - \frac{N_W}{PD_{Wm}^{eff}}\,, \qquad [3.163]$$

$$D = \left[\left(1-s\right)^{-3} - 1\right]\beta_O P\,, \qquad [3.164]$$

$$E = \frac{x_O N_W - x_W N_O}{PD_{WO}^{eff}} + \frac{x_O N_N - x_N N_O}{PD_{ON}^{eff}} - \frac{N_O}{PD_{Om}^{eff}}\,, \qquad [3.165]$$

$$G = -\left(1-s\right)^{-3}\left(\frac{N_W}{PD_{Wm}^{eff}} + \frac{N_O}{PD_{Om}^{eff}} + \frac{N_N}{PD_{Nm}^{eff}}\right), \qquad [3.166]$$

$$H = -\left(\left(1-s\right)^{-3} - 1\right)\frac{D_{W,l}^{eff}}{D_{Wm}^{eff}}\,. \qquad [3.167]$$

Equations [3.158]-[3.160] show how the gas transport equations are split into parts but are redundant with Equations [3.101]-[3.103] and are not included in the model. The linearized solutions are

$$\frac{1}{R\bar{T}\bar{P}}\left[\bar{P}\frac{d\tilde{x}_W}{dz} + \bar{x}_W\frac{d\tilde{P}}{dz} - \frac{d\bar{x}_W\bar{P}}{dz}\left(\frac{\tilde{T}}{\bar{T}} + \frac{\tilde{P}}{\bar{P}}\right)\right] = \frac{\bar{A}}{\bar{B}}\tilde{C} + \frac{\bar{C}}{\bar{B}}\tilde{A} - \frac{\bar{A}\bar{C}}{\bar{B}^2}\tilde{B}\,, \qquad [3.168]$$

$$\frac{1}{R\bar{T}\bar{P}}\left[\bar{P}\frac{d\tilde{x}_O}{dz} + \bar{x}_O\frac{d\tilde{P}}{dz} - \frac{d\bar{x}_O\bar{P}}{dz}\left(\frac{\tilde{T}}{\bar{T}} + \frac{\tilde{P}}{\bar{P}}\right)\right] = \left(1-\bar{s}\right)^{-3}\tilde{E} + 3\left(1-\bar{s}\right)^{-4}\bar{E}\tilde{s} + \frac{\bar{D}}{\bar{B}}\tilde{C} + \frac{\bar{C}}{\bar{B}}\tilde{D} - \frac{\bar{D}\bar{C}}{\bar{B}^2}\tilde{B}\,, \qquad [3.169]$$

$$\frac{1}{R\bar{T}\bar{P}}\frac{d\tilde{P}}{dz} - \frac{1}{R\bar{T}^2\bar{P}}\frac{d\bar{P}}{dz}\tilde{T} - \frac{1}{R\bar{T}\bar{P}^2}\frac{d\bar{P}}{dz}\tilde{P} = \tilde{G} + \frac{\bar{H}}{\bar{B}}\tilde{C} + \frac{\bar{C}}{\bar{B}}\tilde{H} - \frac{\bar{H}\bar{C}}{\bar{B}^2}\tilde{B}\,, \qquad [3.170]$$

where

$$\tilde{A} = \left(2 - 3\bar{s} + \bar{s}^2\right)\left(\bar{\beta}\tilde{P} + \tilde{\beta}\bar{P}\right) + \left(2\bar{s} - 3\right)\bar{\beta}\bar{P}\tilde{s}\,, \tag{3.171}$$

$$\tilde{B} = \left[-3\left(1-\bar{s}\right)^2 + \left(3\bar{s}^2 - 4\bar{s}\right)\bar{\beta}\bar{P}\right]\tilde{s} + \left(2 - 2\bar{s}^2 + \bar{s}^3\right)\left(\bar{\beta}\tilde{P} + \tilde{\beta}\bar{P}\right), \tag{3.172}$$

$$\tilde{C} = \frac{\bar{x}_W\tilde{N}_O + \tilde{x}_W\bar{N}_O - \bar{x}_O\tilde{N}_W - \tilde{x}_O\bar{N}_W}{PD_{WO}^{eff}} + \frac{\bar{x}_W\tilde{N}_N + \tilde{x}_W\bar{N}_N - \bar{x}_N\tilde{N}_W - \tilde{x}_N\bar{N}_W}{PD_{WN}^{eff}} - \frac{\bar{N}_W}{\bar{P}\bar{D}_{Wm}^{eff}}\left(\frac{\tilde{N}_W}{\bar{N}_W} - \frac{\tilde{P}}{\bar{P}} - \frac{\tilde{D}_{Wm}^{eff}}{\bar{D}_{Wm}^{eff}}\right), \tag{3.173}$$

$$\tilde{D} = \left[\left(1-\bar{s}\right)^{-3} - 1\right]\left(\bar{\beta}_O\tilde{P} + \tilde{\beta}_O\bar{P}\right) + 3\left(1-\bar{s}\right)^{-4}\bar{\beta}_O\bar{P}\tilde{s}\,, \tag{3.174}$$

$$\tilde{E} = \frac{\bar{x}_O\tilde{N}_W + \tilde{x}_O\bar{N}_W - \bar{x}_W\tilde{N}_O - \tilde{x}_W\bar{N}_O}{PD_{WO}^{eff}} + \frac{\bar{x}_O\tilde{N}_N + \tilde{x}_O\bar{N}_N - \bar{x}_N\tilde{N}_O - \tilde{x}_N\bar{N}_O}{PD_{ON}^{eff}} - \frac{\bar{N}_O}{\bar{P}\bar{D}_{Om}^{eff}}\left(\frac{\tilde{N}_O}{\bar{N}_O} - \frac{\tilde{P}}{\bar{P}} - \frac{\tilde{D}_{Om}^{eff}}{\bar{D}_{Om}^{eff}}\right), \tag{3.175}$$

$$\tilde{G} = \begin{array}{l} -3\left(1-\bar{s}\right)^{-4}\left(\dfrac{\bar{N}_W}{\bar{P}\bar{D}_{Wm}^{eff}} + \dfrac{\bar{N}_O}{\bar{P}\bar{D}_{Om}^{eff}} + \dfrac{\bar{N}_N}{\bar{P}\bar{D}_{Nm}^{eff}}\right)\tilde{s} + \left(1-\bar{s}\right)^{-3}\left(\dfrac{\bar{N}_W}{\bar{D}_{Wm}^{eff}} + \dfrac{\bar{N}_O}{\bar{D}_{Om}^{eff}} + \dfrac{\bar{N}_N}{\bar{D}_{Nm}^{eff}}\right)\dfrac{\tilde{P}}{\bar{P}^2} \\ -\left(1-\bar{s}\right)^{-3}\left[\dfrac{\tilde{N}_W}{\bar{P}\bar{D}_{Wm}^{eff}} - \dfrac{\bar{N}_W\tilde{D}_{Wm}^{eff}}{\bar{P}\left(\bar{D}_{Wm}^{eff}\right)^2} + \dfrac{\tilde{N}_O}{\bar{P}\bar{D}_{Om}^{eff}} - \dfrac{\bar{N}_O\tilde{D}_{Om}^{eff}}{\bar{P}\left(\bar{D}_{Om}^{eff}\right)^2} + \dfrac{\tilde{N}_N}{\bar{P}\bar{D}_{Nm}^{eff}} - \dfrac{\bar{N}_N\tilde{D}_{Nm}^{eff}}{\bar{P}\left(\bar{D}_{Nm}^{eff}\right)^2}\right] \end{array}, \tag{3.176}$$

$$\tilde{H} = -3\left(1-\bar{s}\right)^{-4}\frac{\bar{D}_{W,l}^{eff}}{\bar{D}_{Wm}^{eff}}\tilde{s} - \left(\left(1-\bar{s}\right)^{-3} - 1\right)\left(\frac{\tilde{D}_{W,l}^{eff}}{\bar{D}_{Wm}^{eff}} - \frac{\bar{D}_{W,l}^{eff}}{\left(\bar{D}_{Wm}^{eff}\right)^2}\tilde{D}_{Wm}^{eff}\right). \tag{3.177}$$

Using the driving force ψ, Darcy's law,

$$\tilde{N}_{W,l} = -\frac{K}{V_m\mu}\frac{\partial\tilde{\Pi}}{\partial z}, \tag{3.178}$$

is linear. Additionally, heat conduction,

$$\tilde{q}_h = -k^{eff}\frac{d\tilde{T}}{dz} \tag{3.179}$$

is linear, and Ohm's law for the electronic phase,

$$\tilde{i}_1 = \sigma^{eff}\frac{d\tilde{\Phi}_1}{dz}, \tag{3.180}$$

is linear.

The transport properties for which concentration-dependence or temperature-dependence is considered also need to be linearized. The gas-phase transport properties defined in the enhanced vapor diffusion model are

$$\tilde{\beta} = \tilde{D}_{W,l}^{eff}\left(\sum_{j\neq W}\frac{\bar{x}_j}{PD_{Wj}^{eff}} + \frac{1}{\bar{P}\bar{D}_{Wm}^{eff}}\right) + \bar{D}_{W,l}^{eff}\left(\sum_{j\neq W}\frac{\tilde{x}_j}{PD_{Wj}^{eff}} - \frac{\tilde{P}}{\bar{P}^2\bar{D}_{Wm}^{eff}} - \frac{\tilde{D}_{Wm}^{eff}}{\bar{P}\left(\bar{D}_{Wm}^{eff}\right)^2}\right), \qquad [3.181]$$

$$\tilde{\beta}_O = \frac{\tilde{x}_O\bar{D}_{W,l}^{eff} + \bar{x}_O\tilde{D}_{W,l}^{eff}}{PD_{WO}^{eff}}, \qquad [3.182]$$

$$\tilde{D}_{W,l} = \frac{Rk_{liq}}{3.81644\times10^8\,\Delta H_v}\left\{3\bar{T}^2 - 4000.96\bar{T} + 2127.9769\right\}\exp\left(-11.6832 + \frac{3816.44}{\bar{T}-46.13}\right)\tilde{T}, \qquad [3.183]$$

$$\tilde{D}_{im}^{eff} = \frac{K}{\mu\sqrt{M_i}}\left(\tilde{P}\sum_j \bar{x}_j\sqrt{M_j} + \bar{P}\sum_j \tilde{x}_j\sqrt{M_j}\right). \qquad [3.184]$$

Note that the temperature dependence of Knudsen diffusivity is small enough to neglect. The ionomer transport properties depend on both water content and temperature,

$$\tilde{\alpha} = \bar{\alpha}\left(\frac{\tilde{D}_{W,i}}{\bar{D}_{W,i}} - \frac{\tilde{T}}{\bar{T}}\right) + \frac{\bar{D}_{W,i}}{R\bar{T}}\frac{\rho_i}{EW}\left\{\frac{\begin{gathered}17.81 - 159.4\bar{a}_W + 324\bar{a}_W{}^2 + \frac{MW\rho_i}{EW\rho_w}\left(0.76583 - 324.0503\bar{a}_W\right.\\ \left. + 2143.12\bar{a}_W{}^2 - 7634.41\bar{a}_W{}^3 + 15780.6\bar{a}_W{}^4 - 11664\bar{a}_W{}^5\right)\end{gathered}}{\left[1 + \frac{MW\rho_i}{EW\rho_w}\left(0.043 + 17.81\bar{a}_W - 39.85\bar{a}_W{}^2 + 36\bar{a}_W{}^3\right)\right]^3}\right\}\tilde{a}_W, \qquad [3.185]$$

$$\tilde{D}_{W,i} = 3.5\times10^{-6}\exp\left(\frac{-2436}{\bar{T}}\right)\left(\tilde{\lambda} + \bar{\lambda}\frac{2436}{\bar{T}^2}\tilde{\mathrm{T}}\right) \quad \left[\mathrm{m}^2/\mathrm{s}\right], \qquad [3.186]$$

$$\tilde{\xi} = \frac{1.8\exp\left[-2\left(\bar{\lambda} - 5.5\right)\right]}{\left\{1 + \exp\left[-2\left(\bar{\lambda} - 5.5\right)\right]\right\}^2}\tilde{\lambda}, \qquad [3.187]$$

$$\tilde{\kappa} = 1.45 \exp\left[1268\left(\frac{1}{353} - \frac{1}{\bar{T}}\right) + 2.29\bar{a}_W\right]\left(\frac{1268}{\bar{T}^2}\tilde{T} + 2.29\tilde{a}_W\right) \quad [\mathrm{S/m}]. \qquad [3.188]$$

Finally, using Equation [3.47] as the starting point, the linear driving force for Darcy's law is

$$\tilde{\Pi} = \bar{s}^4 \tilde{p}_c . \qquad [3.189]$$

The interlayer boundary conditions are identical to those of the steady-state model. At the GDL-channel interfaces, the perturbations in mole fraction, capillary pressure, temperature, pressure, and anode potential are zero. An arbitrary perturbation,

$$\tilde{I} = 1, \qquad [3.190]$$

is applied to the cell current in order to simulate EIS. The magnitude does not matter, as the model has been linearized. Impedance is calculated by

$$\tilde{Z} = \frac{\tilde{E}}{\tilde{I}} = \frac{\tilde{\Phi}_1\Big|_{z=L}^{CGDL}}{\tilde{I}} = \tilde{\Phi}_1\Big|_{z=L}^{CGDL} . \qquad [3.191]$$

3.3 Conclusion

In this chapter, two models are developed to be used in the interpretation of EIS results and flooding losses. For EIS analysis, a one-phase transient model is developed incorporating as its main innovations the oxide layer and several often overlooked effects of the test hardware. The model is fit in Chapter 5 using several independent experiments to determine the most important model parameters and validated against EIS experiments varying both current density and oxygen concentration. For the prediction of flooding losses, a two-phase steady-state model is developed. The model builds on a standard approach, but incorporates the improvements of the one-phase transient model, as well as the first treatment of enhanced vapor diffusion in PEMFC modeling. Additionally, a linearized perturbation model was derived, which can be used by future researchers to simulate EIS under two-phase conditions. The steady-state solutions to the two-phase model are compared to experimental results in Chapter 6, and several improvements are made from the baseline model introduced in this chapter in improve the accuracy of the model.

3.4 References

1. N. Nonoyama, S. Okazaki, A. Z. Weber, Y. Ikogi and T. Yoshida, *J. Electrochem. Soc.*, **158**, B416 (2011).
2. E. L. Redmond, B. P. Setzler, F. M. Alamgir and T. F. Fuller, *PCCP*, **16**, 5301 (2014).
3. B. E. Conway, *Prog. Surf. Sci.*, **49**, 331 (1995).
4. J. X. Wang, J. Zhang and R. R. Adzic, *The Journal of Physical Chemistry A*, **111**, 12702 (2007).
5. M. Moore, A. Putz and M. Secanell, *J. Electrochem. Soc.*, **160**, F670 (2013).
6. M. Alsabet, M. Grden and G. Jerkiewicz, *J. Electroanal. Chem.*, **589**, 120 (2006).
7. M. Mathias, D. Baker, J. Zhang, Y. Liu and W. Gu, *ECS Transactions*, **13**, 129 (2008).
8. M. Boaventura, J. M. Sousa and A. Mendes, *Int. J. Hydrogen Energy*, **36**, 9842 (2011).
9. B. P. Setzler and T. F. Fuller, *ECS Transactions*, **58**, 95 (2013).
10. R. B. Bird, W. E. Stewart and E. N. Lightfoot, *Transport Phenomena*, Wiley, New York (2007).
11. R. C. Reid, *The properties of gases and liquids*, New York, McGraw-Hill (1987).
12. T. F. Fuller and J. Newman, *J. Electrochem. Soc.*, **140**, 1218 (1993).
13. T. E. Springer, T. A. Zawodzinski and S. Gottesfeld, *J. Electrochem. Soc.*, **138**, 2334 (1991).
14. A. Holewinski and S. Linic, *J. Electrochem. Soc.*, **159**, H864 (2012).
15. G. Lin, W. He and T. Van Nguyen, *J. Electrochem. Soc.*, **151**, A1999 (2004).

16. P. J. Linstrom and W. G. Mallard, *NIST Chemistry WebBook, NIST Standard Reference Database Number 69*, National Institute of Standards and Technology (2005).

17. O. Burheim, P. J. S. Vie, J. G. Pharoah and S. Kjelstrup, *J. Power Sources*, **195**, 249 (2010).

18. M. Khandelwal and M. M. Mench, *J. Power Sources*, **161**, 1106 (2006).

19. N. Zamel, E. Litovsky, X. G. Li and J. Kleiman, *Int. J. Hydrogen Energy*, **36**, 12618 (2011).

20. K. C. Neyerlin, W. B. Gu, J. Jorne and H. A. Gasteiger, *J. Electrochem. Soc.*, **153**, A1955 (2006).

21. C. Y. Wang and P. Cheng, *Int. J. Heat Mass Transfer*, **39**, 3607 (1996).

22. P. Cheng and C. Y. Wang, *Int. J. Heat Mass Transfer*, **39**, 3619 (1996).

23. Z. H. Wang, C. Y. Wang and K. S. Chen, *J. Power Sources*, **94**, 40 (2001).

24. D. Natarajan and T. Van Nguyen, *J. Electrochem. Soc.*, **148**, A1324 (2001).

25. L. J. Zheng, A. K. Srouji, R. Dross, A. Turhan and M. M. Mench, *J. Electrochem. Soc.*, **160**, F119 (2013).

26. A. Z. Weber, R. L. Borup, R. M. Darling, P. K. Das, T. J. Dursch, W. B. Gu, D. Harvey, A. Kusoglu, S. Litster, M. M. Mench, R. Mukundan, J. P. Owejan, J. G. Pharoah, M. Secanell and I. V. Zenyuk, *J. Electrochem. Soc.*, **161**, F1254 (2014).

27. J. M. LaManna, J. V. Bothe Jr, F. Y. Zhang and M. M. Mench, *J. Power Sources*, **271**, 180 (2014).

28. N. Zamel and X. Li, *Prog. Energy Combust. Sci.*, **39**, 111 (2013).

29. L. J. Zheng, A. K. Srouji, A. Turhan and M. M. Mench, *J. Electrochem. Soc.*, **159**, F267 (2012).

30. H. Meng and C.-Y. Wang, *J. Electrochem. Soc.*, **152**, A1733 (2005).

31. J. H. Nam and M. Kaviany, *Int. J. Heat Mass Transfer*, **46**, 4595 (2003).

32. G. S. Hwang and A. Z. Weber, *J. Electrochem. Soc.*, **159**, F683 (2012).

33. C. K. Ho and S. W. Webb, *Gas Transport in Porous Media*, Springer (2006).

34. T. R. Marrero and E. A. Mason, *J. Phys. Chem. Ref. Data*, **1**, 3 (1972).

35. M. L. V. Ramires, C. A. Nieto de Castro, Y. Nagasaka, A. Nagashima, M. J. Assael and W. A. Wakeham, *J. Phys. Chem. Ref. Data*, **24**, 1377 (1995).

36. L. M. Pant, S. K. Mitra and M. Secanell, *Int. J. Heat Mass Transfer*, **58**, 70 (2013).

37. J. S. Newman and K. E. Thomas-Alyea, *Electrochemical systems*, p. xx, J. Wiley, Hoboken, N.J. (2004).

38. A. C. West and T. F. Fuller, *J. Appl. Electrochem.*, **26**, 557 (1996).

CHAPTER 4

EXPERIMENTAL METHODS

4.1 Cell Assembly

Three-layer membrane electrode assemblies (MEAs) were purchased from Ion Power Inc. and used in all testing and validation experiments. The MEAs had an active area of 25 cm^2, were based on a Nafion 212 membrane (50 µm thickness), and had a catalyst loading of 0.3 mg_{Pt}/cm^2 each on the anode and cathode. The three-layer MEAs did not include a gas diffusion layer (GDL) and were combined with one of three varieties of GDL: Toray TGP-H-060 with 5% PTFE added for wet-proofing, SGL 25BA (5% PTFE), or SGL 24BC (5% PTFE), which included a microporous layer (MPL). Gaskets were die-cut from PTFE or reinforced silicone of various thicknesses depending on the GDL. Toray TGP-H-060 and SGL 25BA are 190 µm thick and were compressed to approximately 145 µm using two PTFE layers (5+1 mil nominal) with a measured thickness of 160 µm (allowing 15 µm for the catalyst layer). SGL 24BC is based on a similar 190 µm substrate, but has a thickness of 235 µm including the MPL. A “5 mil” PTFE gasket was layered with a “3 mil” silicone gasket for a measured gasket thickness of 210 µm. The GDLs were also die cut to ensure a good fit with the gasket as gaps can provide unwanted gas bypass channels and overlap produces uneven compression.

Single cell research hardware from Fuel Cell Technologies was used for all PEMFC testing. The cell hardware is pictured in Figure 4-1. The main components are aluminum end plates with gas connections, cartridge heaters, and a thermocouple well, gold-plated current collectors, and graphite flow fields. The flow fields have a triple serpentine channel pattern machined into their face, with 10 passes over the 25 cm^2 active area, and an 11th pass on the inlet end. The channel profile is approximately 0.7 mm wide and 1.1 mm deep, with 0.9 mm wide ribs between channels. The cells were assembled by stacking the fuel cell components on the anode flow field in the order: anode gasket, anode GDL, MEA, cathode gasket, cathode GDL, cathode flow field, and cathode end plate. No hot-pressing or other bonding step was used to attach gaskets and GDLs to the MEA. The eight ¼”-28 bolts were tightened by torque wrench to 4.5 N-m (40 in-lbs). The cell was heated by cartridge heaters, with only ambient cooling. For high current or low temperature operation, a fan was aimed at the cell to prevent overheating.

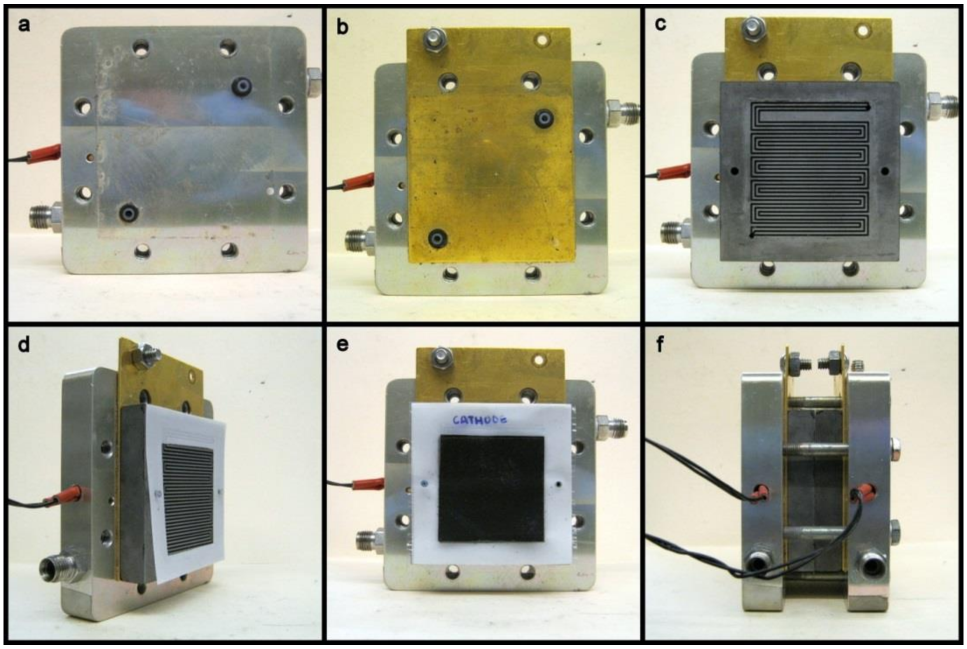

Figure 4-1: Single cell research hardware employed in all PEMFC testing. a) Aluminum end plate with gas inlet and outlet. Heater wires are also visible. b) Gold-plated current collector, insulated from end plate by adhesive-backed PTFE-impregnated fiberglass. c) Graphite flow field with triple serpentine pattern. d) Anode gasket added with alignment pegs e) MEA added (shown without cathode GDL) f) Final assembly. Photo credit: E. Redmond (1). Used with permission.

The triple serpentine flow pattern represents a tradeoff between pressure drop and fuel cell performance. The pressure drop between adjacent flow channels drives convection through the GDL, decreasing the mass-transport resistance and improving performance. Serpentine patterns result in a significant pressure difference between adjacent channels and produce better performance relative to parallel channel designs, where the pressure in adjacent channels is almost identical. At high gas flow rates, however, the pressure drop can be considerable in serpentine channel designs (70-80 kPa at the maximum test stand flow rate of 5 slpm). The pressure drop and convection lead to non-uniform mass transport in the GDL, which is often undesirable for research applications, where uniformity may be more important than raw performance. These issues were not a major problem in the present work, but had to be accounted for in the model. In addition to GDL convection, the channel pressure drop has a large influence on average relative humidity in the cell. As the gas expands, the relative humidity drops proportionally, an effect that must not be ignored when studying flooding losses. These concerns are raised as a caution to the researcher who may be interested in MEA development and find it convenient to ignore the effects of the test hardware.

Pressure drop was measured with an MEA present (TGP-H-060 GDL) using a handheld electronic manometer. The anode channel pressure drop was measured using hydrogen gas at 100 % RH and 80 °C cell temperature. The cathode channel pressure drop was measured for both nitrogen and helium at 75 % RH and 80 °C cell temperature. The cathode pressure drop measurements were assumed to apply regardless of oxygen concentration. The channel pressure drop measurements were also applied as estimates in

Chapter 6, where the reduced flow rates make the error from different temperature and humidity conditions less significant.

4.2 Test Equipment

The fuel cell was connected to a Scribner Associates 850e fuel cell test stand (FCTS) to manage gas flows, relative humidity (RH), temperature, and load. Hydrogen was used as the anode gas in all experiments. The cathode was connected to one or a mixture of nitrogen, helium, oxygen, and air. All gases were UHP grade with the exception of air, which was on-site compressed air passed through filters and a membrane dehumidifier to remove compressor oil, particulates, and water. The FCTS controls RH through sparging humidifiers fed with deionized water. The anode and cathode mass flow controllers had maximum flow rates of 2 and 5 slpm, respectively. Additional flow controllers of 50 sccm and 2 slpm maximum were connected to the cathode to allow gas blending. The FCTS has a built-in electronic load with a 100 A maximum current rating as well as a frequency response analyzer (FRA) (Scribner Model 880) to enable electrochemical impedance spectroscopy (EIS) measurements. For experiments that required a full potentiostat instead of an electronic load, an Autolab PGSTAT302N potentiostat was used with a 2 A current limit. The potentiostat included an FRA module and a true linear sweep generator.

4.3 Electrochemical Characterization Techniques

A variety of electrochemical characterization tests were performed on the MEAs for parameter fitting and model validation. A standard wet-up procedure was used prior to testing to bring the MEA performance to steady-state. The wet-up procedure is given in Table 4-1. During any idle time between experiments, the cell was held at 0.7 V or similar idle condition to minimize degradation. All experiments were conducted without backpressure.

Table 4-1: Details of wet-up procedure.

Step	**Control**	**Time (min)**	**Cell Temp. (°C)**	**Anode Gas / Dew Point (°C) / Flow (slpm)**	**Cathode Gas / Dew Point (°C) / Flow (slpm)**
Initial Humidification					
1a	OCV	30	65	N_2 / 65 / 0.5	N_2 / 65 / 1.25
1b		60	85	H_2 / 85 / 0.5	Air / 85 / 1.25
Limiting current / OCV cycles (repeat 12 times)					
2a	0.2 V	10	85	H_2 / 85 / 0.5	Air / 85 / 1.25
2b	OCV	0.5			
Current Holds (repeat 2 times)					
3a	1200 mA/cm^2	20	85	H_2 / 85 / Stoichiometric ratio = 4	Air / 85 / Stoichiometric ratio = 4
3b	1000 mA/cm^2				
3c	800 mA/cm^2				
3d	600 mA/cm^2				
3e	400 mA/cm^2				
3f	200 mA/cm^2				
3g	100 mA/cm^2				

4.3.1 Polarization Curves

The standard method for characterizing PEMFC performance is the polarization curve, as introduced in Chapter 1. Polarization curves were performed as a sequence of constant current holds, beginning with the highest current density. The cell was controlled by the FCTS electronic load. Each current density was held for 15 minutes, and the average potential over the last 5 minutes was used as the data point. The particular current densities used depended on the cathode gas and performance of the cell. Constant flow rates were used for all polarization curves in order to maintain a constant effect of convection in the GDL. The polarization curves of Chapter 5 were performed at 5 slpm cathode gas flow rate. The anode gas flow rate was 2 slpm when air was used at the cathode, and 0.5 slpm when 1% O_2 mixtures were used at the cathode. The cell temperature was 80 °C and the RH was 75% (73 °C humidifier temperature). DC resistance was measured as the slope of the polarization curve using a three-point quadratic interpolation. In Chapter 6, flow rates depended on the GDL used. For TGP-H-060, the anode and cathode flow rates were both 1 slpm. For SGL 25BA and 24BC, the anode and cathode flow rates were 0.63 slpm and 1.5 slpm, respectively. Cell and humidifier temperatures varied and are specified individually for each result.

In Chapter 6, current sweeps were sometimes used in place of steady-state polarization curves, as noted. Current sweeps consisted of a series of 15 second holds with a step of 5 mA/cm^2, beginning with the lowest current density first. The potential measurements were made at the end of each step. The motivation for using current sweeps instead of traditional steady-state polarization curves was to enable faster measurements, allowing more conditions to be investigated without significant cell degradation, and also to increase the number of measurement points to better observe limiting current behavior. Flow rates were identical to the standard polarization curves unless otherwise noted.

4.3.2 Limiting Current Analysis

Limiting current can be used as a measure of oxygen transport resistance. Limiting current density analysis is best performed with low oxygen concentrations to reduce water generation (preventing flooding) and to reduce the impact of ohmic losses and other cell limitations, ensuring that oxygen transport resistance is the sole limiting factor. By changing the balance gas, the gas-phase diffusion coefficient can modified. In this manner, measurements with 1% O_2 in N_2 and 1% O_2 in He were used to separate gas-phase transport resistance from ionomer-phase transport resistance. Knudsen diffusion, which is independent of the balance gas and would be lumped together with ionomer resistance, was neglected. If separation of Knudsen diffusion from ionomer diffusion is desired, measurements can be taken at multiple temperatures using the different temperature dependence of Knudsen diffusion and ionomer permeation to separate the contributions (2). Limiting current density was measured using polarization curves as described in Section 4.3.1. The FCTS electronic load was used to control current.

For the easiest analysis, limiting current density tests should be performed at very high gas stoichiometric ratios and low channel pressure drop to ensure that uniform gas partial pressures can be assumed along the channel. Using the 25 cm^2 research hardware, these conditions could not be met. Instead, the limiting current analysis was performed using a simplified 1-D along-the-channel model of the cathode. The model is illustrated in Figure 4-2. At the limiting current density, the partial pressure of oxygen is zero at the catalyst surface. The GDL and the ionomer thin film are each represented by mass-transport coefficients. Oxygen flux in the ionomer is proportional to the partial pressure. However, oxygen flux in the GDL is proportional to mole fraction, due to the inverse relationship between the diffusion coefficient and the total pressure. When oxygen is restricted to low concentrations, the total molar flow rate in the flow channel can be assumed constant. The mass balance,

$$N_{ch}\frac{dx_{ch}}{dy} = \frac{-k_{x,g}k_{p,i}P}{k_{x,g}+k_{p,i}P}x_{ch}\,, \qquad [4.1]$$

is then integrated to solve for the outlet mole fraction. The remaining analysis is described in Section 5.1.4, where the limiting current analysis is applied.

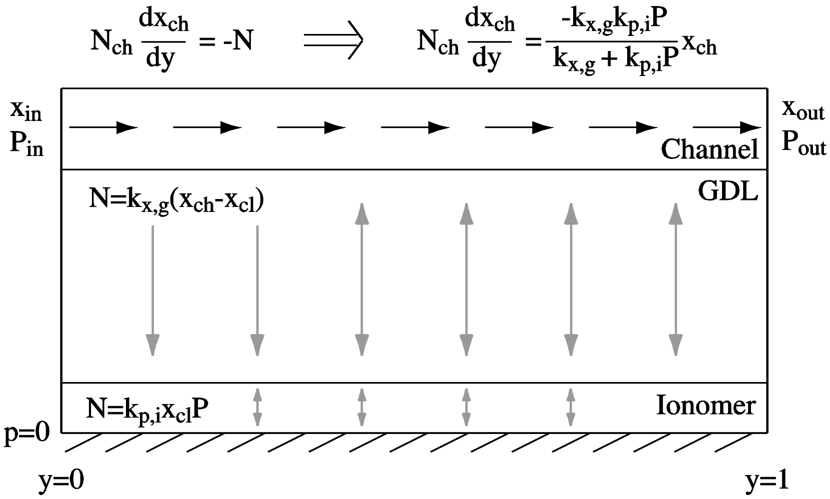

Figure 4-2: Schematic illustration of limiting current model.

4.3.3 Cyclic Voltammetry

Cyclic voltammetry (CV) was used to measure catalyst electrochemically active area (ECA) and oxide layer parameters. The CVs were performed with H_2 (anode) and N_2 (cathode) flow rates of 0.1 slpm and 0.05 slpm, respectively. The CVs were measured using a potentiostat in true linear sweep mode to ensure that accurate measurements of the fast adsorption processes were made. ECA was determined from a CV at 25 °C and 100% RH, using a sweep from 0.05 to 0.60 V at 50 mV/s. The cathodic hydrogen adsorption peak was integrated between the baseline near 0.4 V and the local maximum near 0.09 V, assuming a charge of 210 μC/cm² (3). The oxide growth parameters were determined from a CV at 80 °C and 75% RH, using a sweep from 0.05 to 1.00 V at 50 mV/s.

4.3.4 Electrochemical Impedance Spectroscopy

Electrochemical impedance spectroscopy (EIS) is a commonly used technique that separates differential contributions to overpotential by characteristic time constant. In

EIS, a small sinusoidal perturbation to current or potential is applied to the cell, and the magnitude and phase of the response is monitored. The AC components of current and potential are represented as complex numbers using phasor notation, and impedance is defined as the ratio of the complex potential to the complex current. By this definition, impedance is just the extension of electrical resistance to cover AC responses with varying phase. The impedance measurement is repeated over a range of frequencies spanning many orders of magnitude to complete the EIS experiment. Some processes in the cell are coupled to storage mechanisms, effectively shorting the processes at high frequencies and removing their contribution to cell impedance. This effect explains the usefulness of EIS, as it separates the losses by the different time constants of each process.

Galvanostatic EIS was performed at a range of current densities with air or 1% O_2/N_2 as the cathode gas. Each EIS sweep was preceded by a brief hold at a low potential and a 15 minute hold at the DC current density. The AC amplitude (RMS) was 5% of the DC current density, and the frequency was swept logarithmically from 10 kHz to 10 mHz with 10 points per decade. Flow rates were the same as those used for polarization curves in Chapter 5. The cell temperature was 80 °C and inlet RH was 75% (73 °C humidifier temperature) for the EIS experiments in Chapter 5.

Potentiostatic EIS was used to measure membrane and ionomer conductivity as a function of RH at 80 °C. Anode and cathode gases were hydrogen and nitrogen, respectively, at a flow rate of 0.1 slpm. The DC potential was 0.4 V with an AC amplitude of 5 mV_{RMS}. The frequency range was 10 kHz to 100 Hz with 20 points per decade, and 100 Hz to 1 Hz with 10 points per decade. The inlet RH was varied over a range from 42% to 100%, and a total of 28 EIS spectra were recorded.

The H_2/N_2 EIS results were interpreted using a transmission line porous electrode model. The porous electrode impedance is derived by considering the charge balance throughout the electrode,

$$\frac{\partial \tilde{i}_2}{\partial x} = -Z_{dl}\tilde{\Phi}_2, \tag{4.2}$$

where Z_{dl} is the impedance of the double layer, and x is the dimensionless thickness coordinate. Substituting in Ohm's law results in the second-order ODE,

$$\frac{1}{R_{cl}}\frac{\partial^2 \tilde{\Phi}_2}{\partial x^2} = -Z_{dl}\tilde{\Phi}_2, \tag{4.3}$$

with the boundary conditions,

$$\tilde{\Phi}_2\big|_{x=0} = 1, \tag{4.4}$$

$$\left.\frac{d\tilde{\Phi}_2}{dx}\right|_{x=1} = 0. \tag{4.5}$$

The solution is

$$\tilde{\Phi}_2 = \tanh(\lambda)\sinh(\lambda x) + \cosh(\lambda x), \tag{4.6}$$

where $\lambda = \sqrt{\frac{R_{cl}}{Z_{dl}}}$. Applying Ohm's law, the current is

$$\tilde{i}_2 = \frac{\lambda}{R_{cl}}\tanh(\lambda)\cosh(\lambda x) + \frac{\lambda}{R_{cl}}\sinh(\lambda x). \tag{4.7}$$

The catalyst layer impedance is,

$$Z_{cl} = \left.\frac{\tilde{\Phi}_2}{\tilde{i}_2}\right|_{x=0} = \frac{R_{cl}}{\lambda}\coth(\lambda). \qquad [4.8]$$

Finally, if the double layer behaves as a constant phase element, then

$$Z_{dl} = \frac{1}{Q_{dl}\left(j\omega\right)^{\phi}}, \qquad [4.9]$$

and the catalyst layer impedance is

$$Z_{cl} = \sqrt{\frac{R_{cl}}{Q_{dl}\left(j\omega\right)^{\phi}}}\coth\left(\sqrt{R_{cl}Q_{dl}\left(j\omega\right)^{\phi}}\right). \qquad [4.10]$$

The catalyst layer impedance was combined in series with the parasitic cable inductance, and the membrane resistance. The resulting expression for impedance,

$$Z = j\omega L_{wire} + R_{mem} + \sqrt{\frac{R_{cl}}{Q_{dl}\left(j\omega\right)^{\phi}}}\coth\left(\sqrt{R_{cl}Q_{dl}\left(j\omega\right)^{\phi}}\right), \qquad [4.11]$$

has five fitted parameters: cable inductance, L_{wire}, membrane resistance, R_{mem}, catalyst layer resistance, R_{cl}, and double layer constant phase element (CPE) admittance and exponent, Q_{dl} and ϕ.

4.3.5 Tafel Plot

A Tafel plot (iR-corrected potential vs log current density) was obtained by CV at 0.5 mV/s from 0.7 V to 0.95 V with oxygen as the cathode gas. The anode and cathode flow rates were 2 slpm and 5 slpm, respectively. The high frequency resistance (3 kHz) was used to determine the iR-corrected potential.

4.4 Electro-osmotic Drag Concentration Cell

The electro-osmotic drag coefficient was measured by the streaming potential method using a concentration cell (4). The concentration cell was fabricated from PTFE as pictured in Figure 4-3 with two chambers sealed by O-rings. A membrane strip (Nafion 212) approximately 2 cm x 14 cm was stretched between the two chambers, and platinized platinum mesh electrode were pressed against the membrane in each chamber. The exact membrane dimensions and electrode dimensions are not critical to the experiment and do not need to be controlled, as long as the membrane under the electrode is in equilibrium with the RH in the chamber. The RH was controlled in each chamber by solutions of LiCl in deionized water, using the data in Ref (5) to correlate LiCl concentration to water activity. A slow gas flow of 4% H_2/N_2 was passed through each chamber after being pre-humidified in sparging bottles by LiCl solutions with the same concentration as the solutions in the chambers.

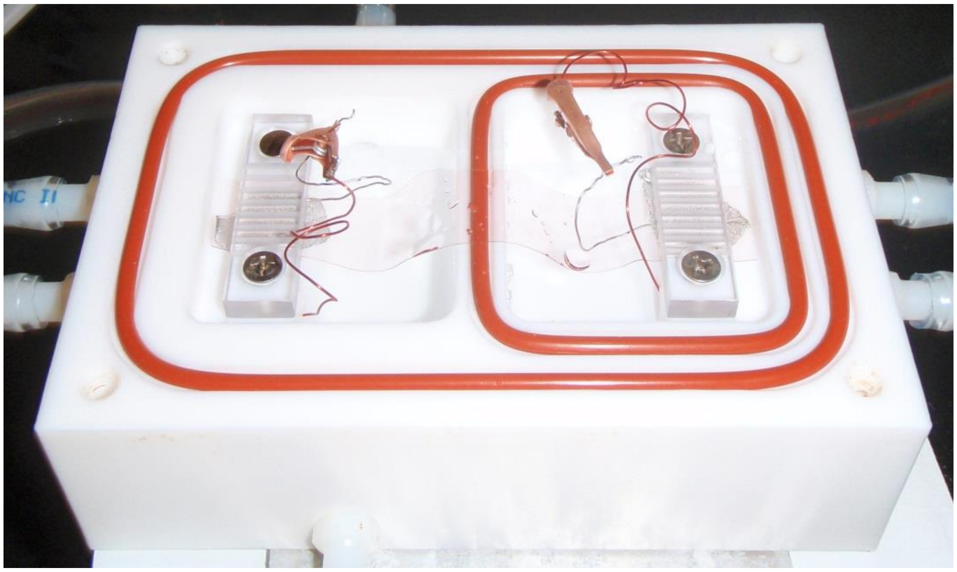

Figure 4-3: Concentration cell for streaming potential measurement.

The cell potential was measured with a Keithley Model 6514 electrometer with an input impedance greater than 200 TΩ. By holding the water vapor activity constant in one chamber and varying the activity in the other chamber, the electro-osmotic drag coefficient was determined as a function of water content in the membrane.

Measurements were conducted both at room temperature and in a temperature chamber at a temperature of 31 °C over a water activity range of 0.135 to 0.997.

4.5 Catalyst Layer Constituents

The catalyst layer thickness was determined by measuring the MEA thickness and subtracting the thickness of the membrane, as measured around the border of the MEA. The catalyst layer thickness was 17 µm. The catalyst layer mass was determined by comparing the mass of pieces cut from the center and the border of the MEA. The catalyst layer mass was 1.4 mg/cm^2. The platinum loading was specified by the manufacturer at 0.3 mg/cm^2. An attempt was made to determine the catalyst layer ionomer content by titration, but the result was approximately an order of magnitude too large to be realistic. It is suspected that acidic surface groups on carbon were responsible for this result. In lieu of experimental data, the remaining mass was assigned assuming a 1:1 ionomer to carbon ratio.

The catalyst layer porosity was calculated to be 65% using values for platinum, carbon, and ionomer densities of 21 g/cm^3, 1.8 g/cm^3 (6), and 1.98 g/cm^3, respectively. Based on the assumed ionomer to carbon ratio, the catalyst and ionomer volume fractions were calculated to be 0.19 and 0.16, respectively.

4.6 References

1. E. L. Redmond, Cathode Durability in PEM Fuel Cells, in *Chemical & Biomolecular Engineering*, Georgia Institute of Technology, Atlanta, GA (2013).

2. N. Nonoyama, S. Okazaki, A. Z. Weber, Y. Ikogi and T. Yoshida, *J. Electrochem. Soc.*, **158**, B416 (2011).

3. R. W. Lindstrom, K. Kortsdottir, M. Wesselmark, A. Oyarce, C. Lagergren and G. Lindbergh, *J. Electrochem. Soc.*, **157**, B1795 (2010).

4. T. F. Fuller and J. Newman, *J. Electrochem. Soc.*, **139**, 1332 (1992).

5. H. F. Gibbard and Scatchar.G, *J. Chem. Eng. Data*, **18**, 293 (1973).

6. G. Droval, J. F. Feller, P. Salagnac and P. Glouannec, *Smart Mater. Struct.*, **17**, 025011 (2008).

CHAPTER 5

EXPERIMENTAL VALIDATION OF A SINGLE-PHASE PHYSICS-BASED IMPEDANCE MODEL

The use of physics-based impedance models in place of typical equivalent circuit analyses is a major goal of the PEMFC modeling community (1). In this chapter, the single-phase transient model developed in Section 3.1 is validated against experimental electrochemical impedance spectroscopy (EIS) results to prove the ability of this model to be used for EIS analysis. These results were published in Ref. (2). A number of approaches to parameter fitting and model validation are possible. Here, several experiments are used that are designed to isolate the most important model parameters, and the model is validated with EIS spectra over a range of current densities and oxygen concentrations. The fitting experiments are: H_2/N_2 EIS for conductivity, concentration cell for electro-osmotic drag coefficient, cyclic voltammetry (CV) for electrochemically active area (ECA) and oxide parameters, Tafel curve for oxygen reduction reaction (ORR) rate constant (from a slow CV under O_2), and limiting current density analysis for mass-transfer parameters (using polarization curves under 1% oxygen in nitrogen and helium). It is important to stress that the validation experiments, EIS under air and 1% O_2, are not used to fit any model parameters.

5.1 Parameter Fitting

5.1.1 Conductivity

To begin, ionomer conductivity and catalyst-layer tortuosity are fit using EIS measurements with N_2 at the cathode (3-5). A total of 28 EIS spectra were acquired at nine values of relative humidity (RH) ranging from 42% to 100%. Figure 5-1a shows representative experimental EIS spectra with the modeled spectra overlaid. The Nyquist plot shows the typical shape for a transmission line with no Faradaic process: a 45° line at high frequencies transitioning into a (nearly) vertical line at low frequencies. The high frequency intercept is the membrane resistance plus electronic resistances and contact resistances, which are assumed to be negligible. If the low frequency line is extrapolated down to the x-axis, this intercept has been shown to be equal to the high frequency resistance plus one-third of the catalyst layer ionomer resistance (3). Although the graphical reading is easiest to understand and is a correct interpretation of the transmission line model, a more precise procedure is to fit the entire spectrum with the transmission line model of Equation [4.11].

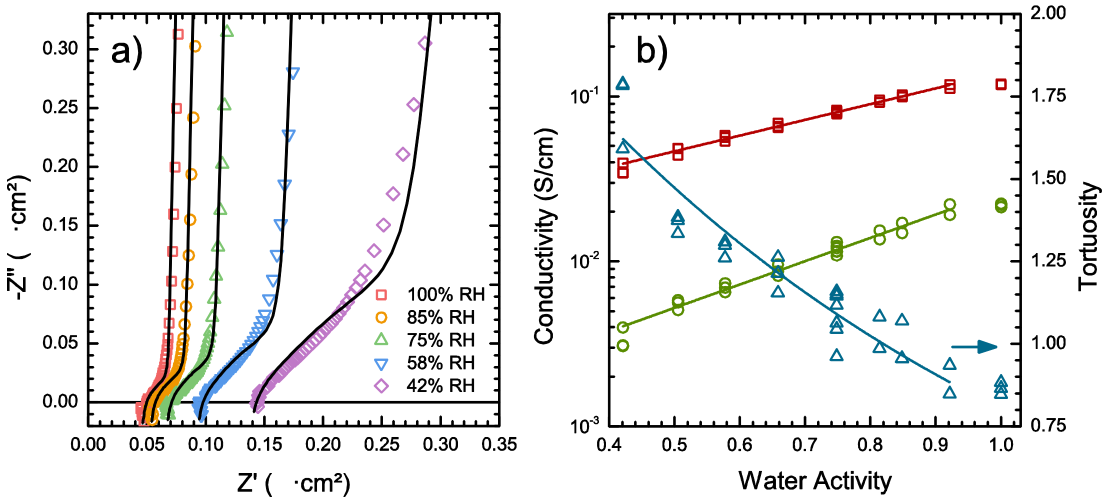

Figure 5-1: Experimental H2/N2 EIS measurements used to determine membrane and catalyst layer conductivities. a) Nyquist plots showing experimental data (symbols) and model fits (lines). b) Membrane (squares) and catalyst layer (circles) conductivities (left axis)

Each of the 28 experimental spectra was fit using Equation [4.11], and the resulting membrane conductivity, effective catalyst layer conductivity, and catalyst layer ionomer tortuosity are shown in Figure 5-1b. The swelling effect was ignored, and the thicknesses used in the calculation were 50 μm for the membrane and 17 μm for the catalyst layer. The remaining fit parameters are not used in the PEMFC model, but are listed in Table A-1 of Appendix A for reference. Except at low RH, the CPE phase parameter was ca. 0.98, indicating nearly ideal double-layer capacitive behavior at 0.4 V on Pt/C. Catalyst layer tortuosity was determined from the ratio of the membrane and catalyst layer conductivities, after accounting for the ionomer volume fraction of 0.16. The ionomer volume fraction was calculated from the measured porosity of 0.65 assuming an ionomer to carbon ratio of 1:1, as detailed in Section 4.5. The catalyst layer effective conductivity exhibits stronger water activity dependence than the membrane conductivity, which is consistent with literature reports on conductivity (4), but at first glance appears contradictory with literature reports finding lower ionomer hydration in catalyst layers (6). However, even with reduced hydration levels, the catalyst layer ionomer will swell with increasing relative humidity. The resulting increase in volume fraction and decrease in tortuosity appears to dominate any difference in bulk vs. thin-film ionomer conductivity. At high water activity, the calculated tortuosity falls below one, although the true tortuosity after accounting for swelling would be larger than one. The data were fit with an exponential function to obtain the correlations used in the PEMFC model, which are listed in Table 2. The data at 100% RH were excluded to achieve a better fit at subsaturated conditions.

5.1.2 Electro-osmotic Drag Coefficient

The electro-osmotic drag coefficient was measured by the concentration cell method, as described in Chapter 4. Figure 5-2 shows the corrected cell potential as a function of the water activity in the variable chamber of the cell. The measurements were conducted at 22 °C and at 31 °C, and no significant temperature dependence is seen. From concentrated solution theory, the potential is linked to the water activity by

$$\frac{F}{RT}\frac{d\Phi}{d\ln a_W}=\xi\,. \qquad [5.1]$$

Therefore, when the dimensionless potential, FU/RT, is plotted against $\ln a_W$, the electro-osmotic drag coefficient is equal to the slope.

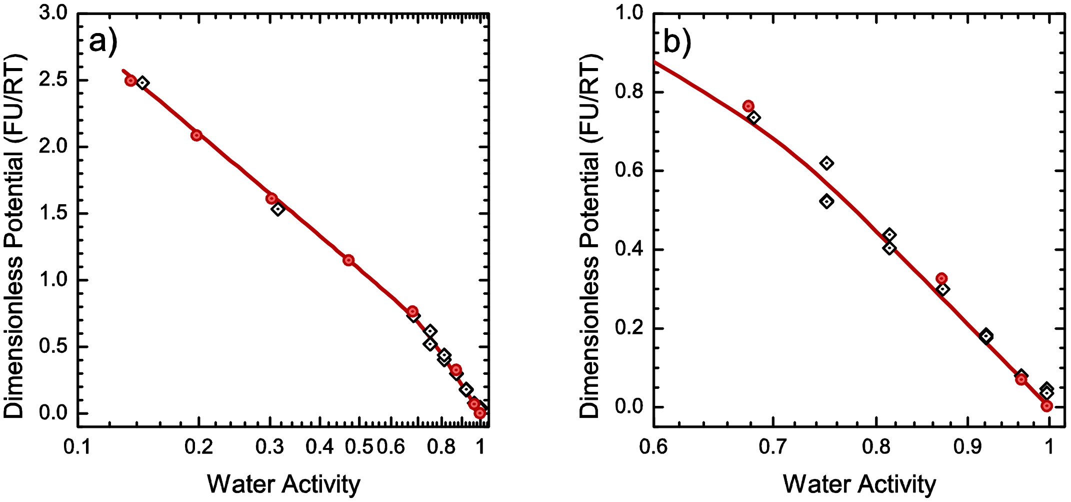

Figure 5-2: Dimensionless streaming potential due to electro-osmosis as measured by the concentration cell method at 22 °C. The x-axis is the water activity on the variable side of the cell, with the fixed side held at a water activity of 0.997. Open circles: experiment at 22°C, filled diamonds: experiment at 31 °C, line: fit described by Equation [5.2]. a) Full range b) Zoomed view of high water activity data.

The data in Figure 5-2 can be divided into two linear regions above and below a water activity of 0.75. Therefore, electro-osmotic drag was fit to a sigmoidal function to provide a smooth transition between the two linear regions. The fitted electro-osmotic drag function is

$$\xi = 1.1 + \frac{0.9}{1+\exp\left[-2\left(\lambda - 5.5\right)\right]}, \qquad [5.2]$$

using the data of Springer et al. (7) to convert between water activity and water uptake. The fitting function has four parameters representing the two limiting values of the electro-osmotic drag coefficient, the transition point, and the smoothness of the transition. Because the electro-osmotic drag coefficient is equal to the slope of the plot, extremely precise data would be needed to determine the fourth fitting parameter with any certainty.

With the present data, some uncertainty remains in the value of ξ near the transition point of $\lambda = 5.5$.

5.1.3 Kinetic Parameters

Cyclic voltammetry was used to determine ECA and the growth of the oxide layer on platinum. ECA was calculated using the charge for hydrogen adsorption, assuming a charge of 210 μC/cm^2 (8). The room temperature CV is shown in Figure 5-3 from which an ECA of 79 m^2/g was obtained. Oxide growth is detailed in Figure 5-4, which consists of experimental and simulated cyclic voltammograms at 80 °C, 75% RH, and 50 mV/s scan rate. The experimental curve has been shifted by the crossover current, 2.5 mA/cm^2. The oxide growth parameters were fit from the CV and are listed in Table 5-1.

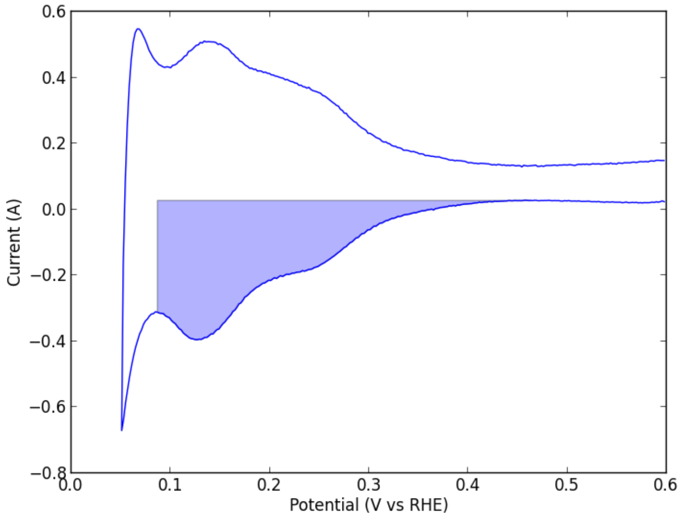

Figure 5-3: Cyclic voltammogram at 50 mV/s, 25 °C, 100% RH, 100 sccm H_2, 50 sccm N_2. The shaded area was integrated to determine ECA.

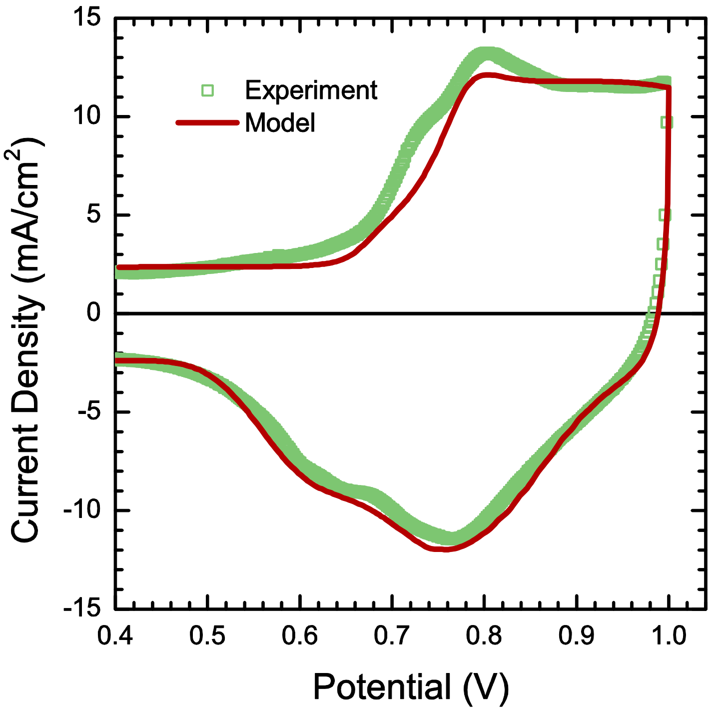

Figure 5-4: Experimental and simulated CVs at 50 mV/s. Conditions: 80 °C, 75% RH, 74 µmol/s H2 / 37 µmol/s N2.

Table 5-1: Oxide growth parameters fit from Figure 5-4.

Symbol	Name	Value
c_{dl}	Double layer capacitance including carbon	2 F/m$^2_{\mathrm{Pt}}$
k_2	Rate constant planar oxide	0.8 s^{-1}
k_3	Rate constant edge oxide	0.04 s^{-1}
U_1	Standard potential of chemisorption	0.815 V
U_2	Standard potential of planar oxide	0.785 V
U_3	Standard potential of edge oxide	0.685 V
σ_2	Heterogeneity planar oxide	13 kJ/mol
σ_3	Heterogeneity edge oxide	7 kJ/mol
ω_1	Frumkin interaction energy chemisorption	15 kJ/mol
ω_2	Frumkin interaction energy planar oxide	130 kJ/mol
ω_3	Frumkin interaction energy edge oxide	550 kJ/mol

Figure 5-5 shows experimental and simulated Tafel plots with pure O_2 at the cathode. The Tafel plot was acquired through a CV from 0.70 to 0.95 V at 0.5 mV/s, with a low potential prehold to reduce the oxide layer. The experimental Tafel plot is corrected for hydrogen crossover of 2.5 mA/cm^2 and high frequency resistance, measured at 3 kHz. The simulated curve is corrected for membrane resistance. A good fit was achieved with an ORR rate constant of 0.46 s^{-1}. The ORR rate constant is defined on a per-site basis, according to Equation [3.16] in Chapter 3. The oxide growth parameters determined from Figure 5-4 reproduce the hysteresis in the Tafel plot nearly perfectly. Additionally, the simulated Tafel slope on an oxide free surface is 140 mV/decade, but the Tafel slope is reduced to ca. 70 mV/decade by the oxide interactions, matching the experimental Tafel plot. The transition in Tafel slope matches the experimental observation of a dual Tafel slope (9) on polycrystalline platinum, although the transition occurs at too low of a potential to be seen in Figure 5-5, which is consistent with reports on MEAs (10).

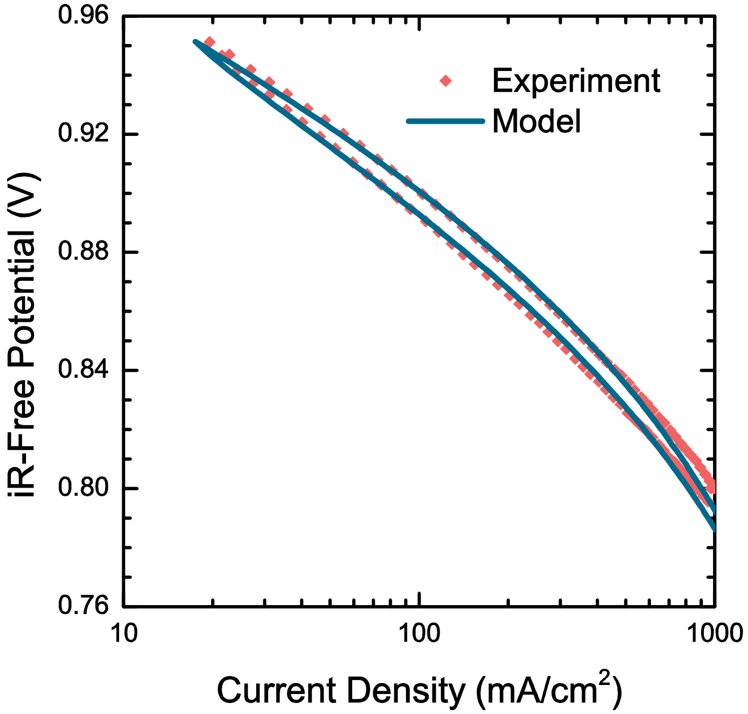

Figure 5-5: Experimental and simulated Tafel plot at 0.5 mV/s. Conditions: 80 °C, 75% RH. Anode: 2 slpm H_2 / 5 slpm O_2.

5.1.4 Mass-Transfer Parameters

Limiting current density analysis was used to calculate the mass-transfer parameters. The three mass-transfer parameters that require fitting are agglomerate radius, thin film thickness, and GDL tortuosity. Although literature values are available for GDL tortuosity (11), the model uses an adjusted parameter which accounts for GDL convection as well. The adjusted GDL tortuosity is the value which produces a mass-transfer resistance through diffusion alone that is equivalent to the actual mass-transfer resistance due to the combined effects of diffusion and convection. This method assumes an equal distribution of mass-transfer resistance through the GDL, which is not strictly valid because convection and diffusion have separate driving forces. Improved convection models would lead to different concentration profiles in the GDL. In reality, the convection effect should be stronger near the channel than near the catalyst layer, essentially changing ℓ more than D_{eff}. As a result the diffusion time constant (ℓ^2 / D_{eff}) may be overestimated. However, in these simulations, the effect on impedance is minimal because GDL mass transfer is already too fast to resolve from the charge-transfer semicircle. Flooded agglomerate parameters are specific to the catalyst layer fabrication technique and also require fitting. Limiting current density analysis is capable of separating ionomer and gas phase mass-transfer resistance (12, 13). However, to separate the two ionomer mass-transfer parameters, agglomerate radius and film thickness, an additional datum is required: the cell potential at 100 mA/cm^2.

For low oxygen concentrations, the mass-transfer limiting current density can be reached with minimal ohmic losses and without significant water buildup or the risk of condensation. Due to the cell hardware, differential conditions were not obtainable; the oxygen stoichiometry was as low as 2.6. Therefore, the down-the-channel concentration gradients need to be accounted for. A simplified 1-D model (down the channel) is used in which the gas phase and ionomer phase are treated as mass-transfer resistances, and the oxygen partial pressure at the catalyst surface is zero. The details of the model are provided in Section 4.3.2 and Figure 4-2. Accounting for the pressure drop in the gas flow channels, the outlet mole fraction is

$$\ln\left(\frac{x_{O_2,out}}{x_{O_2,in}}\right)=\int_0^1 \frac{-k_{p,i}k_{x,g}P(y)}{N_{ch}\left(k_{x,g}+k_{p,i}P(y)\right)}dy\,, \qquad [5.3]$$

where $k_{p,i}$ and $k_{x,g}$ are the ionomer and GDL mass-transfer coefficients, N_{ch} is the molar flow rate per unit MEA area, and $P(y)$ is the flow channel pressure at point y, the normalized distance from the inlet. While $k_{p,i}$ is expressed in terms of a partial pressure driving force, $k_{x,g}$ is expressed in terms of a mole fraction driving force, as gas phase diffusivity is inversely proportional to pressure. Assuming a linear pressure profile, Equation [5.3] becomes

$$\frac{x_{O_2,out}}{x_{O_2,in}}=\left(\frac{P_{out}+k_{x,g}/k_{p,i}}{P_{in}+k_{x,g}/k_{p,i}}\right)^{\left(\frac{-k_{x,g}{}^2}{N_{ch}k_{p,i}(P_{in}-P_{out})}\right)}\exp\left(\frac{-k_{x,g}}{N_{ch}}\right). \qquad [5.4]$$

The gas phase and ionomer phase mass-transfer coefficients may be separated by comparing the limiting current density for O_2/N_2 and O_2/He mixtures. For the O_2/He mixture, $k_{x,g}$ is replaced by $\alpha_D k_{x,g}$, where α_D is the ratio of oxygen diffusivity in humidified helium to diffusivity in humidified nitrogen. The oxygen diffusivity in a gas mixture is estimated from the binary diffusivities according to

$$\frac{1}{D_{o_2}}=\sum_j \frac{x_j}{D_{j,O_2}}\,. \qquad [5.5]$$

The limiting current density was measured at 75% RH with a dry gas flow rate of 5 slpm at the cathode and 0.5 slpm at the anode. The observed pressure drop was 71.6 kPa for nitrogen and 47 kPa for helium. Polarization curves under these conditions are shown in Figure 5-6. Somewhat surprisingly, the limiting current density was 223 mA/cm^2 for nitrogen, and only 214 mA/cm^2 for helium, indicating that the higher pressure in the nitrogen case outweighs the lower gas-phase diffusivity. The calculated mass-transfer coefficients were $k_{p,i}$ = 8.77 × 10^{-3} mol/(m^2·s·kPa) and $k_{x,g}$ = 7.55 mol/(m^2·s) (humidified nitrogen). Ignoring convection, the tortuosity of the GDL is determined from $k_{x,g}$ by

$$\tau_g^G = \frac{\varepsilon_g^G D_{O_2}}{\ell^G RTk_{x,g}}, \qquad [5.6]$$

where D_{O_2} is the diffusion coefficient of oxygen in the humidified nitrogen mixture and ℓ^G is the thickness of the GDL. The calculated tortuosity was 0.62, compared to a typical literature value of 2.85 (11). While $\tau = 0.62$ is suitable for the present model to account for convection, it is not a true measure of the tortuosity of the GDL.

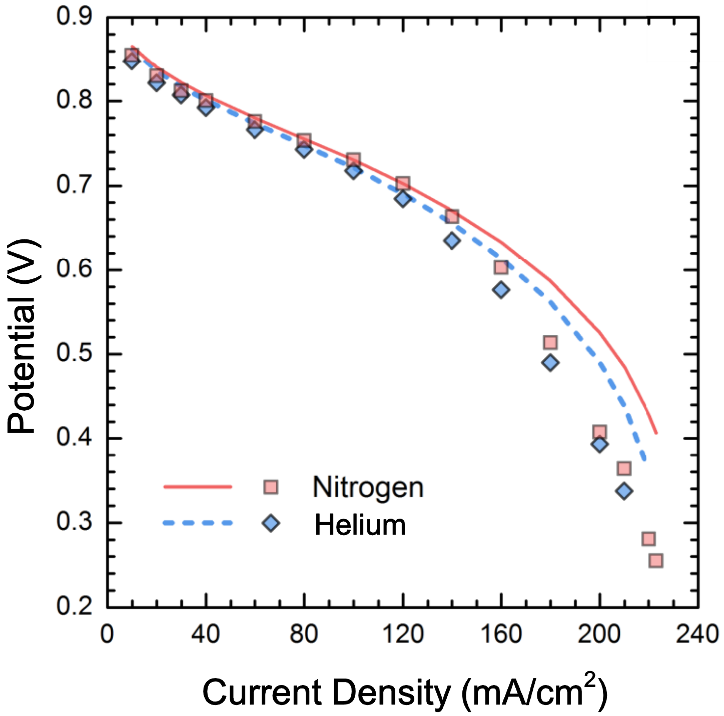

Figure 5-6: Polarization Curve under 1.0% oxygen at 80 °C, 75% RH. Lines: model, points: experiment.

For an agglomerate of radius, R_{agg}, including an ionomer film of thickness d_f, the ionomer phase mass-transfer coefficient is

$$k_{p,i} = \frac{3\left(1-\varepsilon_g^C\right)\ell^C}{R_{agg}} \frac{D_{O_2,i}}{H_{O_2,i}} \left(\frac{1}{d_f} - \frac{1}{R_{agg}} \right). \qquad [5.7]$$

The agglomerate radius was fit by matching the potential at 100 mA/cm^2 for the O_2/N_2 case to the model, with the film thickness determined from Equation [5.7]. The fitted agglomerate radius and film thickness are 420 nm and 27.1 nm, respectively. The experimentally determined model parameters are listed in Table 5-2.

Table 5-2: Experimentally measured model parameters (cf. Figure 5-1,Figure 5-5, and Figure 5-6).

Symbol	Name	Value
d_f	Agglomerate film thickness	27.1 nm
k_0	ORR rate constant	0.46 s^{-1}
R_{agg}	Agglomerate radius	420 nm
κ	Ionomer conductivity	$1.55\exp\left(2.20a_w\right) {}^{\mathrm{S}}\!/_{\mathrm{m}}$
τ_g^G	GDL equivalent tortuosity	0.62
τ_i^C	CCL ionomer tortuosity	$2.70\exp\left(-1.21a_w\right)$
ξ	Electro-osmotic drag coefficient	$1.1+\dfrac{0.9}{1+\exp\left[-2\left(\lambda-5.5\right)\right]}$

The modeled agglomerate size is large and would be easily observable by SEM. However, such large agglomerates are never observed (13). Similar overestimates of agglomerate dimensions are common in the literature (14-17), and may result from assuming bulk permeability values for ionomer thin films. By extrapolating measurements of mass-transport resistance to zero thickness in thin ionomer films, Suzuki et al. (13) concluded that an interfacial mass-transfer resistance is present. When including this extra transport resistance, the modeled agglomerate dimensions were roughly the size of the primary carbon particles, and consistent with catalyst layer images. Furthermore, the present model required the unrealistic assumption that agglomerate tortuosity was unity in order to achieve the correct balance between external and internal mass-transfer limitations. In the present model, it is better to treat the agglomerate model as a purely empirical description of internal and external mass-transfer limitations, and not to treat it as a literal model of the catalyst layer microstructure.

5.2 Model Validation

With the model parameters determined from independent experiments, the model is evaluated by comparing simulated and experimental EIS spectra under a variety of conditions. Figure 5-7 shows EIS results for a cell running on 1% O_2/N_2. The cell temperature was 80 °C, and the dry gas flow rates were 0.5 slpm anode and 5 slpm cathode, both at 75% relative humidity. In addition to simulated and experimental EIS curves, the DC resistance from the polarization curve is included for comparison as filled symbols on the real axis labeled “DC”. Figure 5-7a displays the Nyquist plot for low current densities, and Figure 5-7b shows the Nyquist plot for high current densities. Figure 5-7c and Figure 5-7d are low and high current density Bode plots, respectively, showing the imaginary component of impedance. The spectra were split between “low” and “high” current densities to avoid overcrowding of the plots, but no physical significance in terms of a characteristic current density for a particular process was intended. Each spectrum consists mainly of a single capacitive loop, stretching from the high frequencies to the traditional low frequency intercept near 0.1 Hz. However, there is a significant difference between the ca. 0.1 Hz intercept and the DC resistance. At the higher current densities, the clear beginning of a low frequency inductive loop is observed. Thus, the 0.1 Hz intercept will be referred to as the intermediate frequency intercept to distinguish it from the true low frequency intercept, which is hard to observe in EIS, but can be measured from the polarization curve. Presumably, if it were practical to extend EIS into the µHz range, one would observe the same low frequency intercept at the end of the inductive loop as is measured from the polarization curve.

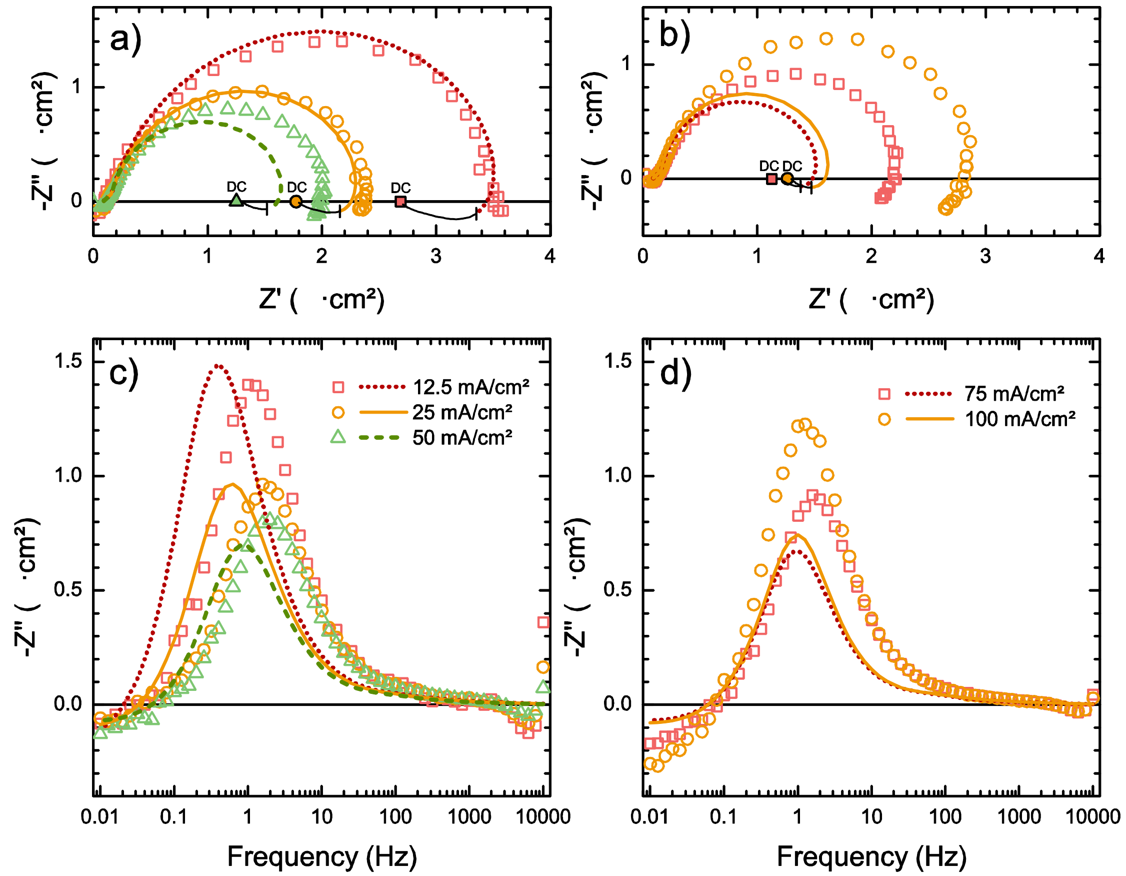

Figure 5-7: EIS spectra with 1% O_2 in N_2. Symbols: Experiment, Closed symbols: DC resistance from the polarization curve in Figure 5-6, Lines: Model, Thin black lines: Extended model results to 1 µHz. a) Low current density Nyquist plot. b) High current density Nyquist plot. c) Low current density Bode plot for imaginary component of impedance. d) High current density Bode plot for imaginary component of impedance.

The modeled spectra show matching features to the experimental results, with a capacitive loop followed by an inductive loop. At high frequencies, the model matches the length and position of the 45° line caused by porous electrode effects and even exhibits non-ideal capacitive behavior. In the model, the non-ideal capacitive behavior, usually requiring an equivalent circuit fit with a CPE, is caused by growth of the oxide layer, for which heterogeneity produces a dispersion of time constants. For current densities up to 50 mA/cm^2 (Figure 5-7a), the model matches the intermediate frequency intercept very closely. Above 50 mA/cm^2 (Figure 5-7b), the model exhibits too small of an inductive loop to properly fit the intermediate frequency intercept, although it does qualitatively match the reversed trend of increasing impedance with increasing current density. To evaluate the model near DC conditions, the simulations were extended to 1 μHz (narrow black lines), capturing the entire inductive loop. At this true low frequency intercept, the model matches the DC resistance for all current densities, an unsurprising result given the choice of fitting experiments. The Bode plots (Figure 5-7c,d) show that the model underestimates the characteristic frequencies by a factor of 2-3. The frequency mismatch is due to extra model pseudocapacitance from the chemisorbed oxide, which must be somewhat overestimated by the oxide growth model for long hold times.

Under H_2 and air, the EIS spectra are shown in Figure 5-8. The cell temperature was 80°C, and the dry gas flow rates were 2 slpm anode and 5 slpm cathode, both at 75% RH. Similar to the 1% O_2 case, the current densities up to 400 mA/cm^2 show excellent agreement in the Nyquist plot (Figure 5-8a), but underestimate the frequencies in the Bode plot (Figure 5-8c). The results at high current density (Figure 5-8b) are mixed, with good agreement at 800 mA/cm^2. At 1600 mA/cm^2, the model underestimates the impedance. The Bode plot (Figure 5-8d) shows that the frequency mismatch begins to be resolved at higher current densities. The model does underestimate the high frequency resistance by about 15%. Whether this is due to RH droop in the humidifiers at maximum flow rate or a model deficiency is unknown. Interestingly, at 1600 mA/cm^2, the model shows a small peak at low frequencies on the Bode plot. This peak is caused by heat generation and storage in the flow field blocks.

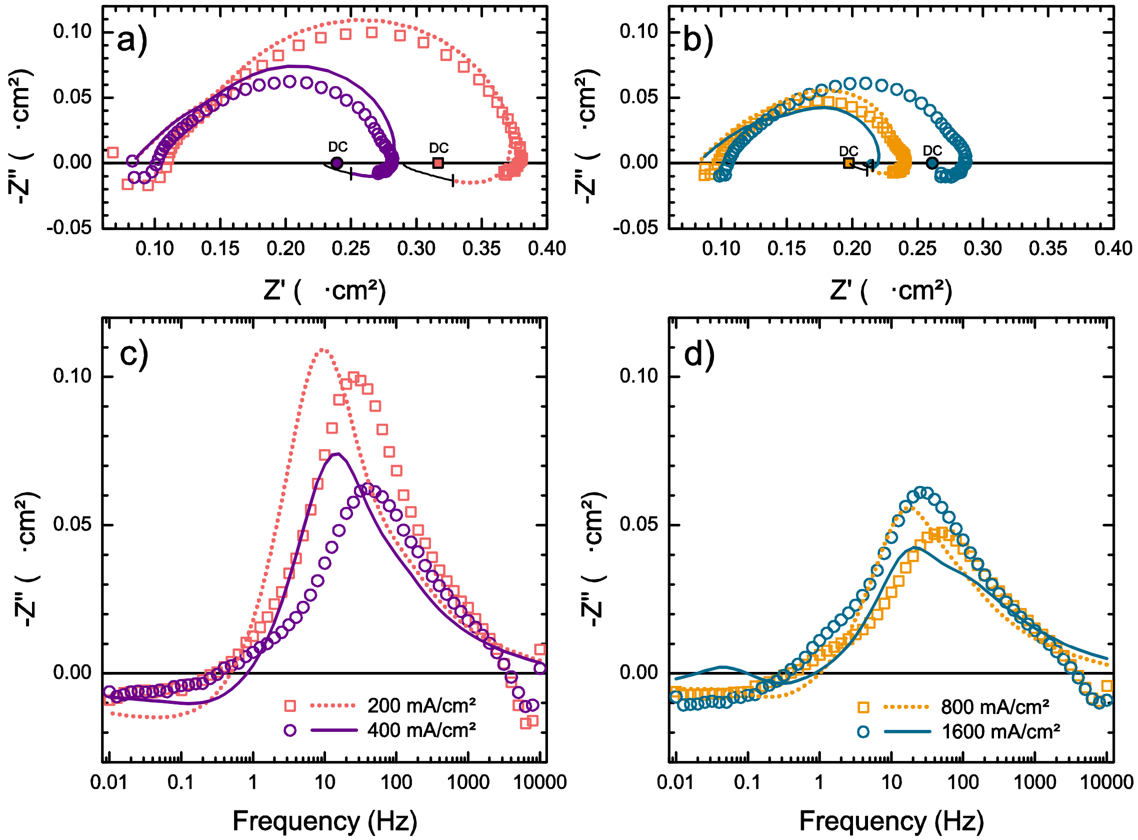

Figure 5-8: EIS spectra for hydrogen and air operation at 80 °C and 75% RH. Symbols: Experiment, Closed symbols: DC resistance from the polarization curve in Figure 5-11, Lines: Model, Thin black lines: Extended model results to 1 μHz. a) Low current density Nyquist plot. b) High current density Nyquist plot. c) Low current density imaginary component Bode plot. d) High current density imaginary component Bode plot.

The inductive loops observed in Figure 5-7 and Figure 5-8 are caused by the relaxation of the oxide layer on platinum. An additional source of inductive loops in PEMFCs is water generation and storage in the membrane (18-22). An isothermal model predicts an inductive loop due to product water buildup. As current density increases, the increased water production causes a drop in the membrane and ionomer resistance, but only if the frequency is low enough for the membrane to absorb the additional water. This modulation of the membrane resistance is effectively negative impedance, thus causing an inductive loop. However, when heat transfer is considered, the cell temperature rise at higher current densities partially or fully offsets the increased water generation. The hydration response of the membrane may be reversed and result in a capacitive loop and positive impedance. In the present model, heat generation offsets the water buildup to the extent that a small capacitive feature is observed in the model at 1600 mA/cm^2. In contrast, the experimental measurements of Schneider et al. (18, 19) were performed at lower temperature, lower inlet relative humidity, lower flow rates, and with a larger cell, resulting in a large inductive loop from water generation. Thus, while water generation is not responsible for an inductive loop under the conditions in the present work, it can be very important under other conditions.

The results of Figure 5-7 and Figure 5-8 are summarized in Figure 5-9 and Figure 5-10, which show the intermediate frequency and DC intercepts at each current density. As mentioned previously, both intercepts are matched almost perfectly up to 25 mA/cm^2 in 1% O_2/N_2, and up to 800 mA/cm^2 in air. At higher current densities, the inductive loop is too small to fit both intercepts. At high current densities, one might suspect that localized condensation could occur and add to the transport losses. However, even at 2 A/cm^2, the model predicts only a 2.6 kPa gradient in water partial pressure from the catalyst layer to the flow channel. The closest the channel partial pressure comes to the vapor pressure is 13 kPa. While there will be spatial variations in the GDL mass-transfer resistance due to the serpentine flow pattern, the margin should be sufficient to prevent any localized condensation under these conditions.

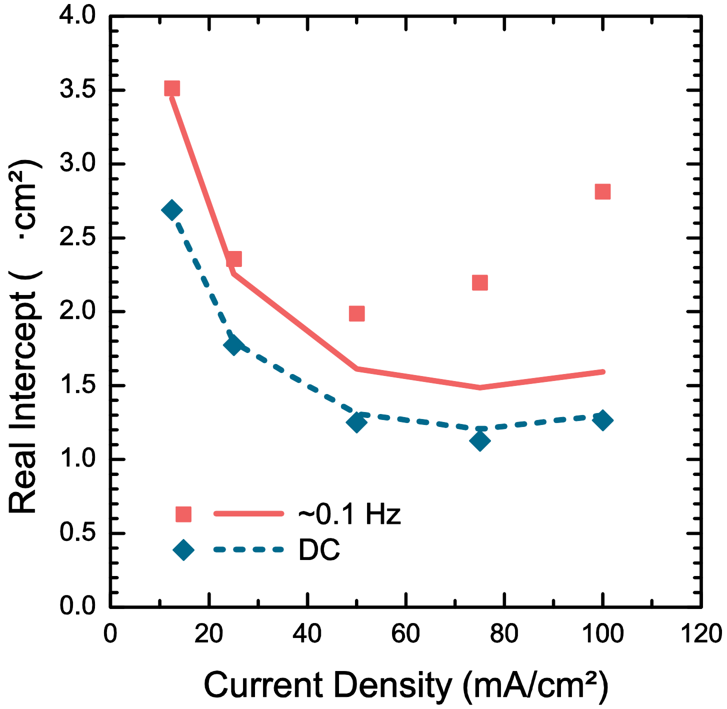

Figure 5-9: Intermediate frequency intercept (~0.1 Hz) and DC resistance as a function of current density for 1% O_2/N_2. Lines: model, symbols: experiment.

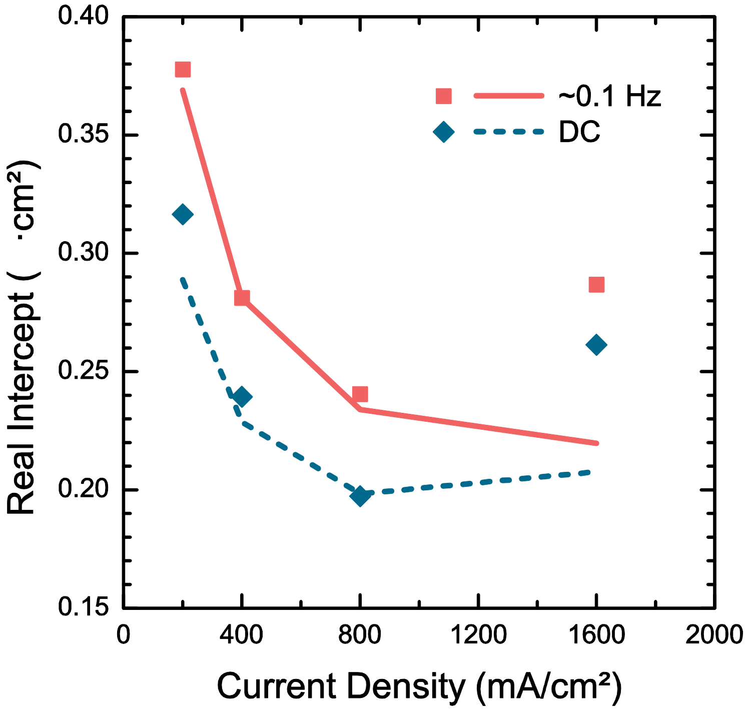

Figure 5-10: Intermediate frequency intercept (~0.1 Hz) and DC resistance as a function of current density for air. Lines: model, symbols: experiment.

Finally, the polarization curve under air is shown in Figure 5-11. The steady-state polarization curve is not a challenging test considering that the mass-transfer parameters were fit from a steady-state polarization curve, albeit at 21 times lower oxygen concentration. However, the air polarization curve does demonstrate that the model performs well under both DC and AC conditions.

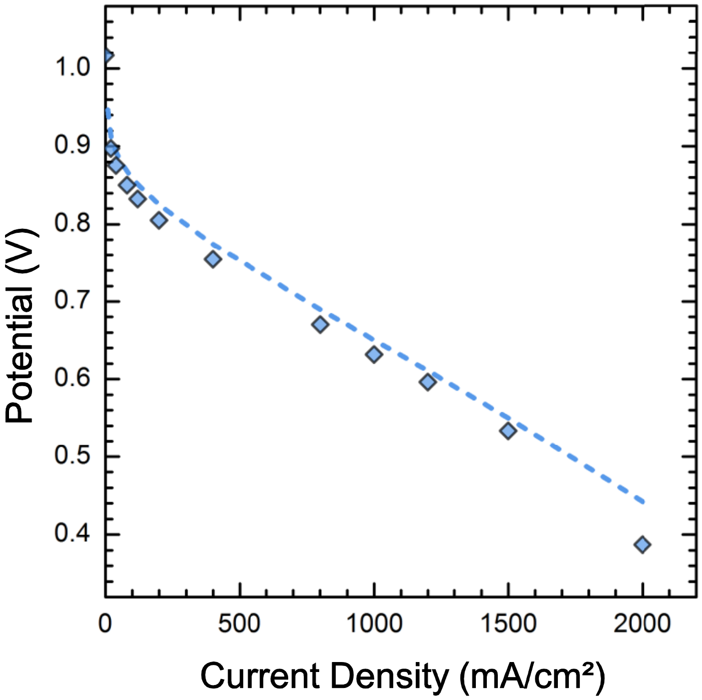

Figure 5-11: Polarization curve under air at 80 °C, 75% RH. Flow rates are 2 slpm / 5 slpm, anode / cathode. Line: model. Symbols: experiment.

5.3 Conclusions

In this work, a physics-based PEMFC impedance model was demonstrated with additional physics to account for the oxide layer, heat generation, and cell hardware effects. With these extra effects, the model matches more of the trends and features of experimental EIS measurements, even while using very different experiments for parameter fitting and model validation. The proposed ORR model, which links the previously published oxide growth model (23) to ORR kinetics through vacant chemisorption sites, is shown to produce a very low frequency inductive loop. This inductive loop quantitatively agrees with the observed inductive loop at current densities up to 800 mA/cm^2 under air and 25 mA/cm^2 under 1% O_2/N_2. The model also can generate an inductive loop through the effect of water buildup, although in the cases studied, heat generation completely offsets the water buildup.

The largest impediment to accurate physics-based impedance models has been the low frequency inductive loop. Without accounting for the processes responsible for this feature, a model can only fit EIS spectra (>0.1 Hz) or steady-state experiments, but not both. The present model was able to explain most of the observed inductive loop, as well as the ORR Tafel slope, ORR hysteresis, and CPE behavior. These results indicate that the oxide layer has a major effect on PEMFC impedance and must not be ignored in modeling.

5.4 References

1. A. Z. Weber, R. L. Borup, R. M. Darling, P. K. Das, T. J. Dursch, W. B. Gu, D. Harvey, A. Kusoglu, S. Litster, M. M. Mench, R. Mukundan, J. P. Owejan, J. G. Pharoah, M. Secanell and I. V. Zenyuk, *J. Electrochem. Soc.*, **161**, F1254 (2014).
2. B. P. Setzler and T. F. Fuller, *J. Electrochem. Soc.*, **162**, F519 (2015).
3. R. Makharia, M. F. Mathias and D. R. Baker, *J. Electrochem. Soc.*, **152**, A970 (2005).
4. Y. X. Liu, M. W. Murphy, D. R. Baker, W. B. Gu, C. C. Ji, J. Jorne and H. A. Gasteiger, *J. Electrochem. Soc.*, **156**, B970 (2009).
5. Y. X. Liu, C. X. Ji, W. B. Gu, D. R. Baker, J. Jorne and H. A. Gasteiger, *J. Electrochem. Soc.*, **157**, B1154 (2010).
6. A. Kusoglu, A. Kwong, K. T. Clark, H. P. Gunterman and A. Z. Weber, *J. Electrochem. Soc.*, **159**, F530 (2012).

7. T. E. Springer, T. A. Zawodzinski and S. Gottesfeld, *J. Electrochem. Soc.*, **138**, 2334 (1991).

8. R. W. Lindstrom, K. Kortsdottir, M. Wesselmark, A. Oyarce, C. Lagergren and G. Lindbergh, *J. Electrochem. Soc.*, **157**, B1795 (2010).

9. A. Holewinski and S. Linic, *J. Electrochem. Soc.*, **159**, H864 (2012).

10. K. C. Neyerlin, W. B. Gu, J. Jorne and H. A. Gasteiger, *J. Electrochem. Soc.*, **153**, A1955 (2006).

11. M. J. Martínez, S. Shimpalee and J. W. Van Zee, *J. Electrochem. Soc.*, **156**, B80 (2009).

12. D. R. Baker, D. A. Caulk, K. C. Neyerlin and M. W. Murphy, *J. Electrochem. Soc.*, **156**, B991 (2009).

13. T. Suzuki, K. Kudo and Y. Morimoto, *J. Power Sources*, **222**, 379 (2013).

14. F. Jaouen, G. Lindbergh and G. Sundholm, *J. Electrochem. Soc.*, **149**, A437 (2002).

15. Q. Z. Guo and R. E. White, *J. Electrochem. Soc.*, **151**, E133 (2004).

16. M. Secanell, K. Karan, A. Suleman and N. Djilali, *Electrochim. Acta*, **52**, 6318 (2007).

17. W. Sun, B. A. Peppley and K. Karan, *Electrochim. Acta*, **50**, 3359 (2005).

18. I. A. Schneider, M. H. Bayer, A. Wokaun and G. G. Scherer, *J. Electrochem. Soc.*, **155**, B783 (2008).

19. I. A. Schneider, M. H. Bayer, P. Boillat, A. Wokaun and G. G. Scherer, *ECS Transactions*, **11**, 461 (2007).

20. K. Wiezell, N. Holmström and G. Lindbergh, *J. Electrochem. Soc.*, **159**, F379 (2012).

21. N. Holmstrom, K. Wiezell and G. Lindbergh, *J. Electrochem. Soc.*, **159**, F369 (2012).

22. B. P. Setzler and T. F. Fuller, *ECS Transactions*, **58**, 95 (2013).

23. E. L. Redmond, B. P. Setzler, F. M. Alamgir and T. F. Fuller, *PCCP*, **16**, 5301 (2014).

CHAPTER 6

INVESTIGATION OF FLOODING LOSSES WITH STEADY-STATE TWO-PHASE MODEL

In this chapter, the two-phase model is compared to experimental results using two different gas diffusion layers (GDLs), SGL 25BA and Toray TGP-H-060 with 5% PTFE. The choice of model parameters for these GDLs is discussed, and the baseline model results are presented. Several improvements are made to the model, which are shown to be essential to matching experimental results. The dramatic performance impact of phase change induced (PCI) flow in the case of the SGL 25BA GDL is used as a test case for heat and mass transport in the model.

6.1 Literature Parameter Values

Water transport in the porous layers is controlled by several key parameters. Of primary importance is the capillary pressure saturation relationship. Capillary pressure is the driving force for liquid water transport, so naturally, the relationship is key to the results. Liquid water transport also depends critically on absolute permeability and relative permeability, which is a function of saturation. Due to the nonlinear relative permeability relationship, even a small liquid water flux has nearly as large of a performance impact as a large liquid water flux. For example, if a linear relationship between capillary pressure and saturation is assumed, the linearized driving force, Π, defined in Equation [3.47], will vary with the 5th power of saturation,

$$\Pi = \int s^4 dp_c \propto s^5 . \qquad [6.1]$$

The liquid water flux is proportional to the driving force, so the saturation required to eject water from the cell has only a one-fifth power dependence on the liquid water flux. Put differently, a tenfold increase in the liquid water flux is only expected to increase the water saturation by around 60%. Therefore, the primary determinant of performance is not the magnitude of the liquid water flux, but simply the requirement of any liquid flux at all. The parameters that govern phase-change-induced (PCI) flow are critical because they determine whether the water transport is one-phase or two-phase. PCI flow is governed primarily by thermal conductivity and effective diffusivity, which encompasses porosity, tortuosity, and pore diameter (if Knudsen effects are considered).

6.1.1 Capillary Pressure

One of the largest sources of uncertainty in the model is the capillary pressure saturation behavior of the various porous layers. Experimental data in the literature vary widely between researchers. For an example of disagreement of literature values, see Figure 5.6 in reference (1). A major reason for the disagreement in the literature is capillary pressure hysteresis. Due to geometry effects, porous media generally exhibit significant hysteresis. To illustrate this effect, consider a cylindrical capillary with a contact angle of exactly 90°, as shown in Figure 6-1. According to the Young-Laplace equation, the capillary pressure in a straight pore of radius R is,

$$\Delta P = \frac{2\gamma \cos\theta}{R} , \qquad [6.2]$$

where γ is the surface tension and θ is the contact angle. In a straight capillary tube, for a contact angle of 90°, the interface is flat, and the capillary pressure is zero. However, if the capillary tube has a narrow neck, the interface will have curvature due to the geometry, regardless of the contact angle. As the interface moves through the neck, the radius of curvature will span a range of positive and negative values, creating a barrier in both directions that must be overcome to move the interface through the constriction. Thus, a positive capillary pressure is required for ingress, and a negative capillary pressure is required for egress. Although the actual geometry of the porous layers is much more complex, the same effect applies, causing capillary pressure hysteresis as observed in the literature (2).

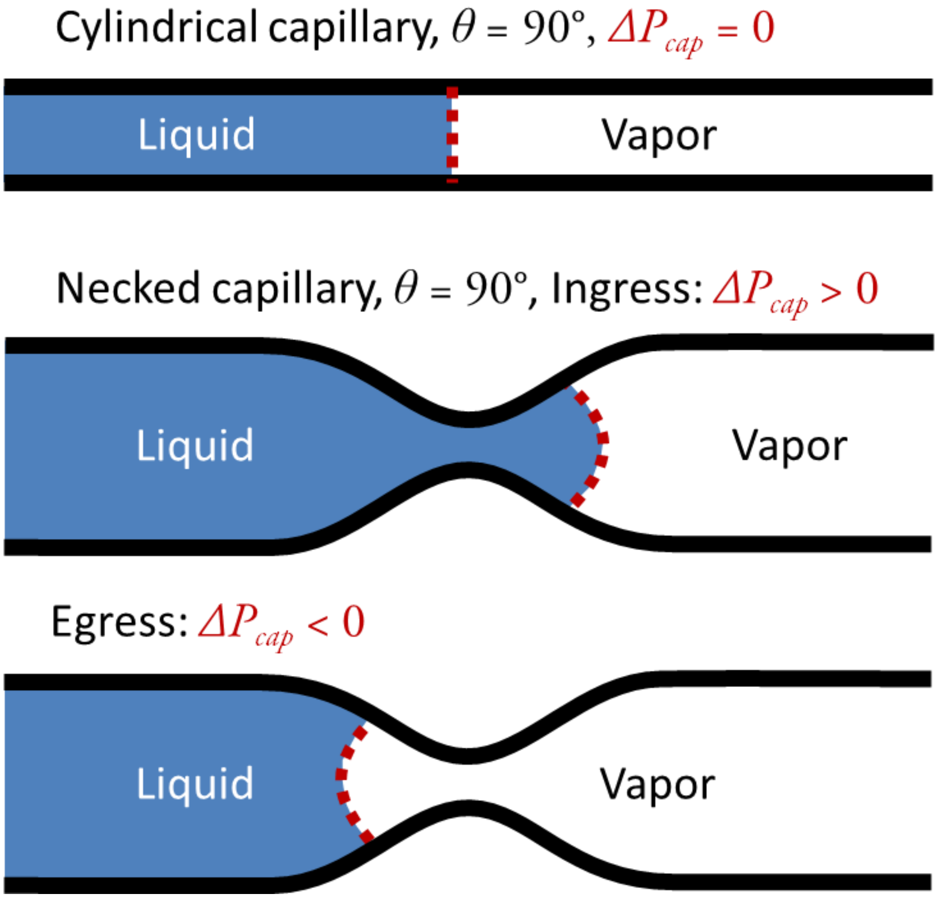

Figure 6-1: Origin of capillary pressure hysteresis in porous media.

Due to capillary pressure hysteresis, different methods of measuring capillary pressure will produce different results. Some methods measure imbibition curves, while others measure drainage curves. The gas controlled porosimetry technique developed by Gostick (1, 2) is notable for the ability to control capillary pressure in an arbitrary manner beginning with a dry GDL, allowing the measurement of both imbibition and drainage curves. Unfortunately, this technique has not been applied to the microporous layer. Likely, this is due to a limitation on the maximum positive capillary pressure which can be measured using the technique. Because the liquid pressure is maintained at atmospheric pressure and the gas pressure is manipulated to control capillary pressure, the maximum positive capillary pressure is limited by the minimum gas pressure that can be applied, which is the difference between atmospheric pressure and the vapor pressure of water. By other techniques, the capillary pressure in microporous layers has been found to reach into the MPa range (3), greatly exceeding the ca. 95 kPa limit of gas controlled porosimetry.

Another technique for measuring capillary pressure is the method of standard porosimetry (MSP). In this technique, the sample to be measured is sandwiched between two porous disks (standards) with known capillary pressure saturation curves. The sandwich is initially saturated with a wetting fluid, often octane, and a dry gas stream is used to gradually remove the fluid. Periodically, the sandwich is separated and the saturation in each layer is determined by weighing. Capillary pressure equilibrium is assumed between the samples, and the capillary pressure is determined from the saturation of the standard. This technique can only measure the capillary pressure of a wetting fluid. Due to hysteresis, a large amount of water is retained at zero capillary pressure in an initially saturated GDL. The drainage of this water can be measured by MSP. Some researchers have interpreted this as a measurement of the hydrophilic pore network and used a wetting fluid like octane to measure the total pore network. The difference is assumed to be the hydrophobic pore network. However, this analysis assumes that hydrophobic pores expel water at zero capillary pressure, a poor assumption due to hysteresis. When the GDLs are submerged in water from an initially dry state, the water uptake is minimal or zero, indicating that the majority of the pores display intermediate wettability where hysteresis spans zero capillary pressure.

When MSP is used to measure the total pore network, the working fluid is usually octane, assumed to have a contact angle of zero. Drainage of octane, the wetting fluid, is equivalent to imbibition of air, the non-wetting fluid. Therefore, the capillary pressure for imbibition of a perfectly non-wetting fluid can be derived from the octane drainage curve. To convert to a water capillary pressure curve, a correction is made using the Young-Laplace equation, Equation [6.2]. However, the Young-Laplace equation is derived for a straight pore, and does not account for the actual pore geometry. Furthermore, the hydrophobic and hydrophilic interactions between water and carbon or PTFE cannot be measured using octane and are only incorporated through the assumed contact angle.

For consistency, it is important that the capillary pressure relationship used for each porous layer be measured by the same technique. Although gas controlled porosimetry would be preferred, measurements of the MPL capillary pressure are not available by that technique. Instead, for the baseline model parameters, MSP measurements of capillary pressure are used. Gostick et al. (4) measured capillary pressure in a variety of GDLs and found that a single fit could be obtained between all of the samples using the Leverett J-function,

$$J = \frac{p_c}{\gamma}\sqrt{\frac{K}{\varepsilon}}, \qquad [6.3]$$

to normalized the curves for different samples. Their combined results were fit using the van Genuchten correlation (5). Here, a modified version is used to allow for cases where full saturation is not achieved at high capillary pressure,

$$1 - \frac{s}{s_0} = \left(1 + \left(\frac{J}{J_c}\right)^n\right)^{-m}, \qquad [6.4]$$

where s_0, J_c, n, and m are fitting parameters. For the GDL, Gostick et al.(4), provide fitted parameters, with s_0 equal to one. For the catalyst layer and microporous layer (when present), the results of LaManna et al.(3) were fit to Equation [6.4].

For thermal conductivity, the results of Sadeghifar et al. (6) were used. Using an empirical fit, the thermal conductivity of SGL 25BA carbon paper is

$$k^{eff} = 3.82 \times 10^{-4} + 4.233 \exp\left(\frac{-\ell[\mu\mathrm{m}]}{62.987}\right) \; [\mathrm{W/m \cdot K}]. \qquad [6.5]$$

For the compressed GDL thickness of 145 µm in this study, the thermal conductivity is 0.42 W/m·K. Sadeghifar et al. also determined the thermal conductivity of the MPL on SGL 24BC/34BC and 25BC/35BC accounting for a thermal contact resistance between the MPL and the GDL. As the model does not have a thermal contact resistance between these layers, an effective MPL thermal conductivity was calculated from the difference in 24BA and 24BC thermal conductivity, assuming the MPL is incompressible and there is no penetration of the MPL into the GDL substrate. The MPL thermal conductivity is

$$k^{eff} = 0.438 - 0.237\exp\left(\frac{p_{comp}}{11.79\left[\mathrm{bar}\right]}\right) \quad \left[\mathrm{W/m\cdot K}\right], \tag{6.6}$$

where p_{comp} is the compression pressure of the GDL.

For permeability, the correlation of Tomadakis and Robertson (7) is used,

$$\frac{K}{r_f^{\;2}} = \frac{\varepsilon}{8\ln^2\varepsilon}\frac{\left(\varepsilon-\varepsilon_p\right)^{\alpha+2}}{\left(1-\varepsilon_p\right)^{\alpha}\left[\left(\alpha+1\right)\varepsilon-\varepsilon_p\right]^2}, \tag{6.7}$$

where $\varepsilon_p = 0.11$ and $\alpha = 0.785$ for through-plane transport through 2-D fibrous media (8). The fiber radius, r_f, is 4.0 µm for SGL 24BA (assumed to be equal for 25BA) and 4.6 µm for Toray TGP-H-060 (9). Gostick et al. measured the permeability of a range of GDL materials as a function of compression and found that Equation [6.7] agrees well. In the MPL, the permeability is 10^{-13} m^2, and the average pore diameter is 81 nm, from the results of LaManna et al. (3). For the catalyst layer, LaManna et al. found an average pore diameter of 40 nm, and for this study, the permeability is estimated from the pore diameter as

$$K = \varepsilon r_p^{\;2} = 2.6\times10^{-16}\ \mathrm{m}^2. \tag{6.8}$$

The above assumption was made to be consistent with the Leverett function, where capillary pressure is normalized by a characteristic pore radius estimated from the permeability. Experimental measurements of the catalyst layer permeability are sparse, and the reported average pore size was deemed more reliable.

6.2 Baseline Model Results

Using the baseline parameters for an SGL 25BA GDL, the model was run for temperatures ranging from 40 °C to 80 °C. The anode and cathode humidifiers were set

10 °C above the cell temperature to ensure fully gas streams. The anode flowrate was 630 sccm H_2, and the cathode flowrate was 1500 sccm air. The simulated polarization curves are shown in Figure 6-2a. In Figure 6-2b, the saturation in the GDL and catalyst layer is shown. The saturation values are taken at z* = 0 for the GDL (the GDL-CL interface) and z* = 0.5 for the catalyst layer ($z^* = z/\ell$ for each layer) which are generally the points with the highest saturation. A representative saturation profile at 1000 mA/cm^2 and 40 °C is shown in Figure 6-3.

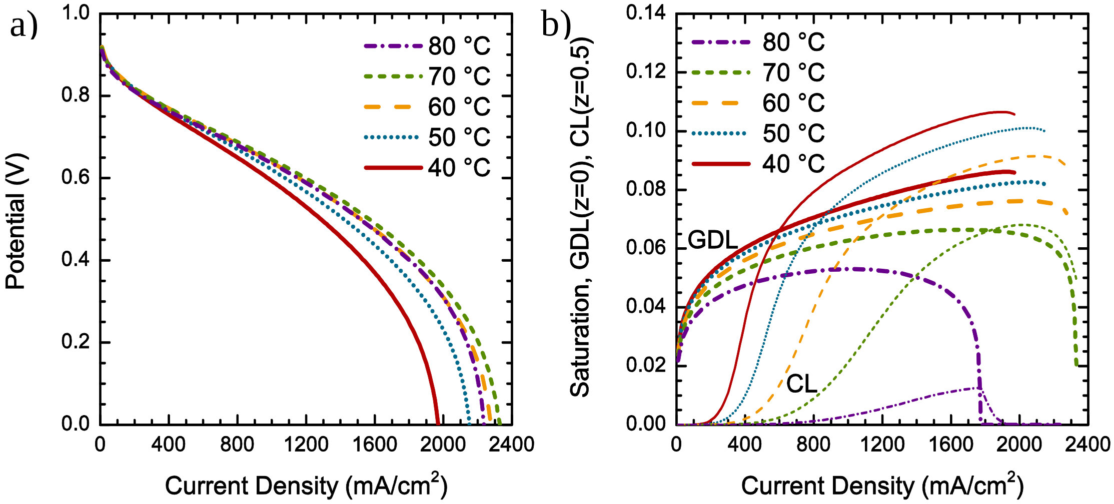

Figure 6-2: a) Simulated polarization curves for MEA with SGL 25BA GDLs. b) Liquid water saturation in the GDL and catalyst layer during polarization curves. Thick lines: GDL saturation at catalyst layer interface (z* = 0). Thin lines: catalyst layer saturation at center (z* = 0.5).

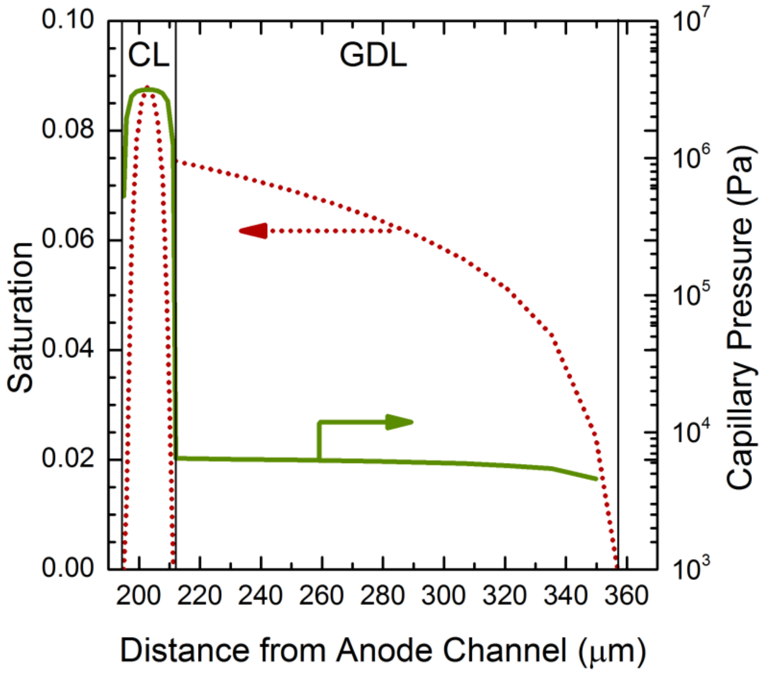

Figure 6-3: Saturation (red, dotted) and capillary pressure (green, solid) profiles at 1000 mA/cm^2 from the 40 °C simulation of Figure 6-2. Anode GDL has zero saturation and is not shown.

The saturation in the GDL and catalyst layer does not exceed 0.11 in any of the simulations, and as a result, the performance impact is small. In Section 5.1.4, it was observed that the majority of mass-transport resistance is in the ionomer under one-phase conditions. Thus, even though a saturation of just 0.05 already reduces oxygen diffusivity by approximately 14%, the diffusion limitation is small to begin with and the effect on performance is small. As temperature increases, the saturation decreases slightly, as PCI flow increases and water viscosity decreases. The limiting current density increases with increasing temperature due to the increasing diffusion coefficients, except at 80 °C, where the dilution effect of increased water vapor pressure outweighs the improvement in diffusion coefficients. In Figure 6-3, the large difference in capillary pressure between the catalyst layer and the GDL can be seen. Capillary pressure is continuous across the CL-

GDL interface, and as a result, there is a discontinuity in liquid saturation. Because the characteristic pore sizes in the GDL and catalyst layer differ by more than two orders of magnitude, any reasonable level of saturation in the GDL will correspond to a near-zero level of saturation in the catalyst layer at the interface. In the GDL, the water saturation profile has a characteristic convex shape, with a steep drop at the channel interface as the relative permeability approaches zero. In the catalyst layer, liquid water flows from the center towards both the membrane interface and the GDL interface. This occurs despite the fact that the water flux in the membrane is towards the catalyst layer. Back diffusion points towards the anode, but electro-osmosis is stronger, and the total water flux points towards the cathode. However, electro-osmosis is confined to the ionomer phase, and vapor and liquid transport matches back diffusion.

In Figure 6-4, the model is compared to experimental polarization curves taken at a cell temperature of 60 °C and a range of oxygen concentrations. The experiment and model are compared for a humidifier temperature of 70 °C to represent flooded conditions and 55 °C (79% RH) to represent dry conditions. For oxygen concentrations of 10.5% and below, there is good agreement under the dry conditions, reflecting the accuracy of the model in predicting one-phase PEMFC performance as demonstrated in Chapter 5. However, under flooded conditions, the model does not show the large performance decrease that is observed experimentally. The model also fails to capture the performance for air at 55 °C humidifier temperature, but this failure is due to the gas streams quickly becoming saturated and the resulting two-phase water transport. These results illustrate that with baseline parameters, the model is not able to predict flooding losses in an SGL 25BA GDL.

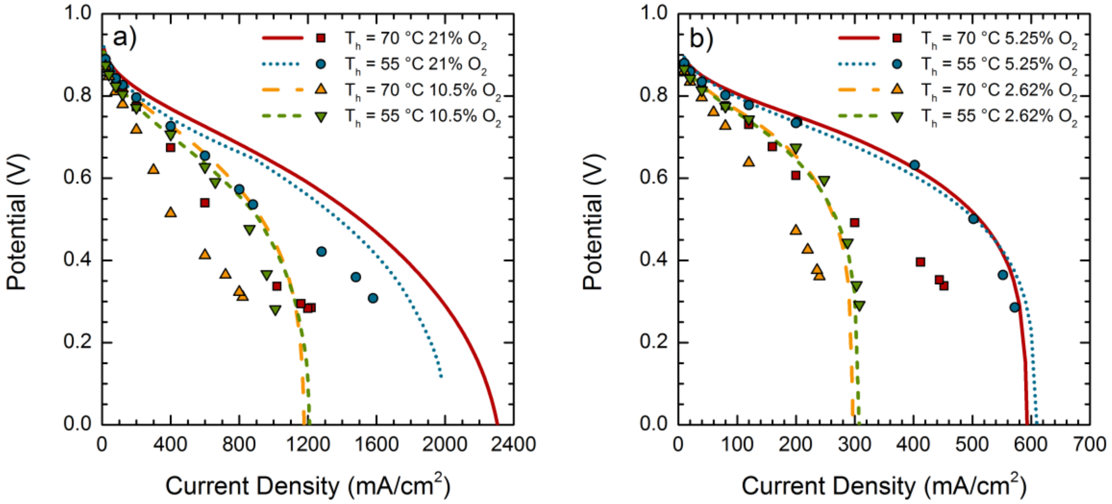

Figure 6-4: Comparison of model (lines) to experiment (symbols) for baseline model parameters, cell temperature of 60 °C, and SGL 25BA GDL. Gas flow rates were 630 sccm H_2 at the anode and 1500 sccm O_2 in N_2 at the cathode. O_2 concentration and humidifier temperature are indicated in the plot legends.

The model was also compared to experimental results using Toray TGP-H-060 GDLs. The main differences are a considerably higher thermal conductivity (1.45 W/m-K) and a reduced porosity (0.70). In Figure 6-5, the model is compared to experiment for a range of cell temperatures under H_2 and air flowrates of 1000 sccm each. The humidifier temperatures were set to 5 °C above the cell temperature to produce saturated gas streams. Again, it is seen that the model fails to predict the severe flooding losses, a deficiency that is addressed in the next section. In the experiment, a limiting current density of 300-400 mA/cm^2 is observed for all temperatures. For the Toray GDL, the flooding losses occur as a sharp limiting current density, unlike the case for SGL 25BA, where large mass transfer overpotentials increased gradually over a wide range of current densities. Although the model does not correctly predict the flooding losses, Figure 6-2b provides a clue to the difference in behavior between the SGL and Toray GDLs. At 80 °C and high current densities, the GDL and CL saturation decrease to zero in the model for

SGL 25BA due to the large temperature gradient, which causes PCI flow. Qualitatively, this same effect may be at work in the experiments at 60 °C for SGL 25BA, causing the cell performance to be determined by the heat generation required to reduce flooding. In the Toray GDL, the 3-4x higher thermal conductivity prevents sufficient PCI flow to dry the cell out.

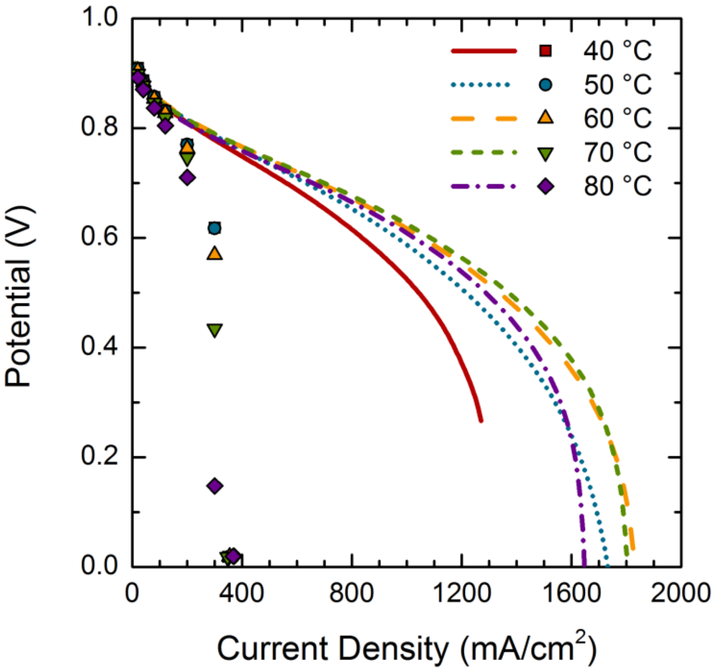

Figure 6-5: Comparison of model (lines) to experiment (symbols) for baseline model parameters and Toray TGP-H-060 GDL. Gas flow rates were 1000 sccm H_2 at the anode and 1000 sccm air at the cathode. Cell temperature was varied from 40 °C to 80 °C as indicated in the plot legend, and humidifier temperatures were 5 °C higher than the cell temperature.

6.3 Model Modifications to Account for Severe Flooding Losses

The comparisons between model and experiment in the previous section demonstrated that the standard method for treating two-phase water transport is inadequate. However, there are several known and hypothesized effects neglected in the model that could account for some of the flooding losses. The most important of these effects are interfacial saturation, capillary pressure hysteresis, and the percolation threshold. Capillary pressure hysteresis would be difficult to address with a steady-state model, as the hysteresis behavior is determined by the time derivative of saturation. However, the percolation threshold and interfacial saturation can be addressed here.

The percolation threshold is the most trivial effect to address in the model. In Figure 6-3, it is seen that a saturation of less than 0.1 is sufficient to drive liquid water out of the cell. However, for such low values of saturation, a continuous network of liquid water does not exist, and liquid water flux is impossible (10, 11). The power-law relative permeability relationship can approximate this behavior, as permeability decreases dramatically for such low values of saturation, but the absolute permeability of the GDL is large and the requisite water velocity is small, so that a very low value of relative permeability is needed to enable liquid water transport. Instead, the percolation threshold can be added explicitly, using

$$K_r = \left(\frac{s - s_p}{1 - s_p} \right)^4 , \tag{6.9}$$

where s_p is the percolation threshold, set to 0.1 (10). In Figure 6-6a, the model is compared with and without a percolation threshold in each of the layers. While the addition of a percolation threshold in the GDL does reduce the limiting current density, the losses are still minor. The addition of a percolation threshold to the catalyst alyer makes no difference in the results, which is surprising at first glance. In Figure 6-6b, it is observed that the saturation level in the GDL increases uniformly by approximately 0.1, the value of the percolation threshold. However, in the catalyst layer, the saturation profile is nearly unchanged.

Due to equilibrium between capillary pressure and water activity, positive values of capillary pressure correspond to a water activity slightly greater than one. Normally, this oversaturation is negligible, but in the catalyst layer, the capillary pressure is so large that the corresponding oversaturation drives vapor and ionomer water flux before the percolation threshold is reached. Overall, while the existence of a percolation threshold for water transport is predicted by theory (12) and confirmed by experiment (10), by itself, it cannot explain the large flooding losses observed in experiments.

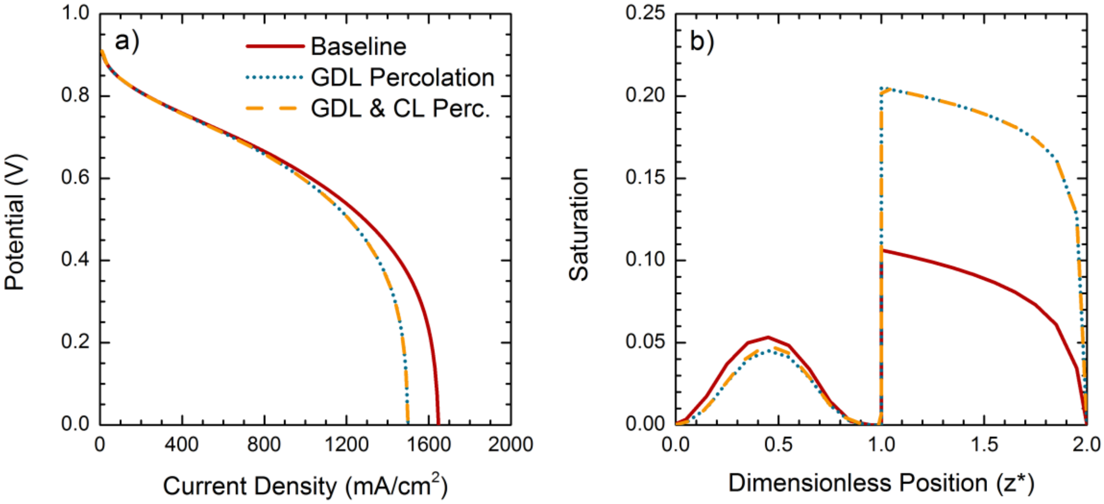

Figure 6-6: Comparison of model results with and without percolation threshold for TGP-H-060 GDL. The cell and humidifier temperatures were 80 °C and 85 °C, respectively. Anode: H_2 at 1000 sccm. Cathode: air at 1000 sccm.

At the CL-GDL interface, there is usually condensation due to the lower temperature of the GDL. Condensation is fundamentally different than the liquid water injection process used to measure capillary pressure saturation curves. In experiments, the entire face of the GDL is exposed to a single reservoir of liquid, and the capillary pressure is uniform. Flow into the GDL can occur at whichever sites have the lowest breakthrough capillary pressures. In an operating fuel cell, water is produced throughout the catalyst layer, and the flux into the GDL is (nearly) uniform. At the individual pore scale, capillary pressure will reach whatever level is required until the water converges into a continuous water network. As discussed by Nam et al. (13) and Owejan et al. (14), the injection of water into every interfacial pore of the GDL will result in a large interfacial saturation. Additionally, due to the large pore size of the GDL and the tendency of droplets to merge across multiple pores, the interfacial droplets are large compared to the thickness of the catalyst layer. As a consequence, portions of the catalyst layer beneath these droplets may be inactive due to the large diffusion path length for oxygen.

As a starting point for investigating the effect of interfacial droplets on performance in a macrohomogeneous PEMFC model, an equivalent mass-transport thickness is estimated for the catalyst layer as a function of droplet radius and interfacial saturation. To arrive at this estimate, the catalyst layer is divided into covered and uncovered regions, and the effectiveness factor in each region is used to estimate an equivalent mass transfer thickness. For catalyst pellets of various shapes, the Thiele modulus can be defined as

$$\phi = a\sqrt{\frac{k}{D}}\,, \tag{6.10}$$

where a is the ratio of volume to surface area. The exact form of rate constant and diffusion coefficient under the radical are not important in this analysis, as only the characteristic length, a, is used. Mass transport under a large interfacial droplet may be approximated by cylindrical diffusion, where

$$a = \frac{R_0}{2}, \qquad [6.11]$$

and R_0 is the radius of the droplet. However, if the droplet size is small enough, the Thiele modulus would be based on catalyst layer thickness, ℓ, instead. In light of this consideration, the Thiele modulus under a liquid droplet is estimated using

$$a_{covered} = \ell + \frac{R_0}{2}. \qquad [6.12]$$

In order to be consistent with the definition of a as the ratio of volume to surface area, a portion of the uncovered catalyst layer surface must be allocated to the covered region. Thus, the covered region is expanded to have a radius of R_1, and the uncovered surface between R_1 and R_0 is calculated to be consistent with Equation [6.12], using

$$\ell + \frac{R_0}{2} = \frac{\pi {R_1}^2 \ell}{\pi\left({R_1}^2 - {R_0}^2\right)}. \qquad [6.13]$$

The result is

$$\left(\frac{R_1}{R_0}\right)^2 = 1 + \frac{2\ell}{R_0}. \qquad [6.14]$$

For a small value of Thiele modulus and a slab-shaped pellet, the Taylor series expansion of the effectiveness factor is

$$\eta = 1 - \frac{\phi^2}{3}. \qquad [6.15]$$

If the overall effectiveness factor is taken as the weighted average of the effectiveness factor in each region, the average value of a is determined from

$$a_{avg}{}^2 = s_{int}\left(1+\frac{2\ell}{R_0}\right)a_{covered}{}^2 + \left[1-s_{int}\left(1+\frac{2\ell}{R_0}\right)\right]a_{uncovered}{}^2, \qquad [6.16]$$

where s_{int} is the fraction of the CL surface covered by liquid water and $\left(1+\frac{2\ell}{R_0}\right)$ is the adjustment factor to account for the uncovered surface allocated to diffusion under the droplet. Substituting in

$$a_{avg}{}^2 = \ell_{eff}{}^2, \qquad [6.17]$$

$$a_{uncovered}{}^2 = \ell^2, \qquad [6.18]$$

and Equation [6.12], the effective mass transport thickness is

$$\frac{\ell_{eff}{}^2}{\ell^2} = 1 + s_{int}\left(2+\frac{3}{2}\frac{R_0}{\ell}+\frac{1}{4}\frac{R_0{}^2}{\ell^2}\right). \qquad [6.19]$$

The oxygen partial pressure gradient in Equation [3.102] is scaled by the ratio $\frac{\ell_{eff}{}^2}{\ell^2}$ in order to account for the increased oxygen mass transport length. The ratio must be squared because ℓ_{eff} was calculated for a thicker catalyst layer with more reaction volume. Finally, the interfacial coverage depends on condensation at the CL-GDL interface,

$$s_{int} = \begin{cases} 0 & if \quad N_l\big|_{z=0}^{G} - N_l\big|_{z=\ell}^{C} \le 0 \\ \dfrac{N_l\big|_{z=0}^{G} - N_l\big|_{z=\ell}^{C}}{N_{0,cond}}\, s_{0,int} & if \quad N_{0,cond} > N_l\big|_{z=0}^{G} - N_l\big|_{z=\ell}^{C} > 0 \\ s_{0,int} & if \quad N_l\big|_{z=0}^{G} - N_l\big|_{z=\ell}^{C} \ge N_{0,cond} \end{cases}, \qquad [6.20]$$

where $N_l\big|_{z=0}^{G}$ is the liquid water flux in the GDL at the catalyst layer interface, $N_l\big|_{z=\ell}^{C}$ is the liquid water flux in the catalyst layer at the GDL interface, $N_{0,cond}$ is a small, arbitrary condensation rate (10^{-3} mol/m^{2}s) used to provide continuity between the dry and wet regimes, and $s_{0,int}$ is an adjustable parameter representing the interfacial saturation when condensation is occurring. As a cautionary note, the effective mass-transport length was calculated assuming the Taylor series expansion in Equation [6.15] holds. For very large droplets, this assumption will eventually overpredict the flooding losses. If the area under a droplet is completely inaccessible to oxygen, an upper bound on flooding losses can be found; limiting current density cannot be scaled by a factor greater than $1-s_{0,int}$, because the uncovered catalyst layer is still accessible. In all of the simulations using interfacial saturation presented in this section, the upper bound on flooding losses is not violated, and Equation [6.19] provides a reasonable estimate of the effect of interfacial saturation.

An estimate for the droplet radius, R_0, is taken from the x-ray tomography results of Zenyuk et al. (15). During injection of water into compressed GDLs, droplets of ca. 150 μm radius were observed. For the interfacial saturation, a value of 0.8 is assumed. No experimental measurements of interfacial saturation in operating fuel cells exist. Given the degree of hysteresis in most capillary pressure saturation curves, a very high value of saturation is possible if condensation causes saturation to increase until the drainage point is reached.

In Figure 6-7, the model is simulated for the SGL 25BA GDL with interfacial saturation. The flooding losses are significantly increased from the previous model iteration without interfacial flooding. Additionally, the effects of PCI flow can be seen at 70 °C and 80 °C. At 60 °C and below, the CL-GDL interface is always flooded, regardless of the cell potential. However, at 70 °C and 80 °C, there is a critical potential where PCI flow is sufficient to remove all of the water from the cell, and condensation no longer occurs. Above the critical potential, the cell is flooded, but below the critical potential, the cell is dry, and the limiting current density increases greatly. The PCI flow is ultimately driven by the vapor pressure gradient, but the vapor pressure gradient is determined by the heat flux via the temperature gradient. The fraction of water flux carried by PCI flow depends on the ratio of heat flux to water flux. Heat generation in the cell is the product of overpotential and current density, while water generation is proportional to current density. To a first approximation, the heat flux to water flux ratio is independent of current density and proportional to overpotential, causing the plateau in the polarization curve.

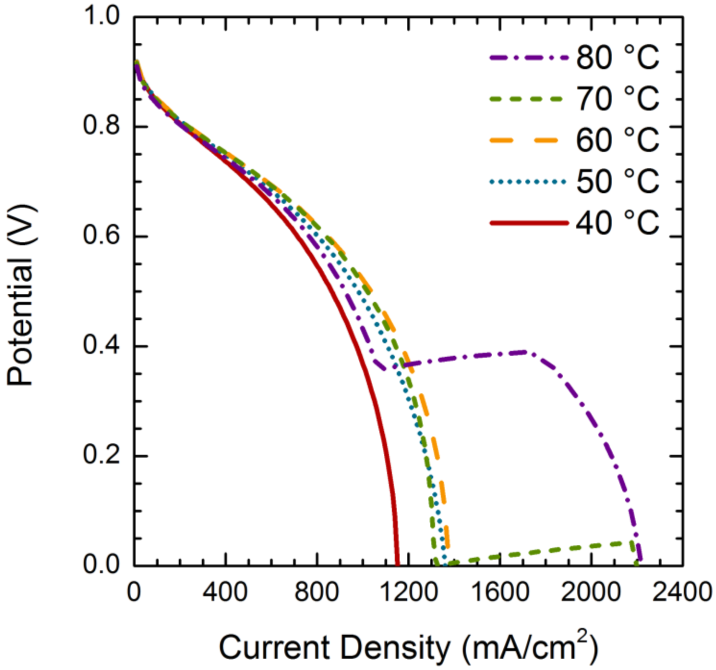

Figure 6-7: Simulated polarization curves for SGL 25BA GDL at a range of temperatures.

Unexpectedly, the model predicts that the plateau slopes slightly upwards, a physically unstable result corresponding to negative resistance ($\frac{d\eta}{dI} < 0$). This result is caused by the dependence of the membrane water flux on current density. At low current densities, the membrane water flux is proportional to current density, but at high current densities, the membrane water flux flattens due to anode dryout. The GDL water flux is the sum of water generation and membrane water flux, and as current density increases, the ratio of GDL water flux to current density falls slightly. As a result, slightly less overpotential is necessary to dry the interface. However, in experiments, this effect cannot be observed because the mass and heat transfer are not uniform from all points on the catalyst layer surface. Instead of a single critical potential, there is a range of potentials over which different parts of the cell dry out. The averaging effect over the entire MEA produces a downward-sloping PCI plateau region, regardless of whether the plateau slopes down or up for uniform mass and heat transfer.

For the cell with Toray carbon paper GDLs, the model and experiments are compared in Figure 6-8. While the addition of interfacial saturation does reduce the limiting current density significantly, it is still insufficient to account for the dramatically reduced limiting current density seen experimentally. As expected, the higher thermal conductivity of Toray GDLs reduces PCI flow, and the temperature gradients are never sufficient to dry out the cell.

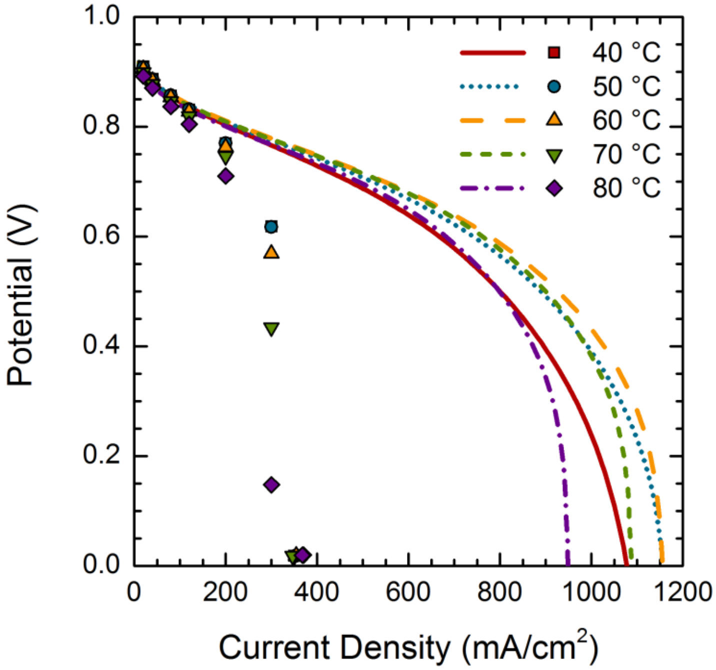

Figure 6-8: Comparison of simulated and experimental polarization curves for Toray GDL under saturated conditions (humidifier temperature is set 5 °C above the cell temperature). The model includes the effects of interfacial saturation.

6.4 Phase-Change-Induced Flow

The dependence of PCI flow on temperature was studied experimentally using the SGL 25BA GDL. Current sweeps at a rate of 0.33 mA/cm^2/s were performed at a range of cell temperatures under saturated conditions and 10.5% O_2 concentration. The humidifiers were set to 70 °C or 10 °C greater than the cell temperature, whichever was greater. The results are shown in Figure 6-9a. The model was simulated under the same conditions and is shown in Figure 6-9b. While the experiments show increased limiting current density due to PCI flow starting around 50 °C, the model does not show the effect until 70 °C. Below 70 °C, the simulated polarization curves are virtually indistinguishable. Over this temperature range, the competing effects of activation energy, thermodynamic potential, oxygen dilution by water vapor, and diffusion coefficients cancel almost completely.

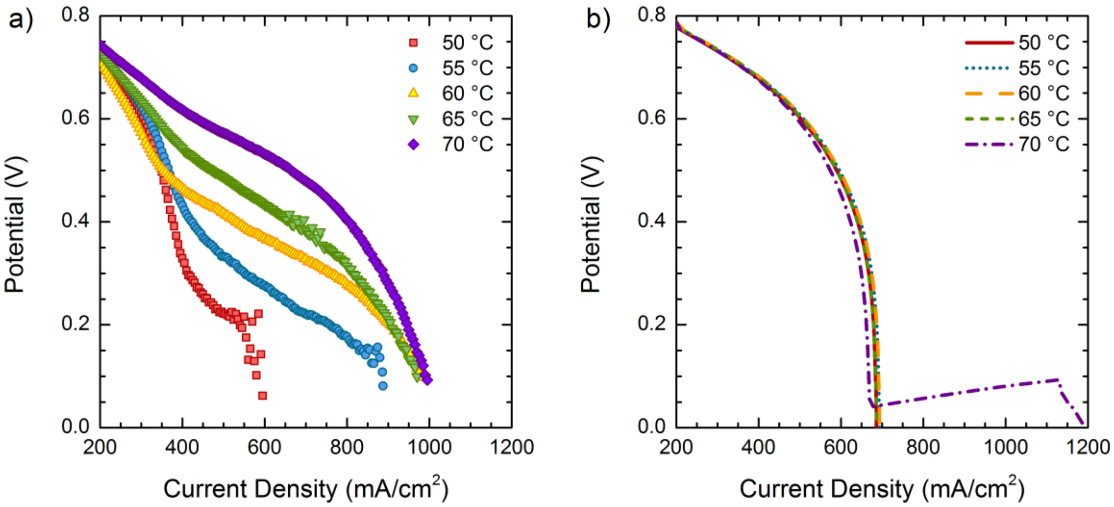

Figure 6-9: Experimental (a) and simulated (b) polarization curves demonstrating the dependence of PCI flow on temperature in SGL 25BA GDLs. Anode: 630 sccm H_2. Cathode: 1500 sccm 10.5% O_2 in N_2. Humidifiers set 10 °C above cell temperature or 70 °C, whichever is greater.

The magnitude of the PCI flow effect differs considerably between the model and the experiment. There are three likely contributions to this disagreement. First, the effective thermal conductivity of the GDL may be overestimated due to the effect of the flow field channel. In the model, only 1-D heat transfer is considered, but in the fuel cell, heat is only conducted through the flow field land; gas channel convective heat transfer is negligible. Measurements of in-plane and through-plane thermal conductivity in similar GDL materials have shown that in-plane thermal conductivity is approximately one order of magnitude larger than through-plane thermal conductivity (16-18). As a result, in-plane heat conduction from the region under the channel is not a large effect, but there is still some reduction in heat transfer. Additionally, through-plane thermal conductivity increases with compression of the GDL, an effect that is accounted for in when specifying thermal conductivity in the model. However, the GDL is less compressed underneath the channel, and this region will have a lower thermal conductivity. The exact compression under the channel will depend on the mechanical properties of the GDL.

To estimate the appropriate thermal conductivity to use in a 1-D model, the normalized 2-D temperature profile in the GDL was solved numerically. The 2-D model domain is shown in Figure 6-10. The normalized heat balance is

$$0 = \frac{k_{tp}\left(\hat{x}\right)}{k_{tp,c}} \frac{\partial^2 \hat{T}}{\partial \hat{z}^2} + \frac{\ell^2}{W^2} \frac{k_{ip}}{k_{tp,c}} \frac{\partial^2 \hat{T}}{\partial \hat{x}^2}, \qquad [6.21]$$

where $\hat{z}$ is the normalized through-plane dimension, $\hat{x}$ is the normalized in-plane dimension, ℓ is the compressed GDL thickness, W is the flow field half-pitch (the distance from the channel center to the land center – see Figure 6-10), k_{ip} is the in-plane thermal conductivity, $k_{tp}\left(\hat{x}\right)$ is the through-plane thermal conductivity, and $k_{tp,c}$ is the compressed through-plane thermal conductivity. For SGL 25BA, the through-plane thermal conductivity is 0.21 W/m-K when uncompressed (under channel), and 0.42 W/m-K when compressed to a thickness of 145 μm (under land). Zero-flux boundary conditions are applied at the sides and at the channel boundary. A constant temperature boundary condition is applied at the land boundary. A constant flux boundary condition,

$$\frac{\partial^2 \hat{T}\left(\hat{x},0\right)}{\partial \hat{z}^2} = -\frac{k_{tp,c}}{k_{tp}\left(\hat{x}\right)}, \qquad [6.22]$$

is applied at the catalyst layer boundary. The effective thermal conductivity for use in the 1-D model is

$$k^{eff} = \frac{k_{tp,c}}{\int_0^1 \hat{T}(\hat{x},0)\,d\hat{x}}. \qquad [6.23]$$

For a GDL of 145 µm thickness, land width of 0.9 mm, channel width of 0.7 mm, and a ratio of uncompressed to compressed through-plane thermal conductivity of 0.5, the normalized effective thermal conductivity is shown in Figure 6-11.

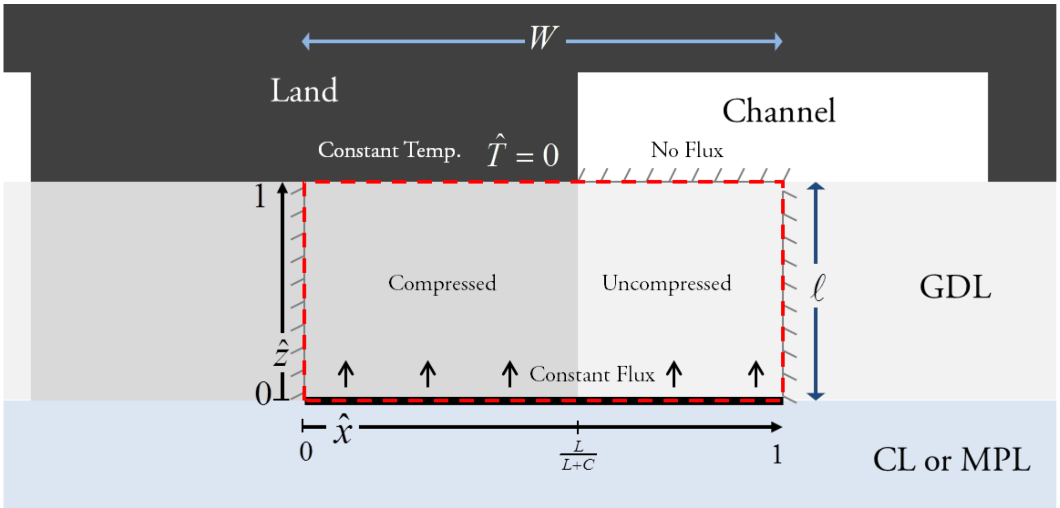

Figure 6-10: GDL conduction model for determining 1-D effective thermal conductivity.

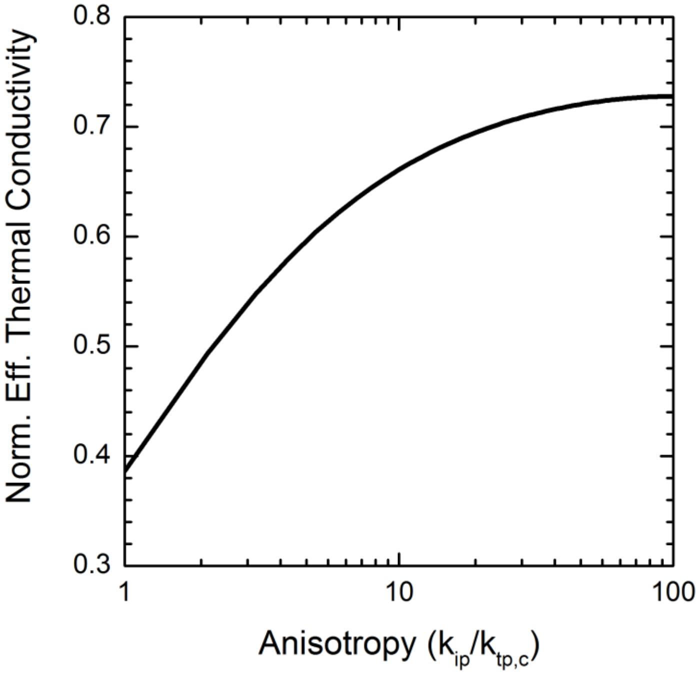

Figure 6-11: Normalized effective thermal conductivity from 2-D GDL heat transfer.

Assuming an anisotropy factor of 10, the thermal conductivity is reduced by 35%. The simulations are repeated with a reduced GDL thermal conductivity of 0.28 W/m-K. The results, shown in Figure 6-12a, are closer to the experimental results, but still require higher temperatures to match the experimental PCI plateau potential.

The second contribution to the discrepancy between simulated and experimental PCI flow is the thermal contact resistance between the GDL and the flow field. Recently, Sadeghifar et al. (19) measured the thermal contact resistance between several GDL materials, including SGL 25BA, and a flat graphite bipolar plate. At 8 bar compression, which was determined from the stress-strain curve in their previous work (6), the contact resistance between SGL 25BA and graphite was ca. 1.5 K-m^2/W. When adjusted for the ratio of land area to total area, the equivalent contact resistance is 2.6 K-m^2/W. Figure 6-12b shows simulated polarization curves including this contact resistance at the GDL-channel interface. Together, the adjusted thermal conductivity and the thermal contact resistance bring the simulated PCI plateau potentials roughly in line with experiment.

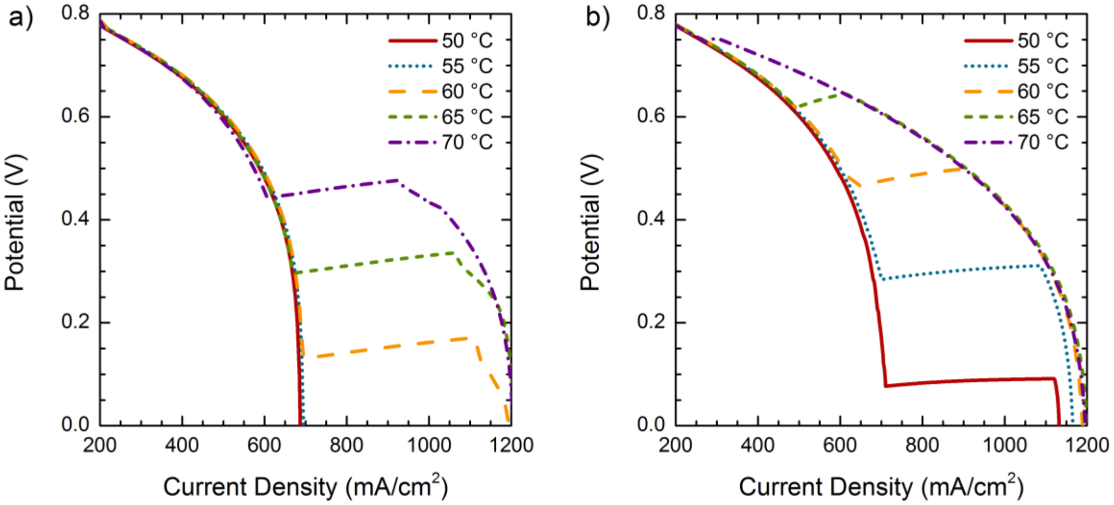

Figure 6-12: a) Simulated polarization curves with reduced GDL thermal conductivity. b) Simulated polarization curves with reduced GDL thermal conductivity and thermal contact resistance at the channel interface. Conditions are identical to those in Figure 6-9.

A final effect modifying the PCI flow, which is not simulated here, is convection in the GDL. In Chapter 5, the effect of GDL convection was measured through limiting current density analysis and incorporated into the model using a modified tortuosity parameter. At the reduced flow rates used in this chapter, the effects of convection are less critical, and for simplicity, convection is ignored. However, the effect of convection remains in the experimental results, and it may have influenced the observed PCI plateau potentials.

Comparing the model simulations in Figure 6-12b and the experiments in Figure 6-9a, it is seen that the effect of temperature on the PCI plateau potential is greater in the simulation than in the experiment. The temperature dependence is primarily determined by the vapor pressure relationship, which determines the driving force for water vapor transport. The dependence of water vapor pressure on temperature is known, and the weaker than predicted temperature dependence in the experiment indicates an additional factor with a strong dependence on temperature.

PCI flow is strongly influenced by the water vapor diffusion coefficient. By replacing N_2 with He as the balance gas, PCI flow can extend to lower temperatures. In Figure 6-13, the model is compared to experiments with two cathode gases: 5% O_2 in N_2, and 5% O_2 in He. The cell operation temperature was 40 °C, and the humidifier temperatures were 50 °C. At 40 °C, the PCI flow in nitrogen is insufficient to remove the product water, but in helium, a PCI plateau potential is observed. The model predicts a higher PCI plateau potential under helium than observed experimentally, but a similar limiting current density. The difference in plateau potential might be explained by the high thermal conductivity of helium gas. The effective thermal conductivity has not been compared experimentally for helium-filled and nitrogen-filled GDLs, but a significant effect is likely. As before, the limiting current density while flooded is overpredicted.

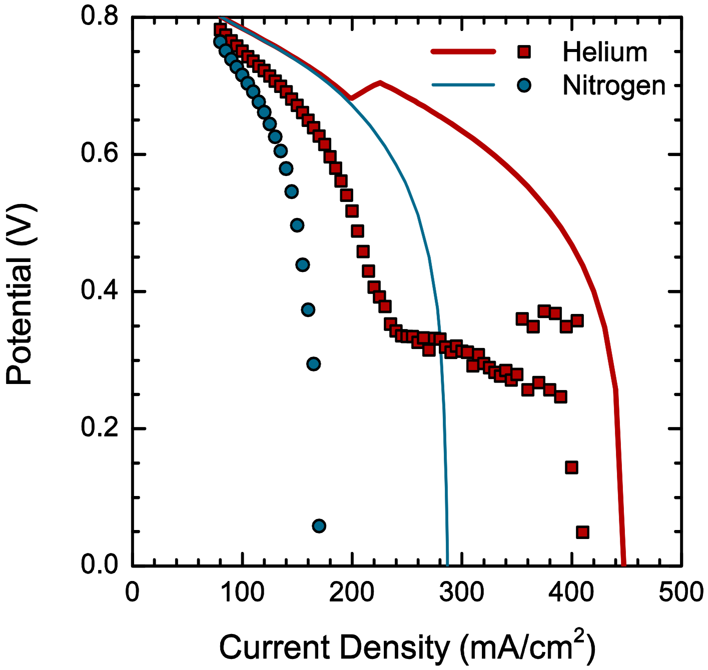

Figure 6-13: Simulated (lines) and experimental (symbols) current sweeps at 40 °C under 5% O_2 in N_2 or He. The humidifier temperature was 50 °C, and gas flow rates were 200 sccm anode and 1000 sccm cathode.

6.5 Conclusions

In this chapter, the conventional treatment of two-phase water transport in PEMFCs was shown to be inadequate and several improvements were introduced to better account for flooding losses. The incorporation of a percolation threshold was found to have only a small effect, and the limiting current density was still four times larger than experimentally observed. Interestingly, the cathode GDL saturation was roughly in line with neutron imaging studies, where cathode saturation was typically 0.1-0.3 (20-23). Therefore, the GDL saturation is considered reasonable, and other sources of flooding losses were considered. To account for the large flooding losses, the model was adapted to consider flooding at the CL-GDL interface. Large flooding losses were predicted due to interfacial saturation, although the losses were still smaller than experimentally measured. Larger flooding losses could be generated by increasing the assumed interfacial saturation and droplet size, but experimental measurements of these parameters would be preferred to improve confidence in the model predictions.

Despite the remaining limitations of the model, useful predictions can be made about the importance of PCI flow. In GDLs without MPLs, the flooding losses can vary dramatically between different GDLs and at different temperatures due to changes in heat transport and PCI flow. Below a certain potential, PCI flow matches the total water generation in the cell, and a transition occurs between the flooded state and the dry state. The model correctly predicted the existence of this PCI plateau potential in SGL 25BA, while in Toray TGP-H-060, the model explained why no such effect is observed.

While potential has a logarithmic dependence on many model parameters because the ORR kinetics are described by the Tafel equation, the PCI plateau potential is determined directly by the balance between heat generation and water generation. As a result, it is sensitive to the key heat- and mass-transport parameters. Using the baseline model parameters, which neglected certain known effects for simplicity, the model required approximately 20 °C higher cell temperature to observe the PCI plateau than in experiments. After accounting for 2-D heat conduction in the GDL and thermal contact resistance between the GDL and flow field, the model correctly predicted the PCI plateau potential over a range of temperatures. The model also showed that PCI flow is greatly increased for helium-oxygen mixtures compared to nitrogen-oxygen mixtures.

Modeling flooding losses in PEMFCs remains a difficult task. Future models should build upon the interfacial saturation effect developed in this chapter, as flooding losses are almost negligible without it. Additionally, PCI flow should be considered both in models and in material development. The model predicts that within a certain range, the thermal conductivity of the GDL can have a very large influence on performance, and tuning the GDL thermal conductivity could provide an alternative to the addition of an MPL for water management, considering that the MPL does add oxygen diffusion resistance under dry conditions.

6.6 References

1. J. Gostick, Multiphase Mass Transfer and Capillary Properties of Gas Diffusion Layers for Polymer Electrolyte Membrane Fuel Cells, in *Chemical Engineering*, University of Waterloo, Waterloo, Ontario, Canada (2008).
2. J. T. Gostick, M. A. Ioannidis, M. W. Fowler and M. D. Pritzker, *Electrochem. Commun.*, **10**, 1520 (2008).
3. J. M. LaManna, J. V. Bothe Jr, F. Y. Zhang and M. M. Mench, *J. Power Sources*, **271**, 180 (2014).
4. J. T. Gostick, M. W. Fowler, M. A. Ioannidis, M. D. Pritzker, Y. M. Volfkovich and A. Sakars, *J. Power Sources*, **156**, 375 (2006).
5. M. T. van Genuchten, *Soil Science Society of America Journal*, **44**, 892 (1980).
6. H. Sadeghifar, N. Djilali and M. Bahrami, *J. Power Sources*, **248**, 632 (2014).
7. M. M. Tomadakis and T. J. Robertson, *J. Compos. Mater.*, **39**, 163 (2005).
8. M. M. Tomadakis and S. V. Sotirchos, *AlChE J.*, **39**, 397 (1993).
9. J. T. Gostick, M. W. Fowler, M. D. Pritzker, M. A. Ioannidis and L. M. Behra, *J. Power Sources*, **162**, 228 (2006).
10. J. T. Gostick, M. A. Ioannidis, M. W. Fowler and M. D. Pritzker, *J. Power Sources*, **194**, 433 (2009).
11. J. H. Nam and M. Kaviany, *Int. J. Heat Mass Transfer*, **46**, 4595 (2003).

12. A. Z. Weber, R. M. Darling and J. Newman, *J. Electrochem. Soc.*, **151**, A1715 (2004).

13. J. H. Nam, K.-J. Lee, G.-S. Hwang, C.-J. Kim and M. Kaviany, *Int. J. Heat Mass Transfer*, **52**, 2779 (2009).

14. J. P. Owejan, J. E. Owejan, W. Gu, T. A. Trabold, T. W. Tighe and M. F. Mathias, *J. Electrochem. Soc.*, **157**, B1456 (2010).

15. I. V. Zenyuk, D. Y. Parkinson, G. Hwang and A. Z. Weber, *Electrochem. Commun.*, **53**, 24 (2015).

16. N. Zamel, E. Litovsky, X. G. Li and J. Kleiman, *Int. J. Hydrogen Energy*, **36**, 12618 (2011).

17. N. Zamel, E. Litovsky, S. Shakhshir, X. Li and J. Kleiman, *Applied Energy*, **88**, 3042 (2011).

18. P. Teertstra, G. Karimi and X. Li, *Electrochim. Acta*, **56**, 1670 (2011).

19. H. Sadeghifar, N. Djilali and M. Bahrami, *J. Power Sources*, **273**, 96 (2015).

20. A. Z. Weber and M. A. Hickner, *Electrochim. Acta*, **53**, 7668 (2008).

21. J. D. Fairweather, D. Spernjak, A. Z. Weber, D. Harvey, S. Wessel, D. S. Hussey, D. L. Jacobson, K. Artyushkova, R. Mukundan and R. L. Borup, *J. Electrochem. Soc.*, **160**, F980 (2013).

22. K. T. Cho and M. M. Mench, *PCCP*, **14**, 4296 (2012).

23. J. M. LaManna, S. Chakraborty, J. J. Gagliardo and M. M. Mench, *Int. J. Hydrogen Energy*, **39**, 3387 (2014).

CHAPTER 7

INDUCTIVE LOOP

As discussed in Chapter 5, the low-frequency impedance measured by electrochemical impedance spectroscopy (EIS) does not match the steady-state value measured from polarization curves. In theory, except for any differences in the operating conditions, the impedance at zero frequency should match the slope of the polarization curve, and in mathematical models, this condition is always true. However, in practice, the frequency range of EIS is rarely extended below 0.01 Hz due to the time required for the measurement. If processes occur below the low-frequency cutoff of EIS, there will be a mismatch between the apparent low-frequency impedance in EIS and the DC resistance from the polarization curve. When models do not account for these low-frequency processes, it is impossible to match both transient (EIS) and steady-state (polarization curve) experiments. However, unlike high-frequency processes that are readily apparent in EIS, the low-frequency processes are only inferred when comparing two different experiments.

Low-frequency processes in PEMFC can be either capacitive or inductive in nature, but most are inductive. The processes are labeled “inductive” because their impedance has a positive imaginary component, as compared to a negative imaginary component for a capacitive process. However, true inductance is only observed as a measurement artifact at high frequencies due to cabling. Instead, the inductive behavior in PEMFCs is caused by a variety of mass-transport, heat-transport, and kinetic effects.

The only requirement is that the process lowers the impedance at low frequencies relative to high frequencies.

The model in Chapter 5 has two processes that produce low-frequency inductive loops. The first is water generation coupled with ohmic losses. As current density increases, the extra water generated hydrates the membrane and catalyst layer ionomer, decreasing the ohmic resistance. It takes time for this water to accumulate, so the improved conductivity is only observed at low frequencies, and an inductive loop occurs. This process was demonstrated experimentally by Schneider et al. (1) and Holmstrom et al. (2), and modeled theoretically by Niya and Hoorfar (3) and Wiezell et al. (4). The second inductive process in the one-phase model is oxide growth on platinum. The oxide layer forms slowly as potential is increased and inhibits the oxygen reduction reaction (ORR). As current density increases, the cathode potential decreases, and the oxide layer is partially reduced. The decrease in oxide coverage speeds up the ORR, and the kinetic overpotential is reduced. The oxide layer takes time to adjust, and a larger kinetic overpotential is required at high frequencies than at low frequencies, meeting the requirement for an inductive loop. The oxide layer was previously studied as a cause of the inductive loop by Roy et al. (5) and by Mathias et al. (6).

In this chapter, the inductive loop is investigated in further detail both theoretically and through experiments. Simplified models are used to analyze the water generation and oxide growth processes. The balance between water generation and heat generation is investigated experimentally. Additionally, the heterogeneity of the oxide layer is studied through EIS in an inert gas atmosphere. In order to maximize the utility of EIS in characterizing fuel cells, the inductive processes must be understood and accounted for. Without this understanding, model parameters will not agree between steady-state and transient experiments.

7.1 Water Generation

The inductive loop due to water generation is caused by a number of linked mass- and heat-transfer processes. In the simplest analysis, mass transfer can be ignored, and an overall cell mass balance on water can be used to determine the average change in flow channel concentration with current density. To this first estimate, the temperature rise in the cell can be added.

If water mass transport is ignored, the entire MEA and flow channels can be treated as a single lumped domain. The mass balance is

$$\frac{\partial n_W}{\partial t} = N_{ch,W}^{A}\big|_{in} + N_{ch,W}^{C}\big|_{in} - N_{ch,W}^{A}\big|_{out} - N_{ch,W}^{C}\big|_{out} + \frac{I}{2F} \qquad [7.1]$$

The change with time in the total moles of water per unit area, n_W, is

$$\frac{\partial n_W}{\partial t} = \left[\frac{\ell_{eff}^{gas}}{RT} + \frac{\ell_{eff}^{ion.}\rho_i}{EW}\left(\frac{\partial \lambda}{\partial p_W}\right)_T\right]\frac{\partial p_W}{\partial t} + \frac{\ell_{eff}^{ion.}\rho_i}{EW}\left(\frac{\partial \lambda}{\partial T}\right)_P\frac{\partial T}{\partial t} \qquad [7.2]$$

where

$$\ell_{eff}^{gas} = 2\left(\ell_{eff}^{ch} + \varepsilon_g^G \ell^G + \varepsilon_g^C \ell^C\right) \qquad [7.3]$$

and

$$\ell_{eff}^{ion.} = \ell^M + 2\varepsilon_i^C \ell^C \qquad [7.4]$$

are the total gas phase thickness and the total ionomer thickness, respectively. EW is the equivalent weight of the membrane ionomer (g/eq SO_3^-), ρ_i is the dry membrane density, and λ is the membrane hydration with units of mol H_2O per mol SO_3^-. The partial derivatives are evaluated from the water sorption isotherm and vapor pressure equation, Equations [3.14] and [3.95]. The water vapor accumulation term is negligible compared to the ionomer water accumulation term for typical cell dimensions and will be neglected. The right hand side of Equation [7.1] can be expressed in terms of current density, inlet relative humidity, and flow stoichiometry. Equation [7.1] becomes

$$\frac{\partial n_W}{\partial t}=\frac{I_0}{4F}\left\{\frac{4\zeta_A}{x_{H,dry}}\frac{\phi_A p_{vap}}{P-\phi_A p_{vap}}+\frac{2\zeta_C}{x_{O,dry}}\frac{\phi_C p_{vap}}{P-\phi_C p_{vap}}-\left(\frac{4\zeta_A}{x_{H,dry}}+\frac{2\zeta_C}{x_{O,dry}}\right)\frac{p_W}{P-p_W}\right\}+\frac{I}{4F}\left(3\frac{p_W}{P-p_W}+2\right), \quad [7.5]$$

where ζ is the stoichiometric ratio, ϕ is the inlet relative humidity, and $x_{H,dry}$ and $x_{O,dry}$ are the dry gas mole fractions of hydrogen in the anode feed and oxygen in the cathode feel, respectively. The actual cell current is I, and the cell current used to calculate gas stoichiometry is I_0. This distinction is made because during EIS, the inlet gas flowrates are not varied with current, but the water generation and reactant consumption terms do vary with current. In order to calculate the average water concentration in the cell, instead of the outlet concentration, the mass balance is applied only to the first half of the cell. This is reflected in Equation [7.5] through the extra factor of two applied to the gas stoichiometric ratios. The steady-state solution for the water partial pressure is best expressed as

$$\frac{p_W}{P-p_W}=\frac{\frac{4\zeta_A}{x_{H,dry}}\frac{\phi_A p_{vap}}{P-\phi_A p_{vap}}+\frac{2\zeta_C}{x_{O,dry}}\frac{\phi_C p_{vap}}{P-\phi_C p_{vap}}+2}{\left(\frac{4\zeta_A}{x_{H,dry}}+\frac{2\zeta_C}{x_{O,dry}}-3\right)}. \quad [7.6]$$

The dynamic solution for an AC perturbation of frequency ω is

$$\begin{gathered}\left\{j\omega\frac{\ell_{eff}^{ion.}\rho_i}{EW}\left(\frac{\partial\lambda}{\partial p_W}\right)_T+\frac{\bar{I}}{4F}\left(\frac{4\zeta_A}{x_{H,dry}}+\frac{2\zeta_C}{x_{O,dry}}-3\right)\frac{P_{out}}{\left(P-\bar{p}_W\right)^2}\right\}\tilde{p}_W \\ =\frac{1}{4F}\left(\frac{3\bar{p}_W}{P-\bar{p}_W}+2\right)\tilde{I}-j\omega\frac{\ell_{eff}^{ion.}\rho_i}{EW}\left(\frac{\partial\lambda}{\partial T}\right)_{p_W}\tilde{T}\end{gathered}, \quad [7.7]$$

where the tilde superscript, $\tilde{p}_W$, signifies the AC perturbation in a variable, and the overbar, $\bar{p}_W$, signifies the steady-state value of a variable. Assuming the anode losses are negligible and that the cathode current distribution is nearly uniform, the ohmic overpotential is

$$\eta_{ohm} = I\left(\frac{\ell^M}{\kappa} + \frac{\ell^C}{3\kappa_{eff}}\right), \qquad [7.8]$$

where κ is the membrane conductivity, κ_{eff} is the effective catalyst layer conductivity, ℓ^M is the membrane thickness and ℓ^C is the catalyst alyer thickness. The ohmic impedance is

$$\tilde{Z}_{ohm} = \left(\frac{\ell^M}{\bar{\kappa}} + \frac{\ell^C}{3\bar{\kappa}_{eff}}\right)\tilde{I} - \left(\frac{\bar{I}\,\ell^M}{\bar{\kappa}^2}\left(\frac{\partial\kappa}{\partial a_W}\right)_T + \frac{\bar{I}\,\ell^C}{3\bar{\kappa}_{eff}{}^2}\left(\frac{\partial\kappa_{eff}}{\partial a_W}\right)_T\right)\left(\frac{1}{\bar{p}_{vap}}\frac{\tilde{p}_W}{\tilde{I}} - \frac{\bar{a}_W}{\bar{p}_{vap}}\frac{dp_{vap}}{dT}\frac{\tilde{T}}{\tilde{I}}\right). \qquad [7.9]$$

The temperature dependence of conductivity is neglected under the assumption that it is small compared to the hydration effect.

When neglecting the temperature fluctuations in the cell, the time constant for water accumulation can be determined from Equation [7.7] by putting frequency dependence into a form similar to $(j\omega\tau + 1)$. The time constant is

$$\tau = \frac{\dfrac{\ell_{eff}^{ion.}\rho_i}{EW}\left(\dfrac{\partial\lambda}{\partial p_W}\right)_T}{\dfrac{I_0}{4F}\left(\dfrac{4\zeta_A}{x_{H,dry}} + \dfrac{2\zeta_C}{x_{O,dry}} - 3\right)\dfrac{P}{\left(P - \bar{p}_W\right)^2}}. \qquad [7.10]$$

The zero-frequency perturbation in water partial pressure is

$$\frac{\tilde{p}_W}{\tilde{I}} = \frac{P}{\bar{I}} \frac{\left(2-\frac{\bar{p}_W}{P}\right)\left(1-\frac{\bar{p}_W}{P}\right)}{\frac{4\zeta_A}{x_{H,dry}} + \frac{2\zeta_C}{x_{O,dry}} - 3}. \qquad [7.11]$$

Substituting Equation [7.11] into Equation [7.9] and subtracting out the high frequency resistance gives the magnitude of the low-frequency inductive loop,

$$\Delta\tilde{Z}_{ohm,LF} = -\left(\frac{\ell^M}{\bar{\kappa}^2}\left(\frac{\partial\kappa}{\partial a_W}\right)_T + \frac{\ell^C}{3\bar{\kappa}_{eff}^{\,2}}\left(\frac{\partial\kappa_{eff}}{\partial a_W}\right)_T\right)\left(\frac{P}{\bar{p}_{vap}} \frac{\left(2-\frac{\bar{p}_W}{P}\right)\left(1-\frac{\bar{p}_W}{P}\right)}{\frac{4\zeta_A}{x_{H,dry}} + \frac{2\zeta_C}{x_{O,dry}} - 3}\right). \qquad [7.12]$$

The effects of water generation are offset by heat generation. As current density increases, the temperature increases, which has a drying effect on the membrane. A variety of factors affect the balance between water and heat generation, including temperature, current density, cell potential, gas flow rates, thermal conductivity, GDL porosity, GDL tortuosity, and GDL convection. Under some conditions, the heat generation effect may be larger than the water generation effect, resulting in higher ohmic impedance at higher current densities and a capacitive loop.

The temperature rise in the cell is determined from an energy balance assuming all heat is generated in the cathode catalyst layer. The thermal resistance of the thin catalyst layer is neglected. The heat capacity of the MEA is negligible compared to the latent heat of water vapor, and the heat accumulation term can be written in terms of the water accumulation,

$$-\Delta H_{vap}\frac{\partial n_W}{\partial t} = -\left(\frac{k^G}{\ell^G} + \frac{k^G k^M}{k^M \ell^G + k^G \ell^M}\right)\Delta T + I\left(U_H - E\right), \qquad [7.13]$$

where ΔH_{vap} is the heat of vaporization of water, k^G is the thermal conductivity of the

GDL, k^M is the thermal conductivity of the membrane, ΔT is the temperature difference between the membrane and flow channels, U_H is the thermoneutral potential (based on enthalpy of combustion), and E is the potential.

For a sinusoidal perturbation, the energy balance is

$$-j\omega\Delta H_{vap}\frac{\ell_{eff}^{ion.}\rho_i}{EW}\left[\left(\frac{\partial\lambda}{\partial p_W}\right)_T\tilde{p}_W+\left(\frac{\partial\lambda}{\partial T}\right)_P\tilde{T}\right]=-\left(\frac{k^G}{\ell^G}+\frac{k^Gk^M}{k^M\ell^G+k^G\ell^M}\right)\tilde{T}+\left(U_H-\bar{E}\right)\tilde{I}-\bar{I}\tilde{E} \quad [7.14]$$

The zero-frequency temperature perturbation is

$$\frac{\tilde{T}}{\tilde{I}}=\frac{U_H-\bar{E}-\bar{I}\dfrac{\tilde{E}}{\tilde{I}}}{\dfrac{k^G}{\ell^G}+\dfrac{k^Gk^M}{k^M\ell^G+k^G\ell^M}}=\frac{U_H-\bar{E}+\bar{I}R_{DC}}{\dfrac{k^G}{\ell^G}+\dfrac{k^Gk^M}{k^M\ell^G+k^G\ell^M}}, \quad [7.15]$$

where the DC impedance, R_{DC}, can be used, if known, to account for the potential perturbation. Equations [7.11] and [7.15] can be substituted into Equation [7.9] to derive the magnitude of the inductive loop,

$$\begin{aligned}\Delta\tilde{Z}_{ohm,LF}&=-\left(\frac{\ell^M}{\bar{\kappa}^2}\left(\frac{\partial\kappa}{\partial a_W}\right)_T+\frac{\ell^C}{3\bar{\kappa}_{eff}{}^2}\left(\frac{\partial\kappa_{eff}}{\partial a_W}\right)_T\right)\\&\quad\times\left(\frac{P}{\bar{p}_{vap}}\frac{\left(2-\dfrac{\bar{p}_W}{P}\right)\left(1-\dfrac{\bar{p}_W}{P}\right)}{\dfrac{4\zeta_A}{x_{H,dry}}+\dfrac{2\zeta_C}{x_{O,dry}}-3}-\frac{\bar{a}_W}{\bar{p}_{vap}}\frac{dp_{vap}}{dT}\frac{U_H-\bar{E}+\bar{I}R_{DC}}{\dfrac{k^G}{\ell^G}+\dfrac{k^Gk^M}{k^M\ell^G+k^G\ell^M}}\right)\end{aligned} \quad [7.16]$$

The relative balance between water generation and heat generation can be determined experimentally by monitoring high frequency resistance (HFR) during current steps. If water generation outweighs heat generation, then HFR will decrease when the current is stepped up. Figure 7-1 shows the changes in HFR with current steps for three different combinations of current and flow rate. In all three cases, the gas flow rate is maintained at a stoichiometric ratio of six based on the upper current step. Cell temperature was 80 °C, and the inlet relative humidity was 75%. At 1600 mA/cm^2, HFR decreases when the current density is reduced by 10%. This indicates that heat generation outweighs water generation, and a capacitive rather than inductive loop should be observed. At 800 mA/cm^2, no change in HFR is discernable, indicating that the two effects are balanced. At 200 mA/cm^2, a slight increase in HFR is observed with decreasing current density, indicating that a very small inductive loop is expected.

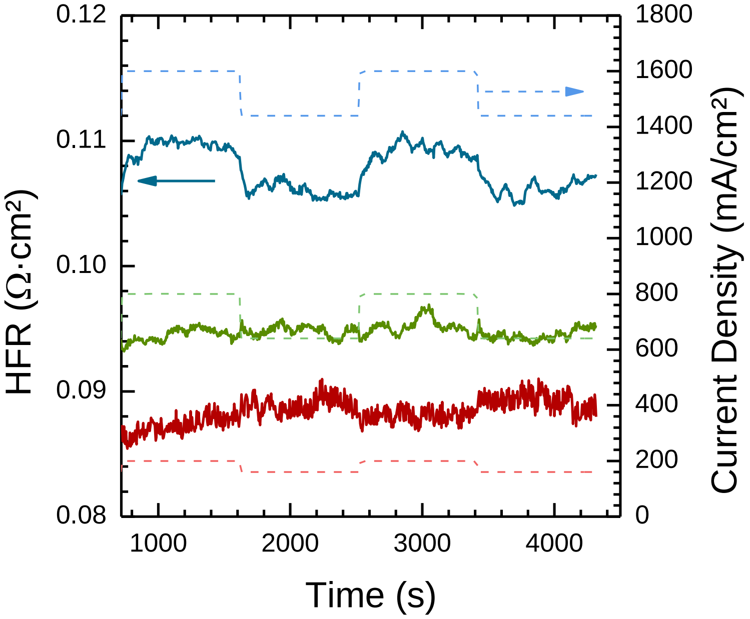

Figure 7-1: HFR response to current steps at constant flow rate.

At lower flow rates, the change in water partial pressure with current density is larger. At lower temperatures, the change in water vapor pressure with heat buildup is smaller. Both of these effects increase the expected magnitude of the inductive loop.

7.2 Oxide Layer

The oxide layer produces an inductive loop under all conditions except low cell potentials. The inductive loop is produced through a change in the Tafel slope with frequency. Oxide inhibits the ORR, so the increase in oxide coverage with increasing potential causes the ORR rate to decrease faster than it would on an oxide-free surface. Thus, the larger the change in oxide coverage with potential, the smaller the Tafel slope. At high frequencies, only the quasi-equilibrated chemisorbed oxide can adjust to the changing potential. As frequency decreases, more of the slow, place-exchanged oxide adjusts to the changing potential, and the Tafel slope decreases. The kinetic and mass-transport contributions to impedance both scale with Tafel slope, so the decreasing Tafel slope with frequency causes an inductive loop.

The steady-state plus perturbation oxide growth model described in Section 3.2.4.4 was used as an isolated model to investigate the ORR Tafel slope as a function of frequency and potential. The potential and oxide terms of the ORR rate equation were linearized, and the ratio of the perturbation in rate including oxide effects to that excluding oxide effects was used to calculate the Tafel slope. Figure 7-2 shows the simulated Tafel slopes as a function of frequency over a range of 10^{-6} to 10^{3} Hz. Curves at 0 Hz and 10^{10} Hz are added to show the low frequency and high frequency limits. Below 0.6 V, no oxide is formed, and the Tafel slope is a constant 140 mV/decade. At 0.6 V, the DC Tafel slope begins to decrease as edge PtO_2 is formed. The high frequency Tafel slope is unchanged until around 0.7 V, when chemisorbed OH begins to form. At 0.8 V, another slope change is observed as the Frumkin effects on chemisorbed OH gain importance and planar-PtO_2 begins to form. Above 0.8 V, the Tafel slope ranges from 40-

90 mV, depending on potential and frequency. At 1.1 V, even the high frequency Tafel slope is only 50 mV compared to the typically observed value of 70 mV, but it is difficult to test this prediction experimentally, as the ORR current density is very small at 1.1 V, and the oxide layer takes a very long time to equilibrate. As potential increases, the equilibration of the oxide layer takes longer, as indicated by a shift to lower frequencies.

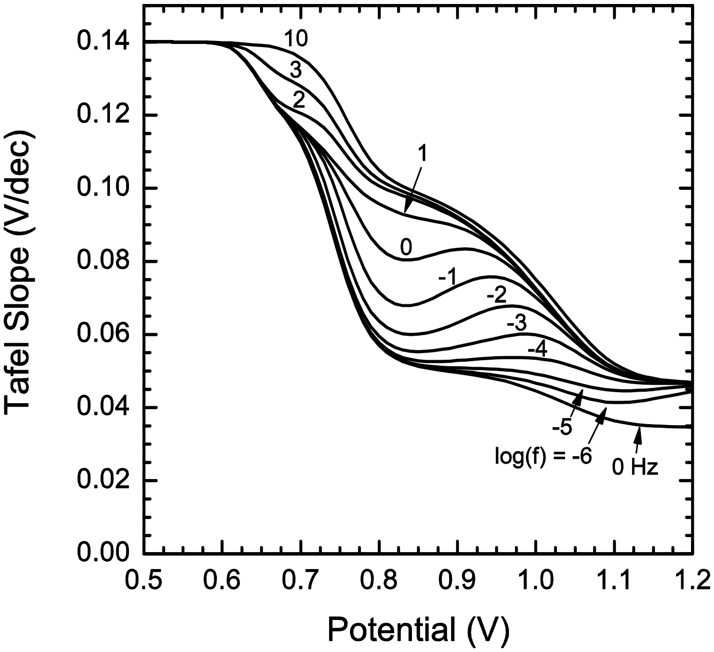

Figure 7-2: Modeled ORR Tafel slope as a function of frequency. Numbers indicate logarithm of frequency, except for 0 Hz.

The difference between the high frequency and DC Tafel slopes determines the largest possible inductive loop. However, if double layer charging overlaps with some slow oxide formation, both a smaller inductive loop and a smaller capacitive loop will be observed. Both loops are smaller because at the intermediate frequency intercept, the Tafel slope will fall below the high frequency and DC limits. In Figure 7-3, the size of the inductive loop is plotted against the potential, assuming the intermediate frequency intercept is 0.1 Hz. The fractional size of the inductive loop is

$$size = 1 - \frac{b_{DC}}{b_{0.1\mathrm{Hz}}}, \qquad [7.17]$$

and represents the ratio of the inductive loop diameter to the capacitive loop diameter.

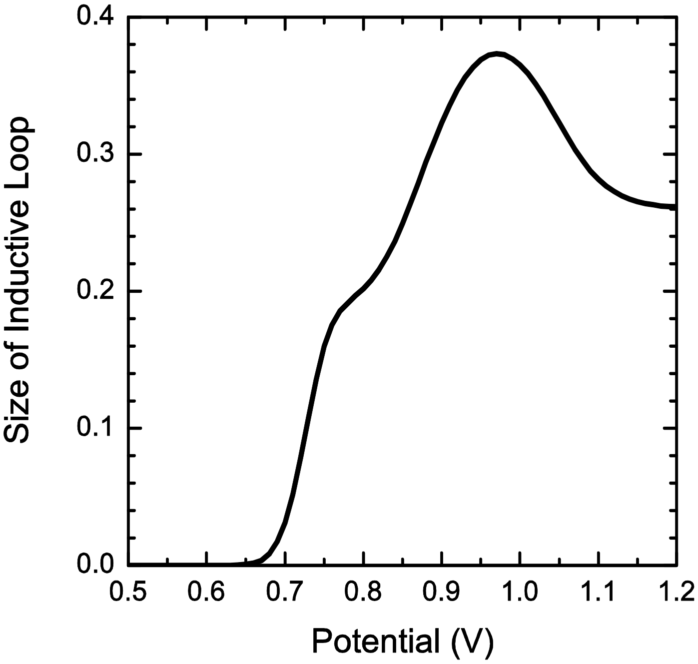

Figure 7-3: Fractional size of inductive loop (relative to charge-transfer loop) assuming 0.1 Hz intermediate frequency intercept.

The heterogeneity of the oxide layer in the model results in a distribution of time constants for oxide growth. Higher stability corresponds to longer time constants. A surface adsorption step such as oxide formation displays capacitive behavior, and the frequency dispersion caused by heterogeneity manifests as constant phase element (CPE) behavior. The impedance of a capacitor has a phase angle of -90°, while that of a resistor is 0°. CPE behavior refers to a process that exhibits a nearly constant phase that is intermediate between that of a capacitor and resistor. This CPE behavior is shown in the EIS Nyquist plots of Figure 7-4. In Figure 7-4a, simulated EIS spectra at potentials varying from 0.5 V to 0.75 V are shown. The frequency range is 10^4 to 10^{-1} Hz, and impedance is normalized to platinum surface area. Only a very slight CPE behavior is observed, noting that the axes are not square. A significant increase in capacitance is observed with increasing potential, as indicated by the reduced imaginary component of impedance. In Figure 7-4b, spectra at 0.8 V to 1.0 V are compared. The main axes are square to properly show the slope. Above 0.8 V, the capacitance decreases with increasing potential, as reversible chemisorbed oxide is replaced with irreversible PtO_2.

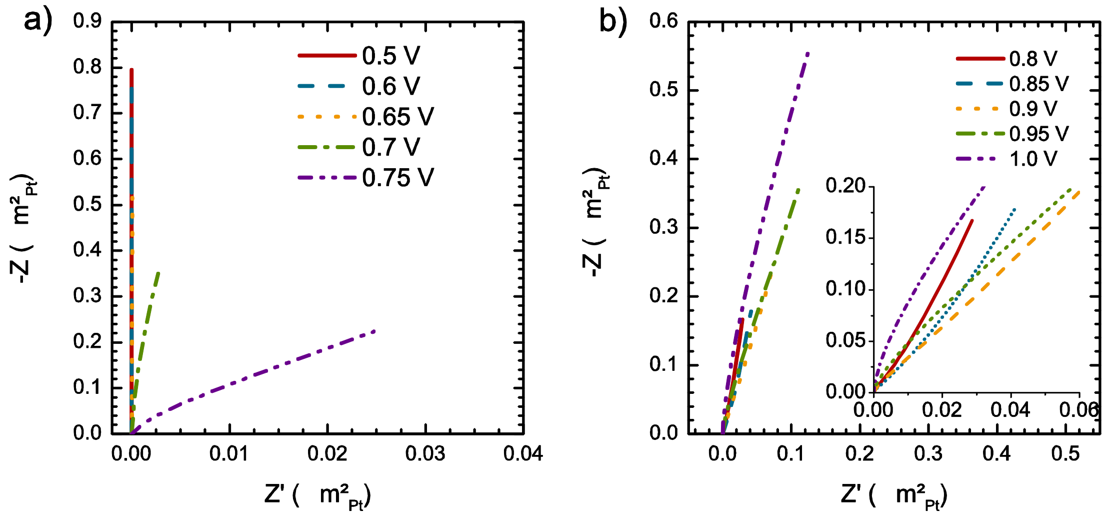

Figure 7-4: Simulated Nyquist plots showing constant phase element behavior. a) 0.5-0.75 V, scaled. b) 0.8-1.0 V, inset zoomed.

Experimental EIS spectra were measured under similar conditions (60 °C cell temperature, 53 °C humidifier temperature) with N_2 at the cathode. A hold of 30 minutes was performed at each potential before an EIS spectrum was recorded over the frequency range 0.1-100 Hz. In Figure 7-5, the EIS Nyquist plots are shown for comparison to

Figure 7-4. Below 0.75 V, a nearly vertical line is observed, indicating ideal capacitive behavior. From 0.8-0.9 V, a significant slope is observed that qualitatively matches the simulation. At 0.95 V and 1.0 V, the EIS spectrum begins to bend backwards to negative values of real impedance. This effect is believed to be related to hydrogen crossover, as increasing oxide thickness decreases the activity of the catalyst for hydrogen oxidation.

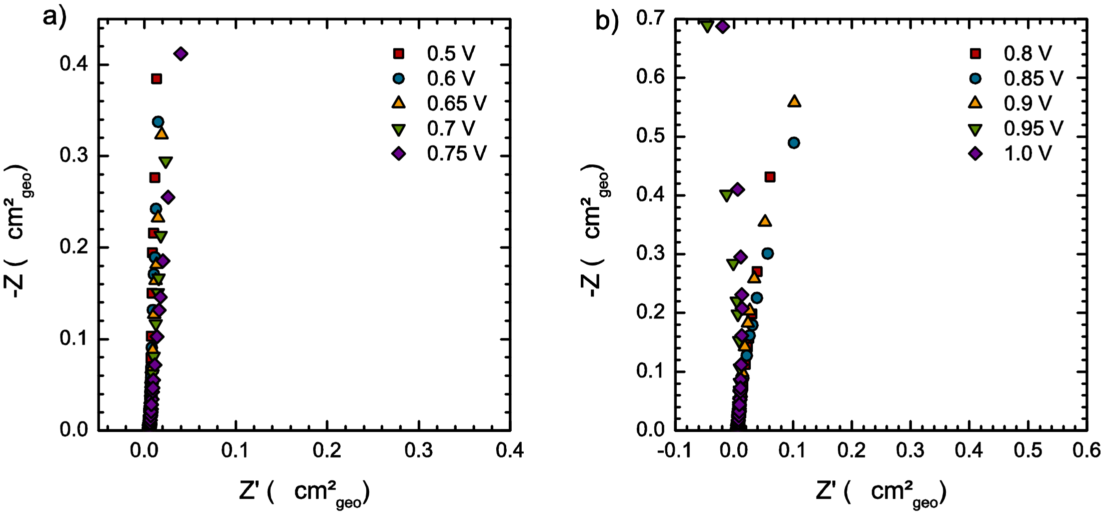

Figure 7-5: Experimental Nyquist plots showing CPE behavior. a) 0.5-0.75 V. b) 0.8-1.0 V.

7.3 Conclusions

In this chapter, the processes responsible for the inductive loop were studied in detail. For water generation, simplified expressions were generated to predict the size of the inductive loop. Additionally, the use of HFR measurement during small current steps was used to determine the tradeoff between water generation and heat generation. At 80 °C and high gas stoichiometry, heat buildup was found to completely nullify the effect of water generation. This result is consistent with the results of Chapter 5, where water generation did not contribute to the observed inductive loop.

Next, the oxide growth model was analyzed to determine the effect on ORR kinetics at various frequencies. A prediction about the size of the inductive loop as a function of potential was made. Finally, CPE behavior due to oxide growth was investigated. The oxide growth model was able to explain the CPE behavior observed at high potentials in PEMFCs. The results of this chapter demonstrate some of the capabilities of physics-based impedance models to explain interesting experimental phenomena.

7.4 References

1. I. A. Schneider, M. H. Bayer, A. Wokaun and G. G. Scherer, *J. Electrochem. Soc.*, **155**, B783 (2008).
2. N. Holmstrom, K. Wiezell and G. Lindbergh, *J. Electrochem. Soc.*, **159**, F369 (2012).
3. S. M. R. Niya and M. Hoorfar, *Electrochim. Acta*, **120**, 193 (2014).
4. K. Wiezell, N. Holmström and G. Lindbergh, *J. Electrochem. Soc.*, **159**, F379 (2012).
5. S. K. Roy, M. E. Orazem and B. Tribollet, *J. Electrochem. Soc.,* **154**, B1378 (2007).
6. M. Mathias, D. Baker, J. Zhang, Y. Liu and W. Gu, *ECS Transactions*, **13**, 129 (2008).

CHAPTER 8

RECOMMENDATIONS

This dissertation has made substantial contributions to physics-based impedance modeling and the modeling of two-phase water transport in PEMFCs, but it has also has spurred a number of ideas for further research. This chapter suggests applications of the physics-based impedance model to study complex, transient process that occur in PEMFCs, which could lead to the development of more stable materials and operating conditions. Furthermore, suggestions are made for additional research into effects included in this model that have yet to receive adequate attention in the literature. Numerical modeling can be mathematically challenging, and to that end some recommendations for simplifying the resulting system of equations are listed. Lastly, experimental validation of the processes included in physics-based models is necessary. Therefore, recommendations for key experiments are made.

In Chapter 5, a detailed physics-based impedance model was validated against EIS experiments over a wide range of current densities, demonstrating the promise of physics-based models for EIS analysis in place of the typical electrical equivalent circuit models. This validation work was necessary to demonstrate the capabilities and limitations of the model in order to show that it can be applied accurately to EIS. Further work should be performed to identify which parameters are best measured by EIS and to integrate parameter fitting algorithms with the model. This technique will give researchers more confidence in analyzing EIS spectra and provide insight to complex processes that occur within the PEMFC.

Additionally, in Chapter 5, it was observed that the oxide layer caused constant phase element (CPE) behavior in the model due to frequency dispersion caused by heterogeneity; demonstrating that EIS is a useful technique for studying the platinum oxide layer. Experimentally, the CPE exponent was found to decrease at high potentials where oxide is formed, indicating increasing frequency dispersion in the response of the electrode. Thus, it appears that EIS offers a direct measurement of the heterogeneity of the oxide formation rate, which previously has been estimated from the width of the CV reduction peak (1). Only the reversible component of the oxide layer is measured at high frequencies, and EIS can be used to differentiate reversible oxide and irreversible oxide at any stage in the oxide growth process. By CV, only the initial reversible stages of oxide growth have been studied (2). Oxide growth is closely linked to platinum dissolution and ORR kinetics. A better understanding of the oxide growth process will guide the development of new materials or operating conditions that lead to improvements in both performance and durability.

A considerable amount of work remains in understanding, predicting, and mitigating flooding losses in PEMFCs. In Chapter 6, phase-change-induced (PCI) flow was shown to be the deciding factor in the performance of GDLs without MPLs under saturated conditions. GDLs with properly optimized thermal conductivity can eliminate flooding losses over certain temperature ranges by ensuring that PCI flow is sufficient to remove all product water. However, PCI flow is strongly temperature dependent, and if thermal conductivity is made low enough to eliminate flooding at low temperatures, the temperature rise would be excessive at high temperatures, leading to increased ohmic losses. The experimental results in Chapter 6 indicated a slightly weaker temperature dependence of PCI than theoretically expected. This result may be linked to enhanced vapor diffusivity, the effect of which increases at low temperatures.

Materials that display increasing thermal conductivity with increasing temperature would greatly expand the range of temperatures for which PCI flow can be optimized, making this water management strategy practical. The thermal conductivity of crystalline materials generally decreases with temperature, while amorphous materials show small increases with temperature until the glass transition temperature is reached (3). A larger effect could be achieved by taking advantage of the heat pipe effect, where the increase of vapor pressure with temperature improves heat transport. In a heat pipe, heat is transported by the evaporation, bulk vapor flow, and condensation of a volatile liquid (e.g. water). The liquid flows countercurrent to the vapor to complete the loop, using gravity or capillary action along a wick. The dependence of effective thermal conductivity on temperature can be further tuned by addition of a small amount of inert gas to impede mass transport at low temperatures.

In Section 3.2.3, an initial treatment of the phenomenon of enhanced vapor diffusion was provided. This effect has been neglected in previous models, but was found to contribute significantly to the water vapor flux in partially saturated PEMFC layers, especially at low temperatures. The implications of this transport mechanism on lower temperature PEMFC operation and cold start should be investigated, as the effect could be significant. At low temperatures, the vapor pressure gradient resulting from a temperature gradient is smaller than at high temperatures, increasing the enhancement factor. For example, at 0 °C, the equivalent diffusivity of water vapor through liquid water is estimated to be 30 times larger than the diffusivity through nitrogen. However, transport through ice cannot occur, so the effect might depend on the transient presence of supercooled water (4).

Introducing model complexity can cause numerical stability issues; thus, the following recommendations address these issues. Full 2-D and 3-D models are more difficult to work with than 1-D models, but the effects of convection and along-the-channel concentration gradients cannot be fully accounted for in 1-D models. In addition, two-phase models can cause difficult numerical stability issues, which are compounded by further model complexity. Therefore, a valuable approach is to use 2-D or 3-D models to derive correction factors for 1-D models. In Chapter 5, convection through the GDL was handled by measuring the mass-transport resistance experimentally at a single flow rate and using that same flow rate for all experiments. A promising approach for future researchers would be to determine the effective mass-transport resistance from a 2-D across-the-channel convection model of the GDL, and use this result in a 1-D model for simplicity. The 2-D across-the-channel model is shown in Figure 8-1. When operating in the single-phase regime, the model is linear, and a correlation for effective diffusion length as a function of Péclet number can be derived. Such a correlation can be easily integrated into a 1-D model if the average pressure drop between channels is known. This quantity could be derived from a simplified channel pressure drop model. Finally, the changing conditions in the along-the-channel dimension could be accounted for by switching to a 1+1-D model, as has been demonstrated by many previous researchers. This modeling scheme, using separate models for 2-D across-the-channel convection and channel pressure drop to parameterize a 1+1-D model, may offer the best tradeoff between accuracy and efficiency.

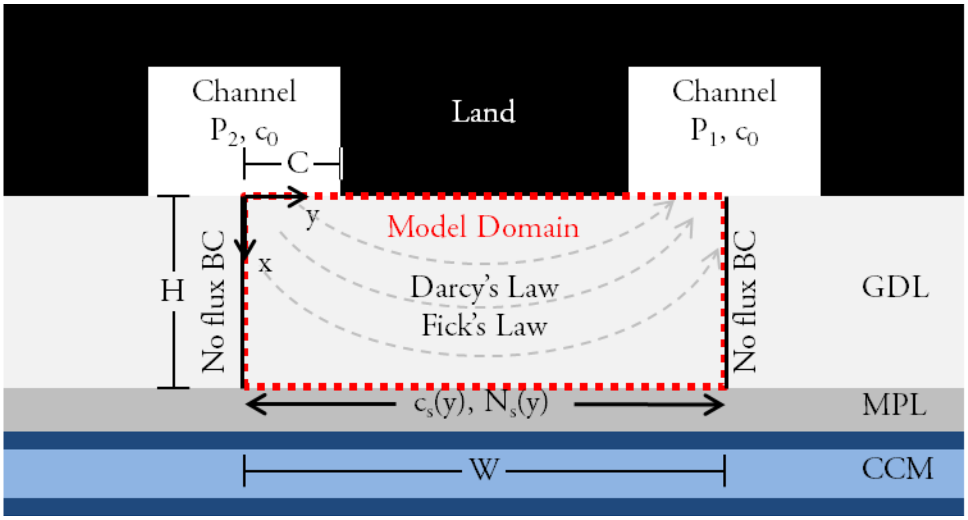

Figure 8-1: Schematic of a 2-D across-the-channel GDL model proposed to model convection.

Experimental validation of mechanistic phenomena is needed to develop a full physics-based model. One of the most critical subjects to study is liquid saturation and transport at interfaces. The severe flooding losses observed experimentally were best modeled by the existence of large water droplets at the CL-GDL interface. In-situ experimental validation of these water droplets is needed, although the resolution limits of the available techniques would prove challenging. Indirect evidence can come from a comparison of flooding losses in catalyst layers of varying thickness. If in-plane diffusion under large water droplets is the major source of flooding losses, then thicker catalyst layers should show improved performance. Additional insight may come from the application of the AC perturbation model described in Section 3.2.4.8. From EIS, the time constant associated with liquid water may be determined. The model can be applied to correlate this time constant with the degree of water accumulation.

A third experiment that could help to elucidate the source of flooding losses is to build a cell using a stack of two GDLs with different thermal conductivities. Toray TGP-H-060 and SGL 25BA are well-suited for this experiment. If conditions are chosen to create one-phase transport due to PCI flow in the SGL layer, but two-phase transport in the Toray layer, the impact of the location of the flooded GDL can be measured. If saturation in the bulk of the GDL is the limiting factor, the stacking order should have little effect on performance. If saturation at the CL-GDL interface is the limiting factor, performance should be good with the SGL layer near the catalyst layer and poor with the Toray layer near the catalyst layer. Finally, if saturation at the channel interface is the limiting factor, performance should be good with the SGL layer near the channel and poor with the Toray layer near the channel.

Lastly, as a general recommendation, more extensive model validation is needed. Ultimately, modeling is a way to clearly express the state of understanding on a topic. If an idea cannot be expressed mathematically and modeled, it probably has not been fully developed. However, if extensive modeling is performed without testing against experiments, hypotheses cannot be falsified, and incorrect ideas cannot be improved. Recognizing that there is a finite amount of resources available, the use of simplified models with more experimental testing is recommended instead of complex models with little validation.

8.1 References

1. E. L. Redmond, B. P. Setzler, F. M. Alamgir and T. F. Fuller, *PCCP*, **16**, 5301 (2014).

2. B. E. Conway, *Prog. Surf. Sci.*, **49**, 331 (1995).

3. D. W. Van Krevelen and K. Te Nijenhuis, in *Properties of Polymers (Fourth Edition)*, D. W. V. K. by and K. T. Nijenhuis Editors, p. 645, Elsevier, Amsterdam (2009).

4. A. Z. Weber, R. L. Borup, R. M. Darling, P. K. Das, T. J. Dursch, W. B. Gu, D. Harvey, A. Kusoglu, S. Litster, M. M. Mench, R. Mukundan, J. P. Owejan, J. G. Pharoah, M. Secanell and I. V. Zenyuk, *J. Electrochem. Soc.*, **161**, F1254 (2014).

APPENDIX A

EQUIVALENT CIRCUIT PARAMETERS FOR CONDUCTIVITY MEASUREMENT

Table A-1:Equivalent circuit parameters

Run Order	Relative Humidity	R_{mem} ($\Omega\cdot cm^2$)	R_{cl} ($\Omega\cdot cm^2$)	Q_{dl} (F/cm^2)	ϕ	L_{wire} ($\mu H\cdot cm^2$)	Res. 2-norm ($m\Omega\cdot cm^2$)
12	42.1%	0.1261	0.4266	0.1692	0.948	2.151	29.3
15	42.1%	0.1446	0.5481	0.1542	0.919	2.578	38.9
16	42.1%	0.1455	0.5530	0.1539	0.918	2.517	41.2
11	50.5%	0.1028	0.2915	0.1882	0.973	2.178	16.8
13	50.5%	0.1033	0.3015	0.1881	0.970	2.107	17.8
17	50.5%	0.1136	0.3342	0.1855	0.966	2.121	19.7
10	57.7%	0.0858	0.2299	0.1962	0.979	2.237	13.4
14	57.7%	0.0888	0.2451	0.1938	0.976	2.247	13.8
18	57.7%	0.0936	0.2606	0.1923	0.975	2.175	14.8
2	65.8%	0.0757	0.1953	0.2093	0.983	2.119	11.1
9	65.8%	0.0724	0.1777	0.2032	0.982	2.127	10.1
19	65.8%	0.0773	0.2074	0.1957	0.979	2.224	12.3
1	74.8%	0.0623	0.1408	0.2073	0.984	2.054	9.1
8	74.8%	0.0615	0.1367	0.2109	0.984	2.080	8.6
20	74.8%	0.0636	0.1567	0.2002	0.982	2.161	9.2
21	74.8%	0.0634	0.1296	0.2009	0.983	1.974	8.8
22	74.8%	0.0606	0.1482	0.2028	0.982	2.176	8.5
23	74.8%	0.0609	0.1482	0.2034	0.982	2.213	8.5
24	74.8%	0.0622	0.1477	0.2051	0.982	2.093	8.5
7	81.4%	0.0525	0.1100	0.2109	0.986	2.089	7.4
25	81.4%	0.0542	0.1246	0.2065	0.983	2.154	7.6
6	84.9%	0.0488	0.0992	0.2171	0.986	2.133	7.3
26	84.9%	0.0502	0.1141	0.2045	0.984	2.189	7.4
5	92.2%	0.0424	0.0766	0.2179	0.986	2.099	6.4
27	92.2%	0.0447	0.0890	0.2053	0.985	2.131	6.4
3	100.0%	0.0423	0.0761	0.2107	0.987	2.196	6.3
4	100.0%	0.0419	0.0771	0.2096	0.987	2.194	6.4
28	100.0%	0.0423	0.0795	0.2046	0.985	2.211	5.9

APPENDIX B

GPROMS MODEL CODE FOR ONE-PHASE TRANSIENT MODEL

(SECTION 3.1)

```
{
  gPROMS input file generated by gPROMS ModelBuilder 3.5.3
  Mon Apr 27 06:48:39 EDT 2015

  PEMFC - One Phase 2014-06-17 -> file:/C:/Users/bsetzler3/Documents/gProms/PEMFC - One
Phase 2014-06-17.gPJ
}

DECLARE TYPE # PEMFC - One Phase 2014-06-17:Activity
    Activity = 0.5 : 1E-010 : 2.0
END

DECLARE TYPE # PEMFC - One Phase 2014-06-17:ChargeDensity
    ChargeDensity = 0.0 : -1.0E+012 : 1.0E+012 UNIT = "C/m^3"
END

DECLARE TYPE # PEMFC - One Phase 2014-06-17:Conductivity
    Conductivity = 10.0 : 0.0 : 1.0E+006 UNIT = "S/m"
END

DECLARE TYPE # PEMFC - One Phase 2014-06-17:Coverage
    Coverage = 1E-010 : 0.0 : 1.0E+010
END

DECLARE TYPE # PEMFC - One Phase 2014-06-17:CurrentDensity
    CurrentDensity = 0.0 : -1.0E+006 : 1.0E+006 UNIT = "A/m^2"
END

DECLARE TYPE # PEMFC - One Phase 2014-06-17:DiffusionCoefficient
    DiffusionCoefficient = 1E-009 : 0.0 : 1.0 UNIT = "m^2/s"
END

DECLARE TYPE # PEMFC - One Phase 2014-06-17:FlowRate
    FlowRate = 1.0 : -1.0E+010 : 1.0E+010 UNIT = "sccm/cm^2"
END

DECLARE TYPE # PEMFC - One Phase 2014-06-17:Flux
    Flux = 1E-006 : -1.0E+020 : 1.0E+020 UNIT = "mol/m^2/s"
END

DECLARE TYPE # PEMFC - One Phase 2014-06-17:Freq
    Freq = 100.0 : 0.0 : 1.0E+007 UNIT = "Hz"
END

DECLARE TYPE # PEMFC - One Phase 2014-06-17:HeatFlux
    HeatFlux = 0.0 : -1.0E+100 : 1.0E+100 UNIT = "W/m^2"
END
```

```
DECLARE TYPE # PEMFC - One Phase 2014-06-17:Heterogeneity
    Heterogeneity = 0.0 : -1.0E+100 : 1.0E+100 UNIT = "mol/J (Fraction of sites /
(J/mol))"
END

DECLARE TYPE # PEMFC - One Phase 2014-06-17:Impedance
    Impedance = 0.0 : -1.0E+020 : 1.0E+020 UNIT = "Ohms cm^2"
END

DECLARE TYPE # PEMFC - One Phase 2014-06-17:IntegratedVoltage
    IntegratedVoltage = 0.0 : -1.0E+020 : 1.0E+020 UNIT = "V*s"
END

DECLARE TYPE # PEMFC - One Phase 2014-06-17:MoleFraction
    MoleFraction = 0.1 : -0.01 : 1.0
END

DECLARE TYPE # PEMFC - One Phase 2014-06-17:Normalized
    Normalized = 0.0 : -1.0E+020 : 1.0E+020
END

DECLARE TYPE # PEMFC - One Phase 2014-06-17:Phase
    Phase = 0.0 : -400.0 : 400.0 UNIT = "rad"
END

DECLARE TYPE # PEMFC - One Phase 2014-06-17:Potential
    Potential = 0.0 : -2.0 : 2.0 UNIT = "V"
END

DECLARE TYPE # PEMFC - One Phase 2014-06-17:Pressure
    Pressure = 50000.0 : -10000.0 : 1.0E+006 UNIT = "Pa"
END

DECLARE TYPE # PEMFC - One Phase 2014-06-17:StoichiometricRatio
    StoichiometricRatio = 10.0 : -1.0E+010 : 1.0E+010
END

DECLARE TYPE # PEMFC - One Phase 2014-06-17:Temperature
    Temperature = 353.0 : -100.0 : 1000.0 UNIT = "K"
END

DECLARE TYPE # PEMFC - One Phase 2014-06-17:TransportNumber
    TransportNumber = 0.0 : -1.0E+010 : 1.0E+010
END

DECLARE TYPE # PEMFC - One Phase 2014-06-17:VolumeRate
    VolumeRate = 100.0 : -1.0E+020 : 1.0E+020 UNIT = "mol/m^3/s"
END

DECLARE TYPE # PEMFC - One Phase 2014-06-17:VolumeRateConstant
    VolumeRateConstant = 1.0 : 1E-040 : 1.0E+020 UNIT = "mol/m^3/s/Pa"
END

DECLARE TYPE # PEMFC - One Phase 2014-06-17:WaterContent
    WaterContent = 14.0 : 1.0 : 50.0 UNIT = "mol H2O / mol H+"
END

CONNECTIONTYPE POP_74714c::GDLPortNewHeat # PEMFC - One Phase 2014-06-17:GDLPortNewHeat

    PARAMETER
        NGasComp AS INTEGER
```

```
    VARIABLE
        i1 AS CurrentDensity
        phi1 AS Potential
        x AS DISTRIBUTION (NGasComp - 1) OF MoleFraction
        N_g AS DISTRIBUTION (NGasComp) OF Flux
        P AS Pressure
        Temp AS Temperature
        qh AS HeatFlux


END # CONNECTIONTYPE GDLPortNewHeat

CONNECTIONTYPE POP_74714c::IonomerPortNewHeat # PEMFC - One Phase 2014-06-
17:IonomerPortNewHeat

    VARIABLE
        activity AS Activity
        N_w AS Flux
        phi2 AS Potential
        i2 AS CurrentDensity
        Temp AS Temperature
        qh AS HeatFlux


END # CONNECTIONTYPE IonomerPortNewHeat

CONNECTIONTYPE POP_74714c::TestLead # PEMFC - One Phase 2014-06-17:TestLead

    VARIABLE
        I AS CurrentDensity
        V AS Potential


END # CONNECTIONTYPE TestLead

MODEL POP_74714c::BPPwAccumulationHeatPFR # PEMFC - One Phase 2014-06-
17:BPPwAccumulationHeatPFR

# This is an attempt at implementing flow rate (stoichiometry) effects without making a
2D model.
# It implements a mass balance for the flow of gas in and out based on the
stoichiometric excess

PORT
    GDLinterface AS GDLPortNewHeat
    CurrentCollector AS TestLead

PARAMETER
    F           AS  REAL DEFAULT 96485  # Faraday's constant
    NGasComp    AS  INTEGER             # Number of gas species
    Pout           AS  REAL                # Total pressure
    p_vap       AS  REAL                # Vapor pressure of water
    n2          AS  REAL                # Stoichiometric coefficient for the reactant
gas
    Left        AS  INTEGER DEFAULT -1
    Right       AS  INTEGER DEFAULT 1
    StackEnd    AS  INTEGER             # We can set StackEnd := Left or Right to get
the signs correct on flux
    I_min       AS  REAL    DEFAULT 100
    c1, c2      AS  REAL    DEFAULT 0
```

```
    R           AS  REAL    DEFAULT 8.3145
    T           AS  REAL
    L           AS  REAL
    h           AS  REAL
    k           AS  REAL
    Lgraphite   AS  REAL
    cpgraphite  AS  REAL
    rhographite AS  REAL
    cpfactor    AS  REAL    DEFAULT 1.24   # We might expect the full graphite volume
to store heat, but in reality, the heat storage ability is approximately 0.532 of the
full volume
                                            # since the edges don't change temeprature
much and the temperature gradients are steepest near the MEA side
    xsectionfactor AS REAL  DEFAULT 1.24    # At steady-state, the heat transfer from
25 cm2 to 58.06 cm2 areas is equivalent to 1-D heat transfer with 1.24*25 cm2 area.
    insfactor  AS  REAL DEFAULT 1.66 # RCorrection factor for non-uniform heat transfer
over 58 cm2 insulator vs  uniform heat transfer over 25 cm2 insulator.

DISTRIBUTION_DOMAIN
    Zee AS [0:Lgraphite]
    Wye AS [0:1]

VARIABLE
    Midpoint    AS  Normalized
    N_in        AS  ARRAY(NGasComp) OF  Flux
    x_dry_in    AS  ARRAY(NGasComp-2) OF MoleFraction
#    N_out       AS  ARRAY(NGasComp) OF  Flux
    p_g_in      AS  ARRAY(NGasComp) OF  Pressure
    p_g         AS  DISTRIBUTION(NGasComp, Wye) OF Pressure
    N_g         AS  DISTRIBUTION(NGasComp, Wye) OF Flux
#    P_g_mid     AS  ARRAY(NGasComp) OF  Pressure
#    P_g_out     AS  ARRAY(NGasComp) OF  Pressure
#    i1          AS  CurrentDensity
#    phi1        AS  Potential
    Vdry        AS  FlowRate                        # Flowrate of dry gas in BPP inlet
(at STP)
    S           AS  StoichiometricRatio
    P,Pin       AS  Pressure
    Temp        AS  DISTRIBUTION(Zee) OF Temperature
    qh          AS  DISTRIBUTION(Zee) OF HeatFlux
#    Peffect     AS  Normalized
#    xeffect     AS  Normalized
#    Teffect     AS  Normalized

BOUNDARY
    #-k*PARTIAL(Temp(0), Zee) = GDLinterface.i1*0.4 ;
    qh(Lgraphite) = insfactor*h*(Temp(Lgraphite)-T) ;
    qh(0) = StackEnd*GDLinterface.qh;
    Temp(0) = GDLinterface.Temp;

EQUATION
    FOR z:= 0|+ TO LGraphite|- DO
        cpfactor*cpgraphite*rhographite*$Temp(z) = -PARTIAL(qh(z), Zee) ;
    END

    qh = -xsectionfactor*k*PARTIAL(Temp, Zee) ;

    GDLinterface.phi1 = CurrentCollector.V  ;
    GDLinterface.P = P;

    P = 5/11*Pin+6/11*Pout;
```

```
    Pin = Pout+c1*Vdry+c2*Vdry^2;
    # The stoichiometric ratio of fuel. Conversion is made from sccm/cm^2 to mol/m^2/s
    # These equations let us specify either Vdry, S, or N_in
    SIGMA(N_in(2:NGasComp)) =   (1e4*Vdry/22414/60) ;
#    S       =   N_in(2)/(MAX(I_min,CurrentCollector.I)/(n2*F)) ;
    MIN(S*(MAX(I_min,CurrentCollector.I)/(n2*F)),
P_g_in(2)/SIGMA(P_g_in(2:NGasComp))*200*1e4/22414/60)       =   N_in(2) ;
#    S       =
N_in(2)/(I_min*((CurrentCollector.I/I_min)^2+(CurrentCollector.I/I_min)+1)/((CurrentCol
lector.I/I_min)+1)/(n2*F)) ;
#    IF CurrentCollector.I > I_min THEN
#        S       =   N_in(2)/(CurrentCollector.I/(n2*F)) ;
#    ELSE
#        S       =   N_in(2)/(I_min/(n2*F)) ;
#    END



    x_dry_in(1:NGasComp-2) = N_in(2:NGasComp-1) / SIGMA(N_in(2:NGasComp)) ;
    Midpoint = 0.5;

    # Mass balances on gas flows
#    N_out = StackEnd*GDLinterface.N_g+N_in ;

    # Calculate partial pressures in inlet gas
    p_g_in(1)               = Pin*N_in(1)/SIGMA(N_in) ;
    SIGMA(N_in(2:NGasComp))*p_g_in(2:NGasComp)    = (Pin-p_g_in(1))*N_in(2:NGasComp) ;
#    p_g_out(1) = P*N_out(1)/SIGMA(N_out) ;
#    SIGMA(N_out(2:NGasComp))*p_g_out(2:NGasComp)   = (P-
p_g_out(1))*N_out(2:NGasComp) ;


    p_g_in*(10/11*Pin+1/11*Pout)/Pin = p_g(,0);
    N_in = N_g(,0);


    FOR y := 0|+ TO 1 DO
        L*$p_g(1:NGasComp-1,y)/(R*Temp(0)) = -PARTIAL(N_g(1:NGasComp-1,y), Wye) +
StackEnd*GDLinterface.N_g(1:NGasComp-1);
        SIGMA(p_g(,y)) = Pout+10/11*(1-y)*(Pin-Pout);
        N_g(1:NGasComp-1,y) / SIGMA(N_g(,y)) = p_g(1:NGasComp-1,y)/(Pout+10/11*(1-
y)*(Pin-Pout));
        L*10/11*(1-y)*$Pin/R/Temp(0) = -PARTIAL(SIGMA(N_g(,y)),Wye) +
StackEnd*SIGMA(GDLinterface.N_g) ;
    END
    FOR ii := 1 TO NGasComp-1 DO
        GDLinterface.x(ii) = INTEGRAL(y:=0:1; p_g(ii,y)/(Pout + 10/11*(1-y)*(Pin-
Pout)));
#        GDLinterface.x(ii) = p_g(ii,0)/(Pout + 10/11*(1)*(Pin-Pout));
    END

#    L/R/Temp(0)*(P*$(GDLinterface.x)+GDLinterface.x*($P-
P*k/(cpgraphite*rhographite*Temp(0))*PARTIAL(Temp(0), Zee, Zee))) =
(Midpoint*StackEnd*GDLinterface.N_g(1:NGasComp-1) + N_in(1:NGasComp-1)) -
GDLinterface.x*SIGMA(Midpoint*StackEnd*GDLinterface.N_g + N_in) ;

# These guys can be used to check which accumulation terms of the mass balance above
actually matter. It turns out that the pressure and (of course) the composition effects
matter, but the temperature changes have a negligible impact on the mass balance.
# Therefore, it would be ok to remove the temperature term if problems arise.
```

```
# Additionally, we should probably try to include the pressure effects in the GDL and
catalyst layer mass balances as well. Temperature may still have it's revenge through
the water flux due to membrane heating, but that should automatically be accounted for
by the existing $lambda term.
#    Peffect = $P*GDLinterface.x(2) ;
#    xeffect = P*$(GDLinterface.x(2)) ;
#    Teffect = -GDLinterface.x(2)*P*k/(cpgraphite*rhographite*Temp(0))*PARTIAL(Temp(0),
Zee, Zee);


END # MODEL BPPwAccumulationHeatPFR

{
No gas phase. Only the necessary variables (plus a couple for convenience)

}
MODEL POP_74714c::CathodeElectrode_SSAggNewHeat_wOxide # PEMFC - One Phase 2014-06-
17:CathodeElectrode_SSAggNewHeat_wOxide

PARAMETER
    # Fundamental Constants
    F               AS  REAL  DEFAULT  96485        # C/mol, Faraday's Constant
    R               AS  REAL  DEFAULT  8.3145       # J/mol*K, Ideal gas constant
    pi              AS  REAL  DEFAULT  3.14159265

    # Physical parameters of electrode
    L               AS  REAL            # Electrode thickness
    EW, rho_n       AS  REAL            # Equivalent weight and density of dry nafion
    MW_w, rho_w     AS  REAL            # Molecular weight and density of water
    epsilon_e       AS  REAL            # Volume fraction of electrolyte in electrode
    epsilon_g       AS  REAL            # Volume fraction of gas pore space in
electrode
    a_ion           AS  REAL    DEFAULT 3

    # Other
    sig             AS  REAL            # Solid phase electronic conductivity
    T               AS  REAL            # Temperature
    k               AS  REAL            # Effective thermal conductivity

    c               AS  REAL            # Double Layer Capacitance

    # Kinetics, thermodynamics, and stoichiometry of reaction
    U               AS  REAL            # Standard potential for surface reaction
    UHov            AS  REAL            # Thermoneutral potential for H2 + 1/2 O2 ->
H2O
    UHRHE           AS  REAL            # Thermoneutral potential for H2 oxidation half
cell
    n               AS  REAL            # Electrons involved in surface reaction
    s_w             AS  REAL DEFAULT -2 # Stoichiometric coefficient of water in
surface reaction
    k0              AS  REAL            # Butler-Volmer rate constant
    alpha_c         AS  REAL            # B-V transfer coefficient for cathodic
reaction
    alpha_a         AS  REAL            # B-V transfer coefficient for anodic reaction
    m_ORR           AS  REAL            # Reaction order wrt oxygen
    dhvap           AS  REAL DEFAULT 41714 # J/mol, Heat of vaporiztion of water from
Nafion, here assumed to be equal to heat of vaporization of liquid water. This
parameter should be a function of lambda, but it's constant for now.
    cprho           AS  REAL DEFAULT 6.6e5 # J/m3, Volumetric heat capacity of catalyst
layer
```

```
    # Gas phase stuff
    NGasComp        AS  INTEGER         # Number of gas phase components. We need at
least 2, water and oxygen, which are components 1 and 2 respectively
    D_g_ij          AS  ARRAY(NGasComp, NGasComp)  OF  REAL  # Stefan-Maxwell
diffusivities
    s_ox            AS  REAL DEFAULT  1 # Stoichiometric coefficient of oxygen in ORR
#    p_vap           AS  REAL            # Vapor pressure of water at T
#    P               AS  REAL            # Total gas pressure

    # Agglomerate parameters
    D_O2_I  AS  REAL                    #   m2/s    Diffusivity of oxygen in ionomer
    H       AS  REAL                    #   Pa-m3/mol   Henry's law constant for oxygen
in ionomer
    R_agg   AS  REAL                    #   m       Flooded agglomerate radius
    th_film AS  REAL                    #   m       Ionomer film thickness (active core
of agglomerate is R_agg-th_film
    tort_agg AS REAL                    #           Tortuosity of ionomer in
agglomerate core
    ECA     AS  REAL                    #   m2/g    Active surface area of catalyst
    loading AS  REAL                    #   mg/cm2  Platinum loading in electrode
    # These two parameters are calculated from other parameters for the convenience of
the model equations. Don't specify them in the process.
    a_pt    AS  REAL                    #   m2/m3   Specific area of platinum in
agglomerate core
    porosity_agg    AS  REAL            #           Volume fraction of ionomer in
agglomerate core

    # Oxide parameters
    sigMu   AS  REAL {   DEFAULT 14500}  # J/mol Standard deviation of the typical
distribution of oxide layer components
    sigMue  AS  REAL  {  DEFAULT 14500 } # J/mol Standard deviation of the typical
distribution of oxide layer components
    U_OH    AS  REAL  {  DEFAULT 0.82 }   #   V           Standard potential for
chemisorption
    U_PtO2  AS  REAL  {  DEFAULT 0.80  }  #   V           Standard potential for place
exchange
    U_PtO2e AS  REAL  {  DEFAULT 0.80  }  #   V           Standard potential for place
exchange
    wOH     AS  REAL  {  DEFAULT 15000  } #   J/mol       Temkin term for chemisorbed
oxide (note squared dependece on coverage)
    wPtO2   AS  REAL  {  DEFAULT 140000}  #   J/mol       Temkin term for place
exchanged oxide
    wPtO2e  AS  REAL  {  DEFAULT 140000  }#   J/mol       Temkin term for place
exchanged oxide
    kOx     AS  REAL  {  DEFAULT 7.35e-2 }#   mol/m2/s    Rate constant for place
exchange
    kOxe    AS  REAL  {  DEFAULT 7.35e-2 }#   mol/m2/s    Rate constant for place
exchange
    alphaOxa    AS  REAL    DEFAULT 1.5 #               Anodic transfer coefficient for
place exchange reaction
    alphaOxc    AS  REAL    DEFAULT 1.5 #               Cathodic transfer coefficient
for place exchange reaction
    alphaOxae   AS  REAL    DEFAULT 2.5 #               Anodic transfer coefficient for
place exchange reaction
    alphaOxce   AS  REAL    DEFAULT 1.5 #               Cathodic transfer coefficient
for place exchange reaction
    qml     AS  REAL    DEFAULT 2.1     #   F/m2        Charge density of a monolayer
of adsorbates (1 e-)
    alphaHet    AS REAL
    chi     AS  REAL    DEFAULT 8
    chie    AS  REAL    DEFAULT 8
```

```
    edgefrac AS REAL DEFAULT 0.37
{
    sigMuE  AS  REAL    DEFAULT 8700
    U_edge  AS  REAL    DEFAULT 0.67
    wedge   AS  REAL    DEFAULT 666667
    kedge   AS  REAL    DEFAULT 7.81e-3
    alphaEda AS REAL    DEFAULT 2.5
    alphaEdc AS REAL    DEFAULT 1.5
}
DISTRIBUTION_DOMAIN
    Zee             AS  [0 : L]         # One dimensional problem
    DelMu           AS  [-3*sigMu:3*sigMu] # The range of energies of the oxide layer
that we simulate



PORT
    mem_interface AS IonomerPortNewHeat
    GDL_interface AS GDLPortNewHeat

VARIABLE
    N_w             AS  DISTRIBUTION(Zee)  OF  Flux            # Flux of water in
ionomer
    i1              AS  DISTRIBUTION(Zee)  OF  CurrentDensity  # Solid phase electronic
current
    i2              AS  DISTRIBUTION(Zee)  OF  CurrentDensity  # Ionomer phase ionic
current
    j               AS  DISTRIBUTION(Zee)  OF  VolumeRate      # Total rate per
electrode volume
    Phi1            AS  DISTRIBUTION(Zee)  OF  Potential       # Solid phase potential
    Phi2            AS  DISTRIBUTION(Zee)  OF  Potential       # Ionomer phase
potential
    activity        AS  DISTRIBUTION(Zee)  OF  Activity        # Activity of water in
ionomer
    lambda          AS  DISTRIBUTION(Zee)  OF  WaterContent    # Ratio of water to
protons in ionomer
    q               AS  DISTRIBUTION(Zee)  OF  ChargeDensity   # Double layer charge
(per unit volume)
    jevap           AS  DISTRIBUTION(zee)  OF  VolumeRate      # Rate of water
evaporation from the ionomer
    Temp            AS  DISTRIBUTION(Zee)  OF  Temperature
    qh              AS  DISTRIBUTION(Zee)  OF  HeatFlux
    p_vap           AS  DISTRIBUTION(Zee)  OF  Pressure        # Vapor pressure (a
function of temperature)
    Dij AS ARRAY(NGasComp, NGasComp) OF DiffusionCoefficient
    p_g             AS  DISTRIBUTION(NGasComp, Zee)  OF  Pressure  # Partial pressure
of each component in the gas phase
    p_O2_i          AS  DISTRIBUTION(Zee)  OF  Pressure        # Partial pressure of
oxygen at the interface between film and agglomerate core
    N_g             AS  DISTRIBUTION(NGasComp, Zee)  OF  Flux      # Flux of each
component in the gas phase
    P               AS  Pressure

    # Oxide Layer (Erin's model)
    Ox_x            AS  DISTRIBUTION(DelMu, Zee)    OF  Coverage
    Ox_xe           AS  DISTRIBUTION(DelMu, Zee)    OF  Coverage
    Ox_dxdt         AS  DISTRIBUTION(DelMu, Zee)    OF  Normalized
    Ox_dxedt        AS  DISTRIBUTION(DelMu, Zee)    OF  Normalized
    Ox_psi          AS  DISTRIBUTION(DelMu)         OF  Heterogeneity
    Ox_psie         AS  DISTRIBUTION(DelMu)         OF  Heterogeneity
#    Ox_ratePX       AS  DISTRIBUTION(DelMu, Zee)    OF
    Ox_RemainingSites   AS  DISTRIBUTION(Zee)           OF  Coverage
```

```
    Ox_thetaOH      AS  DISTRIBUTION(Zee)           OF  Coverage
    Ox_thetaPtO2    AS  DISTRIBUTION(Zee)           OF  Coverage
    Ox_thetaPtO2e   AS  DISTRIBUTION(Zee)           OF  Coverage
    Ox_current      AS  DISTRIBUTION(Zee)           OF  CurrentDensity

#    Ox_thetaV       AS  DISTRIBUTION(Zee)           OF
{
    Ox_xe           AS  DISTRIBUTION(DelMu, Zee)    OF  Coverage
    Ox_psie         AS  DISTRIBUTION(DelMu)         OF  Heterogeneity
    Ox_thetaedge    AS  DISTRIBUTION(Zee)           OF  Coverage
}

    # Concentration dependent transport properties
    kappa           AS  DISTRIBUTION(Zee)  OF  Conductivity    # Conductivity of
ionomer as a function of water content and temperature
    D_w             AS  DISTRIBUTION(Zee)  OF  DiffusionCoefficient # Diffusion
coefficient of water in ionomer as a function of water content and temperature
    xi              AS  DISTRIBUTION(Zee)  OF  TransportNumber # Electroosmotic drag
coefficient of water in ionomer as a function of water content and temperature

    initfactor      AS  Normalized

    thiele          AS  DISTRIBUTION(Zee)  OF  Normalized       # Agglomerate thiele
modulus
    effectiveness   AS  DISTRIBUTION(Zee)  OF  Normalized       # Agglomerate
Effectiveness factor
    rate_constant   AS  DISTRIBUTION(Zee)  OF  VolumeRateConstant # ORR rate constant
such that r(ORR in core) = -rate_constant*P_O2 ;

    tortuosity      AS  DISTRIBUTION(Zee)  OF  Normalized # Ionomer tortuosity
#    n_calc          AS  Normalized


SET
    a_pt    := (ECA*loading*10)/(L*(1-epsilon_g)*(1-th_film/R_agg)^3) ; # Calculated as
surface area of Pt (per MEA area) / Volume of agglomerate core (per MEA area) or
roughness / (thickness * volume fraction of active agglomerate core)
    porosity_agg := (epsilon_e/(1-epsilon_g)-1)/(1-th_film/R_agg)^3+1; # Calculate the
volume fraction of ionomer in the agglomerate core considering the film is pure
ionomer, and the total ionomer loading is known.
#    tort_agg := porosity_agg^(-0.5);

BOUNDARY
# Boundary condition equations
#   There are N+2 balance equations applied only at the interior, so 2N+4 boundary
conditions are needed
#   For N=3 (typical) this is 10 conditions
#   2 Zero current conditions (i1 at membrane & i2 at GDL)
#   N-1 (2) Zero gas flux equations at membrane interface
#   1 Gas phase continuity equation at either boundary
#   2 Potentials or 1 potential and 1 current
#   1 Membrane interfacial lambda
#   N-1 (2) GDL interfacial partial pressures
    i1(0) = 0 ;
    i2(L) = 0 ;
    N_g(2:NGasComp,0) = 0 ;
    SIGMA(PARTIAL(N_g(,L), Zee)) = jevap(L)+(s_w+s_ox)*j(L) ; # Continuity equation

#   When we equate variables across an interface, it basically counts as half a
boundary condition
#   So these ten equations become five boundary conditions.
```

```
    mem_interface.i2        =   i2(0)   ;
    mem_interface.phi2      =   phi2(0) ;
    mem_interface.N_w       =   N_w(0)+N_g(1,0)  ;
    mem_interface.activity  =   activity(0)   ;

    GDL_interface.i1    =   i1(L)   ;
    GDL_interface.phi1  =   phi1(L) ;
    GDL_interface.x(1:NGasComp-1)   =   p_g(1:NGasComp-1,L)/P ;
    GDL_interface.N_g(1)=   N_w(L)+N_g(1,L) ;
    GDL_interface.N_g(2:NGasComp)=   N_g(2:NGasComp,L) ;
#    -PARTIAL(N_w(0), Zee) = jevap(0) ;
#    -PARTIAL(N_w(L), Zee) = jevap(L) ;
    1e-6*PARTIAL(jevap(0), Zee, Zee) = 0;
    1e-6*PARTIAL(jevap(L), Zee, Zee) = 0;


    GDL_interface.P     = P ;

    GDL_interface.Temp = Temp(L);
    mem_interface.Temp = Temp(0);
#    GDL_interface.qh   = -k*PARTIAL(Temp(L), Zee)-N_w(L)*dHvap;
#    mem_interface.qh-N_g(1,0)*dHvap = -k*PARTIAL(Temp(0), Zee);
    GDL_interface.qh   = (qh(L)-N_w(L)*dHvap);
    (mem_interface.qh-N_g(1,0)*dHvap) = qh(0);


EQUATION
# Heat balance
# Interestign thing here. If the cp*rho term at the end is 1e8 (J/m3K), I have no
problems at all. If the cp*rho term is 1e6, I can't get past about 3.5 A/m2/s ramp
rate. Also, the failure seems to be triggered by the changeover from constant to
stoichiometric flow rates.

    4000*(-L^2*PARTIAL(qh(0|+:L|-), Zee) + L^2*n*F*j(0|+:L|-)*(Phi1(0|+:L|-)-
Phi2(0|+:L|-)-(UHov+UHRHE)) - L^2*i2(0|+:L|-)*PARTIAL(Phi2(0|+:L|-), Zee) -
L^2*i1(0|+:L|-)*PARTIAL(Phi1(0|+:L|-), Zee) -L^2*jevap(0|+:L|-)*dHvap)=
4000*L^2*cprho*$Temp(0|+:L|-) ;#10*L^2*dHvap*epsilon_g/(R*Temp(0|+:L|-))*p_g(1,0|+:L|-
)*3816.44*(Temp(0|+:L|-)-46.13)^(-2)*$Temp(0|+:L|-) ;
    10000*L*qh = -10000*L*k*PARTIAL(Temp, Zee) ;

# Flooded agglomerate equations and oxide layer
    FOR z:= 0 TO L DO
    # Oxide layer first
    Ox_thetaPtO2(z) = INTEGRAL(dMu := -3*sigMu:3*sigMu; Ox_x(dMu,z));
    Ox_thetaPtO2e(z) = INTEGRAL(dMu := -3*sigMu:3*sigMu; Ox_xe(dMu,z));
    Ox_RemainingSites(z) = exp(-chi*(Ox_thetaPtO2(z) + edgefrac/(1-
edgefrac)*Ox_thetaPtO2e(z)));
    Ox_thetaOH(z) = (1 - Ox_thetaOH(z))*EXP(F/R/T*(phi1(z)-phi2(z)-U_OH) -
wOH/R/T*Ox_thetaOH(z)^2) ;
    #LOG(Ox_thetaOH(z)) = LOG((1 - Ox_thetaOH(z)))+(F/R/T*(phi1(z)-phi2(z)-U_OH) -
wOH/R/T*Ox_thetaOH(z)^2) ;
    FOR dMu := -3*sigMu TO 3*sigMu DO
        1*Ox_dxdt(dMu,z)/kOx =
1*(MAX(Ox_thetaOH(z),0)*MAX(Ox_RemainingSites(z),0)*Ox_psi(dMu)*EXP(-
(wPtO2*Ox_x(dMu,z)/Ox_psi(dMu) + alphaHet*dMu - wOH*Ox_thetaOH(z)^2)/R/T +
alphaOxa*F/R/T*(phi1(z)-phi2(z)-U_PtO2)) - MAX(Ox_x(dMu,z),0)*exp((1-alphaHet)*dMu/R/T
- alphaOxc*F/R/T*(phi1(z)-phi2(z)-U_PtO2))) ;
        $Ox_x(dMu,z)*1e6 = Ox_dxdt(dMu,z)*1e6;
        1*Ox_dxedt(dMu,z)/kOxe = 1*((Ox_psie(dMu)*EXP(-
(wPtO2e*Ox_xe(dMu,z)/Ox_psie(dMu) + alphaHet*dMu)/R/T + alphaOxae*F/R/T*(phi1(z)-
```

```
phi2(z)-U_PtO2e)) - MAX(Ox_xe(dMu,z),0)*exp((1-alphaHet)*dMu/R/T -
alphaOxce*F/R/T*(phi1(z)-phi2(z)-U_PtO2e)))) ;
        $Ox_xe(dMu,z)*1e6 = Ox_dxedt(dMu,z)*1e6;
#        $Ox_x(dMu,z)/kOx = Ox_thetaOH(z)*Ox_RemainingSites(z)*Ox_psi(dMu)*EXP(-
(wPtO2*Ox_thetaPtO2(z) - wOH*Ox_thetaOH(z)^2)/R/T + alphaOxa*F/R/T*(phi1(z)-phi2(z)-
U_PtO2)) - Ox_x(dMu,z)*exp(dMu/R/T - alphaOxc*F/R/T*(phi1(z)-phi2(z)-U_PtO2)) ;
#        $Ox_xe(dMu,z)/kEdge = Ox_psie(dMu)*EXP(-wedge*Ox_xe(dMu,z)/Ox_psie(dMu) +
alphaEda*F/R/T*(phi1(z)-phi2(z)-U_Edge)) - Ox_xe(dMu,z)*exp(dMu/R/T -
alphaEdc*F/R/T*(phi1(z)-phi2(z)-U_Edge)) ;

    END
    Ox_current(z) = 4*2.1*INTEGRAL(dMu := -3*sigMu:3*sigMu ; Ox_dxdt(dMu,z)*(1-
edgefrac)+edgefrac*Ox_dxedt(dMu,z)) ;
#    Ox_current(z)/kOx = 4*2.1*INTEGRAL(dMu := -2.5*sigMu:2.5*sigMu ;
(Ox_thetaOH(z)*Ox_RemainingSites(z)*Ox_psi(dMu)*EXP(-(wPtO2*Ox_x(dMu,z)/Ox_psi(dMu) +
alphaHet*dMu - wOH*Ox_thetaOH(z)^2)/R/T + alphaOxa*F/R/T*(phi1(z)-phi2(z)-U_PtO2)) -
Ox_x(dMu,z)*exp((1-alphaHet)*dMu/R/T - alphaOxc*F/R/T*(phi1(z)-phi2(z)-U_PtO2)))) ;
#
(Ox_thetaOH(z)*Ox_RemainingSites(z)*Ox_psi(dMu)*EXP(-(wPtO2*Ox_x(dMu,z)/Ox_psi(dMu) +
alphaHet*dMu - wOH*Ox_thetaOH(z)^2)/R/T + alphaOxa*F/R/T*(phi1(z)-phi2(z)-U_PtO2)) -
Ox_x(dMu,z)*exp((1-alphaHet)*dMu/R/T - alphaOxc*F/R/T*(phi1(z)-phi2(z)-U_PtO2)))
        {LOG}(1e5^m_ORR/a_pt*rate_constant(z)/k0) =
{LOG}({activity(z)*}Ox_RemainingSites(z)*(1-Ox_thetaOH(z)))*exp(-
alpha_c/2*n*F/(R*T)*(phi1(z)-phi2(z)-U)) ;
#        LOG(1e5/a_pt*rate_constant(z)/k0) =
LOG(activity(z)*SQRT(1e5/p_g(2,z))*EXP(30000/R*(1/353-1/Temp(z)))*EXP(-
alpha_c*n*F/(R*T)*(0.78-U))/(EXP(alpha_c*n*F/(R*T)*(phi1(z)-phi2(z)-
0.78))+EXP(alpha_c*n*F/(2*R*T)*(phi1(z)-phi2(z)-0.78)))) ;
#        LOG(1e5/a_pt*rate_constant(z)/k0) = LOG(activity(z)*EXP(-
alpha_c*n*F/(R*T)*(0.78-U))/(EXP(alpha_c*n*F/(R*T)*(phi1(z)-phi2(z)-
0.78))+EXP(alpha_c*n*F/(2*R*T)*(phi1(z)-phi2(z)-0.78)))) ;
#        LOG(1e5/a_pt*rate_constant(z)/k0) = LOG(EXP(-alpha_c*n*F/(R*T)*(0.78-
U))/(EXP(alpha_c*n*F/(R*T)*(phi1(z)-phi2(z)-0.78))+EXP(alpha_c*n*F/(2*R*T)*(phi1(z)-
phi2(z)-0.78)))) ;
        #thiele(z) = (R_agg-
th_film)*sqrt((m_ORR+1)/2*abs(H*tort_agg*s_ox*rate_constant(z)*p_g(2,z)^(m_ORR-
1)/(porosity_agg*D_O2_I)));
#        thiele(z) = (R_agg-
th_film)*sqrt((m_ORR+1)/2*abs(H*tort_agg*s_ox*rate_constant(z)*p_g(2,z)^(m_ORR-
1)/(porosity_agg*D_O2_I*exp(LOG(2)*activity(z))/2)));
#        effectiveness(z) = 3/thiele(z)^2*(thiele(z)/TANH(thiele(z))-
1)/(1+th_film/R_agg*porosity_agg/tort_agg*(thiele(z)/TANH(thiele(z))-1)) ;
#        (F*L/1000)*j(z) = (F*L/1000)*(-
effectiveness(z)*rate_constant(z)*p_g(2,z)^m_ORR*(1-epsilon_g)*(1-th_film/R_agg)^3) ;
        -s_ox*j(z)*R_agg/3/(1-epsilon_g) = (p_g(2,z) -
p_o2_i(z))/H*D_O2_I{*exp(LOG(2)*activity(z))/2}*(1/th_film - 1/R_agg) ;
        0.01*thiele(z) = 0.01*(R_agg-
th_film)*sqrt((m_ORR+1)/2*abs(H*tort_agg*s_ox*rate_constant(z)*MAX(p_o2_i(z),1e-
5)^(m_ORR-1)/(porosity_agg*D_O2_I{*exp(LOG(2)*activity(z))/2})));
        effectiveness(z) = 3/thiele(z)^2*(thiele(z)/TANH(thiele(z))-1) ;
        (F*L/1000)*j(z) = (F*L/1000)*(-
effectiveness(z)*rate_constant(z)*MAX(p_o2_i(z),0)^m_ORR*(1-epsilon_g)*(1-
th_film/R_agg)^3) ;
#

# Fake a half order reaction
#        (F*L/1000)*j(z) = (F*L/1000)*(-
effectiveness(z)*rate_constant(z)*sqrt(p_g(2,z))*sqrt(1e5)*(1-epsilon_g)*(1-
th_film/R_agg)^3) ;
    END
```

```
# Model equations - Numbering based on 3 gas phase components
# Trying a different organization scheme. The old scheme is at the bottom commented
out.
####################################################
### Balance equations: Mass and current balances ###
####################################################
#   These equations are applied at the interior only (i.e. only over volume elements,
not boundaries)
    FOR z:= 0|+ TO L|- DO
        # Equation 1:       Electrolyte current balance
#        (L/100)*PARTIAL(i2(z), Zee) = (L/100)*(n*F*j(z)+$q(z)) ;
        (L/100)*PARTIAL(i2(z), Zee) =
(L/100)*(n*F*j(z)+$q(z)+Ox_current(z)*ECA*loading*10/L) ;
        # Equation 2:       Solid phase current balance
#        (L/100)*PARTIAL(i1(z), Zee) = (L/100)*(-n*F*j(z)-$q(z)) ;
        (L/100)*PARTIAL(i1(z), Zee) = -(L/100)*PARTIAL(i2(z), Zee) ;
        # Equation 3:       Mass balance on water for both phases (assuming they are in
equilibrium)
#        (L/(100/F))*(epsilon_g*$p_g(1,z)/(R*T) + epsilon_e*rho_n/EW*$lambda(z)) =
(L/(100/F))*(-PARTIAL(N_w(z), Zee) - PARTIAL(N_g(1,z), Zee) + s_w*j(z)) ;
        (L/(100/F))*(epsilon_g*$p_g(1,z)/(R*T)) = (L/(100/F))*(-PARTIAL(N_g(1,z), Zee)
+ s_w*j(z) + jevap(z)) ;
        # Equation 4:       Mass balance on oxygen (gas phase)
        (L/(100/F))*(epsilon_g*$p_g(2,z)/(R*T)) = (L/(100/F))*(-PARTIAL(N_g(2,z), Zee)
+ s_ox*j(z));
        # Equation 5+:      Remaining gas species mass balances
        FOR i:= 3 TO NGasComp DO
            (L/(100/F))*(epsilon_g*$p_g(i,z)/(R*T)) = (L/(100/F))*(-PARTIAL(N_g(i,z),
Zee)) ;
        END
#    END
#    FOR z:= 0 TO L DO
        # Water evaporation rate
# + epsilon_g/(R*Temp(z))*p_g(1,z)*3816.44*(Temp(z)-46.13)^(-2)*$Temp(z)
        (L/(100/F))*(epsilon_e*rho_n/EW*$lambda(z)) = (L/(100/F))*(-PARTIAL(N_w(z),
Zee) - jevap(z)) ;
    END
    #   For 3 gas phase species, there are 5 balance equations, so 10 boundary
conditions are needed. See BOUNDARY section.

#   Everything else: These equations apply everywhere, including the boundaries
    FOR z:= 0 TO L DO
        #################################################
        ### Transport equations: All phases           ###
        ### Ionomer:     Concentrated solution theory ###
        ### Gas phase:   Stefan-Maxwell diffusion     ###
        ### Solid phase: Simple Ohm's law             ###
        #################################################
        # Equation 6:       Ionomer flux of water (Concentrated solution theory)
        #(1/(1000/F))*N_w(z) = (1/(1000/F))*epsilon_e^1.5*(-
(kappa(z)*xi(z)/F)*PARTIAL(phi2(z), Zee) - (D_w(z)*rho_n/EW*(17.81-
2*39.85*activity(z)+3*36.0*activity(z)^2)/(EW/(EW+lambda(z)*MW_w)) +
R*T*kappa(z)*xi(z)^2/F^2/activity(z))*PARTIAL(activity(z), Zee)) ;
#        N_w(z)/epsilon_e^1.5 = -(kappa(z)*xi(z)/F)*PARTIAL(phi2(z), Zee) -
(D_w(z)*lambda(z)/(lambda(z)*MW_w/rho_w+EW/rho_n)/(R*T) +
kappa(z)*xi(z)^2/F^2)*R*T*PARTIAL(activity(z), Zee)/activity(z) ;
```

```
        # ERROR!! There was a sign error here, which was fixed on 2015-04-13. Used to
be +2*39.85*activity(z), but definitely should be -2*39.85*activity(z).
        (1/(10000/F))*N_w(z) = (1/(10000/F))*epsilon_e/tortuosity(z)*(-
(kappa(z)*xi(z)/F)*PARTIAL(phi2(z), Zee) -
(D_w(z)*rho_n*rho_w/(EW*rho_w+lambda(z)*rho_n*MW_w)*(17.81-
2*39.85*activity(z)+3*36.0*activity(z)^2) +
R*T*kappa(z)*xi(z)^2/F^2/activity(z))*PARTIAL(activity(z), Zee) );
        # Equation 7:       Ionomer proton flux - modified Ohm's law (Concentrated
solution theory)
        1/10000*i2(z) = 1/10000*epsilon_e/tortuosity(z)*(-kappa(z)*PARTIAL(phi2(z),
Zee) - (kappa(z)*xi(z)/F)*R*T*PARTIAL(activity(z), Zee)/activity(z)) ;
        # Equations 8 & 9+: Gas phase flux (Stefan-Maxwell equations)
        FOR i:= 1 TO NGasComp-1 DO
            # 1e5 is the reference pressure for the diffusion coefficient (see GDL
explanation)
            (1e-5/(P*1000/F))*1e5/(R*T)*(epsilon_g^1.5)*PARTIAL(p_g(i,z), Zee) = (1e-
5/(P*1000/F))*SIGMA((p_g(i,z)*N_g(,z)-p_g(,z)*N_g(i,z))/D_g_ij(i,));
        END
        # Equation 10:      Solid phase electron transport (Ohm's law)
        1e-3*i1(z) = 1e-3*(-sig*PARTIAL(phi1(z), Zee));

        ######################
        ### Thermodynamics ###
        ######################
        # Equation 12:      Equation of state for water
        # From Zawodzinski via Fuller's Thesis
        #activity(z) = -0.0505+0.1853*lambda(z)-0.01049*lambda(z)^2+1.712e-
4*lambda(z)^3;
        lambda(z) = 0.043 + 17.81*activity(z) - 39.85*activity(z)^2 +
36.0*activity(z)^3 ;
        # Equation 14:      Water is at equilibrium with the electrolyte phase
        # Note that both phases are actually included in the water mass balance
(Equation 1)
        activity(z) = p_g(1,z) / p_vap(z) ;
        # Equation 15:      Constant total pressure in gas phase - kind of
thermodynamics
        SIGMA(p_g(,z))/P = 1 ;

        10*q(z)/(c*ECA*Loading*10/L) = 10*(Phi1(z)-
Phi2(z)+1/c*Ox_RemainingSites(z)*Ox_ThetaOH(z)*2.1*(1-edgefrac)) ;

        ######################################################
        ### Transport properties (concentration dependent) ###
        ######################################################
        # Equation 17:      Ionomer conductivity (from Springer via Fuller's Thesis)
#        kappa(z) = 100*(0.005139*lambda(z)-0.00326)*EXP(1268*(1/303-1/T)) ; # S/m,
original equation had units of S/cm
# Increased activation energy
#        kappa(z) = 100*(0.005139*(lambda(z)^2/20)-0.00326)*EXP(1268*(1/303-1/T)) ; #
S/m, original equation had units of S/cm
            #kappa(z) = 0.4*exp(3.2*activity(z))*EXP(1268*(1/303-1/T));
#            kappa(z) = 2*0.4*exp(7*activity(z)-3.8)*EXP(1268*(1/303-1/T));
        kappa(z) = 1.551*exp(2.1954*activity(z))*EXP(1268*(1/353-1/T)) ; # S/m
Experimental, with literature activation energy



#        kappa(z) = 100*(0.005139/70*exp(7.67*activity(z)))*EXP(1268*(1/303-1/T)) ; #
S/m, original equation had units of S/cm
```

```
#        kappa(z) = 100*(0.005139*(0.7*lambda(z)+lambda(z)^2/14)-
0.00326)*EXP(1268*(1/303-1/T)) ; # S/m, original equation had units of S/cm
        # Equation 18:      Diffusion coefficient of water in ionomer (Fuller's thesis)
        # Fuller
        D_w(z)*1e9 = initfactor*1e9*1e-4*3.5e-2*EXP(-2436/T)*lambda(z)/14 ; # m^2/s,
original equation had units of cm^2/s
        # Mittelsteadt
#        D_w(z)*1e9 = 1e9*1e-4*EXP(-2436/T)*MIN(7.32e-4*exp(0.12*lambda(z))+5.41e-
6*exp(1.44*lambda(z)), 1.58e5*exp(-4.66*lambda(z))+1.45e-3*exp(0.04*lambda(z))) ; #
m^2/s, original equation had units of cm^2/s

        tortuosity(z) = 2.69853*exp(-1.21103*activity(z));

        # Equation 19:      Electroosmotic drag coefficient (informed by my own
experiments, but just a rough approximation pending better data and fitting)
        xi(z) = 1.1 + 0.9/(1+EXP(-2*(lambda(z)-5.5))) ; # Based on my concentration
cell results, a sigmoidal going from 1.1 to 2.0 with a break point at lambda = 5.5

        p_vap(z)/1e5 = exp(11.6832-3816.44/(Temp(z)-46.13)) ;
    END
    #n_calc = i1(L)/(F*N_g(2,L)) ;

ASSIGN
    FOR dMu := -3*sigMu TO 3*sigMu DO
        Ox_psi(dMu) := exp(-dMu^2/(2*sigMu^2)) /
        #              ----------------------
                       (SQRT(2*pi)*sigMu) ;

        Ox_psie(dMu) := exp(-dMu^2/(2*sigMuE^2)) /
        #              ----------------------
                       (SQRT(2*pi)*sigMuE) ;

    END
    Dij := D_g_ij;

PRESET
    thiele(0:L) := 0.1 ;
    phi1(0:L) := 0.8 ;
    phi2(0:L) := -0.001 ;
    tortuosity := 1;
    Ox_RemainingSites := 0.01;

END # MODEL CathodeElectrode_SSAggNewHeat_wOxide

MODEL POP_74714c::FRA # PEMFC - One Phase 2014-06-17:FRA

# FRA (Frequency Response Analyzer) does impedance spectroscopy on other models.
# It has two ports which need to be connected to the model under test. Connect it just
like you would a real fuel cell or battery.
# The TestLead port just has two variables: current and voltage

PORT
    PositiveTerminal AS TestLead
    NegativeTerminal AS TestLead

VARIABLE
    VCell           AS  Potential               # Volts
    ICell           AS  CurrentDensity          # A/m2
    ExcitationRe    AS  Normalized
    ExcitationIm    AS  Normalized
    VAC             AS  Potential
```

```
    IAC             AS  CurrentDensity
    VDC             AS  Potential
    IDC             AS  CurrentDensity
    VRe             AS  IntegratedVoltage
    VIm             AS  IntegratedVoltage
    IRe             AS  CurrentDensity
    IIm             AS  CurrentDensity
    ZRe             AS  Impedance               # Ohms*cm2 (note cm not m)
    negZIm          AS  Impedance               # -Z" so that the Nyquist plots don't
look upside down
    ZMag            AS  Impedance
    Phase           AS  Phase
    Freq            AS  Freq

EQUATION
    VCell = PositiveTerminal.V-NegativeTerminal.V ;
    ICell = NegativeTerminal.I ;
    ICell = PositiveTerminal.I ;
    # Split the cell voltage and current into AC and DC components. One of these must
be assigned.
    # During equilibration, we set the AC component to 0, so VCell=VDC.
    # Then, we fix VDC and IDC at their post equilibration values, so that VAC and IAC
are just the oscillations
    # This all happens in the Process and Task
    VAC+VDC = VCell ;
    IAC+IDC = ICell ;

    # To calculate impedance, we need the real and imaginary components of the voltage
and current responses
    # We get these by multiplying by sine or cosine and integrating.
    $VRe = freq*VAC * ExcitationRe ;
    $VIm = freq*VAC * ExcitationIm ;
    $IRe = freq*IAC * ExcitationRe ;
    $IIm = freq*IAC * ExcitationIm ;

    # Now we just need to calculate impedance from the voltage and current responses.
Z=V/I
    IF (IRe^2+IIm^2) > 0 THEN   # We don't want to divide by zero when the FRA is off
(like during equilibration)
    ZRe = -10000*(VRe*IRe+VIm*IIm)/(IRe^2+IIm^2) ;      # 10000 is a conversion factor
so Z is in Ohm*cm2
    negZIm = 10000*(-VRe*IIm+VIm*IRe)/(IRe^2+IIm^2) ;
    Phase = 0;#ATAN(-negZIm/MAX(ZRe,1e-10)) ;
    ELSE
    ZRe = 0 ;
    negZIm = 0 ;
    Phase = 0 ;
    END
    ZMag = SQRT(ZRe^2+negZIm^2) ;
END # MODEL FRA

{
No gas phase. Only the necessary variables (plus a couple for convenience)

}
MODEL POP_74714c::GDLwContinuityandLiquidNewHeat # PEMFC - One Phase 2014-06-
17:GDLwContinuityandLiquidNewHeat

# Gas diffusion layer with very poorly implemented liquid water. This keeps water from
building up beyond its vapor pressure in the GDL
```

```
# If the partial pressure of water exceeds the vapor pressure, water condenses and
moves out of the GDL very quickly.
# The liquid water does not interfere with gas transport. I do not attempt to model
liquid water realisitically.

PARAMETER
    # Fundamental Constants
    R                AS  REAL  DEFAULT  8.3145       # J/mol*K, Ideal gas constant

    # Physical parameters of the gas diffusion layer
    L                AS  REAL            # GDL thickness
    epsilon_g        AS  REAL            # Volume fraction of gas pore space in
electrode
    tortuosity       AS  REAL            # Tortuosity for gas phase transport

    # Other
    sig              AS  REAL            # Solid phase electronic conductivity
    T                AS  REAL            # Temperature
    k                AS  REAL            # Thermal Conductivity

    # Gas phase stuff
    NGasComp         AS  INTEGER         # Number of gas phase components. We need at
least 2, water and oxygen, which are components 1 and 2 respectively
    D_g_ij           AS  ARRAY(NGasComp, NGasComp)  OF  REAL  # Stefan-Maxwell
diffusivities
#    P                AS  REAL            # Total gas pressure
    p_vap            AS  REAL            # Vapor Pressure
    cprho            AS  REAL  DEFAULT 4.6e5 # J/m3, Volumetric heat capacity of GDL,
based on specified density, compressed to 140 um, with 5% PTFE

DISTRIBUTION_DOMAIN
    Zee              AS  [0 : L]         # One dimensional problem

PORT
    right AS GDLPortNewHeat           # GDL flowfield interface
    left AS GDLPortNewHeat          # Catalyst layer GDL interface

VARIABLE
    i1               AS  CurrentDensity  # Current
    Phi1_0, Phi1_L   AS  Potential       # Potential at both ends of GDL
    p_g              AS  DISTRIBUTION(NGasComp, Zee)  OF  Pressure  # Partial pressure
of each gas component
    N_g              AS  DISTRIBUTION(NGasComp, Zee)  OF  Flux      # Flux of each gas
component
    N_w_L            AS  DISTRIBUTION(Zee)            OF  Flux      # Flux of liquid
water
    P                AS  Pressure
    Temp             AS  DISTRIBUTION(Zee)            OF  Temperature

BOUNDARY
# Interfaces
    left.i1    =   i1   ;
    left.phi1  =   phi1_0 ;
    left.x     =   p_g(1:NGasComp-1,0)/P ;
    left.N_g(2:NGasComp) =   N_g(2:NGasComp,0) ;
    left.N_g(1) =  N_g(1,0)+N_w_L(0) ;
    PARTIAL(N_w_L(0), Zee)   = 0 ;
    left.P     =   P;
    left.Temp  =   Temp(0) ;
    left.qh    =   -k*PARTIAL(Temp(0), Zee) ;
```

```
    right.i1    =   i1   ;
    right.phi1  =   phi1_L ;
    right.x   =   p_g(1:NGasComp-1,L)/P ;
    right.N_g(2:NGasComp) =   N_g(2:NGasComp,L) ;
    right.N_g(1) =  N_g(1,L)+N_w_L(L) ;
    PARTIAL(N_w_L(L), Zee) = 0 ;
    right.P    =    P;
    right.Temp =    Temp(L) ;
    right.qh   =   -k*PARTIAL(Temp(L), Zee) ;

EQUATION
# Model equations - Numbering based on 3 gas phase components
    L^2*k*PARTIAL(Temp(0|+:L|-), Zee, Zee) - L*i1*(Phi1_L-Phi1_0) =
L^2*cprho*$Temp(0|+:L|-);
    FOR z:= 0|+ TO L|- DO
        # Equation 1+: Gas species mass balances for N-2 components
        FOR i:= 2 TO NGasComp-1 DO
            epsilon_g*$p_g(i,z)/(R*T) = -PARTIAL(N_g(i,z), Zee);
        END
        # Equation 2: Water mass balance (includes liquid flux)
        epsilon_g*$p_g(1,z)/(R*T) = -PARTIAL(N_g(1,z)+N_w_L(z), Zee);
        # Equation 3: Liquid water flux. It acts like the vapor but using d((p-
pvap)^2)/dz instead of dp/dz. Since p is in Pa, the driving force gets very large very
fast. (It's a stupid hack)
        N_w_L(z) = -D_g_ij(1,1)*PARTIAL(MAX(p_g(1,z),p_vap)^2-
2*MAX(p_g(1,z),p_vap)*p_vap, Zee)/(R*T) ;
    END
    FOR z:= 0 TO L|- DO
        # Equation 4: Continuity
        SIGMA(PARTIAL(N_g(,z), Zee))+PARTIAL(N_w_L(z), Zee) = 0 ;
    END
    FOR z:= 0 TO L DO
        # Equations 5 & 6+: Gas phase flux (Stefan-Maxwell equations)
        FOR i:= 1 TO NGasComp-1 DO
            # The extra P/1e5 term on the RHS is to adjust the diffusion coefficients
for their pressure dependence
            L/P*PARTIAL(p_g(i,z), Zee) =
L*R*T/P/1e5*tortuosity/epsilon_g*SIGMA((p_g(i,z)*N_g(,z)-p_g(,z)*N_g(i,z))/D_g_ij(i,));
        END
        # Equation 7: Constant total pressure in gas phase - kind of thermodynamics
        SIGMA(p_g(,z)) = P ;
    END
    # Equation 8: Solid phase electron transport (Ohm's law)
    i1 = -sig*(phi1_L-phi1_0)/L;

END # MODEL GDLwContinuityandLiquidNewHeat

MODEL POP_74714c::MembraneNewHeat # PEMFC - One Phase 2014-06-17:MembraneNewHeat

PARAMETER
    # Fundamental Constants
    F               AS  REAL  DEFAULT  96485        # C/mol, Faraday's Constant
    R               AS  REAL  DEFAULT  8.3145       # J/mol*K, Ideal gas constant

    # Physical parameters of electrode
    L               AS  REAL            # Electrode thickness
    T               AS  REAL            # Temperature
    EW, rho_n       AS  REAL            # Equivalent weight and density of dry nafion
    MW_w, rho_w     AS  REAL            # Molecular weight and density of water
    k               AS  REAL            # Thermal conductivity of membrane
```

```
    cprho           AS  REAL    DEFAULT 2.5E6 # J/m3, Volumetric heat capacity of
Nafion, assumed equal to PTFE (1.26 J/gK)

DISTRIBUTION_DOMAIN
    Zee             AS  [0 : L]         # One dimensional problem

PORT
    leftside        AS IonomerPortNewHeat
    rightside       AS IonomerPortNewHeat

VARIABLE
    N_w             AS  DISTRIBUTION(Zee)  OF  Flux            # Flux of water
    i2              AS  CurrentDensity                         # Ionic current
    Phi2            AS  DISTRIBUTION(Zee)  OF  Potential       # Membrane potential
    activity        AS  DISTRIBUTION(Zee)  OF  Activity        # Activity of water
    lambda          AS  DISTRIBUTION(Zee)  OF  WaterContent    # Ratio of water to
protons
    Temp            AS  DISTRIBUTION(Zee)  OF  Temperature
#    qh              AS  DISTRIBUTION(Zee)  OF  HeatFlux

    # Concentration dependent transport properties
    kappa           AS  DISTRIBUTION(Zee)  OF  Conductivity    # Conductivity of
ionomer as a function of water content and temperature
    D_w             AS  DISTRIBUTION(Zee)  OF  DiffusionCoefficient # Diffusion
coefficient of water in ionomer as a function of water content and temperature
    xi              AS  DISTRIBUTION(Zee)  OF  TransportNumber # Electroosmotic drag
coefficient of water in ionomer as a function of water content and temperature
    initfactor      AS  Normalized
    mem_res         AS  Impedance
    mem_ir          AS  Potential

BOUNDARY
    activity(0) = leftside.activity   ;
    N_w(0)      = leftside.N_w  ;
    i2          = leftside.i2   ;
    phi2(0)     = leftside.phi2 ;
    activity(L) = rightside.activity   ;
    N_w(L)      = rightside.N_w  ;
    i2          = rightside.i2   ;
    phi2(L)     = rightside.phi2 ;

    leftside.Temp  = Temp(0) ;
    rightside.Temp = Temp(L) ;
    leftside.qh    = -k*PARTIAL(Temp(0), Zee);
    rightside.qh   = -k*PARTIAL(Temp(L), Zee);

EQUATION
# Model equations - Numbering based on 3 gas phase components
   L^2*k*PARTIAL(Temp(0|+:L|-), Zee, Zee) - L^2*i2*PARTIAL(Phi2(0|+:L|-), Zee) =
L^2*cprho*$Temp(0|+:L|-);
#    qh = -k*PARTIAL(Temp, Zee);
# Equation 1: Mass balance on water. Applied at the interior only (i.e. only over
volume elements, not boundaries)
    FOR z:= 0|+ TO L|- DO
        (L/(100/F))*rho_N/EW*$lambda(z) = -(L/(100/F))*PARTIAL(N_w(z), Zee) ;
    END
# Equation 2: Ionomer flux of water (Concentrated solution theory). Applied everywhere,
including the boundaries.
    FOR z:= 0 TO L DO
        # ERROR!! There was a sign error here, which was fixed on 2015-04-13. Used to
be +2*39.85*activity(z), but definitely should be -2*39.85*activity(z).
```

```
        (1/(100/F))*N_w(z) = (1/(100/F))*(-(kappa(z)*xi(z)/F)*PARTIAL(phi2(z), Zee) -
(D_w(z)*rho_n*rho_w/(EW*rho_w+lambda(z)*rho_n*MW_w)*(17.81-
2*39.85*activity(z)+3*36.0*activity(z)^2) +
R*Temp(z)*kappa(z)*xi(z)^2/F^2/activity(z))*PARTIAL(activity(z), Zee) );
#        N_w(z) = -(kappa(z)*xi(z)/F)*PARTIAL(phi2(z), Zee) -
(D_w(z)*lambda(z)/(lambda(z)*MW_w/rho_w+EW/rho_n)/(R*T) +
kappa(z)*xi(z)^2/F^2)*R*T*PARTIAL(activity(z), Zee)/activity(z) ;
    END
# Equation 3: Ionomer proton flux - modified Ohm's law (Concentrated solution theory).
This one is applied at one boundary but not the other.
# This makes the total number of equations work out correctly. I don't fully understand
this.
    FOR z:= 0|+ TO L DO
        (1/100)*i2 = (1/100)*(-kappa(z)*PARTIAL(phi2(z), Zee) -
(kappa(z)*xi(z)/F)*R*Temp(z)*PARTIAL(activity(z), Zee)/activity(z)) ;
    END
# Other equations that apply everywhere:
    FOR z:= 0 TO L DO
        # Equation 4:      Equation of state for water
        # From Zawodzinski via Fuller's Thesis
        #activity(z) = -0.0505+0.1853*lambda(z)-0.01049*lambda(z)^2+1.712e-
4*lambda(z)^3;
        lambda(z) = 0.043 + 17.81*activity(z) - 39.85*activity(z)^2 +
36.0*activity(z)^3 ;

        #######################################################
        ### Transport properties (concentration dependent) ###
        #######################################################
        # Equation 7:      Ionomer conductivity (from Springer via Fuller's Thesis)
#        kappa(z) = 100*(0.005139*lambda(z)-0.00326)*EXP(1268*(1/303-1/Temp(z))) ; #
S/m, original equation had units of S/cm
# Increased activation energy
#        kappa(z) = 100*(0.005139*lambda(z)-0.00326)*EXP(1268*(1/303-1/Temp(z))) ; #
S/m, original equation had units of S/cm
#        kappa(z) = 100*(0.005139/70*exp(7.67*activity(z)))*EXP(1268*(1/303-1/T)) ; #
S/m, original equation had units of S/cm
#        kappa(z) = 0.4*exp(3.2*activity(z))*EXP(1268*(1/303-1/T)) ; # S/m
        kappa(z) = 1.551*exp(2.1954*activity(z))*EXP(1268*(1/353-1/T)) ; # S/m
Experimental, with literature activation energy
#        kappa(z) = 100*(0.005139*(0.7*lambda(z)+lambda(z)^2/14)-
0.00326)*EXP(1268*(1/303-1/Temp(z))) ; # S/m, original equation had units of S/cm

#        # Testing a linear dependence on activity (not better!)
#        kappa(z) = 100*(0.005139*14*activity(z)-0.00326)*EXP(1268*(1/303-1/T)) ; #
S/m, original equation had units of S/cm

        # From Sone et al., JES Vol 143, No 4, (1996), pg 1254. Correlation is for N
form Nafion 117 at 80 C. I'm not buying this correlation!!! Do not use!
#        kappa(z) = 100*(-1.45e-3+1.57e-2*activity(z)-4.55E-2*activity(z)^2+8.86e-
2*activity(z)^3);
        # From Yang, Srinivasan, Bocarsly, Tulyani, and Benziger, Journal of membrane
science
#        kappa(z) = 1.3e-5*exp(14*activity(z)^0.2);
        # Equation 8:      Diffusion coefficient of water in ionomer (Fuller's thesis)
#        D_w(z)*1e6 = 1e6*1e-4*3.5e-2*EXP(-2436/Temp(z))*lambda(z)/14 ; # m^2/s,
original equation had units of cm^2/s
        D_w(z)*1e6 = initfactor*1e6*1e-4*3.5e-2*EXP(-2436/Temp(z))*lambda(z)/14 ; #
m^2/s, original equation had units of cm^2/s
        # Equation 9:      Electroosmotic drag coefficient (informed by my own
experiments, but just a rough approximation pending better data and fitting)
```

```
        xi(z) = 1.1 + 0.9/(1+EXP(-2*(lambda(z)-5.5))) ; # Based on my concentration
cell results, a sigmoidal going from 1.1 to 2.0 with a break point at lambda = 5.5
    END
    mem_res = INTEGRAL(z:=0:L; 1/kappa(z)) ;
    mem_ir = i2*mem_res ;
END # MODEL MembraneNewHeat

MODEL POP_74714c::ReversiblePlanarHydrogenElectrodeNewHeat # PEMFC - One Phase 2014-06-
17:ReversiblePlanarHydrogenElectrodeNewHeat

# As described, this is a 0-D hydrogen electrode with no overpotential. The ionic and
electronic potentials are set using the Nernst Equation.
# I use this for the anode instead of simulating a full porous electrode.

PARAMETER
    s_h2        AS  REAL    DEFAULT 1
    n           AS  REAL    DEFAULT 2
    F           AS  REAL    DEFAULT 96485
    R           AS  REAL    DEFAULT 8.3145
    T           AS  REAL
    dHvap       AS  REAL    DEFAULT 41714
    NGasComp    AS INTEGER
    UHRHE       AS  REAL

PORT
    GDL AS GDLPortNewHeat
    Membrane AS IonomerPortNewHeat

VARIABLE
    p_vap AS Pressure

EQUATION
    GDL.x(1) * GDL.P / p_vap = Membrane.activity ; # Water equilibrium
    GDL.i1      = Membrane.i2 ;
    GDL.N_g(1)  = Membrane.N_w ;
    GDL.N_g(2)  = s_h2*GDL.i1/(n*F) ;   # Consumption of hydrogen
    GDL.N_g(3:GDL.NGasComp) = 0 ;
    GDL.phi1 + R*GDL.Temp/(n*F)*LOG(GDL.x(2) * GDL.P / 1e5) = Membrane.phi2  ;   #
Nernst Equation

    GDL.Temp = Membrane.Temp;
    GDL.qh + GDL.N_g(1)*dHvap + GDL.i1*(GDL.Phi1-Membrane.Phi2-UHRHE) = Membrane.qh;

    p_vap = 1e5*exp(11.6832-3816.44/(GDL.Temp-46.13)) ;
END # MODEL ReversiblePlanarHydrogenElectrodeNewHeat

MODEL POP_74714c::PEMFC_SSaggnewHeatPFRwOxide # PEMFC - One Phase 2014-06-
17:PEMFC_SSaggnewHeatPFRwOxide

# This model just pieces together all of the component models into a full PEMFC

PARAMETER
    # Parameters defined here and in submodels can be set once and will propogate
through (instead of setting T, P, etc. for every layer)
    T           AS  REAL
    P           AS  REAL
    p_vap       AS  REAL
    UHov            AS  REAL DEFAULT 1.256 # Thermoneutral potential for H2 + 1/2 O2 ->
H2O
    UHRHE           AS  REAL DEFAULT 0  # Thermoneutral potential for H2 oxidation half
cell
```

```
UNIT
    AnodeBPP    AS  BPPwAccumulationHeatPFR
    AnodeGDL    AS  GDLwContinuityandLiquidNewHeat
    Anode       AS  ReversiblePlanarHydrogenElectrodeNewHeat
    Membrane    AS  MembraneNewHeat
    Cathode     AS  CathodeElectrode_SSAggNewHeat_wOxide
    CathodeGDL  AS  GDLwContinuityandLiquidNewHeat
    CathodeBPP  AS  BPPwAccumulationHeatPFR
    FRA         AS  FRA
#
VARIABLE
#    NetWaterDrag    AS  TransportNumber
#    ModeledHeatGeneration AS HeatFlux
#    TheoreticalHeatGeneration AS HeatFlux
    InterfacialPotential AS Potential
    Virfree, Virdrop, Vmemfree              AS Potential
#    NegICell    AS  CurrentDensity

SET
    AnodeBPP.StackEnd   := AnodeBPP.Left    ; # To get the flux signs right
    CathodeBPP.StackEnd := CathodeBPP.Right ; # To get the flux signs right

TOPOLOGY
    CathodeBPP.GDLinterface = CathodeGDL.right;
    CathodeGDL.left = Cathode.GDL_interface;
    Cathode.mem_interface = Membrane.rightside;
    Membrane.leftside = Anode.Membrane;
    AnodeBPP.CurrentCollector = FRA.NegativeTerminal;
    FRA.PositiveTerminal = CathodeBPP.CurrentCollector;
    AnodeGDL.right = Anode.GDL;
    AnodeGDL.left = AnodeBPP.GDLinterface;

EQUATION
#    IF FRA.ICell>10 THEN
#     #   NetWaterDrag = (AnodeBPP.N_in*AnodeBPP.p_g_in(1)/AnodeBPP.P-
(AnodeBPP.N_g_out(1)+AnodeBPP.N_w_l))/(AnodeBPP.i1/AnodeBPP.F) ;
#       NetWaterDrag = (AnodeBPP.N_in(1)-AnodeBPP.N_out(1))/(FRA.ICell/AnodeBPP.F) ;
#    ELSE
#        NetWaterDrag = 0;
#    END
    AnodeBPP.GDLinterface.i1 = AnodeBPP.CurrentCollector.I ;
#    TheoreticalHeatGeneration = (UHov-
CathodeBPP.CurrentCollector.V+AnodeBPP.CurrentCollector.V)*AnodeBPP.CurrentCollector.I;
#    ModeledHeatGeneration = -AnodeGDL.left.qh + CathodeGDL.right.qh;
    Cathode.Phi1(Cathode.L/2)-Cathode.Phi2(Cathode.L/2) = InterfacialPotential;
#    NegICell = -FRA.ICell;
    FRA.Vcell + Membrane.leftside.phi2 - Membrane.rightside.phi2 = Vmemfree ;
    FRA.Vcell + Membrane.mem_ir = Virfree ;
    Membrane.leftside.phi2 - Membrane.rightside.phi2 = Virdrop;
END # MODEL PEMFC_SSaggnewHeatPFRwOxide

TASK POP_74714c::FRAequilibrate # PEMFC - One Phase 2014-06-17:FRAequilibrate

# Allow the cell to reach steady state before beginning EIS

PARAMETER
    FRA   AS MODEL FRA
    t     AS REAL           # Equilibration time
```

```
SCHEDULE
    SEQUENCE
        MONITOR ON ;
        CONTINUE FOR t ;
        MONITOR OFF ;
        RESETRESULTS ALL
        # Cell is equilibrated. Prepare for EIS by changing which variables are fixed.
        REPLACE
            FRA.VAC, FRA.IAC{, FRA.ICell}
        WITH
            FRA.VDC := OLD(FRA.VDC);    # The DC values are now fixed at the
equilibrated values
#            FRA.IDC := OLD(FRA.IDC);
            FRA.IAC := 0;                     # We'll set IAC once we apply a frequency
        END
    END
END # TASK FRAequilibrate

TASK POP_74714c::singlefrequency # PEMFC - One Phase 2014-06-17:singlefrequency

# This task applies a single frequency to the cell, integrates for a number of cycles,
and records the result

PARAMETER
    FRA AS MODEL FRA
    freq  AS REAL
    amp   AS REAL
    integration_cycles AS REAL
    equilibrate_cycles AS REAL
    minimum_integration_time AS REAL

SCHEDULE
    SEQUENCE
        MONITOR FREQUENCY 1/freq ;
        REASSIGN    # Apply the AC signal
            FRA.ExcitationRe := SIN(2*3.14159265*freq*(TIME-OLD(TIME))) ;
            FRA.ExcitationIm := COS(2*3.14159265*freq*(TIME-OLD(TIME))) ;
            FRA.IAC          := amp*SIN(2*3.14159265*freq*(TIME-OLD(TIME))) ;
            FRA.Freq         := freq ;
        END
        CONTINUE FOR equilibrate_cycles/freq ;  # Equilibrate
        REINITIAL   # These variables accumulate the V or I response over time. They
need to be reset to zero when we want to start an integration.
            FRA.VRe,
            FRA.VIm,
            FRA.IRe,
            FRA.IIm
        WITH
            FRA.VRe = 0 ;
            FRA.VIm = 0 ;
            FRA.IRe = 0 ;
            FRA.IIm = 0 ;
        END
        CONTINUE FOR MAX(integration_cycles/freq,
INT(minimum_integration_time*freq)/freq) ;
        MONITOR ON ;    # Record a data point.
        MONITOR OFF ;   # We want one data point per frequency and nothing else, so
turn recording back off.
    END
END # TASK singlefrequency
```

```
TASK POP_74714c::logfrequencysweep # PEMFC - One Phase 2014-06-17:logfrequencysweep

# This task applies a logarithmic sequence of frequencies to the cell.

PARAMETER
    FRA         AS MODEL FRA
    highfreq    AS  REAL
    lowfreq     AS  REAL
    amp         AS  REAL
    perdecade   AS  REAL

VARIABLE
    freq    AS  REAL

SCHEDULE
    SEQUENCE
        freq := highfreq ;
        WHILE freq > lowfreq*10^(-1/(2*perdecade)) DO
            SEQUENCE
                singlefrequency
                ( FRA IS FRA,
                  freq  IS freq,
                  amp   IS amp,
                  integration_cycles IS 2,
                  equilibrate_cycles IS 2,
                  minimum_integration_time IS 0.001 )
                freq := freq * 10^(-1/perdecade) ;
            END # Sequence
        END # While
    END # Sequence
END # TASK logfrequencysweep

PROCESS POP_74714c::PEMFCwithFRA_SSaggNewHeatPFRwOxide_air # PEMFC - One Phase 2014-06-
17:PEMFCwithFRA_SSaggNewHeatPFRwOxide_air

PARAMETER
    F                   AS  REAL    DEFAULT 96485
    T                   AS  REAL                        # K         Temperature
    P                   AS  REAL                        # Pa        Pressure
    p_vap               AS  REAL                        # Pa        Vapor pressure of
water at T
    NGasProp            AS  INTEGER                     #           Number of gases
whose physical properties are built in
    MW_i                AS  ARRAY(NGasProp)  OF  REAL   # **g/mol** Molecular weight of
built in gases
    LJ_ek               AS  ARRAY(NGasProp)  OF  REAL   # K         Reduced Lennard-
Jones attractive energy of built in gases
    LJ_sigma            AS  ARRAY(NGasProp)  OF  REAL   # ***nm***  Lennard-Jones
molecular diameter
    CE_Omega            AS  ARRAY(NGasProp, NGasProp)  OF  REAL   # unitless  Collision
integral or something like that
    D_g_ij              AS  ARRAY(NGasProp, NGasProp)  OF  REAL   # m^2/s  Binary
diffusion coefficients

    NAnodeGasComp       AS  INTEGER                     #           Number of gas
species in catalyst layer
    NCathodeGasComp     AS  INTEGER                     #           Number of gas
species in catalyst layer
    i_anode_gas_index   AS  ARRAY(NAnodeGasComp)  OF  INTEGER #          Built in gas
index for each gas species in catalyst layer
    i_cathode_gas_index AS  ARRAY(NCathodeGasComp)  OF  INTEGER #
```

```
    RH_Anode_Gas        AS  REAL                        #           Relative humidity
of cathode gas
    y_dry_anode_gas     AS  ARRAY(NAnodeGasComp-2) OF REAL   #           Mole fraction
of oxygen in cathode gas on a dry basis (e.g. 21% for air)
    RH_Cathode_Gas      AS  REAL                        #           Relative humidity
of cathode gas
    y_dry_cathode_gas   AS  ARRAY(NCathodeGasComp-2) OF REAL   #           Mole
fraction of oxygen in cathode gas on a dry basis (e.g. 21% for air)
    S_Anode_Gas         AS  REAL                        #           Anode gas
stoichiometric ratio
    S_Cathode_Gas       AS  REAL                        #           Cathode gas
stoichiometric ratio

    I_DC                AS  REAL                        # A/m2      DC current density
for EIS measurements

    gdltfactor          AS  REAL    DEFAULT 1.3

UNIT
    PEMFC AS  PEMFC_SSaggnewheatPFRwOxide

SET
######################################
### USER DEFINED PARAMETER SECTION ###
######################################
###  These are all of the parameters I would normally want to change
#######################################################################################
########

   I_DC             := 2000        ;   # A/m2      DC current density for EIS
measurements

    T           :=  353             ;   # K         Temperature
    P           :=  1E5             ;   # Pa        Pressure (1 bar)
    NAnodeGasComp       :=  3       ;   #           Number of gas species in catalyst
layer
    i_anode_gas_index   :=  [1, 5, 2] ; #           Gas species in catalyst layer: 1.
Water(1) 2. Hydrogen(5) 3. Nitrogen(2)
    RH_Anode_Gas        := 0.75     ;   #           Relative humidity of cathode gas:
100%
    y_dry_anode_gas     := [1]      ;   #           Mole fraction of hydrogen (and
possibly other gases) in cathode gas on a dry basis (e.g. 21% O2 for air)
    NCathodeGasComp     :=  3       ;   #           Number of gas species in catalyst
layer
    i_cathode_gas_index :=  [1, 3, 2] ; #           Gas species in catalyst layer: 1.
Water(1) 2. Oxygen(3) 3. Nitrogen(2)
    RH_Cathode_Gas      := 0.75     ;   #           Relative humidity of cathode gas:
100%
    y_dry_cathode_gas   := [0.21]   ;   #           Mole fraction of oxygen (and
possibly other gases) in cathode gas on a dry basis (e.g. 21% for air)
                                        #           If we are using more than 3 gas
species, then this is an N-2 array
    S_Anode_Gas      := 6           ;   #           Anode gas stoichiometric ratio
(100% excess hydrogen)
    S_Cathode_Gas    := 6           ;   #           Cathode gas stoichiometric ratio
(100% excess air)

    WITHIN PEMFC DO
        AnodeGDL.L   := 140E-6  ;   # m         Anode GDL thickness
        Membrane.L   := 50E-6   ;   # m         Membrane thickness
```

```
        Cathode.L    := 17E-6   ;   # m         Cathode catalyst layer thickness
        CathodeGDL.L := 140E-6  ;   # m         Cathode GDL thickness

        WITHIN Cathode DO
            # Catalyst layer morphology
#            R_agg     := 400e-9 ;         #   m       Flooded agglomerate radius
#            th_film   := 28.284e-9 ;         #   m       Ionomer film thickness
(active core of agglomerate is R_agg-th_film
            R_agg     := 420e-9 ;         #   m       Flooded agglomerate radius
            th_film   := 27.115e-9 ;         #   m       Ionomer film thickness (active
core of agglomerate is R_agg-th_film
#            R_agg     := 430e-9 ;         #   m       Flooded agglomerate radius
#            th_film   := 26.564e-9 ;         #   m       Ionomer film thickness
(active core of agglomerate is R_agg-th_film
#            R_agg     := 350e-9 ;         #   m       Flooded agglomerate radius
#            th_film   := 31.640e-9 ;         #   m       Ionomer film thickness
(active core of agglomerate is R_agg-th_film


            tort_agg  := 1;#porosity_agg^(-0.5)  ;         #           Tortuosity of
ionomer in agglomerate core
            ECA       := 79   ;         #   m2/g    ECA of platinum catalyst
            loading   := 0.3  ;         #   mg/cm2
            epsilon_e := 0.16  ;         # unitless  Volume fraction of electrolyte in
electrode
            epsilon_g := 0.65  ;         # untiless  Volume fraction of gas pore space
in electrode

            # Conductivity of solid phase
            sig       := 1000 ;         # S/m       Electronic conductivty of solid
phase

            c         := 2    ;         # F/m^2     Double layer capacitance (including
carbon) per unit platinum area
            k         := 0.27    ;

            # Oxygen transport in the ionomer film
#            D_O2_I    := 5e-9 ;         #   m2/s    Diffusivity of oxygen in ionomer
(assumed)
#            H         := 168100 ;       #   Pa-m3/mol   Henry's law constant for
oxygen in ionomer (For water from NIST Webbook)
            D_O2_I    := 3.1e-7*exp(-2768/T) ;  #   m2/s    Diffusivity of oxygen in
ionomer (from Lin, He, and Van Nguyen, JES, 2004, 151, A1999)
            H         := (101325/1e6)*1.33e6*exp(-666/T) ;  # Pa-m3/mol Henry's law
constant for oxygen in ionomer (same source as above) converted from atm-cm3/mol


            # Kinetics, thermodynamics of reaction
            U       :=  1.183 ;         # V         Standard potential for ORR (at
353K)
            k0      :=  6.4e-6  ;     # mol/m^2*s Butler-Volmer rate constant, based on
specific activity of 200 microamps / cm^2, Tafel slope of 70 mV/decade, and U=1.183 V
            alpha_c :=  0.25  ;         # unitless  Transfer coefficient for ORR
            alpha_a :=  0.25  ;         # unitless  Transfer coefficient for ORR
            m_ORR   :=  0.79  ;
#            m_ORR   :=  1  ;

            alphaHet := 0 ;
            sigMu := 13000/(1-alphaHet) ; # J/mol Standard deviation of the typical
distribution of oxide layer components
```

```
            sigMue := 7000/(1-alphaHet) ; # J/mol Standard deviation of the typical
distribution of oxide layer components
            U_OH  := 0.815   ;  #   V           Standard potential for chemisorption
            U_PtO2  := 0.785  ;  #   V           Standard potential for place exchange
            U_PtO2e  := 0.685  ;  #   V           Standard potential for place exchange
            wOH     := 15000 ;  #   J/mol       Temkin term for chemisorbed oxide (note
squared dependece on coverage)
            wPtO2   := 130000 ; #   J/mol       Temkin term for place exchanged oxide
            wPtO2e   := 550000 ; #   J/mol       Temkin term for place exchanged oxide
            kOx     := 0.8 ;#   mol/m2/s    Rate constant for place exchange
            kOxe    := 0.04 ;#   mol/m2/s    Rate constant for place exchange
            chi     := 8;
            edgefrac := 0.36 ;

            a_ion := 1.5; # not used
        END

        WITHIN AnodeGDL DO
            epsilon_g  := 0.6879 ;
            tortuosity := 0.6156 ;
            sig        := 1250 ;
            k          := 1.45;
        END

        WITHIN CathodeGDL DO
            epsilon_g  := 0.6879 ;    # From datasheet, adjusted for compression
#            tortuosity := gdltfactor*2.85 ;    # From Martínez et al. JES, 2009, 156,
B80
            tortuosity := 0.6156 ;    # From limiting current density analysis
            sig        := 1250 ;
            k          := 1.45;
        END



        AnodeBPP.Pout := P;
        CathodeBPP.Pout := P;

        WITHIN AnodeBPP DO
            c1    := 25*1e3*3.888E-3 ;
            c2    := 25^2*1e3*1.671e-6 ;
            L     := 5e-4 ; # m
            h     := 5400 ; # W/m2*K
            Lgraphite := 0.0127 ; # m
            cpgraphite := 707.7 ; # J/mol*kg
            rhographite := 1780 ; # kg/m3
            k           := 95 ; # W/mK
        END
        WITHIN CathodeBPP DO
# Nitrogen 100% RH
#            c1    := 25*1e3*1.39E-2 ;
#            c2    := 25^2*1e3*7.84e-7 ;
# Helium 75% RH
#            c1    := 1000*0.1935 ;
#            c2    := 1000*2.051e-4 ;
# Nitrogen 75% RH
            c1    := 1000*0.2630;
            c2    := 1000*4.756e-4;

            L     := 5e-4 ; # m
            h     := 5400 ; # W/m2*K
```

```
            Lgraphite := 0.0127 ; # m
            cpgraphite := 707.7 ; # J/mol*kg
            rhographite := 1780 ; # kg/m3
            k           := 95 ; # W/mK
        END

        # Domain discretization method. Finite element makes more sense with mass 
balance equations, so I use that method, not finite differences
        # Very good accuracy is obtained with just 10 points, but the simulation runs 
fast enough to use more anyway.
        AnodeBPP.Zee    := [OCFEM, 4, 5] ;
        AnodeGDL.Zee    := [OCFEM, 2, 5] ;
        Membrane.Zee    := [OCFEM, 2, 5] ;
        Cathode.Zee     := [OCFEM, 2, 5] ;
        Cathode.DelMu   := [OCFEM, 2, 20] ;
        CathodeGDL.Zee  := [OCFEM, 2, 6] ;
        CathodeBPP.Zee    := [OCFEM, 4, 5] ;

        AnodeBPP.Wye    := [OCFEM, 3, 1] ;
        CathodeBPP.Wye  := [OCFEM, 3, 1] ;

#######################################################################################
#########
##########################################
### END USER DEFINED PARAMETER SECTION ###
##########################################
### Skip to ASSIGN section
        ### Now, here are some other parameters that are unlikely to change but still 
need to be specified.

        WITHIN Membrane DO
            # Ionomer compositional data
            EW      :=  1.1   ;         # kg/mol    Equivalent weight of Nafion
            rho_n   :=  1980  ;         # kg/m^3    Density of dry Nafion
            MW_w    :=  0.01802 ;       # kg/mol    Molecular weight of water
            rho_w   :=  972  ;         # kg/m^3    Density of water
            k       :=  0.25   ;
        END

        WITHIN Cathode DO
            # Ionomer compositional data
            EW      :=  1.1   ;         # kg/mol    Equivalent weight of Nafion
            rho_n   :=  1980  ;         # kg/m^3    Density of dry Nafion
            MW_w    :=  0.01802 ;       # kg/mol    Molecular weight of water
            rho_w   :=  972  ;         # kg/m^3    Density of water

            # Stoichiometry of reaction
            n       :=  4     ;         # unitless  Number of electrons in ORR
            s_w     :=  -2    ;         # unitless  Stoichiometric coefficient of water 
in ORR
            s_ox    :=  1     ;         # unitless  Stoichiometric coefficient of 
oxygen in ORR
        END
        AnodeBPP.n2   := 2    ;         #           Hydrogen
        CathodeBPP.n2 := 4    ;         #           Oxygen
    END

    ### Finally, here is a tiny library of gas properties that allows me to add 
selected gas species quickly
    NGasProp    :=  6           ;   #           Number of gases whose physical 
properties I am building in
```

```
    MW_i        := [18.02,
                    28.01,
                    32.00,
                    44.01,
                    2.016,
                    4.0026]      ;   # **g/mol** Molecular weights of H2O, N2, O2, CO2,
H2, He

    LJ_ek       := [809.1,
                    71.4,
                    106.7,
                    195.2,
                    59.7,
                    10.22]       ;   # K         Reduced Lennard-Jones attractive
energy of H2O, N2, O2, CO2, H2, He

    LJ_sigma    := [0.2641,
                    0.3798,
                    0.3467,
                    0.3941,
                    0.2827,
                    0.2556]     ;   # ***nm***  Lennard-Jones molecular diameter

    ### Now some equations that calculate additional parameters from the ones specified
above.
    # Calculate binary diffusion coefficients using Chapman-Enskog relation
    FOR i := 1 TO NGasProp DO
        FOR j := 1 TO NGasProp DO
            CE_Omega(i,j)    := 1.06036/((T/SQRT(LJ_ek(i)*LJ_ek(j)))^0.15610) +
0.19300/EXP(0.47635*T/SQRT(LJ_ek(i)*LJ_ek(j))) +
1.03587/EXP(1.52996*T/SQRT(LJ_ek(i)*LJ_ek(j))) +
1.76474/EXP(3.89411*T/SQRT(LJ_ek(i)*LJ_ek(j))) ;
                                    # unitless  Collision integral from Fuller's
Thesis, original source P. D. Nuefeld, J. Chem. Phys., 57, 1100 (1972)
            D_g_ij(i,j) := 1.8583E-
9*SQRT(T^3*(1/MW_i(i)+1/MW_i(j)))/(((LJ_sigma(i)+LJ_sigma(j))/2)^2*CE_Omega(i,j)) ;
# m^2/s Chapman-Enskog equation for binary diffusion coefficients.
            # Note that I removed the pressure term so these are diffusion coefficients
at 1 bar. In the models, the diffusion coefficient can be adjusted for pressure easily.
        END
    END
    # Calculate vapor pressure of water using Antoine's correlation
    p_vap := 1e5*exp(11.6832-3816.44/(T-46.13)) ; # Pa  From Reid, Prausnitz, Sherwood,
The Properties of Gases and Liquids via Fuller's Thesis

    ### And last of all, some parameters are defined in this process and need to be
carried into the model
    #PEMFC.T     :=  T       ;
    PEMFC.P     :=  P       ;
    PEMFC.p_vap :=  p_vap   ;
    WITHIN PEMFC DO
        Cathode.NGasComp    := NCathodeGasComp  ;
        CathodeGDL.NGasComp := NCathodeGasComp  ;
        CathodeBPP.NGasComp := NCathodeGasComp  ;
        Anode.NGasComp      := NAnodeGasComp    ;
        AnodeGDL.NGasComp   := NAnodeGasComp    ;
        AnodeBPP.NGasComp   := NAnodeGasComp    ;
        FOR i := 1 TO NAnodeGasComp DO
            FOR j := 1 TO NAnodeGasComp DO
                AnodeGDL.D_g_ij(i,j)    := D_g_ij(i_anode_gas_index(i),
i_anode_gas_index(j))       ;
```

```
            END
        END
        FOR i := 1 TO NCathodeGasComp DO
            FOR j := 1 TO NCathodeGasComp DO
                Cathode.D_g_ij(i,j)     := D_g_ij(i_cathode_gas_index(i),
i_cathode_gas_index(j))   ;
                CathodeGDL.D_g_ij(i,j)  := D_g_ij(i_cathode_gas_index(i),
i_cathode_gas_index(j))   ;
            END
        END

    END

    ### End parameter carryover section



ASSIGN
### BOUNDARY CONDITIONS ###
    WITHIN PEMFC DO
#        AnodeBPP.S             := S_Anode_Gas          ; #          Specify
stoichiometric ratios
#        AnodeBPP.Vdry           :=
S_Anode_Gas*I_DC/(2*F)/y_dry_anode_gas*22414/1e4*60 ; # sccm/cm2
        AnodeBPP.Vdry           := 80;
#       CathodeBPP.S           := S_Cathode_Gas        ; #           Specify
stoichiometric ratios
#        CathodeBPP.Vdry         :=
S_Cathode_Gas*I_DC/(4*F)/y_dry_cathode_gas*22414/1e4*60 ;
        CathodeBPP.Vdry         := 200;

        AnodeBPP.p_g_in(1)     := RH_Anode_Gas*p_vap   ; # Pa        Specified using
relative humidity
        CathodeBPP.p_g_in(1)   := RH_Cathode_Gas*p_vap ; # Pa        Specified using
relative humidity
        Cathode.initfactor := MIN(0.01+0.1*TIME,1);
        Membrane.initfactor := MIN(0.01+0.1*TIME,1);
        FOR ii := 1 TO NAnodeGasComp-2 DO
            AnodeBPP.x_dry_in(ii)     := y_dry_anode_gas(ii)     ; # Pa
Specified using dry gas composition
        END
        FOR ii := 1 TO NCathodeGasComp-2 DO
            CathodeBPP.x_dry_in(ii)   := y_dry_cathode_gas(ii) ; # Pa        Specified
using dry gas composition
        END
        WITHIN FRA DO
            NegativeTerminal.V   :=  0   ;  # We need a reference somewhere
            IDC           :=  0.5*I_DC + 10000*TIME  ;       # Constant current hold
#            IDC           :=  I_DC  ;       # Constant current hold

            # These variables need to be assigned to zero when the FRA is not turned
on:
            ExcitationRe  := 0 ;
            ExcitationIm  := 0 ;
            VAC           := 0 ;
            IAC           := 0 ;
            Freq          := 0 ;
        END
    END

#PRESET
```

```
#        RESTORE "test_saved_state"
INITIAL
    WITHIN PEMFC DO
        WITHIN AnodeGDL DO
            FOR i := 1 TO NGasComp-1 DO
                p_g(i,0|+:L|-)  = AnodeBPP.p_g_in(i)   ; # Pa        Initialize using
BPP conditions
            END
            Temp(0|+:L|-) = T;
        END
        WITHIN Membrane DO
            FOR z := 0|+ TO L|- DO
                activity(z) = RH_Anode_Gas+(z/L)*(RH_Cathode_Gas-RH_Anode_Gas) ;    #
Initial condition is a linear concentration profile from anode to cathode conditions
            END
            Temp(0|+:L|-) = T;
        END
        WITHIN Cathode DO
            FOR i := 1 TO NGasComp-1 DO
                p_g(i,0|+:L|-)  = CathodeBPP.p_g_in(i) ; # Pa        Initialize using
BPP conditions
            END
            Ox_x = 0;
            Ox_xe = 0;
            Temp(0|+:L|-) = T;
            phi1(0|+:L|-)-phi2(0|+:L|-) = 0.75 ;
# Initial voltage (until crossover is added in, we can't have equilibrium at 0 current
with Tafel kinetics (instead of B-V))
        END
        WITHIN CathodeGDL DO
            FOR i := 1 TO NGasComp-1 DO
                p_g(i,0|+:L|-)  = CathodeBPP.p_g_in(i) ; # Pa        Initialize using
BPP conditions
            END
            Temp(0|+:L|-) = T;
        END
        WITHIN AnodeBPP DO
            FOR y := 0|+ TO 1 DO
                p_g(1:NGasComp-1, y) = p_g_in(1:NGasComp-1)*(1-y*(Pin-Pout)/Pin);
            END
            Temp(0|+:Lgraphite|-) = T;
        END
        WITHIN CathodeBPP DO
            FOR y := 0|+ TO 1 DO
                p_g(1:NGasComp-1, y) = p_g_in(1:NGasComp-1)*(1-y*(Pin-Pout)/Pin);
            END
            Temp(0|+:Lgraphite|-) = T;
        END
        WITHIN FRA DO
            VRe = 0 ;
            VIm = 0 ;
            IRe = 0 ;
            IIm = 0 ;
        END
    END

SOLUTIONPARAMETERS
    OutputLevel := 3
    ReportingInterval := 10
#    DASolver := "DASOLV" [
#        "OutputLevel" := 3,
```

```
#        "VariablesWithLargestCorrectorSteps" := 1
#    ]
    IndexReduction := ON

SCHEDULE
   SEQUENCE
#        CONTINUE FOR 900
#        REASSIGN
#            PEMFC.FRA.ICell := I_DC;
#        END
        CONTINUE UNTIL PEMFC.FRA.ICell > I_DC
        REASSIGN
            PEMFC.FRA.IDC := I_DC;
        END
        FRAequilibrate
            (   FRA IS PEMFC.FRA,
                t   IS 900 )
#        Fix the gas flow rates so they aren't defined stoichiometrically anymore. We
don't want the flowrates to vary sinusoidally during EIS. Maybe this could be avoided
by calculating stoichiometry via IDC instead of ICell
#        REPLACE
#            PEMFC.AnodeBPP.S, PEMFC.CathodeBPP.S
##            PEMFC.CathodeBPP.S
#        WITH
#            PEMFC.AnodeBPP.Vdry := OLD(PEMFC.AnodeBPP.Vdry);
#            PEMFC.CathodeBPP.Vdry := OLD(PEMFC.CathodeBPP.Vdry);
#        END
        logfrequencysweep
            (   FRA         IS PEMFC.FRA,
                highfreq    IS 1E4,
                lowfreq     IS 1e-6,
                amp         IS sqrt(2)*0.05*I_DC,
                perdecade   IS 10 )
    END
END # PROCESS PEMFCwithFRA_SSaggNewHeatPFRwOxide_air
```

APPENDIX C

GPROMS MODEL CODE FOR TWO-PHASE STEADY-STATE MODEL (SECTION 3.2)

Process MEAnoMPL_SGL25BA

```
PARAMETER
Temp AS REAL

UNIT

Flowsheet AS MEANoMPL

SET
Temp := 333;

WITHIN Flowsheet DO
    s0int := 0.8;
    Rdrop := 150e-6;
END

WITHIN Flowsheet.AGDL DO
    numgas := 2;
    L := 145e-6;
    por := 0.843;
    tort := por^(-2.8);
    perm := por/(8*log(por)^2)*(por-0.11)^2.785*(4e-6)^2/((1-0.11)^0.785*(1.785*por-
0.11)^2);
    kh := 2/3*0.42;
    NominalTemp := Temp;
    numvolumes := 10;
    pp1 := 8768;
    pp2 := 12108; # From a fit of Kumbur 2007 at 1.4 MPa, SGL 24BC
    ppa := 21.55; # ADJusted # Placeholder for testing - from Lamanna 2014 GM Exp GDL
    ppb := -21;
    ppc := 7.98;
    jc  := 0.6982;
    ppn := 3.465;
    ppm := 0.7114;
    percthreshold := 0.1;
    Rh_cont := 2.6e-4;

    Gases := ["Water", "Hydrogen"];
END

WITHIN Flowsheet.ACL DO
    NominalTemp := Temp;
END

WITHIN Flowsheet.GDL DO
    numgas := 3;
    L := 145e-6;
    por := 0.843;
    tort := por^(-2.8);
```

```
    perm := por/(8*log(por)^2)*(por-0.11)^2.785*(4e-6)^2/((1-0.11)^0.785*(1.785*por-
0.11)^2);
    kh := 2/3*0.42;
    NominalTemp := Temp;
    numvolumes := 10;
    pp1 := 8768;
    pp2 := 12108; # From a fit of Kumbur 2007 at 1.4 MPa, SGL 24BC
    ppa := 21.55/1e2;
    ppb := -21/1e2; # Adjusted
    ppc := 7.98/1e2;
    jc  := 0.6982; # From Gostick 2006 - the MSP results
    ppn := 3.465;
    ppm := 0.7114;
    percthreshold := 0.1;
    Rh_cont := 2.6e-4;

#    Gases := ["Water", "Oxygen", "Helium"];
    Gases := ["Water", "Oxygen", "Nitrogen"];
END

Flowsheet.ACL.UHRHE := 0;

WITHIN Flowsheet.CL DO
    numgas := 3;
    L := 17e-6;
    por := 0.65;
    tort := por^(-2.8);
    perm := 0.65*(2e-8)^2; # Approximation from pore radius, leverett style.
    kh := 0.27; # From Khandelwal and Mench. Approximate, but not really that critical
anyway.
    NominalTemp := Temp;
    numvolumes := 10;
    pp1 := 3.728e6; # From a fit of LaManna 2014 data
    pp2 := 6.602e6;
    s0  := 0.8178;
    jc  := 0.8904; # Alternative if definition based on pore radius
    ppn := 4.930;
    ppm := 0.1530;
    percthreshold := 0.19;
    ppa := -1084;   # From a fit of Kusoglu et al.
    ppb := 18728;
    ppa2 := 3*10927;
    ppb2 := 2152;
    ppc := 0.5*0.6773;

    Gases := ["Water", "Oxygen", "Nitrogen"];
#    Gases := ["Water", "Oxygen", "Helium"];
    UHov := 1.253;
    UHRHE := 0;
    ECA := 79;
    Loading := 0.3;
    m_orr := 0.79;
    R_agg := 420e-9;
    th_film := 27.1e-9;
    k0 := 6.4e-6*exp(-33500/R*(1/NominalTemp-1/353)); # Neyerlin activation energy, but
divided by two to account for the doubled Tafel slope.
    alpha_c := 0.5;
    epsilon_e := 0.16;
    rho_n := 1980;
    rho_w := 1000;
    EW := 1.1;
```

```
    MW_w := 0.018;
    sig := 1000;
    dpore := 40e-9;
    D_O2_I    := 3.1e-7*exp(-2768/NominalTemp) ;  #   m2/s    Diffusivity of oxygen in
ionomer (from Lin, He, and Van Nguyen, JES, 2004, 151, A1999)
    H         := (101325/1e6)*1.33e6*exp(-666/NominalTemp) ;  # Pa-m3/mol Henry's law
constant for oxygen in ionomer (same source as above) converted from atm-cm3/mol

    alphaHet := 0 ;
    sigMu := 13000/(1-alphaHet) ; # J/mol Standard deviation of the typical
distribution of oxide layer components
    sigMue := 7000/(1-alphaHet) ; # J/mol Standard deviation of the typical
distribution of oxide layer components
    U_OH  := 0.815   ;  #   V           Standard potential for chemisorption
    U_PtO2  := 0.785  ;  #   V           Standard potential for place exchange
    U_PtO2e  := 0.685  ;  #   V           Standard potential for place exchange
    wOH     := 15000 ;  #   J/mol       Temkin term for chemisorbed oxide (note squared
dependece on coverage)
    wPtO2   := 130000 ; #   J/mol       Temkin term for place exchanged oxide
    wPtO2e   := 550000 ; #   J/mol       Temkin term for place exchanged oxide
    chi     := 8;
    edgefrac := 0.36 ;
    alphaOxa := 1.5;
    alphaOxc := 1.5;
    alphaOxae := 2.5;
    alphaOxce := 1.5;

    OxideHeterogeneity := [ffdm, 1, 18];

    PotentialGuess := 1.0; # Try changing this
END

WITHIN Flowsheet.Mem DO
    kh := 0.25;
    L := 50e-6;
    NominalTemp := Temp;
    numvolumes := 10;
    rho_n := 1980;
    EW := 1.1;
    MW_w := 0.018015;
END

WITHIN Flowsheet.CFF DO
    NominalTemp := Temp;
    # Nitrogen 100% RH
    c1    := 25*1e3*1.39E-2 ;
    c2    := 25^2*1e3*7.84e-7 ;
    A     := 0.0025;
    Pout  := 1e5;
    numgas := 3;
    invn1 := 1/2;
    invn2 := -1/4;
END

WITHIN Flowsheet.AFF DO
    NominalTemp := Temp;
    # Hydrogen 100% RH
    c1    := 25*1e3*3.888E-3 ;
    c2    := 25^2*1e3*1.671e-6 ;
    A     := 0.0025;
    Pout  := 1e5;
```

```
    numgas := 2;
    invn1    := 0;
    invn2    := 1/2;
END

Flowsheet.AGDL.L0 := 0;
Flowsheet.Mem.L0 := Flowsheet.AGDL.L0 + Flowsheet.AGDL.L;
Flowsheet.CL.L0 := Flowsheet.Mem.L0 + Flowsheet.Mem.L;
Flowsheet.GDL.L0 := Flowsheet.CL.L0 + Flowsheet.CL.L;


ASSIGN
WITHIN Flowsheet DO
    GDL.ChanPort.I := 100+100*time;
    GDL.ChanPort.T := GDL.NominalTemp;
    CFF.Vdry := 1.5;
    CFF.xdryin(1) := 0.105;
    CFF.TH  := Temp+10;
    AGDL.ChanPort.Phi := 0;
    AGDL.ChanPort.T := GDL.NominalTemp;
    AFF.Vdry := 0.63;
    AFF.TH  := Temp+10;
END


INITIALSELECTOR
Flowsheet.Interface := Flowsheet.Flooded;

WITHIN Flowsheet.GDL DO
ConsiderHeatofVaporization  := Yes; #} No;
ConsiderLiquidBlockage      := Yes;
SimplifyDarcysLaw           := No;
#EdgeScalars                 := Offset;
#EdgeScalars                 := CenteredExceptSS;
END

WITHIN Flowsheet.AGDL DO
ConsiderHeatofVaporization  := Yes; #} No;
ConsiderLiquidBlockage      := Yes;
SimplifyDarcysLaw           := No;
#EdgeScalars                 := Offset;
END

WITHIN Flowsheet.CL DO
HeatMode := Full; # Check
SolidConductivity := Finite; # Check
IonomerTransportProperties := ConcentrationDependent; # Check
CurrentDistribution := NonUniform; # Check
ConsiderIonomerWaterTransport := Yes; # Check

#HeatMode := Constant_Generation;
#SolidConductivity := Infinite;
#IonomerTransportProperties := Saturated;
#CurrentDistribution := IsUniform;
#ConsiderIonomerWaterTransport := No;
END

WITHIN Flowsheet.ACL DO
IgnoreAnode := {Yes ; #}No;
END
```

```
WITHIN Flowsheet.Mem DO
        HeatMode := Full;
        IonomerTransportProperties := ConcentrationDependent;

#        HeatMode := Constant_Generation;
#        IonomerTransportProperties := Saturated;

    END

INITIALIZATION_PROCEDURE
    USE
        Flowsheet : IAmHopeful ;
    END
SOLUTIONPARAMETERS
    ReportingInterval := 1.0
    DASolver := "DASOLV" [
        "InitialisationNLSolver" := "BDNLSOL" [
            "BlockSolver" := "SPARSE" [
                "MaxIterations" := 2000,
                "MaxIterNoImprove" := 50,
                "SLRFactor" := 1
            ]
        ],
        "ReinitialisationNLSolver" := "BDNLSOL" [
            "BlockSolver" := "SPARSE" [
                "MaxIterations" := 2000,
                "MaxIterNoImprove" := 50,
                "SLRFactor" := 1
            ]
        ]
    ]


SCHEDULE
SEQUENCE
CONTINUE UNTIL Flowsheet.GDL.ChanPort.Phi {> 1.1; #}< -0;
END
```

Model ChapmanEnskog

```
PARAMETER
AllGases      AS  Ordered_set
MW            AS  ARRAY(AllGases)  OF  REAL   # **g/mol** Molecular weight of built in
gases
LJ_ek         AS  ARRAY(AllGases)  OF  REAL   # K         Reduced Lennard-Jones
attractive energy of built in gases
LJ_sigma      AS  ARRAY(AllGases)  OF  REAL   # ***nm***  Lennard-Jones molecular
diameter
CE_Omega      AS  ARRAY(AllGases, AllGases)  OF  REAL   # unitless  Collision integral
or something like that
PD_g_ij       AS  ARRAY(AllGases, AllGases)  OF  REAL   # m^2/s  Binary diffusion
coefficients
CE_Omega_visc AS  ARRAY(AllGases)  OF  REAL   # unitless  Collision integral or
something like that
visc_i        AS  ARRAY(AllGases)  OF  REAL   # Pa*s      Viscosity of gas i
vmix_phi      AS  ARRAY(AllGases, AllGases)  OF  REAL   # Unitless  Constant for
viscosity mixing rule
R             AS  REAL
T             AS  REAL

SET
```

```
### Here is a tiny library of gas properties that allows me to add selected gas species
quickly
AllGases    := ["Water", "Nitrogen", "Oxygen", "Carbon Dioxide", "Hydrogen", "Helium"];
R           :=  8.3145      ;
MW          := [0.01802,
                0.02801,
                0.03200,
                0.04401,
                0.002016,
                0.0040026]      ;   # **kg/mol** Molecular weights of H2O, N2, O2, CO2,
H2, He

LJ_ek       := [809.1,
                71.4,
                106.7,
                195.2,
                59.7,
                10.22]       ;   # K         Reduced Lennard-Jones attractive energy of
H2O, N2, O2, CO2, H2, He

LJ_sigma    := [0.2641,
                0.3798,
                0.3467,
                0.3941,
                0.2827,
                0.2556]     ;   # ***nm***  Lennard-Jones molecular diameter

### Now some equations that calculate additional parameters from the ones specified
above.
# Calculate binary diffusion coefficients using Chapman-Enskog relation
FOR i IN AllGases DO
        # unitless  Collision integral from BSL, original source P. D. Nuefeld, J.
Chem. Phys., 57, 1100 (1972)
        CE_Omega_visc(i)    := 1.16145/((T/LJ_ek(i))^0.14874) +
0.52487/EXP(0.77320*T/LJ_ek(i)) + 2.16178/EXP(2.43787*T/LJ_ek(i)) ;
        visc_i(i)           := 2.6693e-
8*sqrt(1e3*MW(i)*T)/(LJ_sigma(i)^2*CE_Omega_visc(i));
    FOR j IN AllGases DO
        # unitless  Collision integral from Fuller's Thesis, original source P. D.
Nuefeld, J. Chem. Phys., 57, 1100 (1972)
        CE_Omega(i,j)       := 1.06036/((T/SQRT(LJ_ek(i)*LJ_ek(j)))^0.15610) +
0.19300/EXP(0.47635*T/SQRT(LJ_ek(i)*LJ_ek(j))) +
1.03587/EXP(1.52996*T/SQRT(LJ_ek(i)*LJ_ek(j))) +
1.76474/EXP(3.89411*T/SQRT(LJ_ek(i)*LJ_ek(j))) ;
        # Pa-m^2/s Chapman-Enskog equation for binary diffusion coefficients.
        PD_g_ij(i,j)        := 1e5*1.8583E-9*SQRT(T^3*(1E-3/MW(i)+1E-
3/MW(j)))/(((LJ_sigma(i)+LJ_sigma(j))/2)^2*CE_Omega(i,j)) ;
        vmix_phi(i,j)       :=
1/(sqrt(8)*sqrt(1+MW(i)/MW(j)))*(1+sqrt(visc_i(i)/visc_i(j))*(MW(j)/MW(i))^(1/4))^2;
    END
END
```

Model CLSteadyState_enhanced_vapor_ngases

```
PARAMETER
numgas      AS INTEGER DEFAULT 3
R           AS REAL DEFAULT 8.3145
kh          AS REAL # Thermal conductivity
por         AS REAL # Porosity
```

```
tort        AS REAL # Tortuosity, where Deff = por/tort*D, which is not the true
definition of tortuosity, but the more common one.
L           AS REAL
perm        AS REAL
NominalTemp AS REAL
numvolumes  AS INTEGER
scalarpoints AS ARRAY(numvolumes) OF REAL
pp1         AS REAL DEFAULT 2e3
pp2         AS REAL DEFAULT 4e3
s_ox        AS REAL DEFAULT 1
s_w         AS REAL DEFAULT -2
n           AS REAL DEFAULT 4
F           AS REAL DEFAULT 96485
UHov        AS REAL
UHRHE       AS REAL DEFAULT 0
apt         AS REAL DEFAULT 1e5
m_orr       AS REAL DEFAULT 1
R_agg       AS REAL DEFAULT 1e-7
th_film     AS REAL DEFAULT 1e-8
k0          AS REAL DEFAULT 1e-6
alpha_c     AS REAL DEFAULT 0.5
epsilon_e   AS REAL
rho_n       AS REAL
rho_w       AS REAL
EW          AS REAL
MW_w        AS REAL
sig         AS REAL
H           AS REAL
D_O2_I      AS REAL
tort_agg    AS REAL
porosity_agg    AS REAL
ECA         AS REAL
Loading     AS REAL
dpore       AS REAL
percthreshold   AS REAL DEFAULT 0
PotentialGuess  AS REAL DEFAULT 0.6
#gasvisc     AS REAL DEFAULT 2e-5
ppa,ppb,ppc AS REAL
ppa2, ppb2  AS REAL DEFAULT 1e4
jc, ppn, ppm    AS REAL
s0          AS REAL DEFAULT 1
Gases       AS ORDERED_SET
MW          AS ARRAY(Gases) OF REAL
sigMu       AS REAL
sigMuE      AS REAL
chi         AS REAL
edgefrac    AS REAL
U_OH        AS REAL
U_PtO2      AS REAL
U_PtO2e     AS REAL
wOH         AS REAL
wPtO2       AS REAL
wPtO2e      AS REAL
alphaHet    AS REAL
alphaOxa    AS REAL
alphaOxc    AS REAL
alphaOxae   AS REAL
alphaOxce   AS REAL
pi          AS REAL DEFAULT 3.14159265
numoxidestdevs  AS REAL DEFAULT 3
L0          AS REAL DEFAULT 0
```

```
DISTRIBUTION_DOMAIN
ZeeVector           AS [0:1]
ZeeScalar           AS [0:1]
OxideHeterogeneity  AS [-numoxidestdevs:numoxidestdevs]

UNIT
ChapmanEnskog   AS ChapmanEnskog

PORT
GDLPort AS GDL_SS_eq_pcap
MemPort AS MemPortSS

VARIABLE
x           AS DISTRIBUTION(Gases,ZeeScalar) OF Norm    # Mole fraction
xx          AS DISTRIBUTION(Gases, ZeeVector) OF Norm   # (vector grid)
P           AS DISTRIBUTION(ZeeScalar) OF Positive      # Total pressure
PP          AS DISTRIBUTION(ZeeVector) OF Positive
T           AS DISTRIBUTION(ZeeScalar) OF Positive
TT          AS DISTRIBUTION(ZeeVector) OF Positive
qh          AS DISTRIBUTION(ZeeVector) OF Norm          # Heat flux
s           AS DISTRIBUTION(ZeeScalar) OF Norm          # Water saturation
ss          AS DISTRIBUTION(ZeeVector) OF Norm
activity    AS DISTRIBUTION(ZeeScalar) OF Positive      # Water activity
aactivity   AS DISTRIBUTION(ZeeVector) OF Positive
lambda      AS DISTRIBUTION(ZeeScalar) OF Positive      # Water uptake
llambda     AS DISTRIBUTION(ZeeVector) OF Positive
Ng          AS DISTRIBUTION(Gases, ZeeVector) OF Norm   # Gas flux
pcap        AS DISTRIBUTION(ZeeScalar) OF Norm          # Water capillary pressure
Nl, Nw, Nwt AS DISTRIBUTION(ZeeVector) OF Norm          # Liquid, ionomer, and total
water flux
xvap        AS DISTRIBUTION(ZeeScalar) OF Positive      # Vapor mole fraction
i1, i2      AS DISTRIBUTION(ZeeVector) OF Norm          # Electronic and ionic current
phi1        AS DISTRIBUTION(ZeeScalar) OF Norm          # Electronic potential
phi2a       AS DISTRIBUTION(ZeeScalar) OF Norm          # Ionic potential
phi2r       AS DISTRIBUTION(ZeeScalar) OF Norm          # (Relative for numerical
reasons)
eff, thiele AS DISTRIBUTION(ZeeScalar) OF Positive      # Effectiveness factor and
thiele mod.
rorr, jorr  AS DISTRIBUTION(ZeeScalar) OF Norm          # ORR surface and volume rates
jevap       AS DISTRIBUTION(ZeeScalar) OF Norm          # Evaporation rate
p_O2_i      AS DISTRIBUTION(ZeeScalar) OF Positive      # p_O2 at the agglomerate-film
interface
joule       AS DISTRIBUTION(ZeeScalar) OF Norm          # Joule heating term
U           AS Norm                                     # ORR standard potential
Lr_MT       AS Norm                                     # Equivalent O2 mass transport
distance
kappa       AS DISTRIBUTION(ZeeVector) OF Positive      # Ionic conductivity
D_w         AS DISTRIBUTION(ZeeVector) OF Positive      # Water diffusivity
xi          AS DISTRIBUTION(ZeeVector) OF Positive      # Electroosmotic drag
coefficient
alpha_diff  AS DISTRIBUTION(ZeeVector) OF Positive      # Chemical potential
diffusivity

Ox_thetaOH          AS DISTRIBUTION(ZeeScalar) OF Norm
Ox_thetaPtO2        AS DISTRIBUTION(ZeeScalar) OF Norm
Ox_thetaPtO2e       AS DISTRIBUTION(ZeeScalar) OF Norm
Ox_RemainingSites   AS DISTRIBUTION(ZeeScalar) OF Norm
Ox_x        AS DISTRIBUTION(OxideHeterogeneity, ZeeScalar) OF Norm
Ox_xe       AS DISTRIBUTION(OxideHeterogeneity, ZeeScalar) OF Norm
Ox_Psi      AS DISTRIBUTION(OxideHeterogeneity) OF Norm
```

```
alpha       AS DISTRIBUTION(ZeeVector) OF Norm
alphai      AS DISTRIBUTION(Gases-Gases.first-Gases.Last, ZeeVector) OF Norm
gasvisc     AS DISTRIBUTION(ZeeVector) OF Norm
Dwl         AS DISTRIBUTION(ZeeVector) OF Norm
Dim         AS DISTRIBUTION(Gases, ZeeVector) OF Norm
dHvap       AS Norm                               # Heat of vaporization
kw          AS Norm                               # Thermal conductivity of water
Visc        AS Norm                               # Water viscosity
PDij        AS ARRAY(Gases,Gases) OF Norm         # Pressure diffusivity product
vmix_phi    AS ARRAY(Gases,Gases) OF Norm         # Used in gas viscosity calc.
visc_i      AS ARRAY(Gases) OF Norm               # Viscosity of pure gas i
dens        AS Norm
vol         AS Norm
DKi         AS ARRAY(Gases) OF Norm               # Knudsen diffusivity
surften     AS Norm                               # Surface tension

zscalar     AS DISTRIBUTION(ZeeScalar) OF Norm
zvector     AS DISTRIBUTION(ZeeVector) OF Norm

SELECTOR
ConsiderHeatofVaporization AS (Yes, No) DEFAULT Yes
HeatMode AS (Isothermal, Constant_Generation, Full) DEFAULT Full
SolidConductivity AS (Infinite, Finite) DEFAULT Finite
IonomerTransportProperties AS (Saturated, ConcentrationDependent) DEFAULT
ConcentrationDependent
CurrentDistribution AS (IsUniform, NonUniform, PhiPO2noOxide, PO2noPhiOxide,
PO2OxideNoPhi) DEFAULT NonUniform
ConsiderIonomerWaterTransport AS (Yes,No) DEFAULT Yes
EdgeScalars AS (Centered, Offset) DEFAULT Centered

SET
FOR ii := 1 TO numvolumes DO
    scalarpoints(ii) := (ii-0.5)/numvolumes;
END
ZeeVector := [BFDM, 1, numvolumes];
ZeeScalar := [FFDM, 1, scalarpoints];
FOR ii in Gases DO
    MW(ii) := ChapmanEnskog.MW(ii);
END
GDLPort.numgas := numgas;
ChapmanEnskog.T := NominalTemp;
# Calculated as surface area of Pt (per MEA area) / Volume of agglomerate core (per MEA
area) or roughness / (thickness * volume fraction of active agglomerate core)
aPt    := (ECA*loading*10)/(L*(1-por)*(1-th_film/R_agg)^3) ;
# Calculate the volume fraction of ionomer in the agglomerate core considering the film
is pure ionomer, and the total ionomer loading is known.
porosity_agg := (epsilon_e/(1-por)-1)/(1-th_film/R_agg)^3+1;
tort_agg := porosity_agg^(-0.5);

BOUNDARY
x(Gases-"Water"-Gases.Last,1) = GDLPort.x;
T(1) = GDLPort.T;
Nl(1){+Nw(1)} = GDLPort.Nliq;
Nwt(1) = GDLPort.Ntot(1);
Ng(Gases-"Water",1) = GDLPort.Ntot(2:numgas);
pcap(1) = GDLPort.pcap;
T(0) = MemPort.T;
Nwt(0) = MemPort.Nw ;
Ng(Gases-"Water",0) = 0;
P(1) = GDLPort.P ;
```

```
GDLPort.I = i1(1);
MemPort.I = i2(0);
i2(1) = 0;
i1(0) = 0;
GDLPort.Phi = phi1(1);
MemPort.Phi = phi2a(0);
MemPort.activity = activity(0);
CASE HeatMode OF
    WHEN Full:
    qh(0) - MemPort.qh = -dHvap*Ng("Water",0); # Account for evaporation at membrane
interface
    WHEN Constant_Generation:
    qh(0) - MemPort.qh = 0;
    WHEN Isothermal:
    qh(0) = 0;
END
phi2r(1)=0;

EQUATION
# Stefan Maxwell wtih enhanced vapor diffusion effect
FOR z:= 0 TO 1|- DO
    PARTIAL(x("Water",z)*P(z), ZeeScalar)/PP(z) = L*R*TT(z)*((1+(2-
3*ss(z)+ss(z)^2)*alpha(z)*PP(z))/((1-ss(z))^3+(2-
2*ss(z)^2+ss(z)^3)*alpha(z)*PP(z))*(SIGMA((xx("Water",z)*Ng(,z)-
xx(,z)*Ng("Water",z))/PDij("Water",)) - Ng("Water",z)/(PP(z)*Dim("Water",z))));
    FOR ii in Gases-"Water"-Gases.Last DO
        PARTIAL(x(ii,z)*P(z), ZeeScalar)/PP(z) = L*Lr_MT^2*R*TT(z)*((1-ss(z))^(-
3)*(SIGMA((xx(ii,z)*Ng(,z)-xx(,z)*Ng(ii,z))/PDij(ii,)) - Ng(ii,z)/(PP(z)*Dim(ii,z))) +
((1-ss(z))^(-3)-1)*alphai(ii,z)*PP(z)/((1-ss(z))^3+(2-
2*ss(z)^2+ss(z)^3)*alpha(z)*PP(z))*(SIGMA((xx("Water",z)*Ng(,z)-
xx(,z)*Ng("Water",z))/PDij("Water",)) - Ng("Water",z)/(PP(z)*Dim("Water",z))));
    END
    PARTIAL(P(z), ZeeScalar)/PP(z) = L*R*TT(z)*((1-ss(z))^(-3)*SIGMA(-
Ng(,z)/(PP(z)*Dim(,z))) - ((1-ss(z))^(-3)-1)/((1-ss(z))^3+(2-
2*ss(z)^2+ss(z)^3)*alpha(z)*PP(z))*Dwl(z)/Dim("Water",z)*(SIGMA((xx("Water",z)*Ng(,z)-
xx(,z)*Ng("Water",z))/PDij("Water",)) - Ng("Water",z)/(PP(z)*Dim("Water",z))));
END
# Convenience Variables
phi2r(0:1|-)-phi2r(1) = phi2a(0:1|-)-phi2a(1);
CASE EdgeScalars OF
    WHEN Offset:
        FOR z:= 0 TO 1 DO
            xx(,z) = x(,z+1); #}(x(,z+1)+x(,z))/2;
            TT(z)  = T(z+1); #(T(z+1) + T(z))/2;
            ss(z)  = s(z+1); #}(s(z+1) + s(z))/2;
            PP(z)  = P(z+1);
            aactivity(z) = activity(z+1);
            llambda(z)   = lambda(z+1);
        END
    WHEN Centered:
        FOR z:= 0 TO 1 DO
            xx(,z) = (x(,z+1)+x(,z))/2;
            TT(z)  = (T(z+1) + T(z))/2;
            ss(z)  = (s(z+1) + s(z))/2;
            PP(z)  = (P(z+1) + P(z))/2;
            aactivity(z) = (activity(z+1) + activity(z))/2;
            llambda(z)   = (lambda(z+1) + lambda(z))/2;
        END
END

FOR z:= 0 TO 1 DO
```

```
    # Used in the enhanced vapor diffusion equations:
    FOR ii in Gases-"Water"-Gases.Last DO
        1e6*alphai(ii,z) = 1e6*xx(ii,z)*Dwl(z)/PDij("Water",ii);
    END
    1e6*alpha(z) = 1e6*(SIGMA(xx(Gases-"Water",z)*Dwl(z)/PDij("Water",Gases-"Water")) +
Dwl(z)/(PP(z)*Dim("Water",z)));
    # Equivalent diffusivity of water vapor through liquid water
    Dwl(z)*dHVap*1e5*3816.44/(TT(z)-46.13)^2*exp(11.6832-3816.44/(TT(z)-46.13)) =
R*TT(z)*kw*por/tort;
    # Mixture equation for gas viscosity
    1e5*gasvisc(z) = 1e5*SIGMA(xx(,z)*visc_i/INTEGRAL(jj OVER Gases;
xx(jj,z)*vmix_phi(,jj)));
    # Wall friction
    FOR ii in Gases DO
        1e6*Dim(ii,z) = 1e6*DKi(ii)*por/tort +
1e6*Perm*SIGMA(xx(,z)*PP(z)*sqrt(MW))/(gasvisc(z){visc_i("Nitrogen")}*sqrt(MW(ii)));
    END
END

# Inert mass balance (steady state, no consumption)
FOR jj IN Gases-"Water"-"Oxygen" DO
    FOR z:= 0 TO 1|- DO
        ng(jj,z) = ng(jj,z+1);
    END
END
# Oxygen mass balance. Integrated form.
FOR z:= 0|+ TO 1 DO
    Ng("Oxygen",z) = -i1(z)/(4*F);
END
# Water mass balance. Integrated form.
FOR z:= 0|+ TO 1 DO
    Nwt(z) = Nwt(0) + i1(z)/(2*F);
END
Ng("Water",)+Nl+Nw = Nwt;
PARTIAL(Nw(0|+:1)+Nl(0|+:1), ZeeVector) = -L*jevap(0|+:1|-);
PARTIAL(Nw(0)+Nl(0), ZeeVector) = -L*jevap(0);
PARTIAL(Nw(1)+Nl(1), ZeeVector) = -L*jevap(1);

# Energy balance reaction heat plus Joule heating plus water evaporation.
CASE HeatMode OF
When Full:
    FOR z:= 0|+ TO 1 DO
       1e-6*( -PARTIAL(qh(z), ZeeVector)/L + n*F*jorr(z)*(phi1(z)-phi2a(z)-
(UHov+UHRHE)) + joule(z) - dHvap*jevap(z) )= 0;
    END
    qh(1)-dHvap*(Nw(1)+Nl(1)) = GDLPort.qh;
When Constant_Generation:
    FOR z:= 0|+ TO 1 DO
        -partial(qh(z), ZeeVector) = i1(1)*(PotentialGuess-(UHov+UHRHE));
    END
    qh(1) = GDLPort.qh;
When Isothermal:
    qh(0|+:1) = 0;
    qh(1) = GDLPort.qh;
END

# Joule heating term has to be calculated separately because gPROMS doesn't want to
have PARTIALs for ZeeVector and ZeeScalar in the same equation.
FOR z:= 0|+ TO 1|- DO
```

```
    L*joule(z) = L*((i2(z)^2/(epsilon_e/(5.53*EXP(-1.16*aactivity(z)))*kappa(z))+i2(z-
1)^2/(kappa(z-1)*epsilon_e/(5.53*EXP(-1.16*aactivity(z-1)))))/2 + (i1(z)^2+i1(z-
1)^2)/(2*sig));
END
L*joule(1) = -i2(1)*PARTIAL(Phi2r(1),ZeeScalar) - i1(1)*PARTIAL(Phi1(1),ZeeScalar);
L*joule(0) = -i2(0)*PARTIAL(Phi2r(0),ZeeScalar) - i1(0)*PARTIAL(Phi1(0),ZeeScalar);

# Heat flux equation
L*qh(0:1)/kh = -PARTIAL(T(0:1|-), ZeeScalar);

# Vapor pressure of water
xvap = 1e5/P*exp(11.6832-3816.44/(T-46.13)) ;

# Capillary Pressure
FOR z:= 0 TO 1 DO
        s(z) = s0*(1-(1+(MAX(pcap(z),0)/(jc*surften*2/dpore))^ppn)^(-ppm));
END

# Darcy's law
FOR z:= 0 TO 1|- DO
    Nl(z) = -perm*(MAX((s(z)-percthreshold)/(1-percthreshold),0)^4+MAX((s(z+1)-
percthreshold)/(1-percthreshold),0)^4)/2/visc/vol/L*PARTIAL(P(z)+pcap(z), ZeeScalar);
END

# Finally, the liquid vapor equilibrium. How to do this? Good question!
FOR z := 0 TO 1 DO
    pcap(z)*vol = R*T(z)*(log(x("Water",z)*P(z)/1e5)-(11.6832-3816.44/(T(z)-46.13)));
END

# Sum of mole fractions
INTEGRAL(jj OVER Gases; x(jj,)) = 1;

FOR z:= 0 TO 1 DO
    # Let's assume that water saturation blocks s fraction of the agglomerates
completely
    # jorr is the homogeneous reaction rate. So when s sites are blocked, the rate per
agglomerate goes up by 1/(1-s)
        -s_ox*jorr(z)*R_agg/3/(1-por)/(1-s(z)) = (P(z)*x("Oxygen",z) -
p_o2_i(z))/H*D_O2_I*(1/th_film - 1/R_agg) ;
        thiele(z) = (R_agg-
th_film)*sqrt((m_ORR+1)/2*abs(H*tort_agg*s_ox*rorr(z)*MAX(p_o2_i(z),1e-10)^(m_ORR-
1)/(porosity_agg*D_O2_I{*exp(LOG(2)*activity(z))/2})));
        eff(z) = 3/thiele(z)^2*(thiele(z)/TANH(thiele(z))-1) ;
END

# Kinetics. Add oxide later
CASE CurrentDistribution OF
    When NonUniform:
        FOR z:= 0 TO 1 DO
            LOG(1e5^m_ORR/apt*rorr(z)/k0) = LOG(Ox_RemainingSites(z)*(1-
Ox_thetaOH(z)))-alpha_c*F/(R*T(z))*(phi1(z)-phi2a(z)-U) ;
            jorr(z) = -rorr(z)*eff(z)*MAX(p_o2_i(z),0)^m_ORR*(1-s(z))*(1-por)*(1-
th_film/R_agg)^3;
        END
    When PO2OxidenoPhi:
        FOR z:= 0 TO 1 DO
            LOG(1e5^m_ORR/apt*rorr(z)/k0) = LOG(Ox_RemainingSites(z)*(1-
Ox_thetaOH(z)))-alpha_c*F/(R*T(z))*(phi1(1)-phi2a(0)-U) ;
            jorr(z) = -rorr(z)*eff(z)*MAX(p_o2_i(z),0)^m_ORR*(1-s(z))*(1-por)*(1-
th_film/R_agg)^3;
        END
```

```
    When PhiPO2noOxide:
        FOR z:= 0 TO 1 DO
            LOG(1e5^m_ORR/apt*rorr(z)/k0) = {LOG(Ox_RemainingSites(z)*(1-
Ox_thetaOH(z)))}-alpha_c*F/(R*T(z))*(phi1(z)-phi2a(z)-U + MAX((phi1(1)-phi2a(0)-
U_OH)/2,0)) ;
            jorr(z) = -rorr(z)*eff(z)*MAX(p_o2_i(z),0)^m_ORR*(1-s(z))*(1-por)*(1-
th_film/R_agg)^3;
        END
    When PO2noPhiOxide:
        FOR z:= 0 TO 1 DO
            LOG(1e5^m_ORR/apt*rorr(z)/k0) = {LOG(Ox_RemainingSites(z)*(1-
Ox_thetaOH(z)))}-alpha_c*F/(R*T(z))*(phi1(1)-phi2a(0)-U + MAX((phi1(1)-phi2a(0)-
U_OH)/2,0)) ;
            jorr(z) = -rorr(z)*eff(z)*MAX(p_o2_i(z),0)^m_ORR*(1-s(z))*(1-por)*(1-
th_film/R_agg)^3;
        END
    When IsUniform:
        FOR z:= 0 TO 1 DO
            LOG(1e5^m_ORR/apt*rorr(z)/k0) = {LOG(Ox_RemainingSites(z)*(1-
Ox_thetaOH(z)))}-alpha_c*F/(R*T(z))*(phi1(1)-phi2a(0) {+ i1(1)*L/kappa(1)/epsilon_e} -U
+ MAX((phi1(1)-phi2a(0)-U_OH)/2,0)) ;
        END
        FOR z:= 0|+ TO 1 DO
            jorr(z) = jorr(z-1);
        END
        jorr(0) = -rorr(0)*1*MAX(P(1)*x("Oxygen",1),0)^m_ORR*(1-por)*(1-
th_film/R_agg)^3;
END

FOR z:= 0 TO 1 DO # Water uptake isotherm
        lambda(z) = 0.043 + 17.81*activity(z) - 39.85*activity(z)^2 +
36.0*activity(z)^3 ;
        activity(z) = x("Water",z) / xvap(z) ;
END

CASE IonomerTransportProperties OF
    When ConcentrationDependent:
        FOR z:= 0 TO 1 DO
#                kappa(z) = 1.45*exp(2.29*aactivity(z))*EXP(1268*(1/353-1/TT(z))) ; #
S/m Experimental, with literature activation energy
                kappa(z) = 100*(0.005139*llambda(z)-0.00326)*EXP(1268*(1/303-1/TT(z)));
# Springer et al.
                # Diffusion coefficient of water in ionomer (Fuller's thesis)
                D_w(z)*1e9 = 1e9*1e-4*3.5e-2*EXP(-2436/TT(z))*llambda(z)/14 ; # m^2/s,
original equation had units of cm^2/s
                # Chemical potential referenced diffusion coefficient.
                1e9*alpha_diff(z) =
1e9*D_w(z)/(R*T(z))*rho_N/EW*(1+MW_w*rho_N/(EW*dens)*(0.043+17.81*aactivity(z)-
39.85*aactivity(z)^2+36*aactivity(z)^3))^(-2)*(17.81*aactivity(z)-
79.7*aactivity(z)^2+108*aactivity(z)^3);
                # Electroosmotic drag coefficient (informed by my own experiments, but
just a rough approximation pending better data and fitting)
                xi(z) = 1.1 + 0.9/(1+EXP(-2*(llambda(z)-5.5))) ;
        END
    When Saturated:
        FOR z:= 0 TO 1 DO
#                kappa(z) = 1.45*exp(2.29*1)*EXP(1268*(1/353-1/NominalTemp)) ; # S/m
Experimental, with literature activation energy
                kappa(z) = 100*(0.005139*14-0.00326)*EXP(1268*(1/303-1/NominalTemp)); #
Springer et al.
                # Diffusion coefficient of water in ionomer (Fuller's thesis)
```

```
                D_w(z)*1e9 = 1e9*1e-4*3.5e-2*EXP(-2436/NominalTemp)*14/14 ; # m^2/s,
original equation had units of cm^2/s
                1e9*alpha_diff(z) =
1e9*D_w(z)/(R*NominalTemp)*rho_N/EW*(1+MW_w*rho_N/(EW*dens)*(0.043+17.81-39.85+36))^(-
2)*(17.81-79.7+108);
                # Electroosmotic drag coefficient (informed by my own experiments, but
just a rough approximation pending better data and fitting)
                xi(z) = 1.1 + 0.9/(1+EXP(-2*(14-5.5))) ;
        END
END

CASE ConsiderIonomerWaterTransport OF
    When Yes:
    FOR z:= 0 TO 1|- DO
        Nw(z) = 1/L*(epsilon_e/(5.53*EXP(-1.16*aactivity(z)))*(-
(kappa(z)*xi(z)/F)*PARTIAL(phi2r(z), ZeeScalar) - (alpha_diff(z) +
kappa(z)*xi(z)^2/F^2)*R*TT(z)/aactivity(z)*PARTIAL(activity(z), ZeeScalar) ));
    END
    When No:
    Nw = 0;
END

FOR z:= 0 TO 1|- DO
        # Ionomer proton flux - modified Ohm's law (Concentrated solution theory)
        L*i2(z) = epsilon_e/(5.53*EXP(-1.16*aactivity(z)))*(-kappa(z)*PARTIAL(phi2r(z),
ZeeScalar) - (kappa(z)*xi(z)/F)*R*TT(z)/aactivity(z)*PARTIAL(activity(z), ZeeScalar)) ;
END
CASE SolidConductivity OF
When Finite:
    FOR z:= 0 TO 1|- DO
        L*i1(z) = sig*PARTIAL(phi1(z), ZeeScalar);
    END
WHEN Infinite:
    PARTIAL(phi1(0:1|-), ZeeScalar) = 0;
END

# Current balances
FOR z:= 0|+ TO 1 DO
     PARTIAL(i2(z), ZeeVector) = L*n*F*jorr(z) ;
END
i1(0:1|-) + i2(0:1|-) = GDLPort.I;

# Oxide Layer
FOR z:= 0 TO 1 DO
    Ox_thetaPtO2(z) = INTEGRAL(dMu := -numoxidestdevs:numoxidestdevs; Ox_x(dMu,z));
    Ox_thetaPtO2e(z) = INTEGRAL(dMu := -numoxidestdevs:numoxidestdevs; Ox_xe(dMu,z));
    1e3*Ox_RemainingSites(z) = 1e3*exp(-chi*(Ox_thetaPtO2(z) + edgefrac/(1-
edgefrac)*Ox_thetaPtO2e(z)));
    wOH*Ox_thetaOH(z)^2/(R*T(z)) + log(Ox_thetaOH(z)/(1 - Ox_thetaOH(z))) =
F/(R*T(z))*MAX((phi1(z)-phi2a(z)-U_OH),-0.2) ;

    FOR dMu := -numoxidestdevs TO numoxidestdevs DO
        1e3*(Ox_thetaOH(z)*Ox_RemainingSites(z))*EXP(-(wPtO2*Ox_x(dMu,z)/Ox_psi(dMu) -
wOH*Ox_thetaOH(z)^2)/R/T(z) ) = 1e3*Ox_x(dMu,z)/Ox_psi(dMu)*exp(-
3*F/R/T(z)*MAX((phi1(z)-phi2a(z)-U_PtO2-sigMu*dMu/(3*F)),-0.2)) ;
        Ox_xe(dMu,z) = Ox_psi(dMu)*EXP(-(wPtO2e*Ox_xe(dMu,z)/Ox_psi(dMu))/R/T(z) +
4*F/R/T(z)*MAX((phi1(z)-phi2a(z)-U_PtO2e-sigMuE*dMu/(4*F)),-0.2)) ;
    END
END
```

```
ASSIGN
dHvap :=
1000*(30.092*NominalTemp/1000+6.832514*(NominalTemp/1000)^2/2+6.793435*(NominalTemp/100
0)^3/3-2.534480*(NominalTemp/1000)^4/4-0.082139/(NominalTemp/1000)-250.8810
    -( -203.6060*NominalTemp/1000+1523.290*(NominalTemp/1000)^2/2-
3196.413*(NominalTemp/1000)^3/3+2474.455*(NominalTemp/1000)^4/4-
3.855326/(NominalTemp/1000)-256.5478)) ; # FROM NIST WEBBOOK

U := 1.229 - 0.00085*(NominalTemp-298);
# Meaningless and unused, but must be assigned due to 3x3 array representation
FOR ii IN Gases DO
    PDij(ii,ii) := 1;
END

# Thermal conductivity from Ramires (see Endnote)
kw := 0.6065*(-1.48445+4.12292*NominalTemp/298.15-1.63866*NominalTemp^2/298.15^2) ;

#Viscosity from Kestin 1978 J Phys Chem Ref Data Vol 7 No 3
visc := 1.002e-3*exp((293.15-NominalTemp)/(NominalTemp-273.15+96)*(1.2378-1.303e-
3*(293.15-NominalTemp)+3.06e-6*(293.15-NominalTemp)^2+2.55e-8*(293.15-NominalTemp)^3));

# Density of water from "ITS-90 Density of Water Formulation for Volumetric Standards
Calibration" J Res Natl Inst Stand Technol 97 335 (1992)
dens := (999.83952+16.945176*(NominalTemp-273.15)-7.9870401e-3*(NominalTemp-273.15)^2-
46.170461e-6*(NominalTemp-273.15)^3+105.56302e-9*(NominalTemp-273.15)^4-280.54253e-
12*(NominalTemp-273.15)^5)/(1+16.89785e-3*(NominalTemp-273.15));

vol := 0.01801528/((999.83952+16.945176*(NominalTemp-273.15)-7.9870401e-3*(NominalTemp-
273.15)^2-46.170461e-6*(NominalTemp-273.15)^3+105.56302e-9*(NominalTemp-273.15)^4-
280.54253e-12*(NominalTemp-273.15)^5)/(1+16.89785e-3*(NominalTemp-273.15)));

surften := 235.8e-3*((647.15-NominalTemp)/647.15)^1.256*(1-0.625*(647.15-
NominalTemp)/647.15); # From Vargaftik, Volkov, and Voljak, J Phys Chem Ref Data, V 12
N 3 1983

FOR ii In Gases DO
    DKi(ii) := dpore/3*sqrt(8*R*NominalTemp/(3.14159*MW(ii)));
END

   FOR dMu := -numoxidestdevs TO numoxidestdevs DO
        Ox_psi(dMu) := exp(-dMu^2/(2)) /
        #              ----------------------
                       (SQRT(2*pi)) ;
    END

FOR z:= 0 TO 1 DO
    zvector(z) := L0 + L*z;
END
FOR z:= 0 TO 1 DO
    zscalar(z) := L0 + L*z;
END

FOR ii in Gases DO
    visc_i(ii) := ChapmanEnskog.visc_i(ii);
    FOR jj in Gases DO
        vmix_phi(ii,jj) := ChapmanEnskog.vmix_phi(ii,jj);
    END
END

FOR ii IN Gases-Gases.Last DO
    FOR jj IN Gases.Subset(Gases.Index(ii)+1) DO
```

```
        PDij(jj,ii) := ChapmanEnskog.PD_g_ij(ii,jj)*por/tort;
        PDij(ii,jj) := ChapmanEnskog.PD_g_ij(ii,jj)*por/tort;
    END
END


PRESET
T := 353:273:373;
TT := 353:273:373;
s := 0:-1e-5:0.99;
ss := 0:-1e-5:0.99;
xx := 0.3:1e-10:1;
x("Water",) := 0.47:1e-3:1;
x("Oxygen",) := 0.12:1e-10:1;
x(Gases-"Water"-"Oxygen",) := 0.41:1e-3:1;
pcap := 10e3:-1e100:1e100;
xvap := 0.47:1e-10:1;
rorr := 1e-6:1e-100:1e100;
activity := 1:1e-10:10;
aactivity := 1:1e-10:10;
thiele := 1:1e-10:1e100;
P:=1e5:1:1e7;
PP:=1e5:1:1e7;
Dim := 1e-6:1e-20:1e100;
#lambda := 14:0:30;
gasvisc := 2e-5:1e-10:1;

eff := 1:0:1;

Ox_thetaOH := 0.01:1e-100:0.999999999;
Ox_thetaPtO2 := 0:0:100;
Ox_thetaPtO2e := 0:0:100;
Ox_x := 1e-5:1e-100:100;
Ox_xe := 1e-5:1e-100:100;
Ox_RemainingSites := 1:1e-100:1;

phi1 := 1:-1:2;
phi2a := 0:-5:10;
phi2r := 0:-1:1;

INITIALIZATION_PROCEDURE test DEFAULT
    START
        ConsiderIonomerWaterTransport := No;
        IonomerTransportProperties := Saturated;
        HeatMode := Isothermal;
        CurrentDistribution := IsUniform;
        SolidConductivity := Infinite;
    END
    NEXT
        JUMP_TO
            CurrentDistribution := NonUniform;
        END
    END
    NEXT
        JUMP_TO
            ConsiderIonomerWaterTransport := Yes;
        END
    END
    NEXT
        JUMP_TO
            IonomerTransportProperties := ConcentrationDependent;
```

```
        END
    END
    NEXT
        JUMP_TO
            HeatMode := Constant_Generation;
        END
    END
    NEXT
        JUMP_TO
            HeatMode := Full;
        END
    END
    NEXT
        JUMP_TO
            SolidConductivity := Finite;
        END
    END

INITIALIZATION_PROCEDURE Isothermal
    START
        ConsiderIonomerWaterTransport := No;
        IonomerTransportProperties := Saturated;
#        HeatMode := Isothermal;
        CurrentDistribution := IsUniform;
        SolidConductivity := Infinite;
    END
    NEXT
        JUMP_TO
            CurrentDistribution := NonUniform;
        END
    END
    NEXT
        JUMP_TO
            ConsiderIonomerWaterTransport := Yes;
        END
    END
    NEXT
        JUMP_TO
            IonomerTransportProperties := ConcentrationDependent;
        END
    END
#    NEXT
#        JUMP_TO
#            HeatMode := Constant_Generation;
#        END
#    END
#    NEXT
#        JUMP_TO
#            HeatMode := Full;
#        END
#    END
    NEXT
        JUMP_TO
            SolidConductivity := Finite;
        END
    END
```

Model ff0d

```
# This is an attempt at implementing flow rate (stoichiometry) effects without making a
2D model.
# It implements a mass balance for the flow of gas in and out based on the
stoichiometric excess

PORT
    GDL AS GDL_SS_eq_pcap

PARAMETER
    F           AS  REAL DEFAULT 96485  # Faraday's constant
    numgas      AS  INTEGER             # Number of gas species
    Pout        AS  REAL                # Total pressure
    invn1          AS  REAL  DEFAULT 1/2     # Stoichiometric coefficient for water
    invn2          AS  REAL  DEFAULT -1/4    # Stoichiometric coefficient for the
reactant gas
#    I_min       AS  REAL    DEFAULT 100
    c1, c2      AS  REAL    DEFAULT 0
    R           AS  REAL    DEFAULT 8.3145
    A           AS  REAL    DEFAULT 0.0025
    NominalTemp AS  REAL

VARIABLE
    xdryin AS ARRAY(Numgas-1) OF Norm
    xin AS ARRAY(Numgas) OF Norm
    Nin,Nout,Nmid AS ARRAY(Numgas) OF Norm
    Vdry AS Norm
    TH AS Norm
    Pin AS Norm
    xmid AS ARRAY(Numgas) OF Norm
    vol AS Norm
    xvap AS Norm

SELECTOR
netwaterdrag AS (yes,no) DEFAULT Yes

EQUATION
    FOR ii:= 2 TO Numgas DO
        Nin(ii) = xdryin(ii-1)*Vdry/22.414/60/A;
        Nin(ii) = xin(ii)*SIGMA(Nin);
    END

    Pin = Pout + c1*(Vdry/10/A) + c2*(Vdry/10/A)^2;

    xin(1)*Pin = 1e5*exp(11.6832-3816.44/(TH-46.13));
    Nin(1)*(1-xin(1)) = SIGMA(Nin(2:numgas))*xin(1);
    SIGMA(xdryin) = 1;

    GDL.P = (Pin+Pout)/2;
#    GDL.Ntot + Nin = Nout;
    CASE netwaterdrag OF
    When No:
        Nin(1) + invn1*GDL.I/F = Nout(1);
    When Yes:
        Nin(1) + GDL.Ntot(1) = Nout(1);
    END
    Nin(2) + invn2*GDL.I/F = Nout(2);
    Nin(3:numgas) = Nout(3:numgas);
```

```
    2*Nmid = Nin+Nout;
    xvap = 1e5*(2/(Pin+Pout))*exp(11.6832-3816.44/(NominalTemp-46.13));
    xmid(1) = MIN(Nmid(1)/SIGMA(Nmid), xvap);
    FOR ii:= 2 to numgas DO
        xmid(ii) = (1-xmid(1))*Nmid(ii)/SIGMA(Nmid(2:numgas));
    END
    FOR ii := 2 TO numgas-1 DO
        xmid(ii) = GDL.x(ii-1);
    END
    GDL.pcap*vol = R*NominalTemp*log(xmid(1)/xvap);

ASSIGN
    vol := 0.01801528/((999.83952+16.945176*(NominalTemp-273.15)-7.9870401e-
3*(NominalTemp-273.15)^2-46.170461e-6*(NominalTemp-273.15)^3+105.56302e-9*(NominalTemp-
273.15)^4-280.54253e-12*(NominalTemp-273.15)^5)/(1+16.89785e-3*(NominalTemp-273.15)));

PRESET
xvap := 0.1:1e-100:1;
xmid(1) := 0.1:1e-100:1;
```

Model GDLSteadyState_enhanced_vapor

```
# GDL model. Shares most equations in common with the gas phase of catalyst layer.

PARAMETER
numgas AS INTEGER DEFAULT 3
R AS REAL DEFAULT 8.3145
kh AS REAL # Thermal conductivity
por AS REAL # Porosity
tort AS REAL # Tortuosity, where Deff = por/tort*D, which is not the true definition of
tortuosity, but the more common one.
L AS REAL
perm AS REAL
NominalTemp AS REAL
numvolumes AS INTEGER
scalarpoints AS ARRAY(numvolumes) OF REAL
pp1 AS REAL DEFAULT 2e3
pp2 AS REAL DEFAULT 4e3
ppa, ppb, ppc AS REAL
jc, ppn, ppm AS REAL
percthreshold AS REAL DEFAULT 0
Rh_cont AS REAL DEFAULT 0
Gases AS ORDERED_SET
L0 AS REAL DEFAULT 0

DISTRIBUTION_DOMAIN
ZeeVector AS [0:1]
ZeeScalar AS [0:1]

UNIT
ChapmanEnskog AS ChapmanEnskog

PORT
ChanPort AS GDL_SS_eq_pcap
CLPort AS GDL_SS_eq_pcap

VARIABLE
x AS DISTRIBUTION(Gases,ZeeScalar) OF Norm
xx AS DISTRIBUTION(Gases, ZeeVector) OF Norm
P AS Norm
```

```
T AS DISTRIBUTION(ZeeScalar) OF Norm
TT AS DISTRIBUTION(ZeeVector) Of Norm
qh AS DISTRIBUTION(ZeeVector) OF Norm
s AS DISTRIBUTION(ZeeScalar) OF Norm
Ng AS DISTRIBUTION(Gases, ZeeVector) OF Norm
pcap AS DISTRIBUTION(ZeeScalar) OF Norm
Nl AS DISTRIBUTION(ZeeVector) OF Norm
Nwt AS Norm
xvap AS DISTRIBUTION(ZeeScalar) OF Norm
ss AS DISTRIBUTION(ZeeVector) OF Norm
alpha AS DISTRIBUTION(ZeeVector) OF Norm
alphai AS DISTRIBUTION(Gases-Gases.First-Gases.Last,ZeeVector) OF Norm
Dwl AS DISTRIBUTION(ZeeVector) OF Norm

dHvap AS Norm
kw AS Norm
Visc AS Norm
PDij AS ARRAY(Gases,Gases) OF Norm
dens AS Norm
vol AS Norm
surften AS Norm

zscalar AS DISTRIBUTION(ZeeScalar) OF Norm
zvector AS DISTRIBUTION(ZeeVector) OF Norm

SELECTOR
ConsiderHeatofVaporization AS (Yes, No) DEFAULT Yes
ConsiderLiquidBlockage AS (Yes,No) DEFAULT Yes
SimplifyDarcysLaw AS (Yes,No) DEFAULT No
EdgeScalars AS (Centered, Offset, CenteredExceptSS) DEFAULT Centered

SET
FOR ii := 1 TO numvolumes DO
    scalarpoints(ii) := (ii-0.5)/numvolumes;
END
ZeeVector := [BFDM, 1, numvolumes];
ZeeScalar := [FFDM, 1, scalarpoints];
ChanPort.numgas := numgas;
CLPort.numgas := numgas;
ChapmanEnskog.T := NominalTemp;

BOUNDARY
x(Gases-Gases.first-Gases.last,1) = ChanPort.x;
T(1) = ChanPort.T + Rh_cont*ChanPort.qh;
CLPort.qh = ChanPort.qh;
Nl(1) = ChanPort.Nliq;
Nwt = ChanPort.Ntot(1);
Ng(Gases-"Water",1) = ChanPort.Ntot(2:numgas);
-3816.44/(ChanPort.T-46.13)+3816.44/(T(1)-46.13)  =  pcap(1)*vol/(R*T(1))-
ChanPort.pcap*vol/(R*ChanPort.T);

x(Gases-Gases.first-Gases.last,0) = CLPort.x;
T(0) = CLPort.T;

Nwt = CLPort.Ntot(1);
Ng(Gases-"Water",0) = CLPort.Ntot(2:numgas);
pcap(0) = CLPort.pcap;

P = ChanPort.P = CLPort.P ;
ChanPort.I = CLPort.I;
ChanPort.Phi = CLPort.Phi;
```

```
EQUATION
FOR ii IN Gases-Gases.Last DO
    FOR jj IN Gases.Subset(Gases.Index(ii)+1) DO
        PDij(ii,jj) = PDij(jj,ii);
        PDij(ii,jj) = ChapmanEnskog.PD_g_ij(ii,jj)*por/tort;
    END
END
# Stefan-Maxwell
CASE Considerliquidblockage OF
When Yes:
FOR z:= 0 TO 1|- DO
    PARTIAL(x("Water",z), ZeeScalar) = L*R*TT(z)*((1+(2-
3*ss(z)+ss(z)^2)*alpha(z)*P)/((1-ss(z))^3+(2-
2*ss(z)^2+ss(z)^3)*alpha(z)*P)*SIGMA((xx("Water",z)*Ng(Gases-"Water",z)-xx(Gases-
"Water",z)*Ng("Water",z))/PDij("Water",Gases-"Water")));
    FOR ii IN Gases-"Water"-Gases.Last DO
        PARTIAL(x(ii,z), ZeeScalar) = L*R*TT(z)*((1-ss(z))^(-3)*SIGMA((xx(ii,z)*Ng(,z)-
xx(,z)*Ng(ii,z))/PDij(ii,)) + ((1-ss(z))^(-3)-1)*alphai(ii,z)*P/((1-ss(z))^3+(2-
2*ss(z)^2+ss(z)^3)*alpha(z)*P)*SIGMA((xx("Water",z)*Ng(Gases-"Water",z)-xx(Gases-
"Water",z)*Ng("Water",z))/PDij("Water",Gases-"Water")));
    END
END
When No:
FOR z:= 0 TO 1|- DO
    FOR ii IN Gases-Gases.Last DO
        PARTIAL(x(ii,z), ZeeScalar) = L*(R*TT(z))*SIGMA((xx(ii,z)*Ng(,z)-
xx(,z)*Ng(ii,z))/PDij(ii,));
    END
END
END

# Convenience Variables
CASE EdgeScalars OF
    When Offset:
    FOR z:= 0 TO 1 DO
        xx(,z) = x(,z+1); #}(x(,z+1)+x(,z))/2;
        TT(z)  = T(z+1); #(T(z+1) + T(z))/2;
        ss(z)  = s(z+1); #}(s(z+1) + s(z))/2;
    END
    When Centered:
    FOR z:= 0 TO 1 DO
        xx(,z) = (x(,z+1)+x(,z))/2;
        TT(z)  = (T(z+1) + T(z))/2;
        ss(z)  = (s(z+1) + s(z))/2;
    END
    When CenteredExceptSS:
    FOR z:= 0 TO 1 DO
        xx(,z) = (x(,z+1)+x(,z))/2;
        TT(z)  = (T(z+1) + T(z))/2;
        ss(z)  = (s(z+1));
    END
END
FOR z:= 0 TO 1 DO
    FOR ii IN Gases-"Water"-Gases.Last DO
        1e6*alphai(ii,z) = 1e6*(xx(ii,z)*Dwl(z)/PDij("Water",ii));
    END
    1e6*alpha(z) = 1e6*SIGMA(xx(Gases-"Water",z)*Dwl(z)/PDij("Water",Gases-"Water"));

    Dwl(z)*dHVap*1e5*3816.44/(TT(z)-46.13)^2*exp(11.6832-3816.44/(TT(z)-46.13)) =
R*TT(z)*kw*por/tort;
```

```
END

# Non-water mass balance (steady state, no consumption)
FOR jj IN Gases-"Water" DO
    FOR z:= 0 TO 1|- DO
        ng(jj,z) = ng(jj,z+1);
    END
END

# Water mass balance
#PARTIAL(Nwt(0|+:1), ZeeVector) = 0;
Ng("Water",)+Nl = Nwt;

# Energy balance just water evaporation
CASE ConsiderHeatofVaporization OF
    When No:
    qh - CLPort.qh = 0 ;
    When Yes:
    qh - CLPort.qh = dHvap*Nl;
END

# Heat flux equation
qh(0:1) = -kh*PARTIAL(T(0:1|-), ZeeScalar)/L;

# Vapor pressure of water
xvap = 1e5/P*exp(11.6832-3816.44/(T-46.13)) ;

# Capillary Pressure
FOR z:= 0 TO 1|- DO
    (1-s(z)) = MAX((1+(MAX(pcap(z),0)/(jc*surften*sqrt(por/perm)))^ppn)^(-ppm),0.01);
END
IF pcap(1) < 1e-3 THEN # This seems to be necessary to get the model to solve.
    s(1)=0;
ELSE
    (1-s(1)) = MAX((1+(MAX(pcap(1),0)/(jc*surften*sqrt(por/perm)))^ppn)^(-ppm),0.01);
END

CASE SimplifyDarcysLaw OF
    When No:
    # Darcy's law
    FOR z:= 0 TO 1|- DO
        Nl(z) = -perm*(MAX((s(z)-percthreshold)/(1-percthreshold),0)^4+MAX((s(z+1)-
percthreshold)/(1-percthreshold),0)^4)/2/visc/vol/L*PARTIAL(pcap(z), ZeeScalar); # Ok,
so this works now. Thanks gPROMS!
    END
    When Yes:
    FOR z:= 0 TO 1|- DO
        Nl(z) = -perm/visc/vol/L*1e-4*pp1*PARTIAL(s(z), ZeeScalar);
    END
END
# Finally, the liquid vapor equilibrium. How to do this? Good question!
FOR z := 0 TO 1 DO
    pcap(z)*vol = R*T(z)*(log(x("Water",z)*P/1e5)-(11.6832-3816.44/(T(z)-46.13)));
#    IF x(1,z)+R*T(z)/(P*vol)*s(z)>xvap(z) THEN
#        x(1,z) = xvap(z);
#    ELSE
#        pcap(z) = 0;
#    END
END

# Sum of mole fractions
```

```
INTEGRAL(jj OVER Gases; x(jj,)) = 1;

ASSIGN
dHvap :=
1000*(30.092*NominalTemp/1000+6.832514*(NominalTemp/1000)^2/2+6.793435*(NominalTemp/100
0)^3/3-2.534480*(NominalTemp/1000)^4/4-0.082139/(NominalTemp/1000)-250.8810
    -( -203.6060*NominalTemp/1000+1523.290*(NominalTemp/1000)^2/2-
3196.413*(NominalTemp/1000)^3/3+2474.455*(NominalTemp/1000)^4/4-
3.855326/(NominalTemp/1000)-256.5478)) ; # FROM NIST WEBBOOK

# Meaningless and unused, but must be assigned due to 3x3 array representation
FOR ii IN Gases DO
    PDij(ii,ii) := 1;
END

# Thermal conductivity from Ramires (see Endnote)
kw := 0.6065*(-1.48445+4.12292*NominalTemp/298.15-1.63866*NominalTemp^2/298.15^2) ;

#Viscosity from Kestin 1978 J Phys Chem Ref Data Vol 7 No 3
visc := 1.002e-3*exp((293.15-NominalTemp)/(NominalTemp-273.15+96)*(1.2378-1.303e-
3*(293.15-NominalTemp)+3.06e-6*(293.15-NominalTemp)^2+2.55e-8*(293.15-NominalTemp)^3));

# Density of water from "ITS-90 Density of Water Formulation for Volumetric Standards
Calibration" J Res Natl Inst Stand Technol 97 335 (1992)
dens := (999.83952+16.945176*(NominalTemp-273.15)-7.9870401e-3*(NominalTemp-273.15)^2-
46.170461e-6*(NominalTemp-273.15)^3+105.56302e-9*(NominalTemp-273.15)^4-280.54253e-
12*(NominalTemp-273.15)^5)/(1+16.89785e-3*(NominalTemp-273.15));

vol := 0.01801528/((999.83952+16.945176*(NominalTemp-273.15)-7.9870401e-3*(NominalTemp-
273.15)^2-46.170461e-6*(NominalTemp-273.15)^3+105.56302e-9*(NominalTemp-273.15)^4-
280.54253e-12*(NominalTemp-273.15)^5)/(1+16.89785e-3*(NominalTemp-273.15)));

surften := 235.8e-3*((647.15-NominalTemp)/647.15)^1.256*(1-0.625*(647.15-
NominalTemp)/647.15); # From Vargaftik, Volkov, and Voljak, J Phys Chem Ref Data, V 12
N 3 1983

FOR z:= 0 TO 1 DO
    zvector(z) := L0 + L*z;
END
FOR z:= 0 TO 1 DO
    zscalar(z) := L0 + L*z;
END

PRESET
T := 328:273:373;
TT := 328:273:373;
s := 0:0:0.9;
ss := 0:0:0.9;
x("Water",) := 0.1:1e-10:1;
x(Gases-"Water",) := 0.3:1e-10:1;

INITIALIZATION_PROCEDURE test DEFAULT
    START
        ConsiderHeatofVaporization := No;
    END
    NEXT
        JUMP_TO
            ConsiderHeatofVaporization := Yes;
        END
    END
```

Model MEAnoMPL

```
# Glue model that connects all of the pieces. Also includes interfacial saturation
equations.

PARAMETER
s0int AS REAL   # Interfacial saturation when flooded
Rdrop AS REAL   # Radius of interfacial droplets

UNIT
AFF  AS FF0D
AGDL AS GDLSteadyState_enhanced_vapor
ACL  AS PlanarAnodeSS
Mem  AS MemSS_relative_phi
CL   AS CLSteadyState_enhanced_vapor_ngases
GDL  AS GDLSteadyState_enhanced_vapor
CFF  AS FF0D

SELECTOR
Interface AS (Flooded, Dry) DEFAULT Dry

VARIABLE
GDLperm AS Norm         # Just so we can see the result
ICell, ECell AS Norm    # Cell current and potential
sint AS Norm            # Interfacial saturation

TOPOLOGY
AFF.GDL         = AGDL.ChanPort;
AGDL.CLPort     = ACL.GDLPort;
ACL.MemPort     = Mem.LeftPort;
Mem.RightPort   = CL.MemPort;
CL.GDLPort      = GDL.CLPort;
GDL.ChanPort    = CFF.GDL;

EQUATION
ICell = GDL.ChanPort.I;
ECell = GDL.ChanPort.Phi-AGDL.ChanPort.Phi;
CASE Interface OF
    When Dry:
        sint = 0;
        # Parts in {} determine whether the interface is looded when there's
condensation
        # or just flooded when there's liquid flux in the GDL
        SWITCH TO Flooded IF GDL.Nl(0) {- GDL.CLPort.Nliq} > 1e-6;
    When Flooded:
        sint  = MIN(((GDL.Nl(0) {- GDL.CLPort.Nliq})/1e-3),1)*s0int;
        #sint  = (GDL.Nl(0) - GDL.CLPort.Nliq)*s0int/(1e-3+(GDL.Nl(0) -
GDL.CLPort.Nliq));
        SWITCH TO Dry IF GDL.Nl(0) - GDL.CLPort.Nliq <-1e-6;
END
# Relative length scaling factor for O2 mass transfer
CL.Lr_MT = sqrt(1+MAX(sint,0)*(2+1.5*(Rdrop/CL.L)+0.25*(Rdrop/CL.L)^2));

ASSIGN
GDLperm := GDL.perm;

INITIALIZATION_PROCEDURE Anodetest
USE
    ACL:ip;
END
```

```
INITIALIZATION_PROCEDURE IAmHopeful # Lots of steps, but this is what it took.
START
    ACL.IgnoreAnode := ACL.Yes;
    CL.HeatMode := CL.Constant_Generation;
    CL.CurrentDistribution := CL.IsUniform;
    Mem.HeatMode := Mem.Constant_Generation;

    AGDL.ConsiderHeatofVaporization := AGDL.No;
    GDL.ConsiderHeatofVaporization := GDL.No;

    CL.EdgeScalars   := CL.Offset;
    GDL.EdgeScalars  := GDL.Offset;
    AGDL.EdgeScalars := AGDL.Offset;
    Mem.EdgeScalars  := Mem.Offset;

    AFF.netwaterdrag := Aff.No;
    CFF.netwaterdrag := Cff.No;
END
NEXT
    JUMP_TO
        ACL.IgnoreAnode := ACL.No;
    END
END
NEXT
    JUMP_TO
        Mem.HeatMode := Mem.Full;
    END
END
NEXT
    JUMP_TO
        CL.HeatMode := Cl.Full;
    END
END
NEXT
    JUMP_TO
        AFF.netwaterdrag := Aff.Yes;
        CFF.netwaterdrag := Cff.Yes;
    END
END
NEXT
    JUMP_TO
        CL.CurrentDistribution  := CL.PO2noPhiOxide;
    END
END
NEXT
    JUMP_TO
#        CL.CurrentDistribution  := CL.PhiPO2noOxide;
        CL.CurrentDistribution  := CL.PO2OxideNoPhi;
    END
END
NEXT
    JUMP_TO
        CL.CurrentDistribution  := Cl.NonUniform;
    END
END
NEXT
    JUMP_TO
        AGDL.ConsiderHeatofVaporization := AGDL.Yes;
        GDL.ConsiderHeatofVaporization := GDL.Yes;
    END
END
```

```
NEXT
    JUMP_TO
        CL.EdgeScalars   := CL.Centered;
        GDL.EdgeScalars  := GDL.Centered;
        AGDL.EdgeScalars := AGDL.Centered;
        Mem.EdgeScalars  := Mem.Centered;
    END
END
```

Model MemSS_relative_phi

```
# Steady-state nonisothermal membrane model using concentrated solution theory.

PARAMETER
R               AS REAL DEFAULT 8.3145
F               AS REAL DEFAULT 96485
pi AS REAL DEFAULT 3.14159265
L0 AS REAL DEFAULT 0    # m, Position of left edge for graphs
L               AS REAL # m, Thickness
NominalTemp     AS REAL # K, Cell operating temperature
kh              AS REAL # W/m-K, Thermal conductivity
rho_n           AS REAL # kg/m3, Density of ionomer
EW              AS REAL # kg/mol, Equivalent weight of ionomer
MW_w            AS REAL # kg/mol, Molecular weight of water
numvolumes      AS INTEGER  # Number of grid points
scalarpoints    AS ARRAY(numvolumes) OF REAL #  Normalized location of those pts

DISTRIBUTION_DOMAIN
ZeeVector AS [0:1]  # Vector variables are defined at the edges of control volumes
ZeeScalar AS [0:1]  # Scalar variables are defined at the centers of control volumes

PORT
LeftPort AS MemPortSS
RightPort AS MemPortSS

VARIABLE
T               AS DISTRIBUTION(ZeeScalar) OF Norm  # Temperature
TT              AS DISTRIBUTION(ZeeVector) OF Norm  # Temperature (vector grid)
qh              AS DISTRIBUTION(ZeeVector) OF Norm  # Heat flux
Nw              AS Norm                             # Water Flux
i2              AS Norm                             # Ionic current
phi2a           AS DISTRIBUTION(ZeeScalar) OF Norm  # Ionic potential - absolute...
phi2r           AS DISTRIBUTION(ZeeScalar) OF Norm  # ...and relative for numerical
reasons
activity        AS DISTRIBUTION(ZeeScalar) OF Norm  # Water activity
aactivity       AS DISTRIBUTION(ZeeVector) OF Norm  # (vector grid)
lambda          AS DISTRIBUTION(ZeeScalar) OF Norm  # Water content (mol/mol SO3-)
llambda         AS DISTRIBUTION(ZeeVector) OF Norm  # (vector grid)
joule           AS DISTRIBUTION(ZeeScalar) OF Norm  # Joule heating term
backdiffusion   AS DISTRIBUTION(ZeeVector) OF Norm  # Backdiffusive flux of water
kappa           AS DISTRIBUTION(ZeeVector) OF Positive  # Conductivity of ionomer
D_w             AS DISTRIBUTION(ZeeVector) OF Positive  # Fick's law diffusivity of
water
xi              AS DISTRIBUTION(ZeeVector) OF Positive  # Electroosmotic drag
coefficient
alpha_diff      AS DISTRIBUTION(ZeeVector) OF Positive  # Water diffusivity (chem.
pot.)
dHvap           AS Norm     # Heat of vaporization of water (from ionomer)
dens, vol       AS Norm     # Density and molar volume of water
```

```
zscalar         AS DISTRIBUTION(ZeeScalar) OF Norm  # Location of scalar points
zvector         AS DISTRIBUTION(ZeeVector) OF Norm  # Location of vector points

SELECTOR
# These selectors are used to simplify the problem, usually for initialization.
HeatMode AS (Isothermal, Constant_Generation, Full) DEFAULT Full
IonomerTransportProperties AS (Saturated, ConcentrationDependent) DEFAULT
ConcentrationDependent
EdgeScalars AS (Centered, Offset) DEFAULT Centered

SET     # Define grids
FOR ii := 1 TO numvolumes DO
    scalarpoints(ii) := (ii-0.5)/numvolumes;
END
ZeeVector := [BFDM, 1, numvolumes];
ZeeScalar := [FFDM, 1, scalarpoints];

BOUNDARY    # Straightforward
T(1) =  RightPort.T;
T(0) =  LeftPort.T;
qh(1)= RightPort.qh;
qh(0)= LeftPort.qh;
Nw   =  RightPort.Nw;
Nw   =  LeftPort.Nw;
i2   =  RightPort.I;
i2   =  LeftPort.I;
activity(1) = RightPort.activity;
activity(0) = LeftPort.activity;
Phi2a(1)    = RightPort.Phi;
Phi2a(0)    = LeftPort.Phi;
phi2r(1)    = 0;    # Relative potential is used to simplify numerical solution

EQUATION


# Energy balance. Joule heating is only generation term.
CASE HeatMode OF
    When Full:
        FOR z:= 0|+ TO 1 DO
            PARTIAL(qh(z), ZeeVector)/L = joule(z);
        END
    When Constant_Generation:
        FOR z:= 0|+ TO 1 DO
            qh(z) = qh(z-1);
        END
    When Isothermal:
        qh(0|+:1) = 0;
END

# Joule heating term has to be calculated separately because gPROMS doesn't want
# to have PARTIALs for ZeeVector and ZeeScalar in the same equation.
FOR z:= 0|+ TO 1|- DO
    L*joule(z) = L*(i2^2/kappa(z)+i2^2/kappa(z-1))/2;
END
L*joule(1) = L*i2^2/kappa(1) ;
L*joule(0) = L*i2^2/kappa(0) ;
#L*joule(1) = -i2*PARTIAL(Phi2r(1),ZeeScalar) ; # Old alternative formula

FOR z:= 0 TO 1 DO   # Water uptake isotherm
    lambda(z) = 0.043 + 17.81*activity(z) - 39.85*activity(z)^2 + 36.0*activity(z)^3 ;
END
```

```
# Heat flux equation
qh(0:1) = -kh*PARTIAL(T(0:1|-), ZeeScalar)/L;

FOR z:= 0 TO 1|- DO     # Water transport equations
    Nw = 1/L*((-(kappa(z)*xi(z)/F)*PARTIAL(phi2r(z), ZeeScalar) - (alpha_diff(z) +
kappa(z)*xi(z)^2/F^2)*R*TT(z)/aactivity(z)*PARTIAL(activity(z), ZeeScalar) ));
    backdiffusion(z) = -1/L*(alpha_diff(z))*R*TT(z)/aactivity(z)*PARTIAL(activity(z),
ZeeScalar) ;
END
FOR z:= 0 TO 1|- DO     # Ionomer proton flux - modified Ohm's law
    L*i2 = (-kappa(z)*PARTIAL(phi2r(z), ZeeScalar) -
(kappa(z)*xi(z)/F)*R*TT(z)/aactivity(z)*PARTIAL(activity(z), ZeeScalar)) ;
END

CASE IonomerTransportProperties OF
    When ConcentrationDependent:
        FOR z:= 0 TO 1 DO
            # Conductivity (various sources)
            #kappa(z) = 1.45*exp(2.29*aactivity(z))*EXP(1268*(1/353-1/TT(z))) ; # S/m
Experimental, with literature activation energy
            kappa(z) = 100*(0.005139*llambda(z)-0.00326)*EXP(1268*(1/303-1/TT(z))); #
Springer et al.
            #kappa(z) = 1.1524*100*(0.005139*llambda(z)-0.00326)*EXP(1268*(1/303-
1/TT(z))); # Corrected to match my conductivity at 100% RH
            #kappa(z) = 1.303*100*(0.005139*llambda(z)-0.00326)*EXP(1268*(1/303-
1/TT(z))); # Corrected to match my conductivity at 90% RH

            # Diffusion coefficient of water in ionomer (Fuller's thesis)
            D_w(z)*1e9 = 1e9*1e-4*3.5e-2*EXP(-2436/TT(z))*llambda(z)/14 ; # m^2/s,
original equation had units of cm^2/s
            # Mittelsteadt
            #IF llambda(z)<4 THEN
            #D_w(z)*1e9 = 1e9*1e-4*EXP(-2436/TT(z))*(7.32e-
4*exp(0.12*llambda(z))+5.41e-6*exp(1.44*llambda(z)));
            #ELSE
            #D_w(z)*1e9 = 1e9*1e-4*EXP(-2436/TT(z))*(1.58e5*exp(-
4.66*llambda(z))+1.45e-3*exp(0.04*llambda(z)));
            #END

            # Chemical potential referenced diffusion coefficient.
            1e9*alpha_diff(z) =
1e9*D_w(z)/(R*T(z))*rho_N/EW*(1+MW_w*rho_N/(EW*dens)*(0.043+17.81*aactivity(z)-
39.85*aactivity(z)^2+36*aactivity(z)^3))^(-2)*(17.81*aactivity(z)-
79.7*aactivity(z)^2+108*aactivity(z)^3);
            # Electroosmotic drag coefficient (informed by my own experiments, but just
a rough approximation pending better data and fitting)
            xi(z) = 1.1 + 0.9/(1+EXP(-2*(llambda(z)-5.5))) ;

        END
    When Saturated:
        FOR z:= 0 TO 1 DO
            kappa(z) = 1.45*exp(2.29*1)*EXP(1268*(1/353-1/NominalTemp)) ; # S/m
Experimental, with literature activation energy
            # Diffusion coefficient of water in ionomer (Fuller's thesis)
            D_w(z)*1e9 = 1e9*1e-4*3.5e-2*EXP(-2436/NominalTemp)*14/14 ; # m^2/s,
original equation had units of cm^2/s
            #D_w(z)*1e9 = 1e9*1e-4*EXP(-2436/NominalTemp)*(1.58e5*exp(-4.66*14)+1.45e-
3*exp(0.04*14));
            # Chemical potential referenced diffusion coefficient.
```

```
            1e9*alpha_diff(z) =
1e9*D_w(z)/(R*NominalTemp)*rho_N/EW*(1+MW_w*rho_N/(EW*dens)*(0.043+17.81-39.85+36))^(-
2)*(17.81-79.7+108);
            # Electroosmotic drag coefficient (informed by my own experiments, but just
a rough approximation pending better data and fitting)
            xi(z) = 1.1 + 0.9/(1+EXP(-2*(14-5.5))) ;
        END
END

phi2r(0:1|-)-phi2r(1) = phi2a(0:1|-)-phi2a(1); # Relative to absolute conversion
CASE EdgeScalars OF # These are the scalar variables needed in eqs. at edge points
    When Offset:    # Simplified for initialization
        FOR z:= 0 TO 1 DO
            TT(z)  = T(z+1);
            llambda(z) = lambda(z+1);
            aactivity(z) = activity(z+1);
        END
    When Centered:  # Preferred form
        FOR z:= 0 TO 1 DO
            TT(z)  = (T(z+1) + T(z))/2;
            llambda(z) = (lambda(z+1)+lambda(z))/2;
            aactivity(z) = (activity(z+1)+activity(z))/2;
        END
END

ASSIGN
dHvap :=
1000*(30.092*NominalTemp/1000+6.832514*(NominalTemp/1000)^2/2+6.793435*(NominalTemp/100
0)^3/3-2.534480*(NominalTemp/1000)^4/4-0.082139/(NominalTemp/1000)-250.8810
    -( -203.6060*NominalTemp/1000+1523.290*(NominalTemp/1000)^2/2-
3196.413*(NominalTemp/1000)^3/3+2474.455*(NominalTemp/1000)^4/4-
3.855326/(NominalTemp/1000)-256.5478)) ; # FROM NIST WEBBOOK

# Density of water from "ITS-90 Density of Water Formulation for Volumetric Standards
Calibration" J Res Natl Inst Stand Technol 97 335 (1992)
dens := (999.83952+16.945176*(NominalTemp-273.15)-7.9870401e-3*(NominalTemp-273.15)^2-
46.170461e-6*(NominalTemp-273.15)^3+105.56302e-9*(NominalTemp-273.15)^4-280.54253e-
12*(NominalTemp-273.15)^5)/(1+16.89785e-3*(NominalTemp-273.15));
# Molar volume of water is just MW / density
vol := 0.01801528/((999.83952+16.945176*(NominalTemp-273.15)-7.9870401e-3*(NominalTemp-
273.15)^2-46.170461e-6*(NominalTemp-273.15)^3+105.56302e-9*(NominalTemp-273.15)^4-
280.54253e-12*(NominalTemp-273.15)^5)/(1+16.89785e-3*(NominalTemp-273.15)));

FOR z:= 0 TO 1 DO   # Position of vector points
    zvector(z) := L0 + L*z;
END
FOR z:= 0 TO 1 DO   # Position of scalar points
    zscalar(z) := L0 + L*z;
END

PRESET  # Initial guesses for certain variables in the solver which were necessary
        # to converge during initialization
T           := 353:273:373;
TT          := 353:273:373;
activity    := 1:1e-10:10;
aactivity   := 1:1e-10:10;
lambda      := 14:0:30;
llambda     := 14:0:30;
phi2r       := 0:-1:1;

INITIALIZATION_PROCEDURE test DEFAULT
```

```
    # This initialization procedure is only used when testing the submodel in
isolation.
    START
        HeatMode := Constant_Generation;
    END
    NEXT
        JUMP_TO
            HeatMode := Full;
        END
    END
```

Model PlanarAnodeSS

```
PARAMETER
R AS REAL DEFAULT 8.3145
#kh AS REAL # Thermal conductivity
#L AS REAL
numgas AS INTEGER DEFAULT 2
NominalTemp AS REAL
F AS REAL DEFAULT 96485         # C/eq, Faraday's constant
UHRHE AS REAL DEFAULT 0         # V, Thermoneutral potential of RHE, Assumed
L0 AS REAL DEFAULT 0            # Position in stack for graphs

PORT
GDLPort AS GDL_SS_eq_pcap
MemPort AS MemPortSS

VARIABLE
pH2, pVap, dHvap AS Norm
Vol AS Norm

SELECTOR
IgnoreAnode AS (Yes,No) DEFAULT No

SET
GDLPort.numgas := numgas;

BOUNDARY
# The anode GDL is basically backwards. It goes from 0 at anode CL to 1 at channel
# Fluxes are all opposite of what they should be. Ugly, but it works.
-GDLPort.I = MemPort.I;
CASE IgnoreAnode OF
    When No:
    -GDLPort.Ntot(1) = MemPort.Nw;
    MemPort.qh = -GDLPort.qh + MemPort.I*(GDLPort.Phi-MemPort.Phi-UHRHE) +
dHVap*MemPort.Nw;
    GDLPort.pcap*vol = R*MemPort.T*log(MemPort.activity);
    When Yes:
    MemPort.Nw = 0;
    MemPort.qh = 0;
    GDLPort.Ntot(1) = 0;
END
GDLPort.T = MemPort.T;
-GDLPort.Ntot(2) = MemPort.I/(2*F);
GDLPort.Nliq = 0;

EQUATION
GDLPort.Phi-MemPort.Phi=-R*MemPort.T/(2*F)*log(pH2/1e5);    # Nernst equation
pVap = 1e5*exp(11.6832-3816.44/(MemPort.T-46.13)) ;         # Antoine Equation
pH2 = GDLPort.P-pVap*MemPort.activity;  # Hydrogen partial pressure in anode
```

```
ASSIGN
dHvap :=
1000*(30.092*NominalTemp/1000+6.832514*(NominalTemp/1000)^2/2+6.793435*(NominalTemp/100
0)^3/3-2.534480*(NominalTemp/1000)^4/4-0.082139/(NominalTemp/1000)-250.8810
    -( -203.6060*NominalTemp/1000+1523.290*(NominalTemp/1000)^2/2-
3196.413*(NominalTemp/1000)^3/3+2474.455*(NominalTemp/1000)^4/4-
3.855326/(NominalTemp/1000)-256.5478)) ; # FROM NIST WEBBOOK
vol := 0.01801528/((999.83952+16.945176*(NominalTemp-273.15)-7.9870401e-3*(NominalTemp-
273.15)^2-46.170461e-6*(NominalTemp-273.15)^3+105.56302e-9*(NominalTemp-273.15)^4-
280.54253e-12*(NominalTemp-273.15)^5)/(1+16.89785e-3*(NominalTemp-273.15)));

PRESET
pH2 := 8e4:1e-10:1e7;
MemPort.activity := 1:1e-10:10;

INITIALIZATION_PROCEDURE ip DEFAULT
START
    IgnoreAnode := Yes;
END
NEXT
    JUMP_TO
        IgnoreAnode := No;
    END
END
```

Variables and Connections:

```
{
  gPROMS input file generated by gPROMS ModelBuilder 3.5.3
  Thu Apr 23 00:23:36 EDT 2015

  Channel Model -> file:/C:/Users/bsetzler3/Documents/gProms/Channel Model.gPJ
}

DECLARE TYPE # Channel Model:Norm
    Norm = 0.0 : -1.0E+100 : 1.0E+100
END

DECLARE TYPE # Channel Model:Positive
    Positive = 0.1 : 1E-100 : 1.0E+100
END

CONNECTIONTYPE CM_16686c8::GDL_SS_eq_pcap # Channel Model:GDL_SS_eq_pcap

    PARAMETER
        numgas AS INTEGER DEFAULT 3

    VARIABLE
        x AS DISTRIBUTION (numgas - 2) OF Norm
        T AS Norm
        qh AS Norm
        Ntot AS DISTRIBUTION (numgas) OF Norm
        pcap AS Norm
        Nliq AS Norm
        I AS Norm
        Phi AS Norm
        P AS Positive
```

```
END # CONNECTIONTYPE GDL_SS_eq_pcap

CONNECTIONTYPE CM_16686c8::MemPortSS # Channel Model:MemPortSS

    VARIABLE
        T AS Norm
        qh AS Norm
        Nw AS Norm
        I AS Norm
        Phi AS Norm
        activity AS Positive


END # CONNECTIONTYPE MemPortSS
```